



8-2014

Characterizing the relationship of part of the Inner Piedmont and Pine Mountain window, Georgia, from detailed geologic mapping, geochemistry, geochronology, and structural analysis at the southwestern end of the Cat Square terrane

Justin Randolph Rehrer
University of Tennessee - Knoxville, jrehrer@utk.edu

Follow this and additional works at: https://trace.tennessee.edu/utk_gradthes

 Part of the [Geochemistry Commons](#), [Geology Commons](#), and the [Tectonics and Structure Commons](#)

Recommended Citation

Rehrer, Justin Randolph, "Characterizing the relationship of part of the Inner Piedmont and Pine Mountain window, Georgia, from detailed geologic mapping, geochemistry, geochronology, and structural analysis at the southwestern end of the Cat Square terrane. " Master's Thesis, University of Tennessee, 2014.
https://trace.tennessee.edu/utk_gradthes/2845

This Thesis is brought to you for free and open access by the Graduate School at TRACE: Tennessee Research and Creative Exchange. It has been accepted for inclusion in Masters Theses by an authorized administrator of TRACE: Tennessee Research and Creative Exchange. For more information, please contact trace@utk.edu.

To the Graduate Council:

I am submitting herewith a thesis written by Justin Randolph Rehrer entitled "Characterizing the relationship of part of the Inner Piedmont and Pine Mountain window, Georgia, from detailed geologic mapping, geochemistry, geochronology, and structural analysis at the southwestern end of the Cat Square terrane." I have examined the final electronic copy of this thesis for form and content and recommend that it be accepted in partial fulfillment of the requirements for the degree of Master of Science, with a major in Geology.

Robert D. Hatcher Jr., Major Professor

We have read this thesis and recommend its acceptance:

Theodore C. Labotka, Micah Jessup

Accepted for the Council:

Carolyn R. Hodges

Vice Provost and Dean of the Graduate School

(Original signatures are on file with official student records.)

**Characterizing the relationship of part of the Inner Piedmont
and Pine Mountain window, Georgia, from detailed geologic
mapping, geochemistry, geochronology, and structural analysis
at the southwestern end of the Cat Square terrane**

A Thesis Presented for the
Master of Science
Degree
The University of Tennessee, Knoxville

Justin Randolph Rehrer
August 2014

Copyright © 2014 by Justin Randolph Rehrer
All rights reserved.

“Let those whom this picture does not satisfy paint their own; from the confrontation and the resulting search for more facts a better hypothesis than any present one may evolve.”

—John Rogers (1972)

Acknowledgments

Most importantly I want to express my gratitude toward my fellow brothers in arms and all those who have gone before me in military service. Thank you for all that you have done and all that you have sacrificed.

Thanks are owed to Dr. Robert D. Hatcher, Jr., for his willingness to accept a “rough around the edges” student (me), and for his mentoring throughout this project. Dr. Hatcher’s philosophy of a multidisciplinary approach to seeing the world through “structural geology-colored glasses” was one that caught my attention and now, after having experienced it first hand, has become a philosophy in which I truly believe. Thank you, Bob, for the freedom to develop ideas and come to conclusions on my own terms, and also for the guidance that made certain I didn’t fall flat on my face while doing so. I also extend thanks to my committee members, Drs. Ted Labotka and Micah Jessup, for their reviews, comments, and direction.

There are always people who work tirelessly behind the scenes, who make sure things run smoothly on a daily basis, and who never get enough recognition for the things they do. Those people for me are Nancy Meadows and Andrew Wunderlich. Nancy has read through every page of this thesis several times and corrected countless grammatical and spelling mistakes. Any errors that remain are not a reflection of her editing skills but instead are a product of my poor writing habits. Although still not perfect, my writing has improved greatly as a result of her influence. Andrew has been a good friend and a great asset for learning anything related to GIS, Adobe software, document formatting, Henley Street Bridge construction, and countless other things. He was great at teaching me how to do something in five minutes that took me several hours to accomplish the week before. Innumerable thanks to both of you.

I have acquired many colleagues and friends during my time at UT and they deserve credit for the influence they had on the outcome of this project. My first six months were spent mapping in the field with Chris Howard, who showed me how things were done in the Georgia Inner Piedmont. Thanks, Chris, for introducing me to the art of home brewing, and for “uno mas”, which never meant just one more. Matt Huebner has been a great friend, colleague, collaborator, and mentor over the past three years and a lot of what I know about southern Appalachian geology is owed to conversations with him. Thanks to Mike Lucas, who graciously reviewed and edited several chapters

presented in this thesis, and to Phil Derryberry, Remy Leger, Tim Diedisch, and Kyle White for our intellectual conversations and entertainment at professional meetings and excursions downtown.

My gratitude is extended to several individuals outside of the University of Tennessee. Arthur Merschat, Joe Hill, Mike Higgins, Ralph Crawford, John Costello, and Randy Kath participated in summer field reviews in Georgia and offered invaluable advice and encouragement about my work. Randy Kath and Deana Sneyd graciously shared some of their unpublished research in the Barnesville quadrangle, which was incorporated into this study. Drew Coleman, Ryan Mills, and Jez Ingles at UNC-Chapel Hill have my appreciation for the use of their rock preparation facilities for zircon separation, along with Matt Coble and the SUMAC SHRIMP-RG facility staff for their time and instruction while using that instrument. Clayton Loehn and Mark Pecha from the Arizona LaserChron Center likewise have my appreciation for their assistance preparing zircon mounts and using the LA-ICPMS. Recognition is also owed to the land owners in Spalding and Lamar Counties, Georgia, who allowed access to their property, without which no mapping could have been accomplished. I am also grateful for the patience demonstrated by the call center operator at the Lamar County Sheriff's Office, who received numerous calls about a suspicious person wandering neighborhoods wearing an orange vest with a hammer strapped to his belt. Thank you to the Sheriff's deputies who came to investigate and were kind enough not to arrest me.

Lastly, I am forever indebted to those who instilled in me from a young age, curiosity and a passion for science, and to those that have cultivated and groomed those interests over the years. A sincere thank you to my parents and grandparents for having the patience to let me find my own way in life, and for always being there to set me back on the right path. Jane Fennelly mentored me throughout my high school years and championed my success when few others would. Joe Hill was my undergraduate advisor and among other things showed me that it's important to attend lectures on a regular basis, lest one be excluded from a discussion wherein one would have been informed that the midterm project deadline had been extended. Joe taught structural geology to me the same way that Dr. Hatcher had taught him several years earlier; this proved to be a great advantage.

Thank you.

Abstract

Geologic investigations at the southwestern end of the Cat Square terrane (CSt) in central Georgia provided new insight into the complex tectonic history of the Pine Mountain window (PMw) and neighboring Inner Piedmont terranes. Detailed 1:24,000-scale geologic mapping of an approximately 180 km² area near Barnesville, Georgia has provided the foundation for further geochemical, geochronologic, and structural analyses refining models for tectonic development and emplacement of the CSt and PMw.

Whole-rock geochemical analyses of several CSt amphibolites yielded data suggesting a continental back-arc setting for genesis of the Cat Square basin (CSb). Major element data confirm derivation from a basaltic protolith and support the hypothesis that CSt amphibolites represent vestiges of ocean crust once comprising the CSb floor. Mid-ocean ridge basalt normalized multi-element diagrams and tectonic discriminant diagrams indicate that, while the CSb likely developed as a back-arc basin, basalt generated was not homogenous and involved mixing of at least two distinct magma components.

Zircon geochronologic analyses of select lithologies provided new data regarding the crystallization and deformation history of basement units of the PMw, plus a maximum depositional age of the CSb. SHRIMP-RG ages of zircons from basement felsic gneiss, the Woodland Gneiss, and basement tonalite yielded approximate ages of 1158, 1040, and 1011 Ma, respectively. Analysis of three detrital samples of CSt biotite gneiss via LA-ICPMS yielded a 602 ± 8 Ma age for the youngest zircon and peak ages of 1356, 1232, 1171, 1054, 1030, 954, and 858 Ma for the suite. The older of the two ages provides a robust upper limit on the depositional age of the CSb, but does not refute the younger interpreted age of the basin proposed by others.

Structural analysis of the study area supports the hypothesis that the PMw is structurally complex and is framed by at least three faults of different ages. These interpretations have advanced our understanding of the tectonic history of the PMw from once inferring a simple erosional hole in a thrust sheet to now suggesting the Pine Mountain terrane was a microcontinent rifted from the Laurentian margin during the breakup of Rodinia.

Table of Contents

Chapter 1

Introduction

Research Objectives	2
Location of Study Area.....	3
Methods	6
Previous Work.....	9
Geologic Background.....	12

Chapter 2

Lithologic Units in the Study Area

Tugaloo terrane/Western Inner Piedmont.....	18
Lower(?) Tallulah Falls Formation	18
Cat Square terrane/Eastern Inner Piedmont.....	24
Pine Mountain window	36
Fault rocks.....	47

Chapter 3

Geochemistry of Inner Piedmont amphibolites at the southwestern end of the

Cat Square terrane

Introduction	49
Methods	50
Element Mobility.....	56
Major Element Data	61
Trace Element Data.....	66
Discussion	78
Tectonic Synthesis	81
Summary	83
Conclusions	84

Chapter 4

Zircon geochronology of selected samples from the Cat Square terrane and

Pine Mountain window, central Georgia

Introduction	85
Samples	85
Methods	88
Results	95
Summary and discussion.....	117

Chapter 5

Structural analysis of the Inner Piedmont and Pine Mountain window at the southwestern end of the Cat Square terrane

Introduction	119
Structural observations	120
Faults	134
Description of cross sections	139
Structural and Tectonic Synthesis	144
References Cited	147
Appendices	
Appendix I	
Geologic Map Station Data	159
Appendix II	
SHRIMP-RG Data	183
Appendix III	
LA-ICPMS Data	188
VITA	196

List of Tables

Chapter 1

Introduction

Chapter 2

Lithologic Units in the Study Area

Table 2-1. Modal analyses of Cat Square terrane metagraywacke 28

Table 2-2. Modal percentages of igneous rocks..... 35

Chapter 3

Geochemistry of Inner Piedmont amphibolites at the southwestern end of the Cat Square terrane

Table 3-1. Major, trace, and rare earth element whole-rock geochemical analyses
of central Georgia Inner Piedmont amphibolites 54

Table 3-2. Normative analyses of central Georgia Inner Piedmont amphibolites 62

Chapter 4

Zircon geochronology of selected samples from the Cat Square terrane and Pine Mountain window, central Georgia

Chapter 5

Structural analysis of the Inner Piedmont and Pine Mountain window at the southwestern end of the Cat Square terrane

List of Figures

Chapter 1

Introduction

Figure 1-1. Location of the study area in central Georgia and mapping credit for data incorporated into the study	3
Figure 1-2. Simplified geologic map of the Pine Mountain window and adjacent terranes	4
Figure 1-3. Digital shaded relief maps	7
Figure 1-4. Index map of nearby detailed geologic mapping	11
Figure 1-5. Simplified tectonic map of the southern Appalachians	13
Figure 1-6. Cat Square stump and crossroads in Lincoln County, North Carolina	14

Chapter 2

Lithologic Units in the Study Area

Figure 2-1. Simplified geologic map of the study area showing major structural boundaries and distribution of rock units	19
Figure 2-2. Saprolite outcrop of lower(?) Tallulah Falls Formation	20
Figure 2-3. Biotite gneiss of the lower(?) Tallulah Falls Formation	22
Figure 2-4. Ancillary rocks exposed northwest of the Brindle Creek-Jackson Lake fault in the Tugaloo terrane	23
Figure 2-5. Biotite gneiss in the Cat Square terrane	25
Figure 2-6. Biotite gneiss sample OH032	26
Figure 2-7. Saprolite outcrop of layered migmatitic biotite gneiss cut by a late brittle fault	27
Figure 2-8. Modified quartz-feldspar-mica ternary sandstone classification diagram	28
Figure 2-9. Sillimanite schist in the Cat Square terrane	29
Figure 2-10. Weathered sillimanite schist in the Cat Square terrane	29
Figure 2-11. High Falls Granite	32
Figure 2-12. Indian Springs Granodiorite	34
Figure 2-13. Quartz-alkali feldspar-plagioclase ternary IUGS classification diagram of igneous rocks from the study area	35
Figure 2-14. Representative hand samples of amphibolite gneiss in the Cat Square terrane	37
Figure 2-15. Woodland Gneiss at the northeast end of the Pine Mountain window	38
Figure 2-16. Hornblende tonalite	39
Figure 2-17. Hollis Quartzite at the northeast end of the Pine Mountain window	40
Figure 2-18. Fault rocks of the study area	42

Chapter 3

Geochemistry of Inner Piedmont amphibolites at the southwestern end of the Cat Square terrane

Figure 3-1. Central Georgia Inner Piedmont amphibolite sample locations	51
---	----

Figure 3-2. Major element variation diagrams using Zr as the differentiation index	57
Figure 3-3. Trace element variation diagram using Zr as the differentiation index	59
Figure 3-4. Primary igneous trends of central Georgia and North Carolina Inner Piedmont amphibolites.....	63
Figure 3-5. Magma series of Inner Piedmont amphibolite protoliths	64
Figure 3-6. Rock type discrimination diagrams	65
Figure 3-7. MORB-normalized six-element spider diagrams	67
Figure 3-8. MORB-normalized multi-element spider diagrams	70
Figure 3-9. Interpretation of a bi-modal magma system that accounts for the continental calc-alkaline basalt geochemical pattern	72
Figure 3-10. Google Earth image depicting the locations of several modern-day back-arc basin analogues	73
Figure 3-11. Comparison of Cat Square terrane amphibolite geochemistry with modern-day intraoceanic back arcs	74
Figure 3-12. Comparison of Cat Square terrane amphibolite geochemistry with Sea of Japan basalts	76
Figure 3-13. Tectonic discrimination diagrams	77
Figure 3-14. Tectonic diagrams illustrating two phases of Cat Square basin development	82

Chapter 4

Zircon geochronology of selected samples from the Cat Square terrane and Pine Mountain window, central Georgia

Figure 4-1. Sample locations for geochronologic analyses	86
Figure 4-2. Illustrative representation of zircon mounting techniques used	91
Figure 4-3. SHRIMP-RG analyses of sample J360 (hornblende tonalite)	96
Figure 4-4. SHRIMP-RG analyses of sample IS632 (felsic gneiss)	99
Figure 4-5. SHRIMP-RG analyses of sample J182 (Woodland Gneiss)	101
Figure 4-6. SHRIMP-RG analyses of sample HF1465 (Woodland Gneiss)	103
Figure 4-7. SHRIMP-RG analyses of sample J182 (Woodland Gneiss) mounted using the indium metal technique	105
Figure 4-8. SHRIMP-RG analyses of sample HF1465 (Woodland Gneiss) mounted using the indium metal technique	109
Figure 4-9. Representative zircons from detrital (biotite gneiss) samples analyzed via LA-ICPMS	111
Figure 4-10. Detrital (biotite gneiss) zircon analyses	113

Chapter 5

Structural analysis of the Inner Piedmont and Pine Mountain window at the southwestern end of the Cat Square terrane

Figure 5-1. Early figure depicting the structure of the Pine Mountain window and surrounding terranes	120
Figure 5-2. Cross section and 3-dimensional block model of the Inner Piedmont, Pine Mountain terrane, and Carolina superterrane at the northeast end of the Pine Mountain window	121
Figure 5-3. Form-line map of homogeneous structural domains of S_2	122
Figure 5-4. Stereonet plots of all fabric data	124
Figure 5-5. Stereonet plots of planar fabrics	125
Figure 5-6. Typical F_{2-3} fold mechanisms	130
Figure 5-7. Photomosaic of a saprolite outcrop along the northeast side of Crane Road	131
Figure 5-8. Towaliga fault brittle deformation of basement units of the Pine Mountain window	137
Figure 5-9. Reduced-scale cross sections through the study area	140

List of Attachments

- Plate I:** Geologic Map of the Barnesville, Johnstonville, and a portion of the Orchard Hill Quadrangles, central GeorgiaRehrer2014-Plate I.pdf
- Plate II:** Station Geologic Map of the Barnesville, Johnstonville, and a portion of the Orchard Hill Quadrangles, central Georgia Rehrer2014-Plate II.pdf
- Plate III:** Form-Line Map and Structural Domains of the Barnesville, Johnstonville, and a portion of the Orchard Hill Quadrangles, central GeorgiaRehrer2014-Plate III.pdf

Chapter 1

Introduction

Geologic understanding is advanced by aggregation of piecemeal data stockpiled in scientific writings that are supplemented until a viable answer to a question or “thesis” is achieved. The thesis presented herein summarizes investigations and mapping across parts of several suspect terranes in the southern Appalachian Inner Piedmont.

Geologic investigations and detailed geologic maps of an orogen provide additional basis for exploration and development of mineral, energy, and water resources. They help identify geologic hazards, contribute vast amounts of geologic data, and provide greater understanding of deep crustal processes resolved in the exposed roots of a mountain chain. Detailed mapping requires that geologists go into the field to observe rocks and measure the orientation of mesostructures. Laboratory work and sample analysis are crucial, but the lack of detailed and accurate maps would likely invite an incorrect representation of geologic events. The U.S. Congress recognized the necessity of current geologic maps and passed legislation (National Geologic Mapping Act of 1992), therein affirming the importance of quality geologic maps as the basis for virtually all subsequent earth-science investigations.

The Appalachian orogen consists of an ~3,000-km mountain chain extending from the continental margin off Newfoundland to beneath the Gulf Coastal Plain in southern Alabama and Georgia (Hatcher, 2010). This orogen has a long and complex geologic history, whose development chronicles the breakup of one supercontinent, Rodinia, and culminates with the formation of another, Pangea. The Appalachian orogen is the product of orogenic processes that evolved over several hundred million years and involved three successive accretionary and collisional events (Thomas, 2006; Hatcher et al., 2007; Hatcher, 2010). Current understanding of the development of this orogen is the product of a remarkable paradigm shift from geosynclinal theory to adaptation of plate tectonics (Wilson, 1966, 1968; Rankin, 1975) as a mechanism driving continental drift; the concept of terrane analysis (e.g., Coney et al., 1980; Williams and Hatcher, 1983) provided a systematic approach to understanding developmental history.

Terrane analysis affords the opportunity to intricately study certain aspects of an orogen, without having to immediately incorporate those findings into an overarching model of

development (Williams and Hatcher, 1983). This type of analysis then lends itself to the systematic accumulation of data beginning with characterization of a suspect terrane, the basis of which is founded in detailed geologic mapping. The Cat Square terrane in North Carolina is a suspect terrane comprising a portion of the composite Inner Piedmont, and was first recognized through detailed mapping (e.g., Giorgis, 1999; Mersch, 2003; Byars, 2010; Gilliam, 2010) and geochronologic studies (Bream, 2003; Bream et al., 2004). Recent investigations, including the one presented herein, were focused on testing the hypothesis that the Cat Square terrane continues into central Georgia, and delimiting its boundaries and relationships among surrounding terranes.

Research Objectives

One key research goal was to provide field experience in constructing a 1:24,000-scale detailed geologic map in a previously unmapped area to provide a more complete understanding of eastern Inner Piedmont and Pine Mountain window geology, and the tectonic history of the southern Appalachians. Detailed mapping and cross sections of the study area (Plate I) were essential to providing context within which analytical results could be applied. Additional research objectives brought to the study area were:

- 1.) Testing hypotheses regarding continuity of large faults, including the Brindle Creek fault.
- 2.) Delimiting the southwestern extent of the Cat Square terrane in central Georgia.
- 3.) Performing kinematic analyses to resolve the structural and timing relationships of major faults framing the northeastern end of the Pine Mountain window.
- 4.) Performing detailed petrographic analyses of major rock units.
- 5.) Employing commercial lab whole-rock geochemical analyses of selected amphibolite samples.
- 6.) Conducting SHRIMP-RG and LA-ICPMS zircon geochronologic analyses to satisfy several objectives:
 - a.) establishing provenance of metasedimentary rocks in the study area, which is one major criterion used to distinguish Inner Piedmont terranes;
 - b.) determining the absolute age and timing of emplacement of a hornblende quartz diorite stock within one of several klippen of Inner Piedmont rocks in the Pine Mountain window;

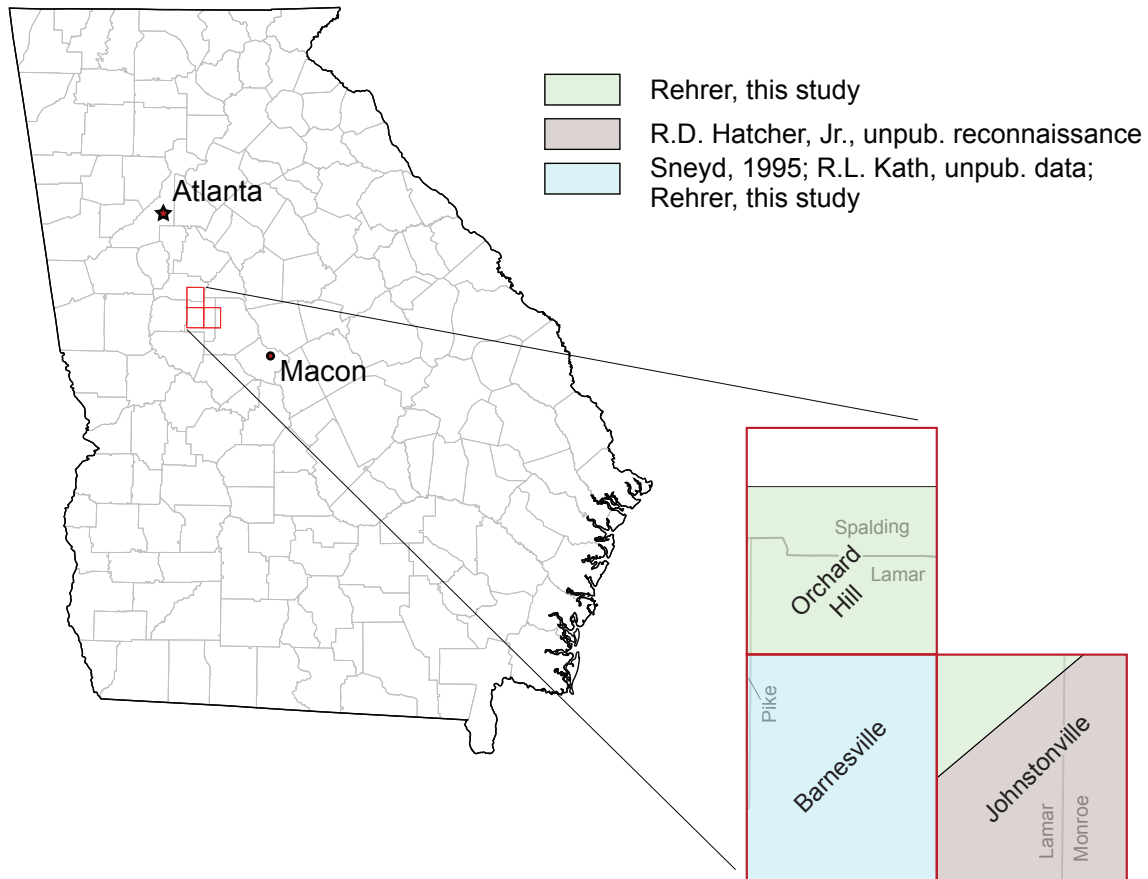


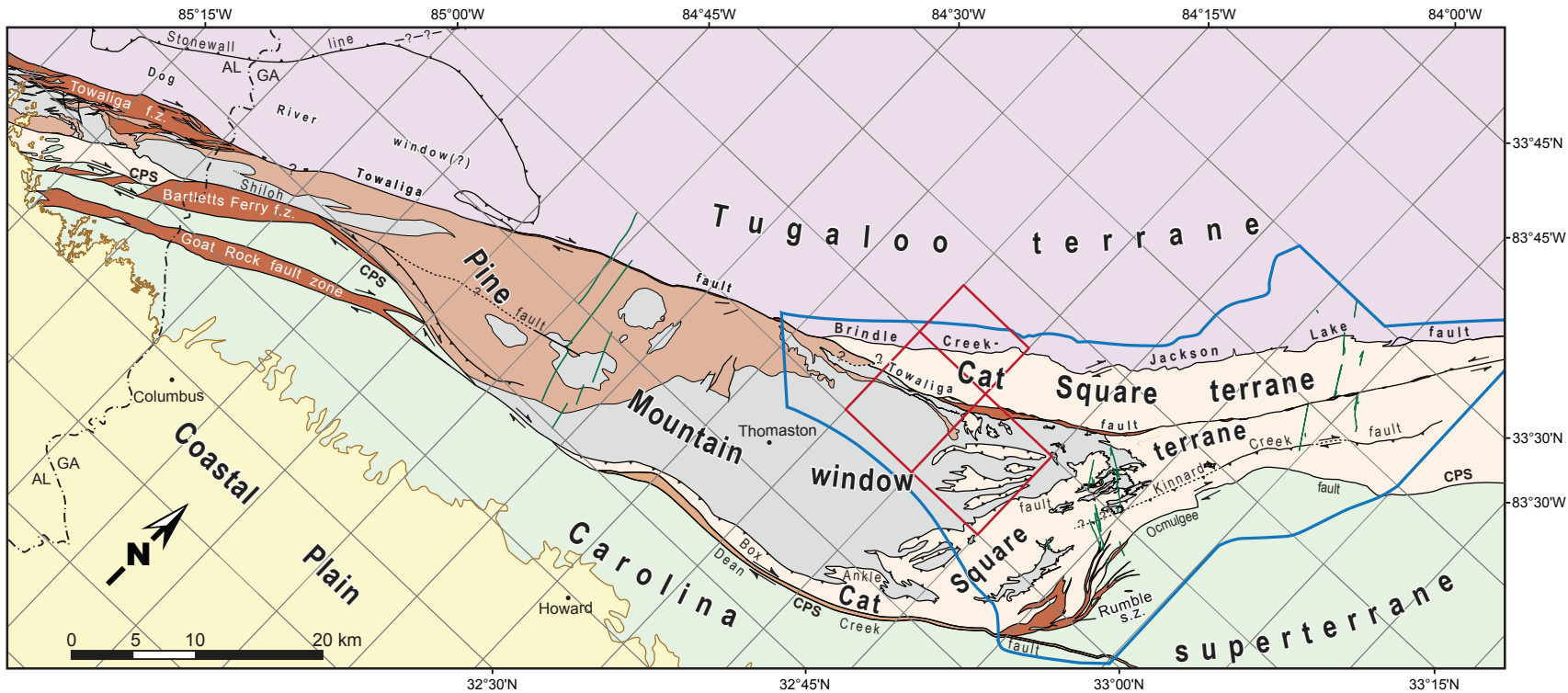
Figure 1-1. Location of the study area in central Georgia and mapping credit for data incorporated into the study. Study area is outlined in red.

- c.) using low Th/U metamorphic overgrowths to delimit movement timing along the Box Ankle fault.

Location of Study Area

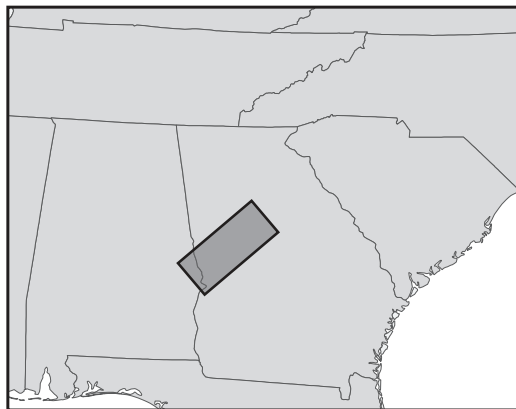
The study area encompasses portions of Spalding, Lamar, Pike, and Monroe Counties, Georgia (Fig. 1-1), and is situated astride two major fault systems in the southeastern Inner Piedmont (Fig. 1-2). These faults delineate the Cat Square terrane, and separate it from the Tugaloo terrane (Brindle Creek fault) to the northwest and the Pine Mountain window (Towaliga fault) to the southeast. A portion of the Box Ankle fault, which juxtaposes rocks of the Cat Square terrane and Grenville basement and Paleozoic(?) cover rocks at the northeast end of the Pine Mountain window, is also present within the study area.

Figure 1-2. Simplified geologic map of the Pine Mountain window and adjacent terranes. Study area outlined in red. Locations of nearby detailed and reconnaissance mapping in Figure 1-4 outlined in blue. Modified from Steltenpohl et al. (2010). f.z.—fault zone; s.z.—shear zone.



Location Map

Rock Units



Pine Mountain window		Pine Mountain group	Inner Piedmont		Cat Square terrane		Carolina-Uchee superterrane
		Mesoproterozoic basement			Tugaloo terrane		Coastal Plain
							Diabase

Tectonic Boundaries and Fault Rocks

	Sub-greenschist facies mylonite and cataclasite		Amphibolite facies mylonite		Thrust fault
	Greenschist facies mylonite	CPS	Central Piedmont suture		Normal fault
					Strike-slip fault

The mapped area consists of parts of three USGS 7.5 min quadrangles bound by 84° 00' W and 84° 15' W longitude and 33° 00' N and 33° 15' N latitude. It is located ~64 km southeast of Atlanta, Georgia, and west of Interstate 75. The majority of the ~180 km² mapped area lies in the Barnesville and Orchard Hill 7.5 min quadrangles, with an additional ~26 km² area in the Johnstonville quadrangle. The Johnstonville portion was added to maintain mapped continuity of the Towaliga fault zone between this study area and Howard's (2012) previously mapped area. Data gathered in portions of the Barnesville quadrangle by Sneyd (1995), later reinterpreted by R.L. Kath (unpublished data), along with the remainder of the Johnstonville quadrangle mapped in reconnaissance by R.D. Hatcher (unpublished data), have also been included in this study.

The topography of the study area is generally rolling and varies slightly at different locations as a result of differential erosion between more-resistant and less-resistant rock units (Fig. 1-3). Topography in the Orchard Hill and northwest portion of the Barnesville quadrangles consists of rolling hills dissected by streams. Relief in the remaining portion of the study area is similarly low, with the exception of a series of ~100 m-high ridges (Pine Mountain and Hog Mountain) trending roughly west-east through the Barnesville quadrangle, and a slight increase in relief in the southeastern corner of the Johnstonville quadrangle where most drainages are better developed.

A few modest-sized drainage networks are present in the study area that contain excellent exposures in areas where the stream gradients are higher; conversely, where the stream gradients are low, exposures are masked by vast swamps and extensive flood plains filled with alluvium. Potato Creek is a moderate-sized stream that flows north to south at the western edge of the Barnesville and Orchard Hill quadrangles exposing a portion of the Brindle Creek-Jackson Lake fault at Woodfin Mill dam. The Little Towaliga Creek headwaters are in the north-central portion of the Barnesville quadrangle where it flows northeast along a trend similar to that of the Towaliga fault. It joins Eddie Creek in the Johnstonville quadrangle to form the Little Towaliga River. An expansive marsh area encompasses much of this drainage network, concealing portions of a sizeable mylonite zone along the Towaliga fault.

Methods

Detailed geologic mapping of the study area has been conducted using classic tools and equipment (e.g., rock hammer, hand lens, Brunton compass, etc.). A geologic field book and USGS

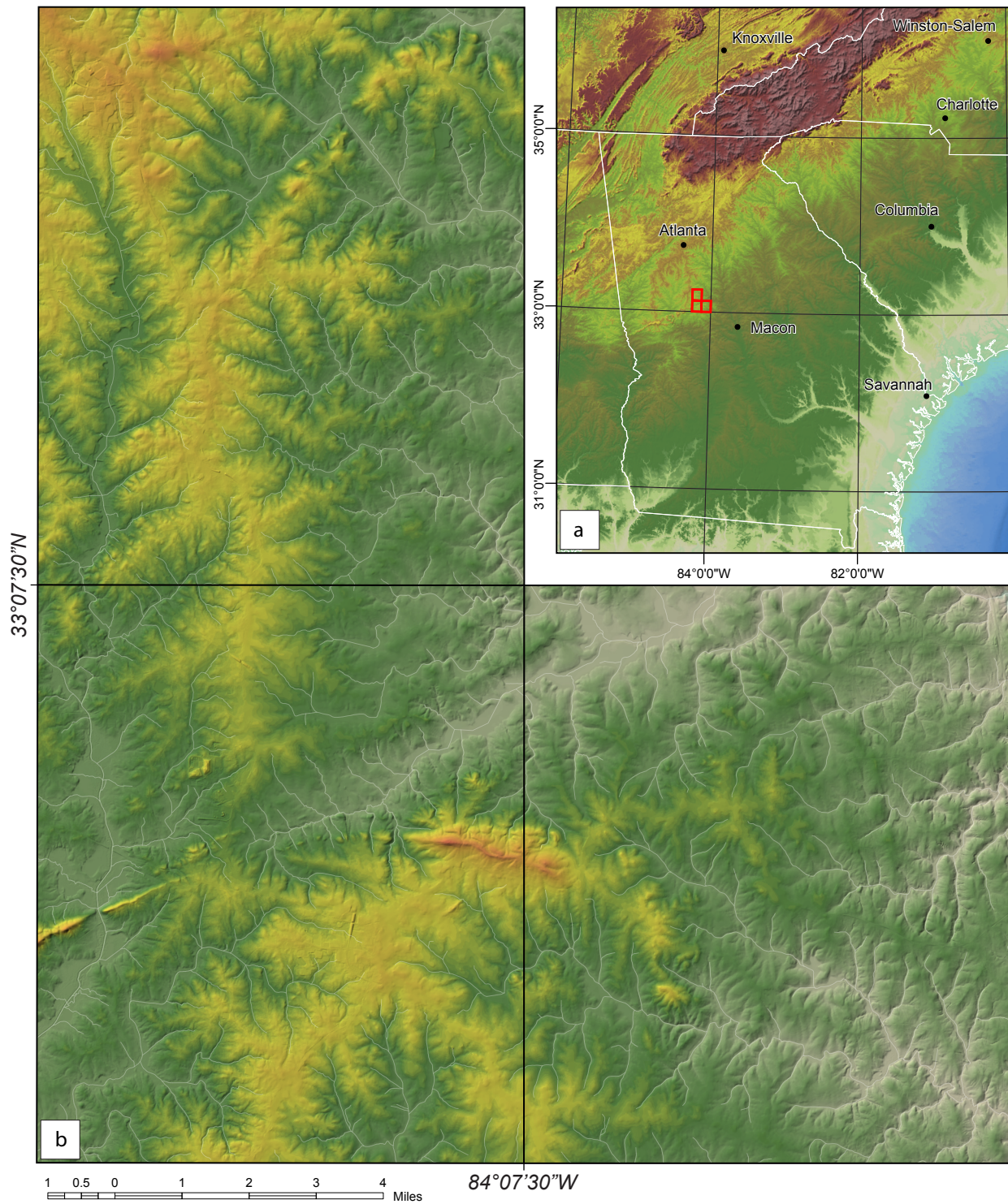


Figure 1-3. Digital shaded relief maps. (a) Shaded relief map of the southern Appalachians. Study area is outlined in red (counterclockwise from the top; Orchard Hill, Barnesville, and Johnstonville 7.5-minute quadrangles). (b) Shaded relief map of the study area showing topography and drainage patterns.

1:24,000-scale topographic maps were used to manually record geologic data. Data were also collected using a Trimble hand-held GPS/GIS unit operating Esri ArcPad software for greater precision and accuracy securing reproducible locations. Electronic structural data (Appendix I) were downloaded from the GPS/GIS unit into Esri ArcMap GIS software, and used for initial drafting and editing of the digital geologic map. A final version of the geologic map has been prepared using Adobe Illustrator software and converted to an Adobe Acrobat portable document file (pdf) for ease of distribution and printing. Three geologic cross sections perpendicular to strike of foliation of rock units and major structures in the study area have also been constructed (Plate I).

Billets of selected samples were cut at The University of Tennessee-Knoxville and shipped to a commercial lab to prepare thin sections. Petrographic analyses of thin section samples from all major rock units and fault zones have been made using both transmitted and reflected light microscopy on a Nikon Eclipse LV100 POL petrographic microscope equipped with a Nikon DS-Fi1 high-definition digital camera for producing high resolution photomicrographs. Chemical analyses of primary phases were performed at UTK using a CAMECA SX 100 electron microprobe (EMP), with beam size of 1-5 microns at 15 KV and a current of 10-20 nanoamps. Both natural and synthetic minerals were used for calibration of the EMP and standardization of the results (Appendix II).

Samples of two amphibolite boudins in Cat Square terrane biotite gneiss were prepared for whole-rock geochemical analysis by a commercial lab using rock preparation facilities at the University of Tennessee-Knoxville. Results from these analyses were plotted on compositional diagrams using Igpet® software. Normalized multi-element diagrams and tectonic discriminant diagrams were used to better refine models for Cat Square basin development.

Zircon geochronologic analyses were made using samples collected from within and immediately adjacent to the present study area. Three samples contained detrital zircons from samples of Cat Square terrane biotite gneiss, two were from Woodland Gneiss collected from the suspected Box Ankle fault zone, and one sample each were from a quartz diorite stock and from felsic gneiss in the Pine Mountain window. Zircons from these samples were separated using mechanical, gravity, and magnetic techniques at both the University of Tennessee-Knoxville and the University of North Carolina-Chapel Hill. Isotopic ratios used to establish ages were analyzed using a Laser-Ablation Inductively Coupled Plasma Mass Spectrometer (LA-ICPMS) at the University of

Arizona LaserChron Center in Tucson, and using the Sensitive High Resolution Ion Microprobe-Reverse Geometry (SHRIMP-RG) at the Stanford-USGS Micro Analysis Center (SUMAC) in Stanford, California. The SHRIMP-RG is capable of analyzing very small volumes of material, making it possible to examine small portions of complex zircons, therefore enabling the acquisition of ages from thin metamorphic overgrowths. The faster ablation rate and greater ablation volume achieved by a larger spot size and penetration depth with the LA-ICPMS permits much quicker analysis times, making it better suited for establishing age populations in detrital samples by analyzing large numbers of zircons.

Previous Work

The central Georgia Piedmont has not typically been a focus of intensive geological study, and the lack of interest is likely attributed to near-flat topography, extensive vegetative cover, and susceptibility of rock units to weathering, creating vast expanses of saprolite. Exceptional exposure is limited and outcrops are confined mostly to drainages and non-vegetated roadcuts. The paucity of systematic detailed study and recognized importance of this region prompted Sears and Cook (1984) to assemble a literature review, citing even their own previous work in Georgia as being mostly reconnaissance, intending to prompt further work in “an interesting but difficult area.”

Early research in the vicinity of the present study area was performed in recognition of the need for a broad assessment of the potential for exploitation of construction- and monument-quality stone and mineral deposits. Watson (1902) conducted reconnaissance work evaluating the extent of mining of granites and gneisses in what was then described as the crystalline area of Georgia. The study was intended to be a preliminary investigation that focused mainly on reconnaissance mapping and characterizing physical and chemical properties of granite and gneiss bodies already being exploited. As such this work did not include the present study area, and involved only areas several miles to the west near Zebulon in Pike County, and northwest near Griffin in Spalding County. Galpin (1915) conducted a similar study aimed at the assessment and reconnaissance mapping of large pegmatitic areas containing minable quantities of mica and feldspar. This survey similarly focused on locations outside of the present study area, although, it did briefly describe the occurrence of several diorite bodies within the Pine Mountain window, one of which was vaguely defined as being located 2.4–2 km east of Barnesville. That diorite body may

be the diorite stock described as part of the present study. Diorite intrusions in the Pine Mountain window have not been discussed in subsequent literature, although later workers (e.g., Clarke, 1952) have mapped rocks of intermediate composition as belonging to Cunningham Granite or the Charnockite series (Schamel and Bauer, 1980).

Subsequent and more extensive reconnaissance surveys in Georgia produced state geologic maps (Stose and Smith, 1939; Pickering, 1976) and investigated unusual geologic occurrences. As a consequence of investigations of the crystalline area in Georgia, Crickmay (1933) described mylonites of several major faults and named the Towaliga fault for a locality north of Barnesville. Further detailed work by Hewitt and Crickmay (1937) focused on investigating the springs located in the aptly named Warm Springs 15-minute quadrangle, southwest of the present study area. Their work identified structural features, and named and characterized many of the rock units (e.g., Woodland Gneiss, Sparks schist, Hollis Quartzite, Manchester schist) present in the Wacoochee belt (Pine Mountain window). Clarke (1952) mapped the Thomaston 15-minute quadrangle, immediately east of the Warm Springs quadrangle, which contributed further characterization of units in the Pine Mountain window and described a complete charnockite series exposed in the quadrangle. Clark (1952) also first proposed that the Wacoochee belt was a window through an over-riding thrust sheet and that the faults framing the northern (Towaliga) and southern (Goat Rock) portions of the window were possibly related (Schamel and Bauer, 1980). Subsequent investigations by several authors (e.g., Bentley and Neathery, 1970; Sears et al., 1981; Sears and Cook, 1984), focused on the western end of the Pine Mountain window and attributed the structural style of the window to development of several type F crystalline thrust sheets assembled into a series of vertically stacked nappes. Detailed geologic mapping at the northeast end of the of the Pine Mountain window (Hooper, 1986; R.D. Hatcher, Jr., unpublished data) immediately east of the present study area, was conducted in response to the window hypothesis and focused on resolving timing and structural relations at its eastern terminus (R.D. Hatcher, Jr., personal communication). Hooper and Hatcher (1988a) concluded that the Pine Mountain terrane was exposed in a complex window framed by three faults of different ages. Hooper and Hatcher (1988a, 1988b) also characterized mylonites and kinematics of the Towaliga and Box Ankle faults at the northeast end of the window, as well as the Rumble Shear zone, and Dean Creek faults along the southern margin of the window.

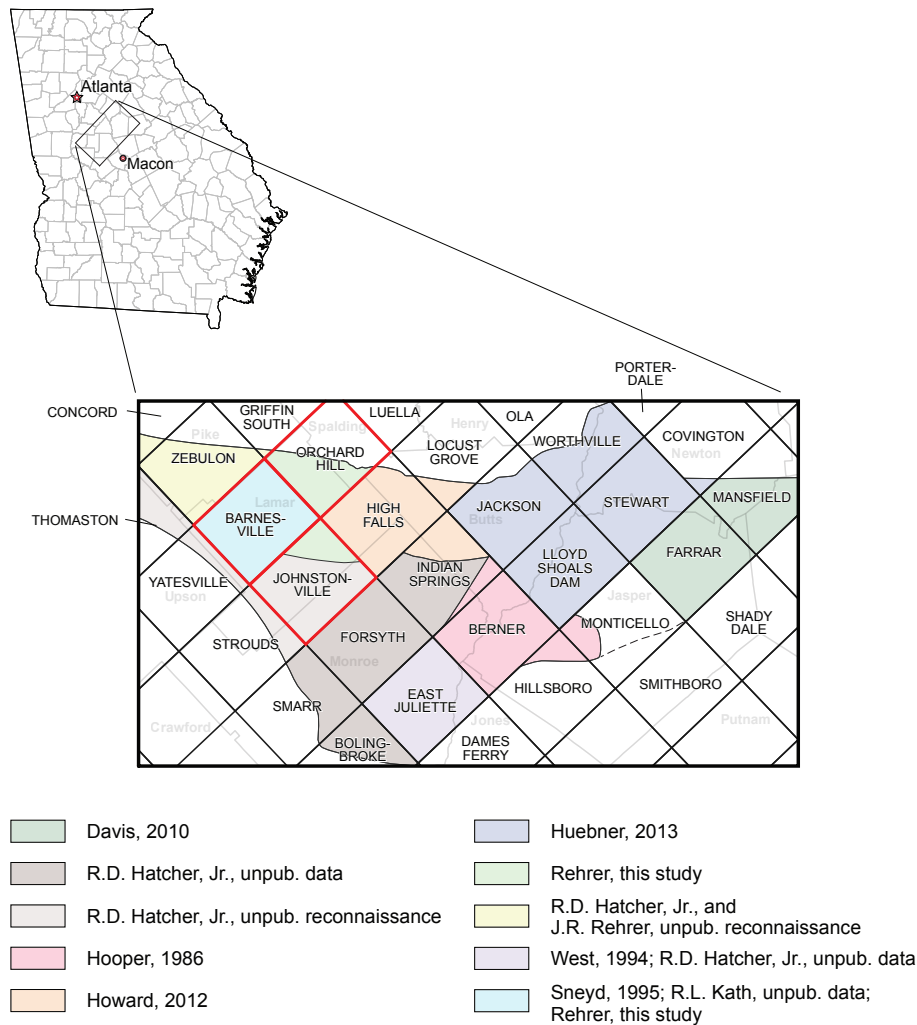


Figure 1-4. Index map of nearby detailed geologic mapping. Study area is outlined in red, Georgia county borders are outlined in light gray, and USGS 7.5 min quadrangles are outlined in black. Colored polygons represent areas of detailed mapping. Modified from Huebner et al. (2014).

With discovery of the Cat Square terrane in the Carolinas (Bream, 2003; Merschat and Hatcher, 2007), and, as an effort to prove its southwest continuation, several more recent detailed investigations have been conducted in the central Georgia Inner Piedmont, resulting in a large island of detailed geologic mapping and research at the northeast end of the Pine Mountain window (Fig. 1-4). At the far northeast portion of this area Davis (2010) produced a geologic map of the Farrar and a portion of the Mansfield 7.5 min quadrangles. Huebner (2013) has mapped the Stewart and Lloyd Shoals Dam, and portions of the Jackson and Worthville quadrangles immediately southwest of Davis (2010). Howard (2012) mapped portions of the Locust Grove, Indian Springs, and High Falls quadrangles between the present study area and that of Huebner (2013).

Geologic Background

Regional geology and tectonic history of the southern Appalachians is complex and has yielded a plethora of viable and sometimes conflicting models (e.g., Higgins et al., 1988; Hibbard, 2000; Hatcher, 2010) for its development; therefore only a basic summary of major lithotectonic terranes, fault zones, and terrane boundaries present within the study area is presented here. Detailed descriptions of the rock units present in these terranes are discussed in the following chapter.

Inner Piedmont

The Inner Piedmont consists of the Tugaloo terrane (western Inner Piedmont) and Cat Square terrane (eastern Inner Piedmont), which are separated by the Brindle Creek fault in North Carolina and the Brindle Creek-Jackson Lake fault, its likely equivalent in central Georgia (Fig. 1-5). The main distinguishing characteristics between the terranes are contrasting detrital zircon age populations (Bream et al., 2004; Merschat et al., 2010), contrasting ages of granitic plutons, and the occurrence of an extensive plutonic complex in the Cat Square terrane, along with the absence of continental basement in the Cat Square terrane (Huebner et al., 2011a). The Inner Piedmont contains the high-grade crystalline core of the southern Appalachians and stretches ~ 700 km along strike from near Winston-Salem, North Carolina, into central Alabama where it disappears beneath the Gulf Coastal Plain (Hatcher et al., 2007; Merschat and Hatcher, 2007). It is bound to the west by the Brevard fault zone, separating it from the western Tugaloo terrane in the eastern Blue Ridge, and to the east by the Central Piedmont suture, which separates it from the Carolina superterrane.

Tugaloo terrane

The Tugaloo terrane comprises the eastern Blue Ridge and western Inner Piedmont and is situated astride the Brevard fault zone. The Brevard fault zone is a 1-3 km-wide gently southeast-dipping fault zone that extends ~ 750 km from Alabama to Virginia (Hatcher et al., 2007). This fault zone represents the geologic boundary between the eastern Blue Ridge and Inner Piedmont and, amid some controversy, was previously thought to represent a suture and terrane boundary, among other things (Rankin, 1975; Hatcher, 2001). Detrital zircon ages determined from several samples on opposing sides of the fault (Bream, 2003; Bream et al., 2004) and an identical stratigraphic sequence, provide evidence that the Brevard fault zone is not a suture and that the Tugaloo terrane

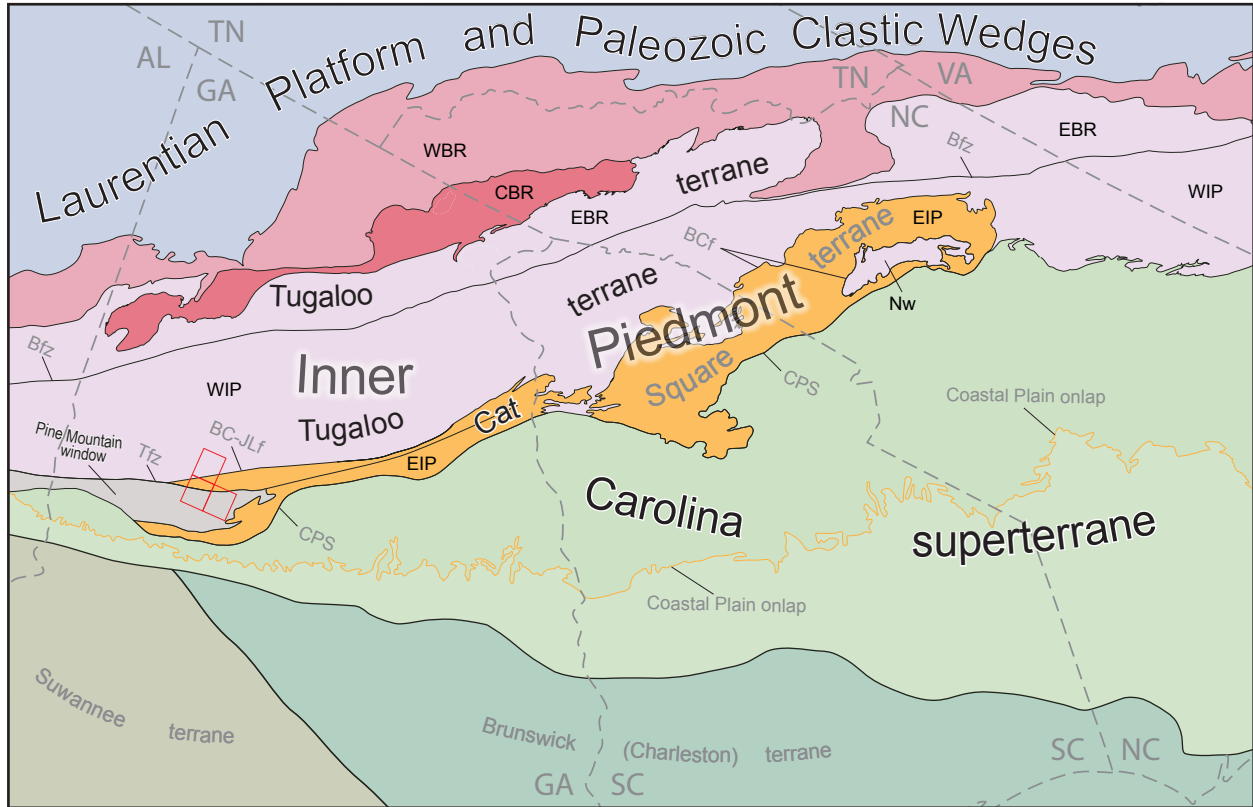


Figure 1-5. Simplified tectonic map of the southern Appalachians. Study area, outlined in red, is shown in relation to the composite Inner Piedmont and Pine Mountain window. Modified from Hatcher et al. (2007) and Huebner et al. (2011b). WBR—western Blue Ridge terranes; CBR—central Blue Ridge terranes; EBR—eastern Blue Ridge terranes; WIP—western Inner Piedmont; EIP—eastern Inner Piedmont; Nw—Newton window; Bfz—Brevard fault zone; Tfz—Towaliga fault zone; BC-JLf—Brindle Creek-Jackson Lake fault; BCf—Brindle Creek fault; CPS—central Piedmont suture.

is a distinct lithotectonic unit in both the eastern Blue Ridge and western Inner Piedmont (Hatcher et al., 2007). This terrane is comprised of distal rifted margin sediments shed from Laurentia and consists mainly of the Tallulah Falls Formation, Poor Mountain Formation, and several granitic and mafic plutons, along with small amounts of Grenville basement (Hatcher et al., 2007). The Tallulah Falls Formation consists of a three-part stratigraphy (Hatcher, 1971; Hatcher et al., 2007; Howard, 2012); only a small portion of the Tugalo terrane is present in the study area, and consists entirely of the lower member. In the study area this formation consists of well-foliated biotite gneiss with discontinuous interlayered sillimanite schist and amphibolite. It was intruded by at least one mappable Ordovician granitic pluton.



Figure 1-6. Cat Square stump and crossroads in Lincoln County, North Carolina. (L–R) Robert D. Hatcher Jr., and Justin R. Rehrer.

Cat Square terrane

The Cat Square terrane is so named for the Cat Square crossroads (Fig. 1-6) in Lincoln County, NC (Hatcher, 2002) and was first recognized as a distinct terrane in the Inner Piedmont from detrital zircon geochronology (Bream, 2002, 2003; Bream et al., 2004). Metasedimentary rocks yielded detrital zircon ages of both Laurentian and peri-Gondwanan affinity. Sediments from Laurentia and approaching peri-Gondwanan terranes were deposited on ocean crust in a possible remnant ocean basin that was closed during the Acadian-Neocadian orogeny by subduction of the Cat Square terrane and part of the Tugaloo terrane beneath the Carolina superterrane at ~407 Ma (Merschhat and Hatcher, 2007; Hatcher, 2010; Huebner et al., 2011a). The Cat Square terrane comprises the eastern portion of the composite Inner Piedmont and, with the exception of the Newton window in North Carolina, lies east of the Tugaloo terrane with its eastern extent marked by the Central Piedmont suture. In central Georgia the terrane widens where the Pine Mountain window exposes Grenville basement and a Neoproterozoic-Paleozoic(?) cover sequence, creating a “fork-like” shape at the southwestern end of the terrane. Because of this separation, within the present study area the eastern boundary of the Cat Square terrane is marked by both the Towaliga

and Box Ankle faults, which separate it from rocks of the Pine Mountain window. Its northwestern extent here is delimited by the Brindle Creek-Jackson Lake fault. The Cat Square terrane in central Georgia consists of several mappable units, including well-foliated and deformed migmatitic biotite gneiss and sillimanite schist, along with a large plutonic complex comprised of coarse-grained megacrystic granite and finer-grained granodiorite (Davis, 2010; Huebner et al., 2011a; Howard, 2012; Huebner, 2013).

Brindle Creek-Jackson Lake fault

The Brindle Creek fault separates the western Inner Piedmont (Tugaloo terrane) from the eastern Inner Piedmont (Cat Square terrane) in North Carolina and was first mapped as a lithologic contact (Goldsmith et al., 1988). It was later identified as a shallowly dipping thrust fault (Giorgis, 1999), but was not initially interpreted as a terrane boundary, although subsequent detrital zircon geochronologic studies (Bream, 2003; Bream et al., 2004) proved the existence of a separate terrane east of the fault. The Brindle Creek fault was thus later described as a sinuous low-angle fault and terrane boundary extending from northwest of Winston-Salem, North Carolina, to Athens, Georgia, and truncated at both ends by the central Piedmont suture (Hatcher et al., 2007; Mersch and Hatcher, 2007). The interpretation of a conspicuous lineament observed in aeromagnetic data led to the hypothesis that the Cat Square terrane continued into central Georgia and that Brindle Creek fault did not truncate against the central Piedmont suture and is instead represented by the aeromagnetic lineament that truncates against the Towaliga fault at the northeast end of the Pine Mountain window (Hatcher et al., 2007; Huebner et al., 2010; Huebner, 2013). Recent detailed geologic mapping (Davis, 2010; Howard, 2012; Huebner, 2013; Rehner, this study) has shown that the aeromagnetic lineament does represent a fault, referred to as the Jackson Lake fault by Huebner et al. (2014), that separates distinct lithologies and granitoid bodies of different ages. While granitoid ages and aeromagnetic interpretations indicate that this is likely the southwest equivalent of Brindle Creek fault and terrane boundary, it differs in structural style from the Brindle Creek fault in North Carolina (Huebner, 2013; Huebner et al., 2014). Taking into account the evidence both for and against correlating the Jackson Lake fault in central Georgia with the Brindle Creek fault in North Carolina, this terrane boundary is herein termed the Brindle Creek-Jackson Lake fault. In the study area, the Brindle Creek-Jackson Lake fault is a narrow (~10 m), moderately steep, northwest-

dipping, dextral strike-slip fault that contrasts with the low-angle southwest-directed thrust geometry observed in the Brindle Creek fault in North Carolina. The Brindle Creek-Jackson Lake fault continues beyond the study area on a southwest trend and is likely truncated by the Towaliga fault in the adjacent quadrangle near Zebulon, Georgia (R.D. Hatcher, Jr., and J.R. Rehrer, unpublished reconnaissance mapping).

Towaliga fault

The Towaliga fault is a northeast-trending, steeply northwest-dipping, dextral strike-slip fault that separates the Cat Square terrane from the Pine Mountain window in the study area. The fault is characterized by garnet-grade mylonite with rounded, brittlely deformed feldspar porphyroclasts in a very fine-grained biotite-rich garnetiferous matrix. Porphyroclasts exhibit quartz-mica strain shadows with no feldspar tails. Several quartz-tailed σ - and δ -type porphyroclasts, asymmetric folds of quartz ribbons, and S-C fabrics provide shear sense (Hooper and Hatcher, 1988a). The Towaliga fault was sinistrally reactivated brittlely during the Late Triassic-Early Jurassic (Huebner and Hatcher, 2011), producing numerous rhomb-shaped step-overs filled with multiply broken hydrothermal veins and vuggy quartz. In areas between the rhombs a brittle fabric has overprinted quartz mylonite, creating a cataclasite (Hadizadeh et al., 1991; Huebner and Hatcher, 2011; Rehrer et al., 2012). The fault was named by Crickmay (1933) for an exposure in the present study area along the Little Towaliga Creek just north of Barnesville, Georgia.

Pine Mountain window and Paleozoic(?) cover sequence

The Pine Mountain window is the southernmost basement massif in the Appalachian orogen that exposes Grenville orthogneiss and a Neoproterozoic-Paleozoic(?) cover sequence (Hatcher et al., 2007; Steltenpohl et al., 2010). The window is structurally complex and is not formed by a simple erosional hole in an overriding thrust sheet (e.g., Clarke, 1952); it is alternatively bounded by several Acadian(?)-Alleghanian faults (Hooper and Hatcher, 1988b; Huebner et al., 2014) of demonstrably different rheologies and ages and is thus a complex window that formed during a long history of terrane accretion, faulting, and erosion. At its northeastern end, the Pine Mountain window is closed by the sinuous trace of the Box Ankle fault, which separates rocks of the Inner Piedmont from Grenville basement. To the northwest, the window is bounded by the lower amphibolite facies youngest Towaliga fault (Hooper and Hatcher, 1988a; Hatcher et al., 2007), which

separates Inner Piedmont and rocks from basement and cover sequence rocks. To the south it is delimited by the greenschist facies Dean Creek fault (Hooper and Hatcher, 1988a; R.D. Hatcher, Jr., unpublished data), forming part of the Central Piedmont suture, and separating rock units of the Pine Mountain window along with the Cat Square terrane from the Carolina superterrane.

Box Ankle fault

The Box Ankle fault is an ~2 km-thick, tightly folded, gently southeast- and northwest-dipping, northwest-vergent thrust and terrane boundary that separates footwall Pine Mountain window rocks from Cat Square terrane rocks in the hanging wall. Mylonite here contains an upper amphibolite facies mineral assemblage, a well-developed S-C fabric, and rotated feldspar porphyroclasts with abundant myrmekite rims that confirm northwest transport (Hooper and Hatcher, 1988a; Rehrer et al., 2012; Huebner et al., 2014). Folding of the fault produced a sinuous trace at the northeastern boundary of the Pine Mountain window, just east of the present study area, with several klippen appearing west of the main trace and several windows to the east (Hatcher et al., 1988; Huebner et al., 2014).

Chapter 2

Lithologic Units in the Study Area

Introduction

The area mapped as part of this research spans three lithotectonic terranes in the southern Appalachian Inner Piedmont, each containing several lithologic units. Terranes have been identified on the basis of stratigraphy, metamorphism, plutonism, and recognition of structural boundaries. Rock units have been differentiated by mineralogy and local occurrence. Identification and naming of rock units have been supplemented by petrography, zircon geochronology, and knowledge gained by previous workers (e.g., Hewitt and Crickmay, 1937; Clarke, 1952; Hatcher, 1971; Davis, 2010; Huebner et al., 2011a; Howard 2012). The following rock unit descriptions were established by observations recorded at outcrops, by examination of hand specimens, and by petrographic analysis of representative lithologies. Where plagioclase composition is provided, it has been determined by the Michel-Lévy Method (Nesse, 2004). This method requires a specific orientation of several plagioclase grains in a thin section from which extinction angles can be measured. This orientation was not present in some samples and therefore plagioclase compositions could not be determined. The method was also hindered by plagioclase deformation, which is exhibited by most samples. Modal analyses of select samples were performed using a mechanical stage on a petrographic microscope utilizing a 0.3 mm step size in rocks of about the same average grain size.

Tugaloo terrane/Western Inner Piedmont

The Tugaloo terrane comprises the majority of the Orchard Hill quadrangle and a small portion of the northwestern corner of the Barnesville quadrangle (Fig. 2-1). It is separated from the Cat Square terrane to the southeast by the northeast-trending northwest-dipping Brindle Creek-Jackson Lake fault. In the study area the Tugaloo terrane consists of the lower(?) Tallulah Falls Formation, which was intruded by an Ordovician granitic pluton (Lithonia Gneiss).

Lower(?) Tallulah Falls Formation

The portion of the study area mapped as the Tugaloo terrane consists predominantly of biotite paragneiss (metagraywacke) with lesser, interlayered and discontinuous bodies of muscovite-sillimanite schist (Fig. 2-2). Small (< 15 cm) gondite and amphibolite boudins are

List of Map Units

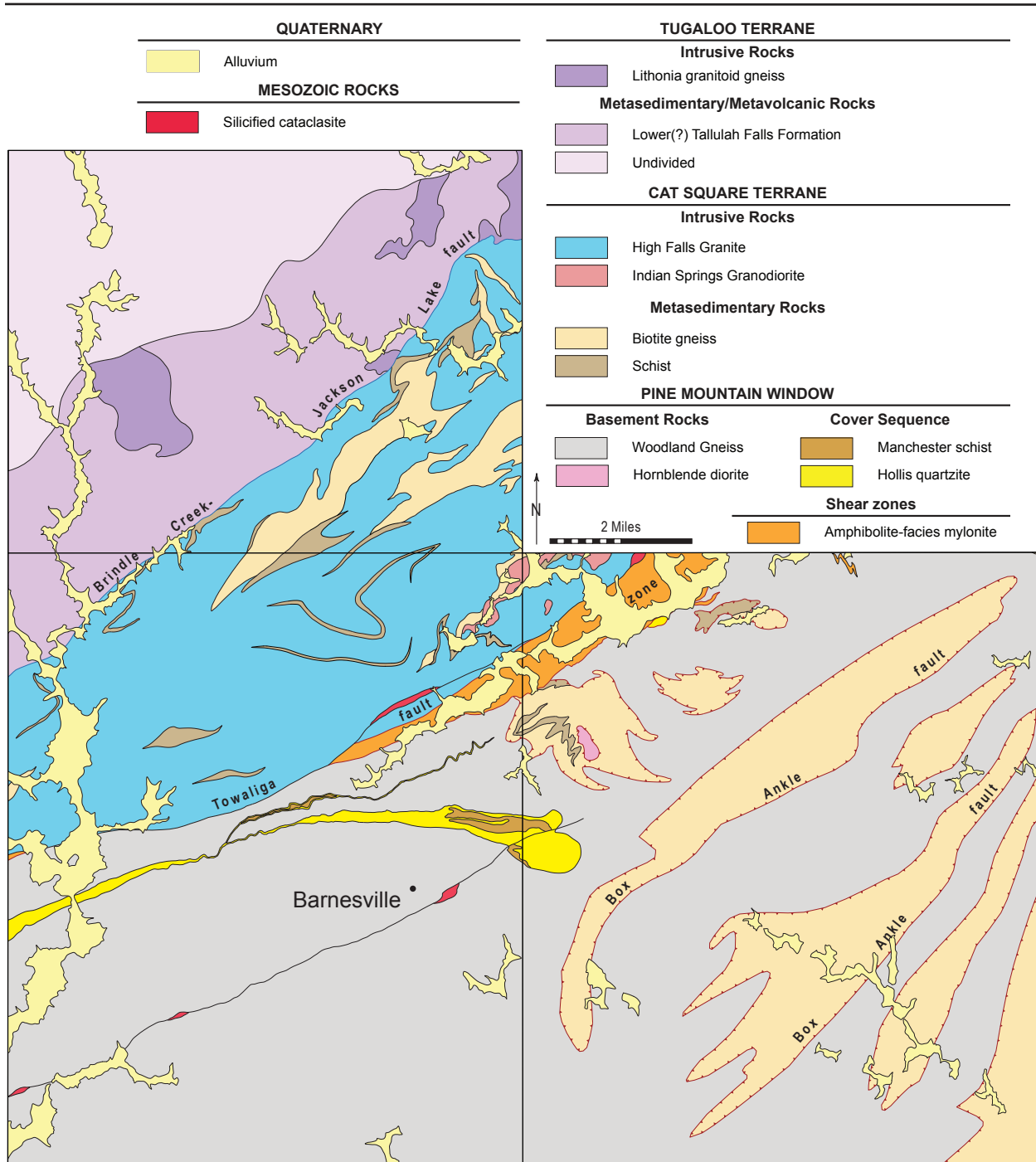


Figure 2-1. Simplified geologic map of the study area showing major structural boundaries and distribution of rock units. Modified from Plate I.

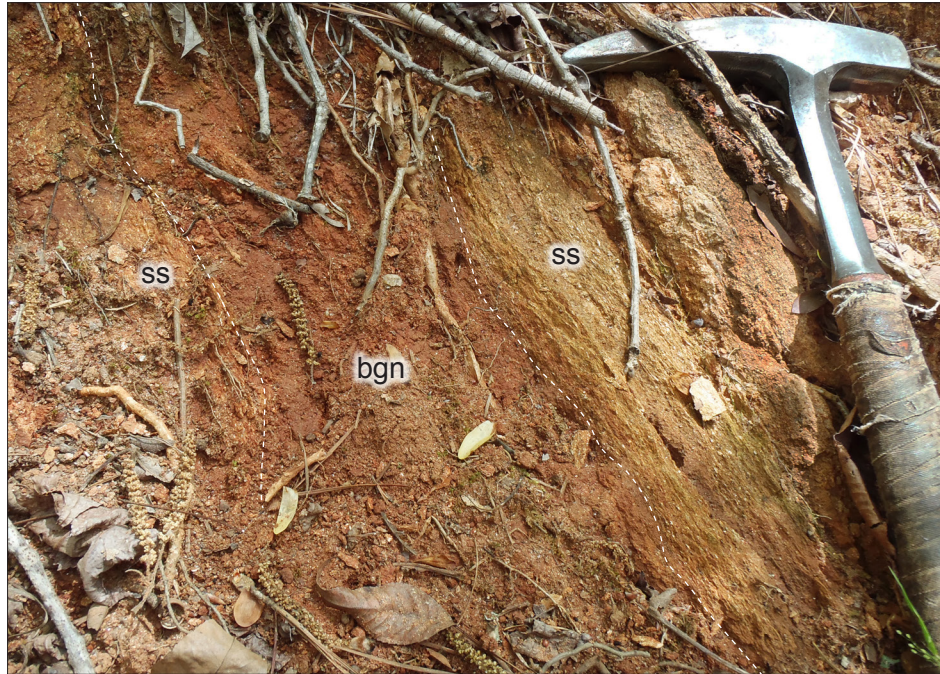


Figure 2-2. Saprolite outcrop of lower(?) Tallulah Falls Formation, located at station OH341 along Little Buck Creek, ~1 km northeast of McKneely Road in the Orchard Hill quadrangle, showing the contact between biotite gneiss (center) and muscovite-sillimanite schist (left and right). bgn—biotite gneiss; ss—muscovite-sillimanite schist.

ubiquitous in the formation and occur predominantly in the biotite gneiss. Hatcher (1971) described a garnet-aluminous schist member of the Tallulah Falls Formation overlying an interlayered metagraywacke-schist-amphibolite unit (lower Tallulah Falls Formation). While the schist mapped in the Tugaloo terrane as part of this study locally contains garnet and sillimanite and could represent the garnet-aluminous schist member, it is deeply weathered, discontinuous, and cannot be mapped as a separate lithology at the scale of the present study. If the garnet-aluminous schist member of the Tallulah Falls Formation is present in the mapped area, it is indistinguishable from rocks identified as the lower member and thus imparts some uncertainty in the unit being classified solely as lower Tallulah Falls Formation. On that basis, the biotite paragneiss and schist identified northwest of the Brindle Creek-Jackson Lake fault have been mapped as lower(?) Tallulah Falls Formation.

Biotite paragneiss is medium-grained and commonly migmatitic with lenticular pods of coarse-grained granitic material that is often more prevalent with closer proximity to the Brindle Creek-Jackson Lake fault. Foliation is well-developed and readily identifiable by parallel alignment

of phyllosilicates (Fig. 2-3a). Typical mineral assemblage is quartz + plagioclase + biotite ± garnet ± sillimanite ± muscovite, with zircon, sphene, and opaques as common accessory minerals (Fig. 2-3b). Soils formed from biotite gneiss tend to be dark red to reddish-brown and are easily discernable from other soils. Schist units consist chiefly of medium- to coarse-grained quartz and muscovite ± sillimanite ± garnet ± biotite. Coarse-grained pegmatites are common and produce muscovite sheets up to 7 cm in diameter. Muscovite-schist soils are lighter brown; where sillimanite is abundant, the soil develops a purple hue.

Lithonia Gneiss

The Lithonia Gneiss is a voluminous, well-foliated granitic gneiss exposed northwest of the Brindle Creek-Jackson Lake fault that is intrusive to metasedimentary rocks of the Tugaloo terrane, and is named for exposures near Lithonia, Georgia (Crickmay, 1952). The dominant mineral assemblage consists of quartz + plagioclase (An_{9-13}) + alkali feldspar + biotite ± garnet ± muscovite with accessory zircon, sphene, and apatite (Huebner et al., 2014). It is medium- to coarse-grained, light-gray, and has a gneissic foliation defined by the segregation and parallel alignment of fine-grained biotite into thin (5–10 mm) layers (Fig. 2-4a). Felsic layers of coarser-grained quartz and feldspar occur between layers of biotite, which are typically distorted into a series of parallel folds. This characteristic, however, is not as consistently present within the study area as it is in adjacent areas to the northeast (e.g., Howard, 2012; Huebner, 2013). Large (1–10s km²) pavement exposures, the most prominent being Arabia Mountain, in southern DeKalb County, have been reported by Huebner et al. (2011a, in review) and Howard (2012) in areas to the northeast. The Lithonia Gneiss typically occurs in the study area as small (< 2 m²) pavement outcroppings and more commonly as ~1 m diameter boulders exposed in streams. A large underground gas storage facility was developed in this unit near the intersection of McKenzie Road and Old Georgia Highway 41. This storage facility is no longer in use, but refuse material excavated from the facility (Grant, 1967) is still present and is readily identifiable as Lithonia Gneiss. U-Pb SHRIMP-RG analyses of zircon from two samples yielded an average 444 ± 7.6 Ma age of the unit (Huebner et al., 2014).

Gondite

Fermor (1909) proposed the gondite nomenclature for regionally metamorphosed quartz-manganese silicate rocks in India (Roy and Purkait, 1968), and is applied here for rocks that are

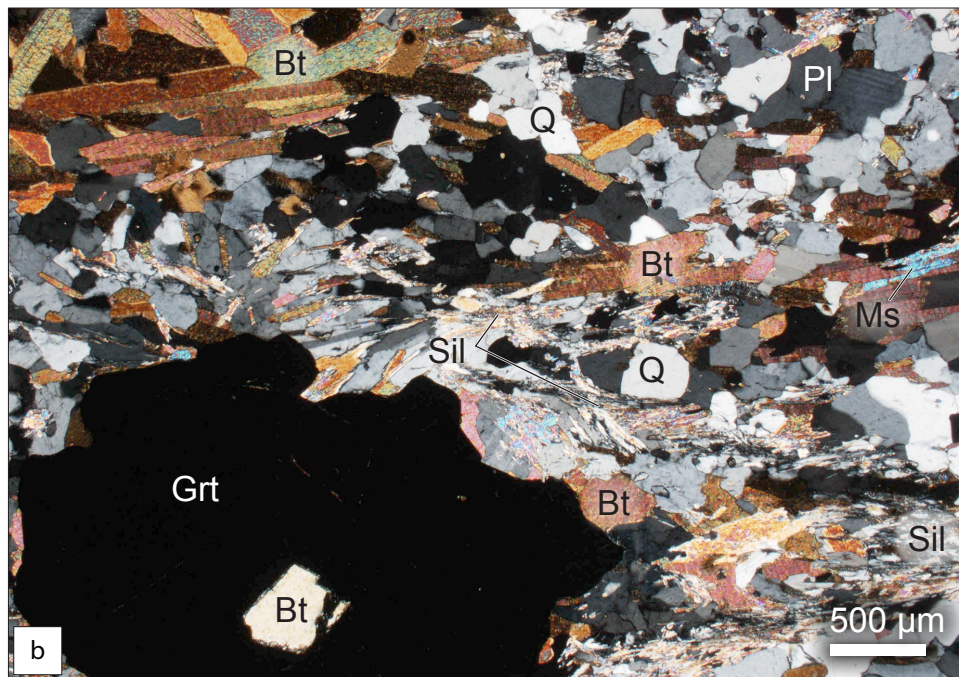


Figure 2-3. Biotite gneiss of the lower(?) Tallulah Falls Formation. (a) Representative hand sample of biotite gneiss from station OH495, located just west of the intersection of Hoyt Road and Cauthen Road in the Orchard Hill quadrangle. (b) Photomicrograph of thin section OH495 showing dominant mineralogy and texture. Bt—biotite; Grt—garnet; Ms—muscovite; Pl—plagioclase; Q—quartz; Sil—sillimanite.



Figure 2-4. Ancillary rocks exposed northwest of the Brindle Creek-Jackson Lake fault in the Tugaloo terrane. (a) Characteristic exposure of Lithonia Gneiss in the study area, showing well-developed foliation and absence of characteristic folding. Outcrop is located just north of Skinners Bypass Road, and west of the intersection with Crown Springs Road in the Orchard Hill quadrangle. (b) Gondite hand sample showing typical reddish-orange oxidized outer surface with pinkish-white fresh inner core, and possible F_1 fold preserved in the sample. Sample was collected as float along Little Buck Creek, east of McKneely Road, and just north of the Brindle Creek-Jackson Lake fault.

comprised almost entirely of quartz and spessartine garnet. Gondite is fine-grained and pinkish-white on fresh surfaces, but more commonly appears reddish orange or black as a consequence of extensive oxidation of Mn- and Fe- bearing minerals and weathering (Fig. 2-4b). It is more resistant to erosion than the surrounding metasedimentary rocks and is commonly exposed as 10–20 cm pieces of float and less commonly as distinct layers, up to 10 cm thick and 2–3 m long. While metasedimentary rocks of the Tugaloo and Cat Square terranes are similar in appearance and metamorphic grade, only rocks of the lower(?) Tallulah Falls Formation contain abundant gondite and, although this rock type is uncommon in the Cat Square terrane, few small (5–10 cm) pieces of gondite float have been identified in limited locations. Huebner (2013) has traced individual layers of gondite for several tens of kilometers in the Tugaloo terrane but, given the scarcity of in-place exposures along with lack of mappable continuity among these exposures in this study area, no attempt has been made to assemble gondite exposures into one (or several) distinct map-scale layers. As a result, gondite lithology does not appear on the map but is still discussed here, because its recognition and abundance remain an important marker for distinguishing between lower(?) Tallulah Falls Formation and Cat Square terrane biotite gneiss in the area (Byars, 2010; Gilliam, 2010; Huebner et al., 2011a; Howard, 2012; Huebner, 2013; Huebner et al., 2014).

Cat Square terrane/Eastern Inner Piedmont

Clastic deposition in the remnant Cat Square basin is represented by metasedimentary units (biotite paragneiss and sillimanite schist) present in the Cat Square terrane southeast of the Brindle Creek-Jackson Lake fault. These rocks were subsequently intruded by two mineralogically, texturally, and temporally distinct plutons, which form a portion of the Lloyd Shoals plutonic complex (Huebner et al., 2014).

Biotite Gneiss

The most voluminous metasedimentary rock unit in this portion of the Cat Square terrane is migmatitic biotite paragneiss with a well-developed foliation defined by parallel alignment of platy minerals. Biotite gneiss is typically medium-grained, light to dark gray, and is almost exclusively migmatitic. Where this unit has been extensively migmatized, it is interlayered with 5–10 cm-thick coarse-grained granitic leucosome (Fig. 2-5a-b). Small volumes of very coarse-grained pegmatite with exceptionally large feldspars that are several cm in both length and width are locally exposed.

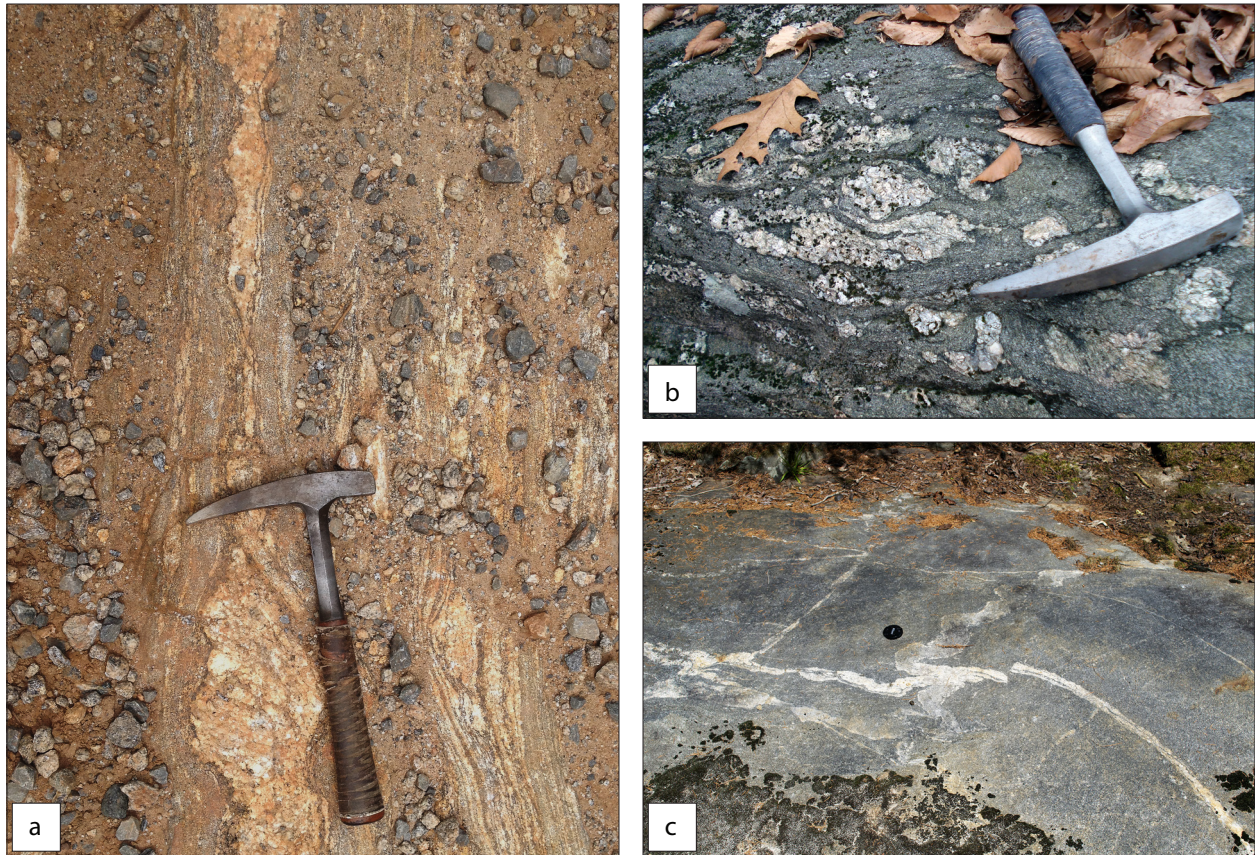


Figure 2-5. Biotite gneiss in the Cat Square terrane. (a-b) Extensively migmatized biotite gneiss with boudinaged coarse-grained granitic leucosome. Loose material in (a) is allochthonous gravel used as road aggregate. (c) Less extensive migmatization of biotite gneiss with fine-grained ptgmatically folded leucosome. Also note the offset of leucosome in (c) by brittle faulting. Photograph in (a) was taken along Brinkley Road, west of Georgia Highway 36 in the Barnesville quadrangle. (b) was taken along Pepper Creek at station J022 in the Johnstonville quadrangle, and (c) was taken along Turner Creek at station B154 in the Barnesville quadrangle. Lens cap (5 cm diameter) for scale.

Finer-grained, thinner (< 3 cm), and often ptgmatically folded felsic leucosome is present where migmatization has not been as intense (Fig. 2-5c). Common mineral assemblage is quartz + plagioclase + biotite + microcline \pm muscovite \pm sillimanite \pm garnet with accessory zircon, sphene, allanite, and opaque minerals (Fig. 2-6a-b). This unit is susceptible to weathering and, due to large concentrations of biotite, produces a dark red to reddish-brown soil. Saprolite outcrops are extensively common and, while mineralogy is drastically altered by weathering processes, mesoscale structures remain readily apparent. Simple preparation of a saprolite roadcut by using a hoe to scrape off loose dirt will often reveal detailed and measureable structures (Fig. 2-7). Results from a modal analysis of OH032 (Table 2-1) were plotted on a modified quartz-mica-feldspar

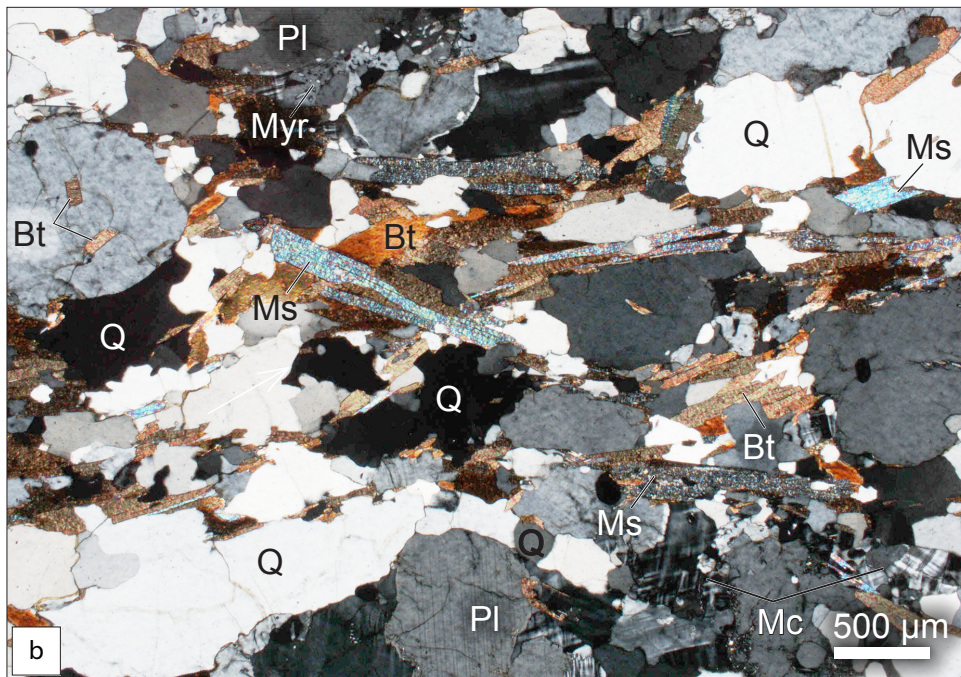
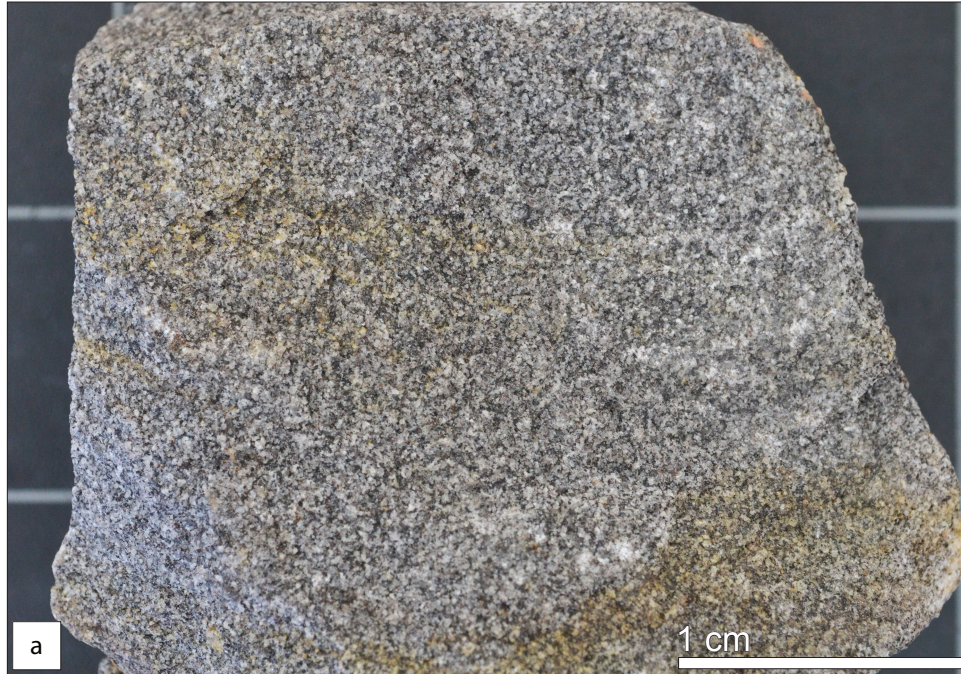


Figure 2-6. Biotite gneiss sample OH032. (a) Representative hand sample of biotite gneiss, collected for petrographic and detrital zircon analysis from an exposure in Edie Creek in the Orchard Hill quadrangle at station OH032. (b) Photomicrograph of thin section OH032 showing dominant mineral assemblage of Cat Square terrane biotite gneiss. Bt—biotite; Mc—microcline; Ms—muscovite; Myr—myrmekite; Pl—plagioclase; Q—quartz.



Figure 2-7. Saprolite outcrop of layered migmatitic biotite gneiss cut by a late brittle fault of ~5 cm displacement (indicated by arrows, left of center). Outcrop located along Crane Road in the Barnesville quadrangle, Lamar County; view is looking east. Hoe (1.5 m length) for scale. Photograph by M.T. Huebner.

ternary diagram (Pettijohn, 1949), along with data from previous geologists in the Inner Piedmont in North Carolina and central Georgia (Fig. 2-8). These results are interpreted with a high degree of caution because the likelihood that mineralogy present in rocks subjected to upper-amphibolite facies conditions (e.g., Cat Square terrane biotite gneiss) represents original depositional composition or abundance is very slight. This method is employed here, however, only to facilitate comparison with results from previous studies. Cat Square terrane metapsammites from central Georgia typically plot within the mica-poor graywacke and arkosic sandstone fields. Two populations are observed in Cat Square terrane metapsammites in North Carolina: one population lies well within the graywacke field, and the other lies in the arkose field. Data from Tugaloo terrane metapsammites exhibit a wider distribution and typically plot within the graywacke field, while a few outliers plot within the arkose field. Mineral modes obtained from sample OH495, as part of this study, plot within the graywacke field and are the only data represented from Tugaloo terrane metapsammites in central Georgia.

Table 2-1. Modal analyses of Cat Square terrane metagraywacke

Mineral	OH032		OH495	
	Points	%	Points	%
Quartz	412	41.20	448	41.25
Alkalai Feldspar	81	8.10	0	0.00
Plagioclase	368	36.80	222	20.44
Sericite	2	0.20	0	0.00
Myrmekite	0	0.00	0	0.00
Biotite	102	10.20	224	20.63
Muscovite	24	2.40	42	3.87
Chlorite	8	0.80	2	0.18
Garnet	0	0.00	38	3.50
Hornblende	0	0.00	0	0.00
Sillimanite	0	0.00	104	9.58
Zircon	2	0.20	4	0.37
Apatite	0	0.00	0	0.00
Allanite	1	0.10	0	0.00
Rutile	0	0.00	0	0.00
Opakes	0	0.00	2	0.18
Total:	1000	100.00	1086	100.00

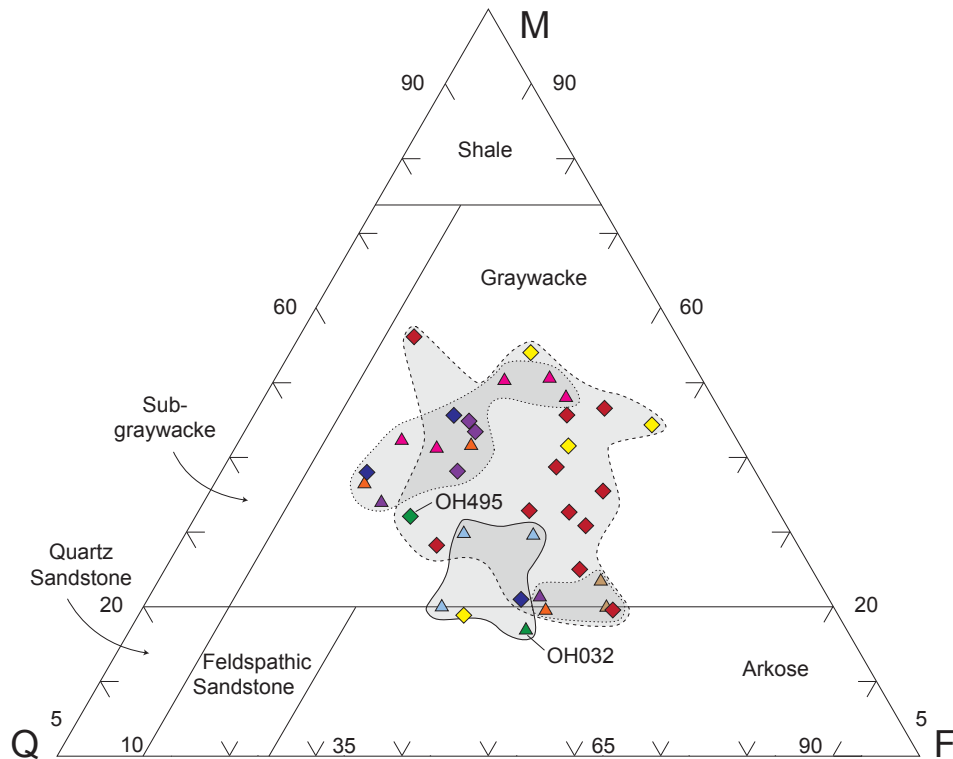


Figure 2-8. Modified (Hadley and Goldsmith, 1963) quartz-feldspar-mica ternary sandstone classification diagram (Pettijohn, 1949). Modes from Cat Square terrane (colored triangles) and Tugaloo terrane (colored diamonds) metapsammitic rocks are plotted. Dashed field line silhouettes Tugaloo terrane samples from North Carolina; dotted field line silhouettes Cat Square terrane rocks from North Carolina; solid field line silhouettes Cat Square terrane samples from central Georgia. Orange—Giorgis (1999); Yellow—Williams (2000); Pink—Bier (2001); Red—compiled by Bream (2003); Purple—Kalbas (2003); Brown—Wilson (2006); Dark blue—Gatewood (2007); Light blue—Davis (2010); Green—this study.

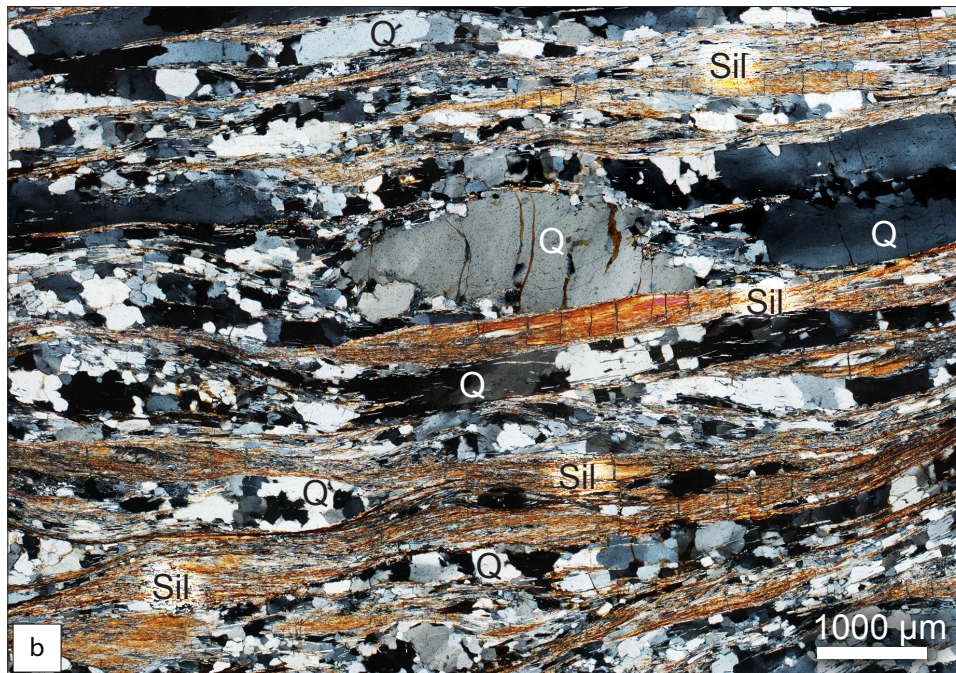
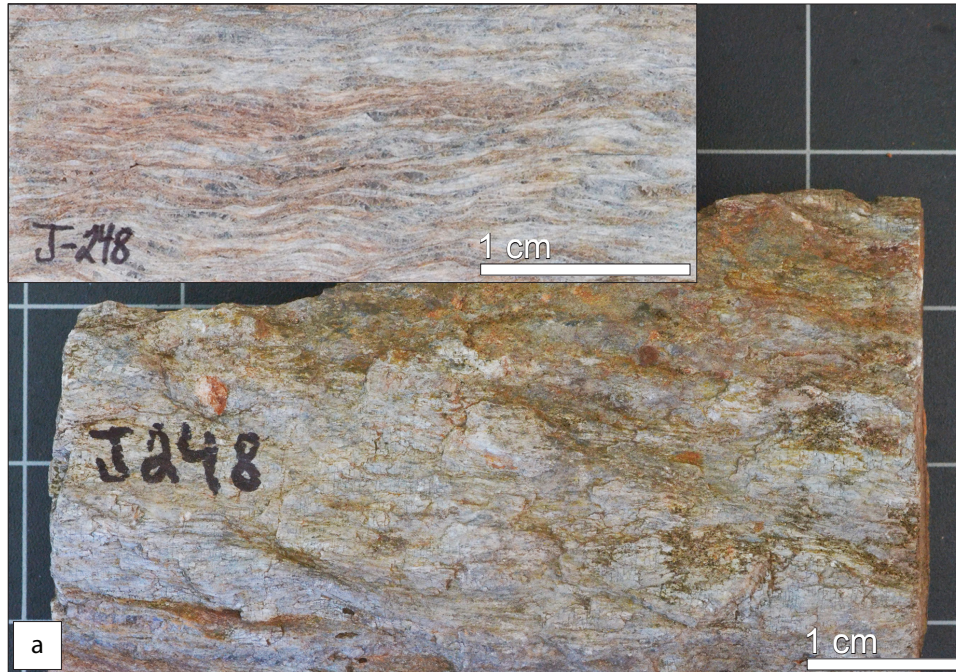


Figure 2-9. Sillimanite schist in the Cat Square terrane. (a) Hand sample and sawed billet of schist, in which abundant sillimanite is present. Sample was collected as float at station J248, south of City Pond Road, and west of Edie Creek in the Johnstonville quadrangle. (b) Photomicrograph of thin section J248, showing abundance of sillimanite and development of S-C fabric. Pl—plagioclase; Q—quartz; Sil—sillimanite.

Sillimanite Schist

Sillimanite schist is present throughout the study area and consists predominantly of muscovite and quartz with varying amounts of sillimanite, biotite, plagioclase, and garnet. The nomenclature is indicative of metamorphic grade and does not imply relative abundance of sillimanite. Both prismatic and fibrolitic sillimanite are present and occur locally in high concentrations, so much so that sillimanite constitutes a large percentage of modal abundances (Fig. 2-9a-b). Fresh exposures of this unit are exceedingly rare and it is most often observed in saprolite outcrops (Fig. 2-10a). Sillimanite schist weathers to various shades of brown that vary with mineralogical composition and are characteristically lighter than those developed by weathering of biotite gneiss. Higher amounts of sillimanite in the schist impart a purplish hue, while higher concentrations of biotite impart a reddish color to the soil (Fig. 2-10a-b).

High Falls Granite

The most extensive lithology in the study area is the High Falls Granite, which occupies the majority of the southwestern part of the Cat Square terrane. It is named for excellent exposures in High Falls State Park in Butts County, Georgia, just northeast of the present study area (Atkins and Lineback, 1992). The High Falls Granite is a coarse-grained porphyritic biotite granite, characterized by large rectangular (1 x 3 cm) euhedral white microcline megacrysts (Fig. 2-11a). Megacrysts are typically fractured lengthwise on a plane oriented along their long axes, which is easily recognizable in both outcrop and hand specimen. Matrix material is composed of a coarse-grained granoblastic assemblage of quartz and feldspar with abundant biotite. Typical euhedral megacrystic High Falls Granite is generally present only in a portion of the study area located near the Barnesville Reservoir, where corners of four quadrangles meet, and is designated Dhf₁ on the map (Fig. 2-1). The majority of High Falls Granite mapped in the remainder of the study area does not typically contain undeformed euhedral megacrysts, and has been informally termed “non-megacrystic High Falls Granite.” It is designated Dhf₂ on the map. Dhf₂ is a coarse-grained granite comprised of a matrix of granoblastic quartz and feldspar with an abundance of biotite, which is often porphyritic enclosing white microcline phenocrysts. Where phenocrysts are present, they are extensively sheared and rounded (Fig. 2-11d), and texturally do not resemble the rectangular euhedral megacrysts observed at the type locality of the High Falls Granite (Dhf₁). Portions of this lithology

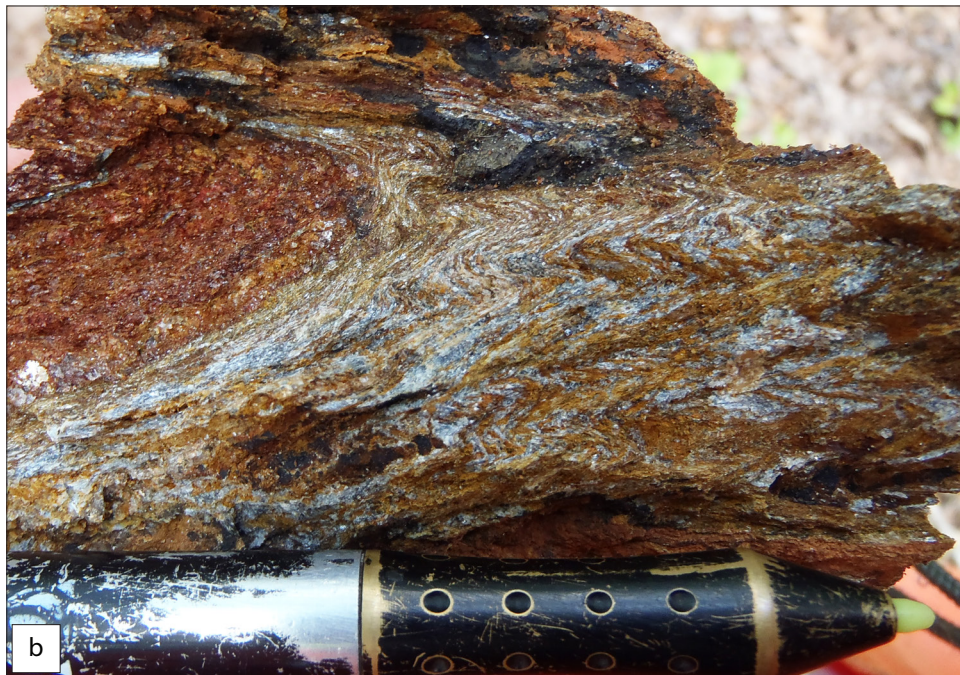


Figure 2-10. Weathered sillimanite schist in the Cat Square terrane. (a) Characteristic purplish hue of migmatitic sillimanite schist in weathered outcrop located on the southwest side of McKneely Road in the Orchard Hill quadrangle near station OH268. (b) Sillimanite visible in hand sample from outcrop near (a) with crenulation cleavage in sillimanite-rich layers.

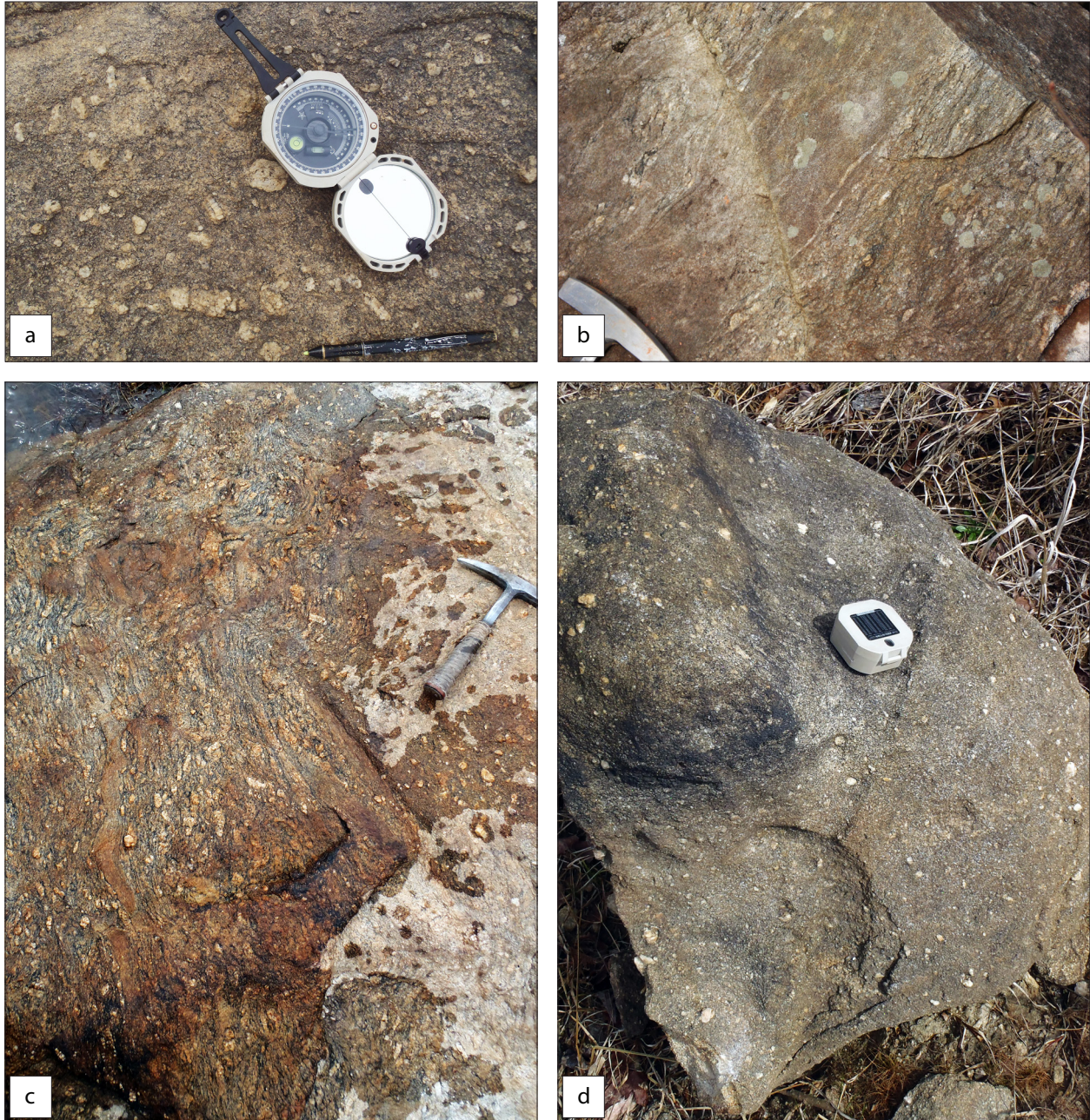


Figure 2-11. High Falls Granite. (a) Typical megacrystic High Falls Granite (Dhf₁), showing two dominant foliations of aligned euhedral white microcline megacrysts, indicated by Brunton compass and Trimble stylus. Outcrop is located on the northern shoreline of the Barnesville Reservoir in the Johnstonville quadrangle at station J148. (b-c) Crosscutting relationships of fine-grained Indian Springs Granodiorite and High Falls Granite. (b) Photograph of outcrop along Turner Creek in the Barnesville quadrangle near station B068, where Indian Springs Granodiorite (center) intruded “non-megacrystic” High Falls Granite (Dhf₂). (c) Outcrop in which Indian Springs Granodiorite intruded Dhf₁. This exposure is in the same vicinity as (a). (d) Characteristic outcrop of Dhf₂ northwest of the Barnesville reservoir in the Orchard Hill quadrangle near station OH010, which contains several rounded microcline phenocrysts that do not resemble the typical euhedral variety in (a) and (c).

were likely correlated with the Hollonville granite by Atkins and Lineback (1992), and to a porphyroblastic gneiss, equivalent to the Zebulon Formation of Higgins et al. (1988), by Sneyd (1995) and R.L. Kath (unpublished data). Atkins and Lineback (1992) described the Hollonville granite as a late Paleozoic medium-grained porphyritic biotite granite, which is petrographically similar to the High Falls Granite. A late Paleozoic age of the Hollonville granite was based on unpublished preliminary whole rock Rb/Sr analyses (Atkins and Lineback, 1992), which could not be substantiated by field relationships with the older High Falls Granite. Atkins and Lineback (1992) did show that the Hollonville granite crosscuts what we now know are middle Paleozoic structural fabrics, related to the Brindle Creek-Jackson Lake fault, and a regional (S_2) foliation (Huebner et al., 2014) northeast of the present study area; however, work in that area by Howard (2012) contradicted the suggestion that regional fabric is cut by the granite and demonstrated that the foliation in the granite is concordant with regional (S_2) foliation. Field relationships, mineralogical similarities, and matrix textures observed as a part of this study indicate this lithology should be classified as a distinct phase of the High Falls Granite, but not a different granitic unit. Foliation of Dhf_2 in the study area is predominantly concordant with regional (S_2) foliation, with few local exceptions that could be attributed to magmatic flow during syn-deformational emplacement (Howard, 2012; Huebner et al., 2014). Field relationships between Dhf_1 and Dhf_2 have not been established, but it does not appear that either phase is intrusive into the other. Both phases are truncated by the Brindle Creek-Jackson Lake and Towaliga faults, and are intruded by the younger Indian Springs Granodiorite (Fig. 2-11b-c). U-Pb SHRIMP-RG geochronologic analyses of one sample of Dhf_2 were inconclusive, and while those data permit interpretation of a late Paleozoic age for this granite (see chapter 4), it is unlikely given crosscutting relationships. U-Pb ion microprobe analyses of four samples of Dhf_1 northeast of this study area yielded Late Devonian ages of 407-371 Ma (Huebner et al., 2014).

Indian Springs Granodiorite

The Indian Springs Granodiorite is a white to light gray fine-grained granite-granodiorite (Howard, 2012) that is typically weakly foliated (Fig 2-12a). Common mineral assemblage is plagioclase + quartz + microcline + biotite \pm muscovite with accessory apatite and zircon (Fig. 2-12b). Myrmekite is extensively present as convex bulges into K-feldspar. Minor sericitic alteration

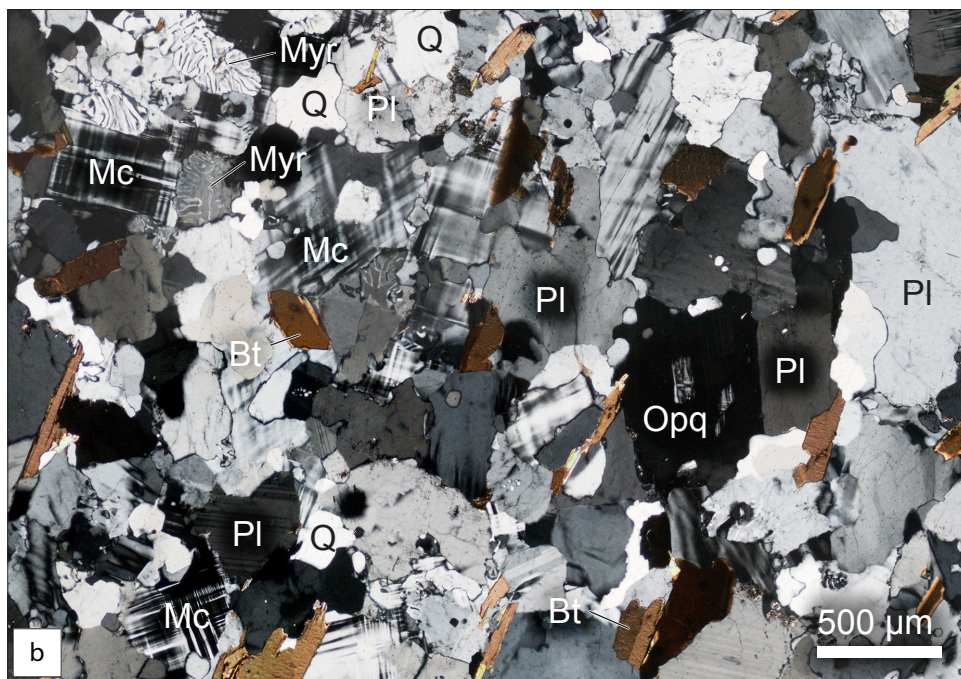


Figure 2-12. Indian Springs Granodiorite. (a) Representative hand sample of fine-grained equigranular Indian Springs Granodiorite at station B053. (b) Photomicrograph of thin section B053 showing dominant mineralogy. Bt—biotite; Mc—microcline; Myr—myrmekite; Opq—opaque mineral; Pl—plagioclase; Q—quartz.

Table 2-2. Modal percentages of igneous rocks.

Mineral	B053			J360		
	Points	%	QAP Norm %	Points	%	QAP Norm %
Quartz	299	29.78	31.24	261	25.41	42.23
Alkalai Feldspar	209	20.82	21.84	17	1.66	2.75
Plagioclase	399	39.74	46.92	284	27.65	55.02
Sericite	4	0.40		45	4.38	
Myrmekite	46	4.58		11	1.07	
Biotite	40	3.98		153	14.90	
Muscovite	4	0.40				
Chlorite						
Garnet				98	9.54	
Hornblende				94	9.15	
Sillimanite						
Zircon	1	0.10		1	0.10	
Apatite	2	0.20		20	1.95	
Allanite				27	2.63	
Rutile				3	0.29	
Opaques				13	1.27	
Total:	1004	100.00	100.00	1027	100.00	100.00

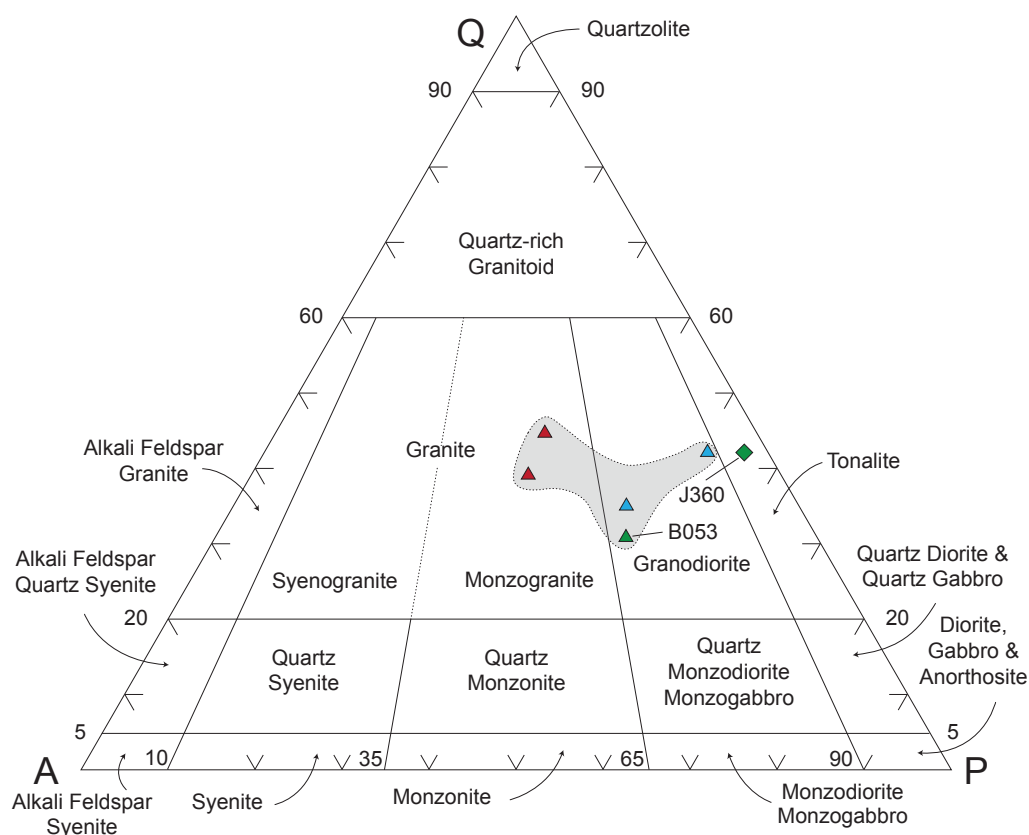


Figure 2-13. Quartz-alkali feldspar-plagioclase ternary IUGS classification diagram (Streckeisen, 1976) of igneous rocks from the study area, Davis (2010), and Howard (2012). Colored triangles represent Indian Springs Granodiorite; colored diamond represents hornblende tonalite. Blue—Davis (2010); Red—Howard (2012); Green—this study. Shaded field silhouettes data Indian Springs Granodiorite samples.

of plagioclase is also common. Feldspars are typically deformed and contain undulatory extinction and distorted twins. Both modal and geochemical analyses of the Indian Springs Granodiorite by Davis (2010) and Howard (2012) revealed that the granitoid plots across both the granite and granodiorite classification fields. Data from modal analysis of sample B053 from the study area (Table 2-2) plotted on a quartz-alkali feldspar-plagioclase ternary diagram (Streckeisen, 1976) agree with the granodiorite classification (Fig. 2-13). This granitoid is not extensive in the study area and occupies only the northeast corner of the Barnesville quadrangle and northwestern corner of the Johnstonville quadrangle. It is more voluminous to the northeast and is named for excellent exposures near Indian Springs State Park, Butts County, Georgia (Huebner et al., 2014). Typical exposures of this unit occur as ~1 m-sized spheroidal boulders and, where extensively weathered, it forms a light tan to yellow sandy soil. The Indian Springs Granodiorite is intrusive into both phases of the High Falls Granite. Huebner et al. (2014) reported ion microprobe ages from two samples of 316.5 ± 4.2 and 305.0 ± 7.0 Ma for this granitoid.

Amphibolite

Small (< 10–15 cm) amphibolite boudins are not uncommon in the Cat Square terrane and, given their greater resistance to erosion than the surrounding metasedimentary rocks, commonly occur as float. Amphibolite is fine- to medium-grained, dark gray to black and, depending on the amount of feldspar present, can have a “salt and pepper” appearance (Fig. 2-14a-b). Typical mineral assemblage is hornblende + plagioclase + opaque minerals \pm garnet \pm quartz \pm epidote.

Pine Mountain window

Woodland Gneiss

The Woodland Gneiss is the most widespread exposed basement orthogneiss in the mapped area in the Pine Mountain window, and was named by Hewett and Crickmay (1937) for the town of Woodland, Talbot County. This unit is composed predominantly of dark-gray, coarse-grained biotite-microcline-quartz augen gneiss, consisting of large (1–2 cm long) sheared microcline distributed throughout a fine- to medium-grained biotite-quartz-plagioclase-K-feldspar matrix (Fig. 2-15a). Garnet locally occurs in the gneiss as a primary phase, with muscovite, apatite, sillimanite, and zircon occurring as common accessory phases. Although the Woodland Gneiss typically occurs as

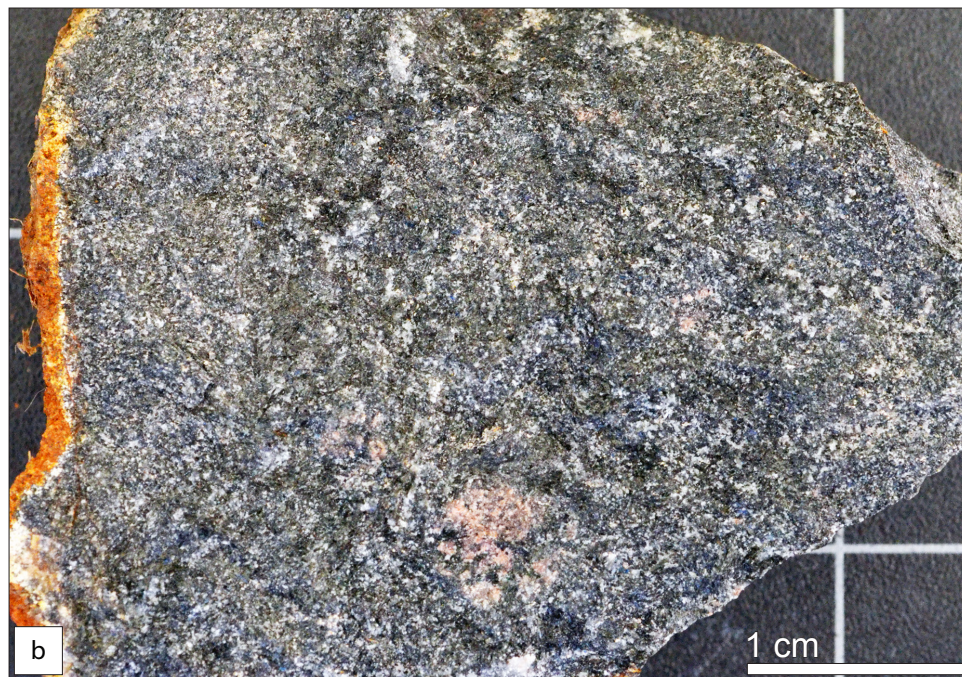
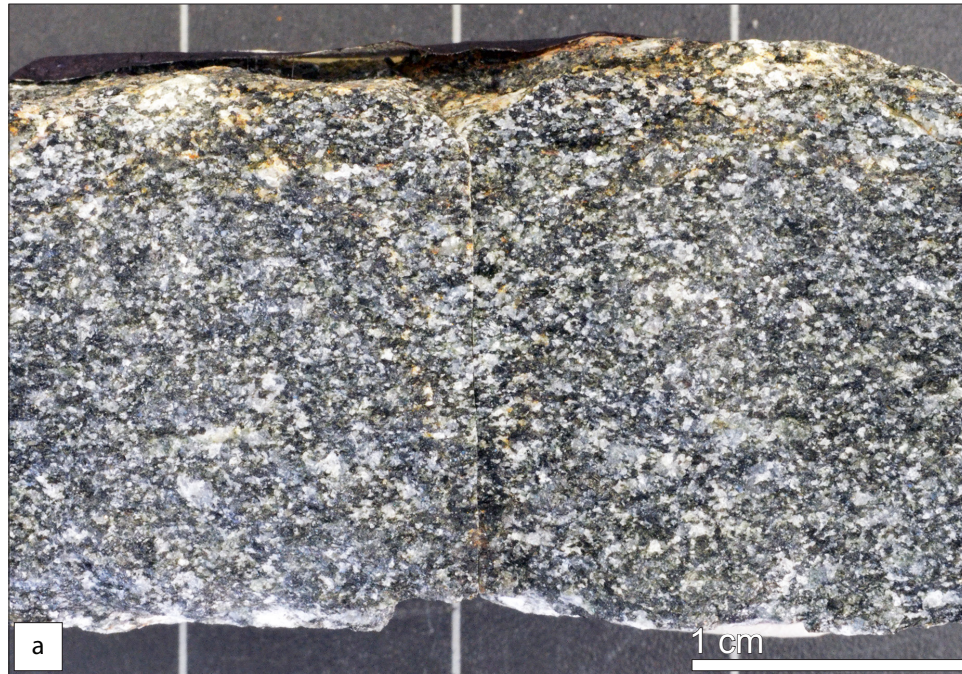


Figure 2-14. Representative hand samples of amphibole gneiss in the Cat Square terrane. (a) Medium-grained sample of amphibolite with a moderate amount of feldspar giving a “salt and pepper” appearance to the rock. Sample collected as float at station OH330. (b) Finer-grained sample of amphibolite with large (3–4 mm) garnets and lesser amounts of feldspar. This sample exhibits a reddish-orange weathering rind and was collected as float at station OH301. Portions of both samples were prepared and used for whole-rock geochemical analysis. Both samples are from the Orchard Hill quadrangle.



Figure 2-15. Woodland Gneiss at the northeast end of the Pine Mountain window. (a) Typical exposure of sheared Woodland Gneiss exposed in a clear-cut area just south of the Towaliga fault, northeast of the intersection of Brook Road and Crawford Road in the Johnstonville quadrangle, at station J222. (b) Outcrop of locally occurring, undeformed Woodland Gneiss, with euhedral K-feldspar megacrysts up to 7 cm long, exposed in a creek west of Flemming Cemetery in the Johnstonville quadrangle at station J263. (c) Large pavement outcrop of sheared Woodland Gneiss exposed in shoals of the Little Towaliga River at Higgins Mill in the southwest corner of the Indian Springs quadrangle. Note the strong lineation developed by the elongation of feldspars. View at the center of the photograph is oriented 10° west of north, houses in background for scale.

sheared gneiss with extensively deformed feldspars, in some locations it does occur as undeformed granitic gneiss characterized by large euhedral microcline megacrysts up to 10 cm long (Fig. 2-15b). Exposures of this unit are common throughout the Pine Mountain window and generally occur as small (< 50 m²) pavement outcrops with few large (> 1 km²) outcrops occurring locally, such as the shoals in the Little Towaliga River at Higgins Mill (Fig. 2-15c). The weathering characteristics of this gneiss produce a dark red-colored soil and is largely responsible for the gentle rolling topography observed to the southeast of the Towaliga fault. U-Pb ion microprobe analyses of zircon revealed a 1011 ± 12 Ma (Heatherington et al., 2006) age of the Woodland Gneiss.

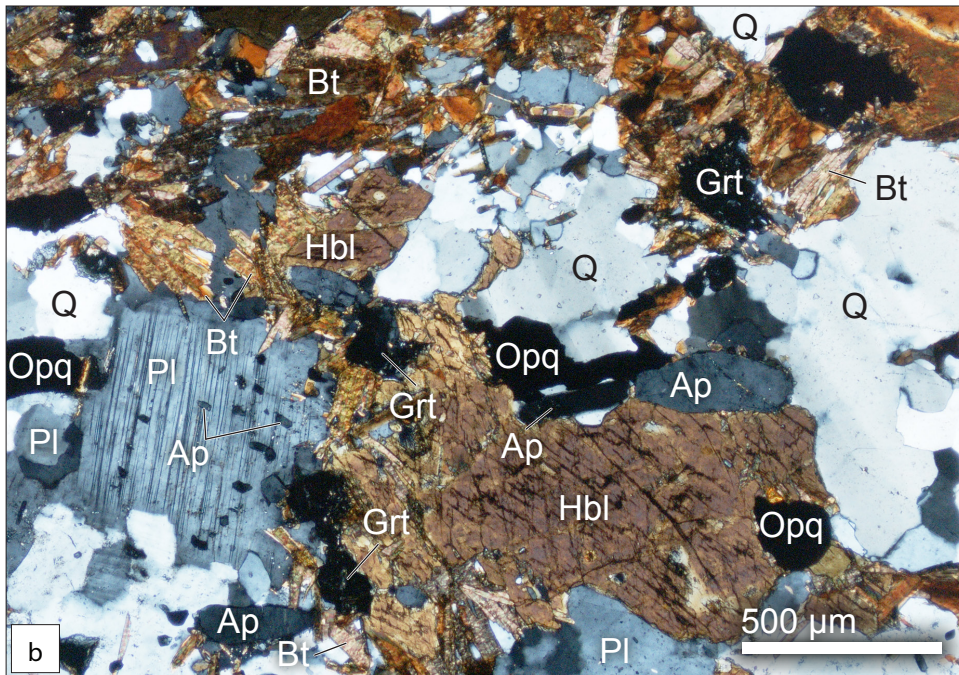


Figure 2-16. Hornblende tonalite. (a) Spheroidally weathered boulder of hornblende tonalite exposed east of Brook Road in the Johnstonville quadrangle at station J360. (b) Photomicrograph of thin section J360, showing dominant mineralogy and texture. Ap—apatite; Bt—biotite; Grt—garnet; Hbl—hornblende; Opq—opaque mineral; Pl—plagioclase; Q—quartz.



Figure 2-17. Hollis Quartzite at the northeast end of the Pine Mountain window. (a-b) Two varieties of Hollis Quartzite exposed on a ridge east of Potato Creek and north of Turner Bridge Road in the Barnesville quadrangle. (a) Muscovite-rich, well-foliated Hollis Quartzite that locally grades upward into massively bedded more pure quartzite (b).

Hornblende tonalite

A large body of light- to medium-gray coarse-grained tonalite is exposed in a klippe of Cat Square terrane rocks in the Pine Mountain window at the northwestern corner of the Johnstonville 7.5 min quadrangle. Outcrops typically occur as large (1–5 m) rounded boulders, resulting from spheroidal weathering of thick exfoliation surfaces (Fig. 2-16a). Data from a modal analysis of tonalite sample J360 (Table 2-2) indicate it is composed predominantly of plagioclase, quartz, biotite, garnet, and hornblende with minor amounts of apatite and alkali feldspar and accessory allanite, zircon, rutile, and opaque phases (Fig. 2-16b). These data plot in the tonalite field of a quartz-alkali feldspar-plagioclase ternary diagram (Streckeisen, 1976) (Fig. 2-13). Garnet is typically mantled by biotite, which, along with dark hornblende, gives the rock a “speckled” appearance. Plagioclase is extensively altered to sericite and typically exhibits both albite and pericline twins. Alkali feldspars are distinguished from doubly twinned plagioclase by common perthitic texture and convex bulges of myrmekite along rims where in contact with plagioclase feldspars. A foliation defined by parallel alignment of biotite tends to be well developed near the contact with the enclosing Cat Square terrane rocks, becoming more weakly developed and almost non-existent toward the interior of the exposure. SHRIMP-RG analyses of zircon from one sample of tonalite yielded an age of 1011 ± 10 Ma (Rehrer, this study). This age is favored over the 1007 ± 9 Ma age reported for this sample (Huebner et al., 2014), which was based only on preliminary data interpretation.

Pine Mountain cover sequence

Metasedimentary units comprising the Neoproterozoic-Paleozoic(?) cover group of the Pine Mountain window terrane in Georgia consist of the Sparks Schist, Hollis Quartzite, and Manchester Schist (Hewett and Crickmay, 1937). The Sparks Schist is composed of feldspathic quartz-mica schist, which lies stratigraphically above basement units of the Pine Mountain window and below the Hollis Quartzite. It is not exposed in the map area; here the Hollis Quartzite is in apparent unconformable contact with the underlying basement units (e.g., Woodland Gneiss). The Hollis Quartzite consists of fine- to medium-grained, micaceous-feldspathic quartzite that is typically thin-bedded and interlayered with coarse-grained muscovite that defines a foliation sub-parallel to compositional layering (Fig. 2-17a). Locally this unit grades upward into a massively bedded, more

Figure 2-18. Fault rocks of the study area. (a) Mylonitic exposure of the Brindle Creek-Jackson Lake fault below the Woodfin Mill dam in the Barnesville quadrangle, Lamar County. (b) Sawed slab of Brindle Creek-Jackson Lake fault mylonite sampled from an exposure along Buck Creek Road in the Orchard Hill quadrangle at station OH286. (c) Sawed slab of Towaliga fault mylonite sampled from a large exposure along the Towaliga Creek in the northwestern Johnstonville quadrangle east of Brook Road. Asymmetric folds and tailed porphyroclasts were used to infer top to the right sense of shear. (d) Exposure of Towaliga fault mylonite in the same vicinity as (c). An ultramylonite layer separates mylonite (top) from protomylonite-mylonite (bottom). (e) Specimen exhibiting “box work” texture in which large quartz crystals are forming normal to surfaces of a void created by brittle fracture. Sample is from the large area of cataclasis associated with the Towaliga fault in the northeastern portion of the Barnesville quadrangle. (f) Sawed quartz mylonite hand sample showing mm-sized deformed quartz ribbons. Sample was collected as float along a hillside just north of where Crawford Road crosses Pepper Creek in the Johnstonville quadrangle. (g) Scan of thin section J006b in plane-polarized light showing brittle overprint of quartz mylonite resulting in a microbreccia. (h) Photomicrograph of thin section J006 in cross-polarized light. Area of photomicrograph is indicated by a yellow and white dashed box in (e). Sample J006 was collected as float in the same vicinity as the quartz mylonite sample in (f).



Figure 2-18.



Figure 2-18 *continued*.



Figure 2-18 *continued.*



Figure 2-18 *continued.*

pure quartzite (Fig. 2-17b). The Hollis Quartzite is resistant to weathering and forms steep ridges that are obvious in the topography and stand in relief at the southwestern portion of the map. Where there is extensive weathering the unit develops a fine-grained, sandy, light yellow to tan soil. Biotite-quartz-feldspar schist lying stratigraphically above the Hollis Quartzite has been mapped in the Barnesville quadrangle (Sneyd, 1995; R.L. Kath, unpublished data). Petrographic descriptions of this unit, along with its stratigraphic position above the Hollis Quartzite, indicate that it is most likely part of the Manchester Schist described by Hewitt and Crickmay (1937) and Clarke (1952).

Fault rocks

The majority of fault rocks present in the study area are products of ductile processes and are represented by various types of mylonite. Mylonite is not generally regarded as a separate lithology and is often represented by symbology indicating a shear zone in some variety of protolith, or pre-existing rock type. Given the intensive mylonitization and similarities among lithologies on opposite sides of major fault zones (e.g., coarse-grained porphyritic biotite granite in the Cat Square terrane and coarse-grained biotite augen gneiss in the Pine Mountain window) in the study area, it is often difficult to speculate as to the protolith of a particular mylonite. In that regard, amphibolite facies mylonite of the Towaliga fault does appear on the map as a separate lithology. Mylonites of the Brindle Creek-Jackson Lake fault and ribbon quartz mylonites are not represented by a distinct lithology, as their exposure is not recognizable at the scale of this study.

Brindle Creek-Jackson Lake fault mylonite

The Brindle Creek-Jackson Lake fault is recognized by a narrow (~10 m) northeast-trending high temperature mylonite zone. A variety of protoliths are represented within the fault zone and vary from mica-rich metasedimentary rocks to coarse-grained granitoids (e.g., High Falls Granite). Extensive migmatization is common of rocks in close proximity to the fault zone. S-C fabrics are well developed and exceedingly evident where the protolith contained abundant phyllosilicates (Fig 2-18a). Asymmetric tailed feldspar porphyroclasts dominate where the protolith was a porphyritic granitoid, such as the exposure at the dam at Woodfin Mill (Fig. 2-18b). The narrow width and sometimes subtle nature of mylonitization in the fault zone can make the Brindle Creek-Jackson Lake fault difficult to recognize in certain locations.

Towaliga fault mylonite

The Towaliga fault is characterized by garnet-grade mylonite with rounded, brittlely deformed feldspar porphyroclasts in a very fine-grained biotite-rich matrix. Porphyroclasts exhibit quartz-mica strain shadows with no feldspar tails; however, several quartz-tailed σ - and δ -type porphyroclasts, asymmetric folds of quartz ribbons, and S-C fabrics yield dextral shear sense (Fig 2-18c). Towaliga fault zone rocks range from protomylonite with large (up to 4 cm) porphyroclasts to fine-grained ultramylonite. It is also common to observe strain localized into bands of ultramylonite in a coarse-grained mylonite (Fig. 2-18d).

Cataclasite

Brittle reactivation of the Towaliga fault produced numerous dilational step-overs filled with multiply broken hydrothermal quartz cataclasite (Huebner and Hatcher, 2013). A rhomb-shaped pod of siliceous cataclasite has also been identified west of Barnesville, the geometry of which suggests sinistral movement along a brittle fault not directly related to the Towaliga fault zone. Cataclasite is recognizable by 0.5–1 cm angular clasts cut by mm-size irregular fractures filled by later fine-grained quartz mineralization. Another common occurrence among these brittle faults and dilational step-overs is a “boxwork” texture (Huebner and Hatcher, 2013) of coarse quartz intergrowths oriented normal to fracture walls (Fig. 2-18e).

Quartz mylonite

Ribbon quartz mylonite is a common occurrence near faults in the Inner Piedmont in this part of Georgia (Huebner and Hatcher, 2013), and occurs primarily along the Towaliga fault zone in the study area. The mylonite consists of > 90 percent quartz with minor amounts of muscovite and feldspar. It is characterized by the ductile deformation of quartz into ~1–5 mm ribbons (Fig. 2-18f) and contains evidence of dynamic recrystallization by subgrain rotation and bulging at ribbon grain boundaries. Quartz mylonites are frequently overprinted by a brittle fabric (Fig. 2-18g-h) that may be attributed to late Alleghanian deformation or early stages of Mesozoic rifting (Huebner and Hatcher, 2013).

Chapter 3

Geochemistry of Inner Piedmont amphibolites at the southwestern end of the Cat Square terrane

Introduction

Following recognition of the Cat Square terrane from detrital zircon geochronology in North Carolina (Bream, 2003), its formation was interpreted to be the result of deposition in a remnant ocean basin. The basin closed during the Acadian/Neoacadian orogeny by obduction of the Carolina superterrane onto the Laurentian margin (Merschat and Hatcher, 2007). Merschat and Hatcher (2007) proposed deposition of sediments on ocean crust, and suggested enriched-mid-ocean ridge basalt (E-MORB) and back-arc affinity for the ocean crust based on geochemical analyses of amphibolites by Wilson (2006). Wilson (2006) recognized the necessity for addressing the nature of Cat Square basin development and included its genesis in tectonic models, permitting a more complete understanding of the origin of the Cat Square terrane. Amphibolite boudins and several map-scale mafic bodies have been identified in the Cat Square terrane in North Carolina, and were hypothesized to be vestiges of oceanic crust that formed the floor of the Cat Square basin. These rocks possibly represent vestiges of crust that were thrust onto the margin as ophiolites(?) as the basin closed (Wilson, 2006; Merschat and Hatcher, 2007; Byars, 2010). One map-scale body of amphibolite has been identified in the Cat Square terrane in central Georgia (Huebner, 2013), along with ubiquitous boudinaged amphibolite layers in Cat Square terrane metasediments (Davis, 2010; Howard, 2012; Huebner, 2013; Rehrer, this study). If Cat Square terrane sediments were deposited on ocean crust in a remnant ocean basin, and mafic rocks that occur in the terrane as amphibolite do represent vestiges of that crust, a thorough investigation identifying the affinity of the amphibolites would be key to composing a viable tectonic model for Cat Square basin development. As part of the characterization of the southwestern end of the Cat Square terrane in central Georgia, seven amphibolite samples were collected for whole-rock geochemical analysis from both the Tugaloo and Cat Square terranes, and used to identify possible eruptive tectonic settings. These data were also compared with results from similar amphibolite studies in the North Carolina Inner Piedmont (Wilson, 2006; Byars, 2010).

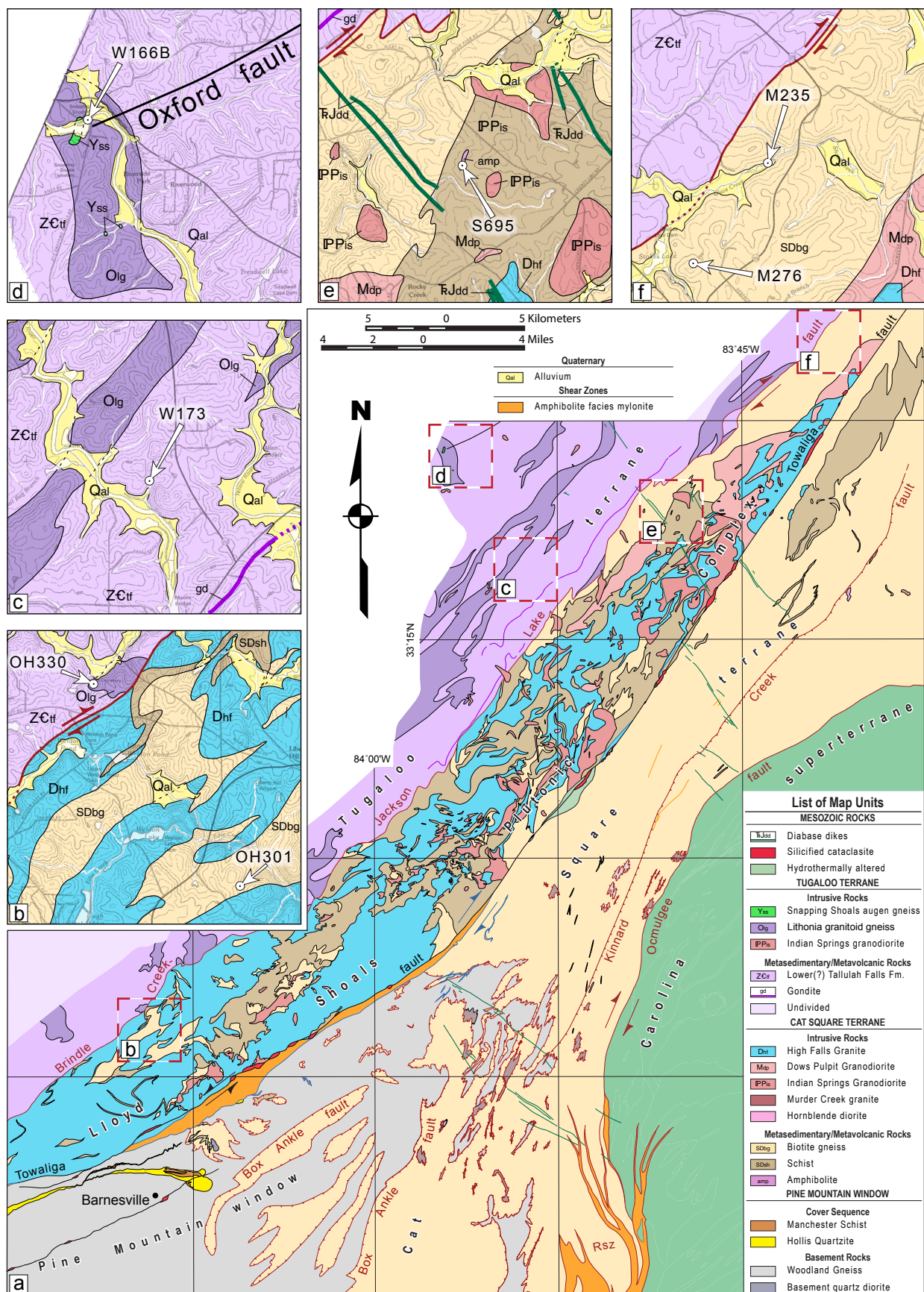
Whole-rock geochemical analyses of two samples of amphibolite were completed as part of this study. These data have been compiled with unpublished data from analyses of five samples obtained by previous workers in the central Georgia Inner Piedmont (Davis, 2010; Huebner, 2013). This assemblage of seven samples comprises an Inner Piedmont dataset from Georgia that can be compared with a much larger dataset from Inner Piedmont researchers in North Carolina (Davis, 1993; Yanagihara, 1994; Giorgis, 1999; Bream, 1999; Kalbas, 2003; Wilson, 2006; Byars, 2010).

Methods

Seven amphibolite samples were collected either as float or sampled directly from boudins or large exposures in the central Georgia Inner Piedmont (Fig. 3-1) and prepared for whole-rock geochemical analysis. It proved difficult to sample amphibolite directly from boudins in outcrop and float samples facilitated more efficient collection. Float samples were, however, only used for geochemical analysis if the original source could be verified and was in close proximity to the sample site. Samples OH301 and OH330 were collected from the southeastern portion of the Orchard Hill quadrangle as part of this study. Sample OH330 was collected as float from the Tugaloo terrane near the contact between lower Tallulah Falls(?) metagraywacke and a small body of Lithonia Gneiss just northwest of the Brindle Creek-Jackson Lake fault. Sample OH301 was collected as float from a large body of Cat Square terrane biotite gneiss. Huebner (2013) collected sample W173 in the southeast portion of the Worthville quadrangle from an outcrop of lower Tallulah Falls(?) metagraywacke containing abundant amphibolite boudins, and sample W166B from the northwestern portion of the Worthville quadrangle as float near the contact of Snapping Shoals augen gneiss (Grenville basement) and enclosing Lithonia Gneiss. Huebner (2013) also collected sample S695 from a mesoscale body of amphibolite southeast of the Brindle Creek-Jackson Lake fault in the central portion of the Stewart quadrangle. Davis (2010) collected samples M235 and M276 from Cat Square terrane biotite gneiss in the central portion of the Mansfield quadrangle southeast of and close to the Brindle Creek-Jackson Lake fault.

Samples were prepared for geochemical analysis using rock preparation labs at the Department of Earth and Planetary Sciences, University of Tennessee-Knoxville. In order to obtain representative samples, each specimen was cut lengthwise into several ~2 cm x 2 cm segments using a diamond-impregnated lapidary blade mounted on a Barranka tile saw. Fresh segments from

Figure 3-1. Central Georgia Inner Piedmont amphibolite sample locations. (a) Simplified geologic map of the southwestern end of the Cat Square terrane and northeastern end of the Pine Mountain window showing locations of inset maps (b-f). Inset maps display detailed geology and sample locations. Rsz—Rumble shear zone. (b) Sample locations from Rehrer (this study). (c-e) Sample locations from Huebner (2013). (f) Sample locations from Davis (2010). Regional map modified from Huebner et al. (2014).



the interior portions of the rock samples were subsequently cut into smaller (~5 mm diameter) chips, mixed, and quartered into subsamples containing ~30 g of material. Chips were rinsed with tap water, dried, and rinsed again with isopropyl alcohol to remove contaminants from the cutting process. Samples W166B, W173, S695, M235, and M276 were pulverized (95% -200 mesh grain size) using an alumina ceramic grinding mill in a SPEX 8530 Shatterbox, with a grinding time of three to four minutes. Samples OH301 and OH330 were pulverized using an alumina ceramic mill by the commercial analytical laboratory. Multi-element whole-rock geochemical analyses (Table 3-1) were performed by Activation Laboratories, Ancaster, Ontario, using the following methods:

- 1.) INAA: Concentrations of rare earth elements (REE) La, Ce, Nd, Sm, Eu, Tb, Yb, Lu, and other trace elements Au, As, Br, Co, Cr, Hg, Ir, Sb, Sc, Se, and W were determined using instrumental neutron activation analysis (INAA). An ~1 g aliquot of each sample was irradiated with standards in a neutron flux (7×10^{12} neutrons/cm²/second) and allowed to decay for a period of one week. Gamma-ray emissions from samples were counted on a spectrometer equipped with a high purity germanium detector (Hoffman, 1992).
- 2.) FUS-ICP: Major and minor element oxides and selected trace elements Ba, Be, Sr, V, and Y, were prepared using a lithium metaborate/tetraborate fusion technique and analyzed by inductively coupled plasma optical-emission spectrometry (FUS-ICP). An ~0.2 g aliquot was mixed with lithium metaborate/tetraborate, fused in a graphite crucible, and dissolved in 5 percent nitric acid. The solution was then analyzed for major and minor element oxides and selected trace elements using a combination simultaneous/sequential Thermo Jarrell-Ash Enviro II ICP.
- 3.) TD-ICP: Transition metals Cu, Ni, Pb, and selected trace elements Cd and S, prepared analyzed using a total dilution technique and analyzed by inductively coupled plasma mass spectrometry (TD-ICP). An ~0.25 g aliquot was digested with a series of four acids (HF-HClO₄-HNO₃-HCl), and analyzed using a Varian Vista ICP. Elements Ag and Zn were analyzed using multiple (INAA/TD-ICP) techniques.
- 4.) FUS-MS: Remaining trace elements Bi, Cs, Ga, Ge, Hf, In, Mo, Nb, Rb, Sn, Ta, Th, U, Zr, and REE were prepared using a lithium metaborate/tetraborate fusion technique, which was diluted and analyzed using an inductively coupled plasma emission mass spectrometer (ICP-MS) method (FUS-MS). REE concentrations were determined by both INAA and FUS-MS methods. Analyses by FUS-MS method are herein favored over analyses by INAA for REE because of superior detection limits and precision of FUS-MS (Lett and Paterson, 2011).

Igpet software was used to produce compositional diagrams illustrating data from whole-rock geochemical analyses compiled in Table 3-1.

Normative mineralogy (Table 3-2) was calculated for amphibolite samples from the central Georgia Inner Piedmont using major element data from whole-rock geochemical analyses.

Table 3-1. Major, trace, and rare earth element whole-rock geochemical analyses of central Georgia Inner Piedmont amphibolites.

Analyte Symbol	Method	Unit Symbol	Detection Limit	Cat Square terrane				Tugaloo terrane		
				OH301	S695	M235	M276	OH330	W166B	W173
SiO ₂	FUS-ICP	%	0.01	45.33	53.4	46.1	50.68	48.14	47.02	48.67
TiO ₂	FUS-ICP	%	0.001	4.295	1.398	2.082	2.219	0.354	1.58	1.29
Al ₂ O ₃	FUS-ICP	%	0.01	15.52	15.16	16.7	13.11	16.82	15.41	15.66
Fe ₂ O ₃	FUS-ICP	%	0.01	15.17	15.79	12.51	14.62	7.54	14.32	12.23
MgO	FUS-ICP	%	0.01	3.44	7.1	6.83	5.25	8.79	7.26	6.6
MnO	FUS-ICP	%	0.001	0.286	0.242	0.198	0.223	0.136	0.418	0.202
CaO	FUS-ICP	%	0.01	12.01	12	13.21	10.99	15.39	10.54	11.75
Na ₂ O	FUS-ICP	%	0.01	0.76	0.95	1.28	1.03	1.22	0.8	1.28
K ₂ O	FUS-ICP	%	0.01	0.29	0.51	0.51	0.79	0.33	0.51	0.47
P ₂ O ₅	FUS-ICP	%	0.01	0.62	0.13	0.23	0.23	0.03	0.27	0.09
LOI	FUS-ICP	%		0.49	-6.59	0.29	0.39	1.09	0.82	0.26
Total		%	0.01	98.21	100.09	99.94	99.53	99.84	98.95	98.5
Au	INAA	ppb	1	< 1	< 1	< 1	3	< 1	< 1	< 1
Ag	*	ppm	0.5	< 0.5	< 0.5	< 0.5	< 0.5	< 0.5	< 0.5	< 0.5
As	INAA	ppm	1	< 1	< 1	< 1	< 1	< 1	< 1	< 1
Ba	FUS-ICP	ppm	1	116	21	15	104	106	268	33
Be	FUS-ICP	ppm	1	< 1	< 1	< 1	2	2	3	< 1
Bi	FUS-MS	ppm	0.1	0.2	0.2	< 0.1	< 0.1	< 0.1	< 0.1	< 0.1
Br	INAA	ppm	0.5	< 0.5	< 0.5	< 0.5	< 0.5	< 0.5	< 0.5	< 0.5
Cd	TD-ICP	ppm	0.5	< 0.5	< 0.5	< 0.5	< 0.5	< 0.5	< 0.5	< 0.5
Co	INAA	ppm	0.1	48.8	42	51.7	51.2	47.8	57	46.3
Cr	INAA	ppm	0.5	65.7	156	55.2	131	51.7	338	116
Cs	FUS-MS	ppm	0.1	< 0.1	< 0.1	0.2	0.5	< 0.1	0.2	0.3
Cu	TD-ICP	ppm	1	112	38	< 1	8	70	30	36
Ga	FUS-MS	ppm	1	26	12	19	22	19	19	17
Ge	FUS-MS	ppm	0.5	2.4	1.4	2.5	2.8	0.9	1.8	1.5
Hf	FUS-MS	ppm	0.1	8.7	0.4	2.3	3.3	4.5	3.3	2.5
Hg	INAA	ppm	1	< 1	< 1	< 1	< 1	< 1	< 1	< 1
In	FUS-MS	ppm	0.1	< 0.1	< 0.1	< 0.1	< 0.1	< 0.1	< 0.1	< 0.1
Ir	INAA	ppb	1	< 1	< 1	< 1	< 1	< 1	< 1	< 1
Mo	FUS-MS	ppm	2	< 2	< 2	< 2	< 2	< 2	< 2	< 2
Nb	FUS-MS	ppm	0.2	28.2	< 0.2	4	12.8	16.7	25.6	1.6
Ni	TD-ICP	ppm	1	52	110	64	59	49	213	44
Pb	TD-ICP	ppm	5	< 5	< 5	< 5	< 5	< 5	< 5	< 5
Rb	FUS-MS	ppm	1	4	3	11	9	6	10	6
S	TD-ICP	%	0.001	0.848	0.111	0.005	0.013	0.15	0.552	0.111
Sb	INAA	ppm	0.1	< 0.1	< 0.1	< 0.1	< 0.1	< 0.1	< 0.1	0.1
Sc	INAA	ppm	0.01	39.5	49.6	51.3	33.6	39.2	23.1	45
Se	INAA	ppm	0.5	< 0.5	< 0.5	< 0.5	< 0.5	< 0.5	0.9	< 0.5
Sn	FUS-MS	ppm	1	7	< 1	< 1	2	2	2	< 1
Sr	FUS-ICP	ppm	2	893.0	173	291	135	264	450	118
Ta	FUS-MS	ppm	0.01	1.67	< 0.01	0.26	0.88	1.1	1.95	0.07
Th	FUS-MS	ppm	0.05	2.45	0.26	0.24	1.36	1.79	2.24	0.54
U	FUS-MS	ppm	0.01	0.75	0.28	0.12	0.47	0.6	0.66	1.73
V	FUS-ICP	ppm	5	504.0	244	458	313	405	189	318
W	INAA	ppm	1	< 1	< 1	< 1	< 1	< 1	< 1	< 1
Y	FUS-ICP	ppm	1	49	6	33	27	40	20	30
Zn	*	ppm	1	134	39	90	87	95	158	74
Zr	FUS-MS	ppm	1	409	14	79	124	179	129	84

Table 3-1 *continued*.

Analyte Symbol	Method	Unit Symbol	Detection Limit	Cat Square terrane				Tugaloo terrane		
				OH301	S695	M235	M276	OH330	W166B	W173
La	FUS-MS	ppm	0.05	34.3	6.97	18.2	18.1	1.89	22	3.26
Ce	FUS-MS	ppm	0.05	77.8	17.8	38	41.5	3.87	43.5	10
Pr	FUS-MS	ppm	0.01	10.7	2.66	5.28	5.27	0.55	5.34	1.77
Nd	FUS-MS	ppm	0.05	48	12.6	22.4	23.8	2.66	22	9.57
Sm	FUS-MS	ppm	0.01	11.2	3.96	5.45	6.08	0.76	5.23	3.52
Eu	FUS-MS	ppm	0.005	2.71	1.36	1.89	1.89	0.296	1.61	1.28
Gd	FUS-MS	ppm	0.01	11	4.92	5.34	6.41	0.94	5.03	4.56
Tb	FUS-MS	ppm	0.01	1.79	0.97	0.91	1.07	0.18	0.83	0.94
Dy	FUS-MS	ppm	0.01	9.89	6.18	5.11	6.09	1.13	4.47	5.82
Ho	FUS-MS	ppm	0.01	1.88	1.34	1.04	1.25	0.24	0.82	1.25
Er	FUS-MS	ppm	0.01	4.94	3.8	2.69	3.46	0.67	2.08	3.55
Tl	FUS-MS	ppm	0.05	< 0.1	< 0.05	< 0.05	< 0.05	< 0.1	< 0.05	< 0.05
Tm	FUS-MS	ppm	0.005	0.832	0.614	0.398	0.494	0.123	0.295	0.555
Yb	FUS-MS	ppm	0.01	4.27	4.07	2.53	3.08	0.66	1.83	3.58
Lu	FUS-MS	ppm	0.002	0.679	0.58	0.355	0.44	0.114	0.247	0.505

* Abundances determined by multiple INAA/FUS-ICP analyses.

Calculations were performed using the CIPW method and a Microsoft Excel spreadsheet formatted by K. Hollocher, Department of Geology, Union College, Schenectady, NY. Normative calculations are particularly sensitive to the oxidation state of iron (Fe), which is further influenced by having all Fe from geochemical analyses reported as Fe_2O_3 . An igneous origin and basaltic compositions were determined for all samples and an iron oxidation ratio ($\text{Fe}_2\text{O}_3/\text{FeO}$) of 0.2 was applied in normative calculations, based on recommendations by Middlemost (1989).

Element Mobility

When characterizing the origin of metamorphosed igneous rocks, geochemical data must be approached with caution, and the effects of element mobility taken into consideration. There can be some ambiguity in determining whether geochemical characteristics are indicative of primary magmatic processes or if they have been superimposed and altered by later hydrothermal processes or regional metamorphism. The behavior of major elements at amphibolite facies conditions, as experienced by amphibolites of this study, are well documented (e.g., Pearce, 1983; Rollinson, 1983, 1993) and show that major elements Ti, Al and P are typically immobile while Ca, Na, Si, Fe, Mg, and K are generally mobilized. Because of major element mobility, many diagrams using these types of data (e.g., total alkali vs. silica diagram; Harker variation diagrams) have been avoided where possible, and diagrams employing trace element data were used as alternatives. Trace elements Cs, Sr, K, Rb, and Ba belong to the low field-strength elements group, also referred to as large ion lithophile elements (LILE). This group is generally considered to be mobile under conditions of hydrothermal alteration and metamorphism (Pearce, 1983). Remaining trace elements belong to the high field strength (HFS) elements group and include the REE along with Sc, Y, Th, Zr, Hf, Ti, Nb, Ta and P. HFS elements are considered immobile under most conditions (Pearce, 1983; Rollinson, 1993).

Given the likelihood of element mobility in metamorphosed rocks, it is essential in any geochemical study to establish that elemental concentrations reflect original magmatic processes before any petrogenetic inferences can be made (Rollinson, 1993). The use of variation diagrams, with an established immobile element plotted along the x-axis, is common practice (e.g., Donato, 1991; Misra and Conte, 1991) and is efficient in demonstrating effects of element mobility in samples. Where systematic covariance is displayed among elements, it can be attributed to primary

Figure 3-2. Major element variation diagrams using Zr as the differentiation index. Zr concentration is expressed in parts per million, and major element concentrations are expressed as weight percent oxides (wt %). Blue symbols represent Tugaloo terrane samples while red symbols represent Cat Square terrane samples. Blue circles—North Carolina Tugaloo terrane after Wilson (2006); Red circles—North Carolina Cat Square terrane after Wilson (2006) and Byars (2010). Blue Triangles—central Georgia Tugaloo terrane after Huebner (2013) and Rehrer (this study). Red triangles—central Georgia Cat Square terrane after Davis (2010), Huebner (2013), and Rehrer (this study). c.c.—correlation coefficient.

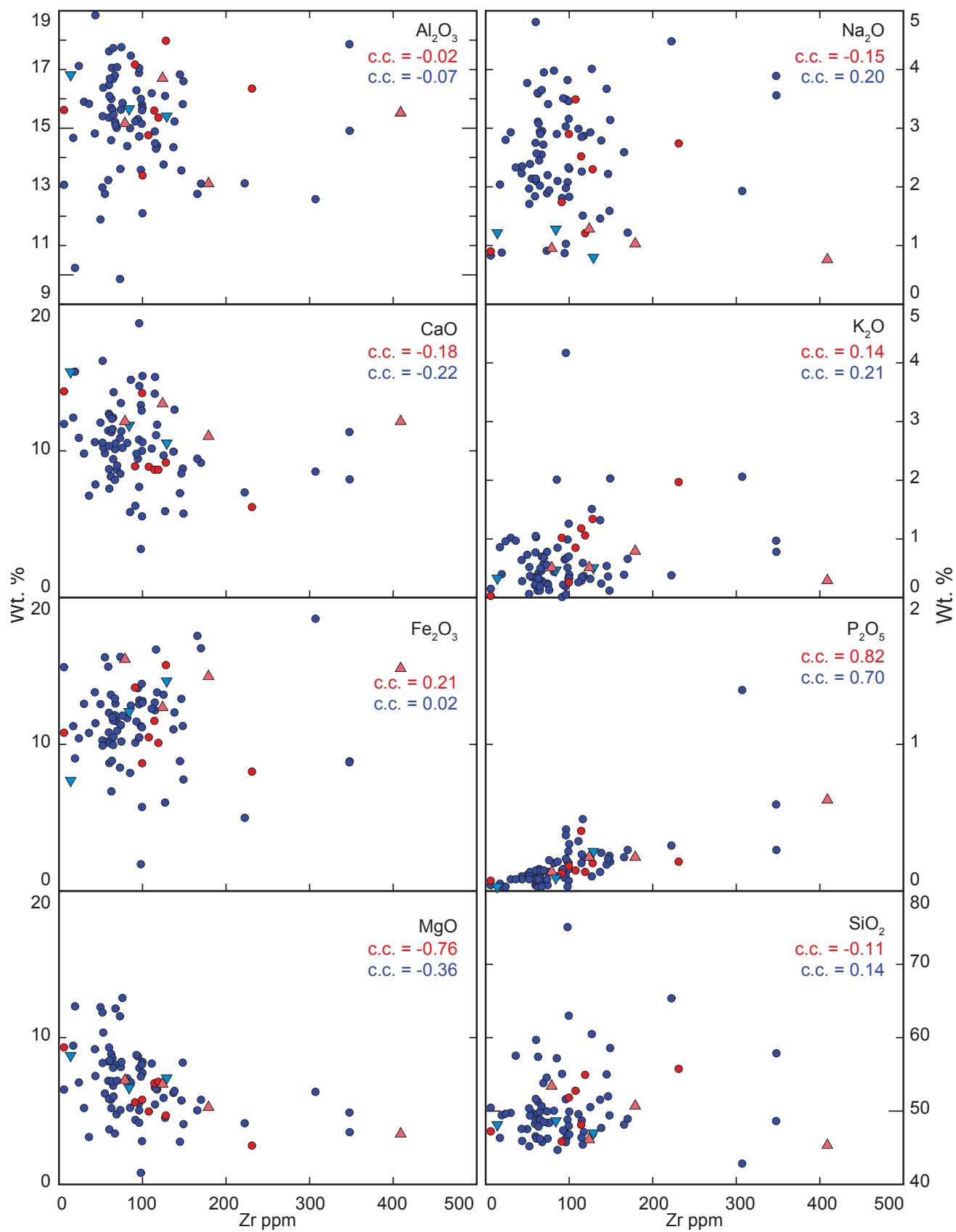
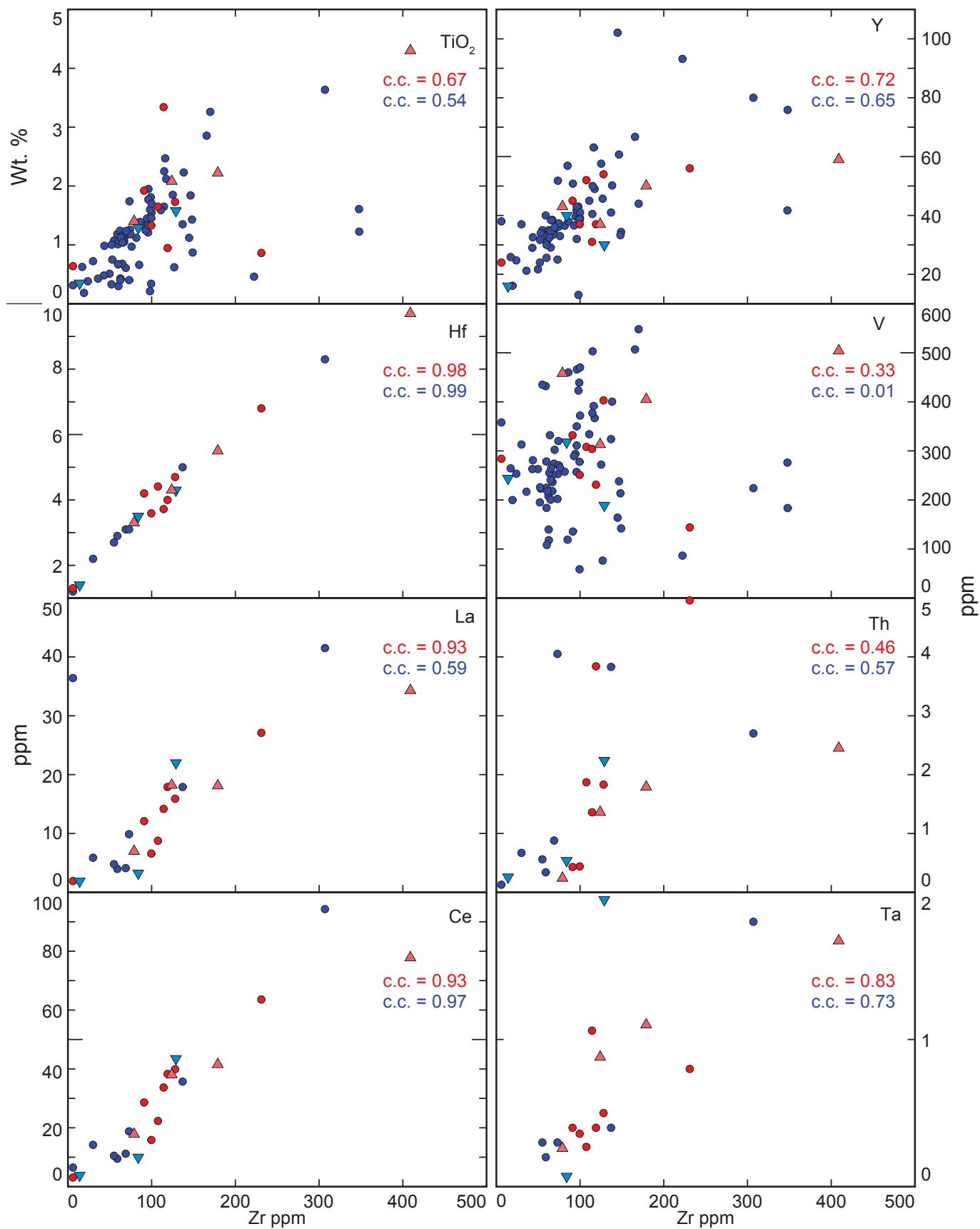


Figure 3-3. Trace element variation diagram using Zr as the differentiation index. Trace element abundances are expressed as parts per million, with the exception of Titanium (TiO_2), which is expressed as weight percent oxide. Symbology is the same as in Figure 3-2.



igneous processes and, where considerable scatter is exhibited, it is likely the result of post-magmatic processes and element mobility (Donato, 1991). Variation diagrams were employed in this study using Zr as the fractionation index (Figs. 3-2, 3-3). Zr is an immobile and relatively incompatible element that increases concentration with increasing differentiation (Pearce, 1983; Rollinson, 1993), and its immobile nature is established for samples in this study by the strong linear covariation with TiO_2 and with REE La and Ce (Fig. 3.3).

Statistically viable inferences were difficult to obtain from the small dataset compiled thus far for central Georgia amphibolite. Therefore, to gain meaningful insight, central Georgia data were used along with background data from a much larger dataset compiled from North Carolina. Plots of major element data are shown in Figure 3-2. P_2O_5 and MgO, respectively, display strong positive and negative linear covariation trends, while considerable scatter is exhibited in plots of CaO, Fe_2O_3 , Na_2O_3 , K_2O , and SiO_2 . These element oxide concentrations do maintain some linear covariability among Georgia samples, suggesting that mobility was possibly limited to North Carolina samples, or that trends may exist between smaller subsets of North Carolina data that are not distinguished here. Generally negative trends exhibited by CaO and generally positive trends displayed by Na_2O_3 , K_2O , and SiO_2 are indicative of expected trends for magmatic processes (Donato, 1991), and support an igneous origin for these amphibolites. Al_2O_3 displays substantial scatter that reflects post-magmatic effects. It is possible to have data scatter resulting from inadvertent contamination through sample preparation procedures, although with Al_2O_3 concentrations ranging 9–19 percent, the effects of contamination by use of an alumina-ceramic mill ($\sim 0.2\%$ Al) are negligible. Selected trace elements Hf, La, Ce, Y, Th, and Ta, along with TiO_2 , exhibit significantly strong positive linear covariation. V exhibits some scattering, but still maintains a slight positive correlation (Fig. 3-3).

Major Element Data

Normative Analyses

Normative mineralogy is presented in Table 3-2, separated by terrane, and expressed as both weight and volume percent norms. Norms are calculated on an anhydrous basis and as such do not include hydrous minerals such as amphiboles. The idealized mineralogy represented by this analysis does include a significant abundance of normative pyroxene, which was not observed in thin section. With the exception of sample OH330, which exhibits a small proportion of normative

Table 3-2. Normative analyses of central Georgia Inner Piedmont amphibolites.

Normative Minerals	Cat Square terrane								Tugaloo terrane					
	OH-301		S-695		M-235		M-276		OH-330		W-166B		W-173	
	Wt. % Norm	V. % Norm	Wt. % Norm	V. % Norm	Wt. % Norm	V. % Norm	Wt. % Norm	V. % Norm	Wt. % Norm	V. % Norm	Wt. % Norm	V. % Norm	Wt. % Norm	V. % Norm
Quartz	9.6	11.21	5.43	6.34	1.91	2.16	10.07	11.68	0.0	0.0	4.03	4.7	3.87	4.45
Plagioclase	46.03	52.01	41.42	46.85	52.2	57.39	38.24	43.11	50.66	55.85	44.94	50.72	47.73	53.32
Orthoclase	1.81	2.19	2.84	3.43	3.23	3.78	4.82	5.79	2.01	2.36	3.18	3.84	2.84	3.37
Diopside	15.34	14.01	18.28	16.73	21.96	20.02	20.58	18.76	30.09	27.47	11.61	10.71	18.66	16.99
Hypersthene	12.58	10.87	26.98	23.43	13.56	12.1	17.06	14.8	8.64	7.69	28.06	24.79	20.47	17.9
Olivine	0.0	0.0	0.0	0.0	0.0	0.0	0.0	0.0	5.58	4.82	0.0	0.0	0.0	0.0
Ilmenite	8.43	5.49	2.53	1.64	4.2	2.65	4.29	2.78	0.68	0.43	3.1	2.01	2.53	1.62
Magnetite	4.55	2.71	2.17	1.29	2.32	1.34	4.32	2.55	2.23	1.29	4.28	2.54	3.64	2.13
Apatite	1.48	1.43	0.28	0.27	0.56	0.52	0.53	0.51	0.07	0.07	0.65	0.63	0.21	0.2
Zircon	0.09	0.06	0.01	0.01	0.03	0.02	0.03	0.02	0.0	0.0	0.03	0.02	0.01	0.01
Chromite	0.01	0.01	0.01	0.01	0.03	0.02	0.01	0.01	0.03	0.02	0.07	0.04	0.03	0.02

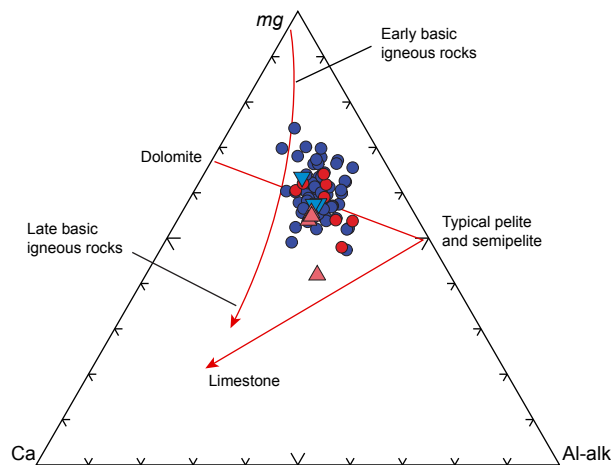


Figure 3-4. Primary igneous trends of central Georgia and North Carolina Inner Piedmont amphibolites. Primary igneous and sedimentary trends after Leake (1964) are indicated by red arrows. $mg = [MgO/(FeO + MnO + 2Fe_2O_3 + MgO)]$; $Ca = CaO$; $Al-alk = Al_2O_3 - (Na_2O + K_2O)$. Symbology is the same as in Figure 3-2.

olivine, all samples exhibit low amounts of normative quartz ranging from 1.91 percent (M235) to 10.07 percent (M276) that agree with established limits for amphibolite classification (Cannon, 1963; Coutinho et al., 2007).

Ortho- Vs Para-amphibolite

Amphibolites can be derived from a variety of protoliths, both igneous and sedimentary, and it is therefore crucial to determine the nature of their origin. An igneous origin for amphibolites from the Inner Piedmont in North Carolina has previously been established (Wilson, 2006) and, although a correlation between the Cat Square terrane in Georgia and the Cat Square terrane in North Carolina has been argued (Huebner, 2013; Huebner et al., in review; Rehrer, this study), it is still necessary to determine the origin of amphibolites in this study. No relict igneous textures were identified in thin sections of central Georgia amphibolites, thereby requiring discrimination on the basis of geochemistry and stratigraphy. Para-amphibolites are generally the result of metamorphism of calcareous or dolomitic shale, which are the only sediments with primary compositions near that of amphibolite (Leake, 1964). This type of stratigraphy has not yet been recognized in the Cat Square terrane. Ortho-amphibolites typically result from metamorphism of mafic rocks such as basalt, diabase, and mafic tuffs, which are abundant in the Cat Square terrane. Leake (1964) proposed plots based on geochemistry that identify differences between chemical trends of ortho-

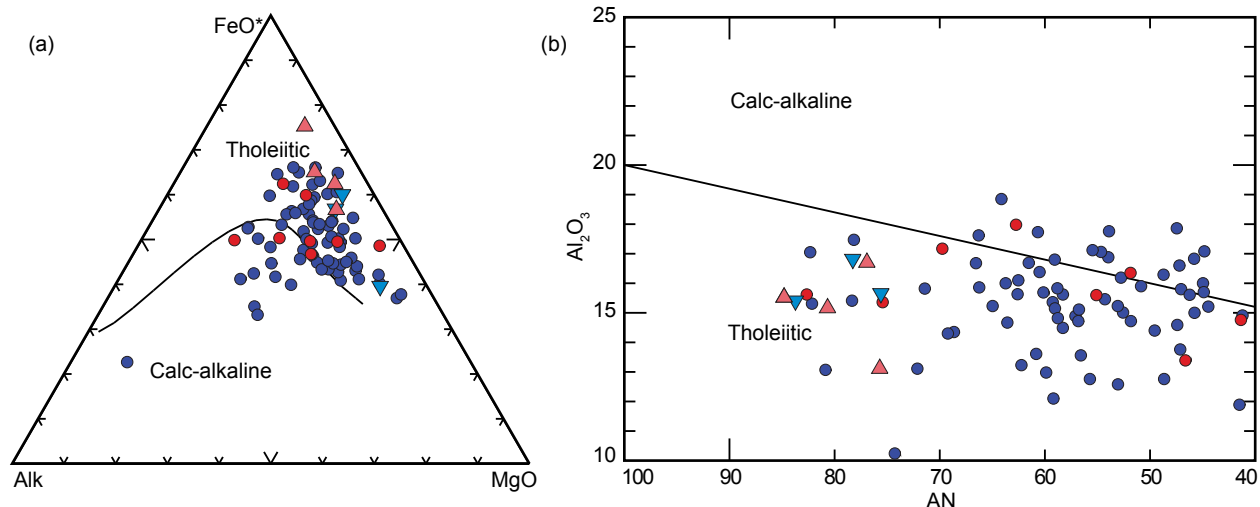


Figure 3-5. Magma series of Inner Piedmont amphibolite protoliths. (a) AFM diagram showing the boundary between tholeiitic and calc-alkaline magma fields from Irvine and Baragar (1971). (b) Alternative diagram from Irvine and Baragar (1971), which uses Al₂O₃ and anorthite content to display the boundary between tholeiitic and calc-alkaline magma fields. Symbology is the same as in Figure 3-2. FeO*—total iron reported as FeO; Alk—total alkalis (Na₂O + K₂O); AN—Anorthite content.

and para-amphibolites, one of which uses Niggli mg values, CaO, and Al-alk plotted on a triangular diagram (Fig. 3-4). Samples from central Georgia, which admittedly comprise a very small dataset, plot along the trend for igneous rocks delimited by Leake (1964), as do samples from North Carolina, previously reported by Wilson (2006). More analyses are needed, however, to definitively confirm the igneous trend for central Georgia amphibolites.

Characterization of Inner Piedmont amphibolite protoliths is further defined by use of discrimination plots that delimit rock types based on magma series. A triangular AFM diagram (Alkalis—Na₂O+Fe₂O₃, total Fe, and MgO) from Irvine and Baragar (1971) shows that all central Georgia samples plot within the tholeiitic series along with several samples from North Carolina (Fig. 3-5a). The majority of Cat Square terrane samples from North Carolina plot within the tholeiitic series, although some plot along the transition to and just inside of the calc-alkaline field. A large quantity of North Carolina Tugaloo terrane samples plot within the tholeiitic field, while a much smaller amount plot within the calc-alkaline series. Figure 3-5b represents an alternative diagram, also from Irvine and Baragar (1971), which discriminates by magma series using a bivariate plot of Al₂O₃ versus anorthite content. Data within this diagram plot in fields consistent

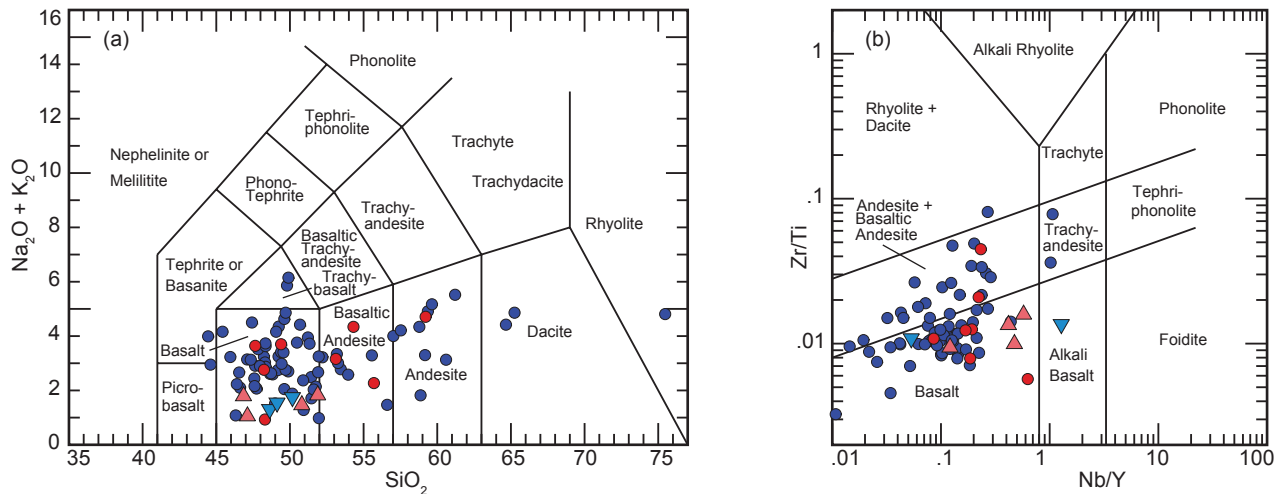


Figure 3-6. Rock type discrimination diagrams. (a) Total alkalis vs. silica diagram that discriminates volcanic rock types, after Le Maitre et al. (1989). (b) Trace element volcanic rock type discrimination diagram, after Winchester and Floyd (1977). Symbology is the same as in Figure 3-2.

with the AFM diagram. Although consistent, these diagrams should still be interpreted with some caution since they incorporate the generally mobile LIL elements.

Rock Classification

Arguably one of the most useful applications of major element data is in rock classification. Using geochemical data to classify rocks provides an objective method for determining protolith rock type that avoids subjective estimates from mineral modes, and also circumvents inaccuracies inherent in estimating modes for matrix-rich rocks and aphanitic volcanics. One widely used diagram is the total alkalis vs. silica (TAS) plot of Le Maitre et al. (1989), which uses SiO_2 as the abscissa and $\text{Na}_2\text{O} + \text{K}_2\text{O}$ as the ordinate (Fig. 3-6a). This diagram displays discriminant fields based on 24,000 fresh volcanic analyses (Rollinson, 1993). All samples from the central Georgia Inner Piedmont plot within the basalt field, while several North Carolina Inner Piedmont samples plot well outside and even into the rhyolite field. Use of this diagram to classify amphibolite protoliths is largely inappropriate because of the likelihood of major element mobility. It is only included here because of its usage by several previous authors working on Inner Piedmont amphibolites, and as a comparison to the less often used trace element diagram (Fig. 3-6b) of Pearce (1996) after Winchester and Floyd (1977). This trace element classification diagram uses immobile elements that display strong positive linear covariation (Fig. 3-3) that should represent original igneous

compositions. All central Georgia samples, excluding sample W166B, plot in the basalt field using this classification. Sample W166B plots well within the alkali basalt field. North Carolina Inner Piedmont samples plot overlapping the basalt and andesite + basaltic andesite fields, with two samples plotting in the trachyandesite field, and one sample plotting in the rhyolite + dacite field.

Trace Element Data

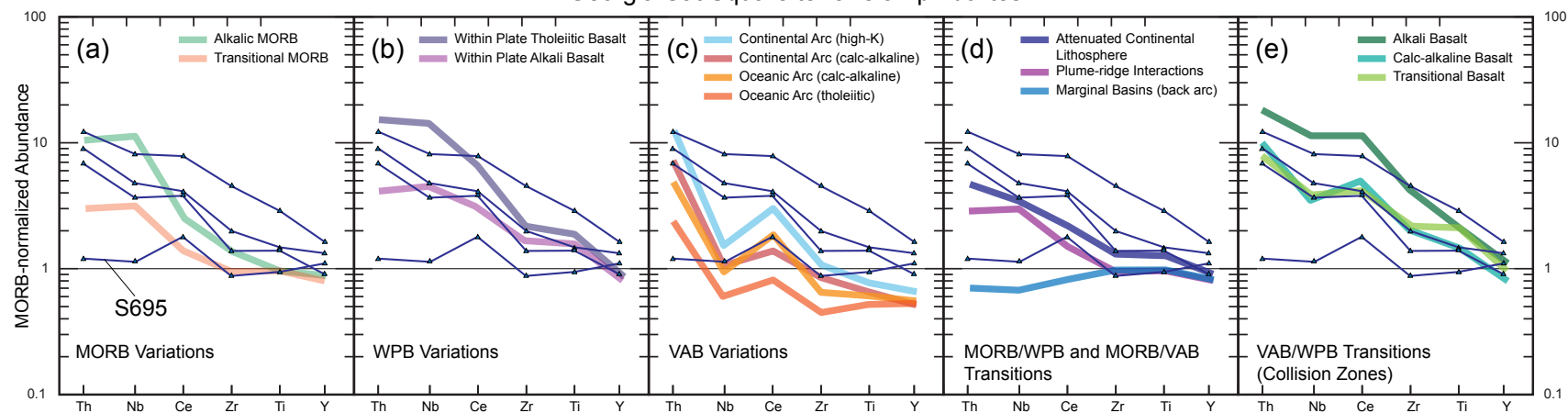
Trace element data are presented using traditional normalized multi-element diagrams (spider diagrams), and through the use of bivariate and triangular tectonic discriminant diagrams. Spider diagrams illustratively depict sample geochemistry that can be compared with diagrams from basalts of known origin. Tectonic discriminant diagrams were used to fingerprint possible tectonic settings for the eruption of basalts based on chemical signatures of select trace elements, namely Th, Nb, Hf, Zr, Ti, and Y. Amphibolite samples from the Tugaloo terrane have not been interpreted using trace element spider diagrams or tectonic discriminant diagrams, so as not to detract from the main focus of this study, which is the characterization of the Cat Square terrane. Tugaloo terrane amphibolites are excluded from any further discussion. Amphibolite geochemical data compiled from North Carolina comprise analyses by Wilson (2006) and Byars (2010).

Spider Diagrams

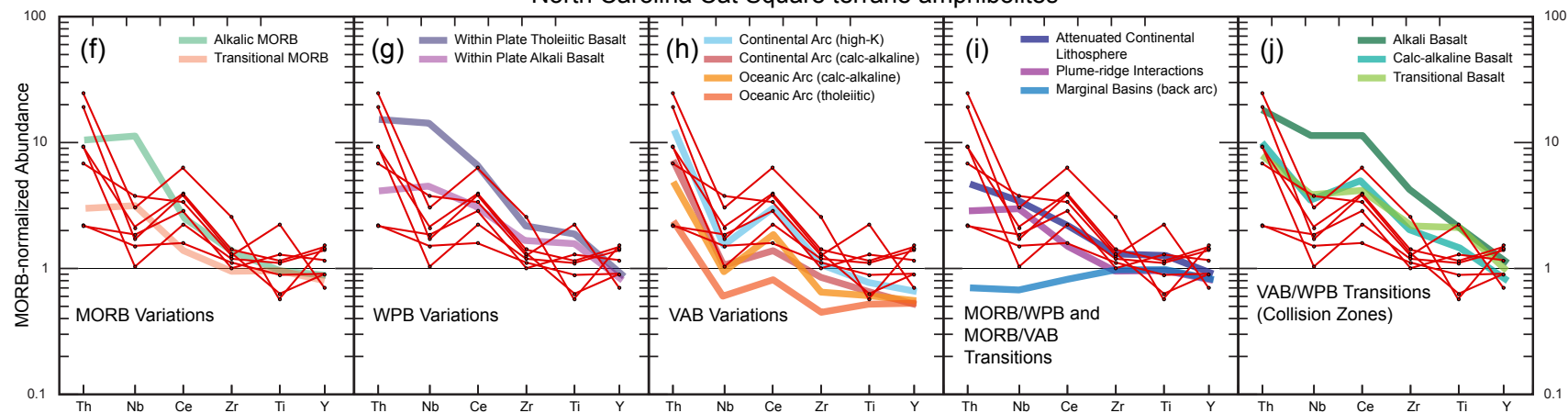
A condensed set of elements, normalized to mid-ocean ridge basalt (MORB) (Pearce, 1996), was used for initial comparisons (Fig. 3-7). This condensed set of elements is based on recommendations by Pearce (1996) who suggested an overabundance of trace elements plotted in a diagram would merely add noise to the discrimination and that some elements (e.g., Nb and Ta, or Zr and Hf) duplicate each other because of geochemical similarities, and need not be incorporated together. It is also practical to avoid the use of LIL elements where possible, given their potential for mobility during post-magmatic processes (Jenner, 1996). Only Th was used as a representative in the condensed set of elements. All but one of the Georgia samples display a slightly negative-sloping trend with a selective enrichment of elements, relative to MORB (Fig. 3-7a-e). The level of enrichment increases from Y (generally similar to MORB) to Th. There is also a very slight negative Nb anomaly, with respect to Th and Ce, observed in these samples. While three samples display similar trends, one (S695) exhibits an outlying trend very similar to MORB, with the exception of a slight enrichment in Ce, relative to Nb and Zr. Comparison with representative basaltic trends

Figure 3-7. MORB-normalized six-element spider diagrams. (a-e) Central Georgia Cat Square terrane amphibolites. (f-j) North Carolina Cat Square terrane amphibolites. Background data represent average basalt geochemical patterns for possible eruptive settings, from Pearce (1996). All data are normalized to average tholeiitic mid ocean ridge basalt, using normalizing values from Pearce (1983). MORB—mid ocean ridge basalt; WPB—within-plate basalt; VAB—volcanic arc basalt.

Georgia Cat Square terrane amphibolites



North Carolina Cat Square terrane amphibolites

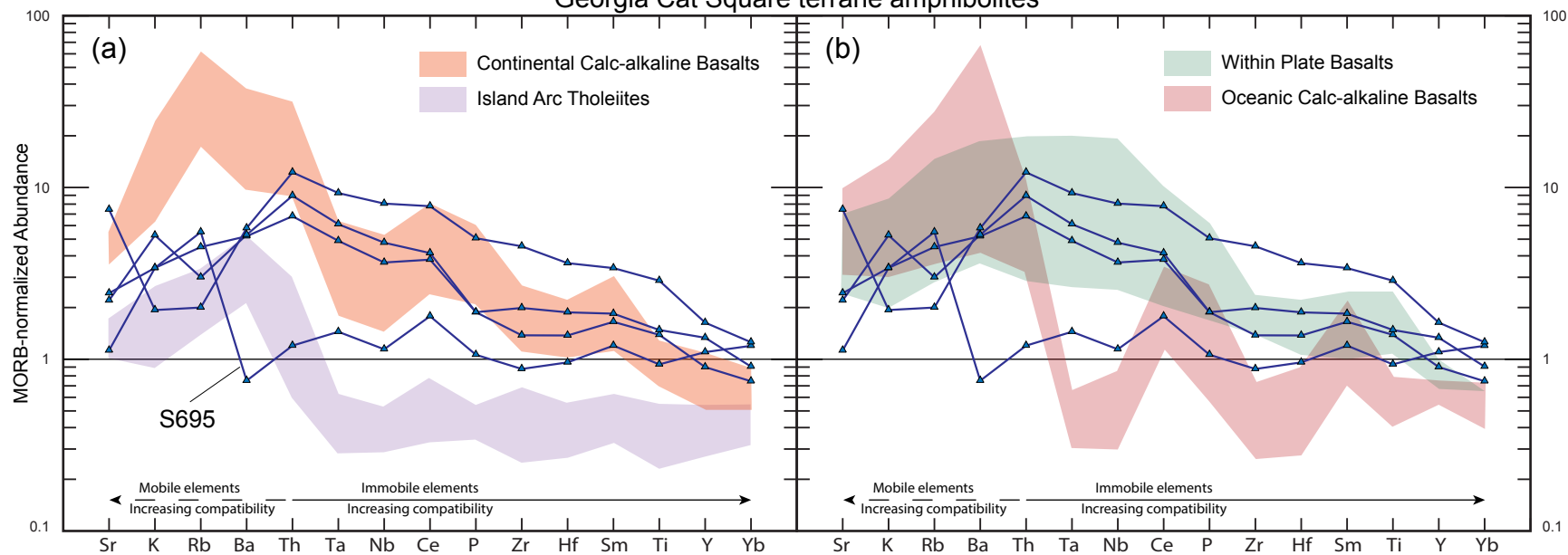


(Pearce, 1996) demonstrates that Georgia amphibolites, excluding sample S695, best correspond to within-plate basalt (WPB) variations, and transitional volcanic arc basalts/within-plate basalts (VAB/WPB). A negative slope, enrichment, relative to MORB, in all elements except Y, and a high Ti/Y ratio, characterize geochemical patterns of WPB. These characteristic patterns are similarly displayed by the VAB/WPB transitions with the addition of a significant negative Nb anomaly. Patterns for North Carolina samples (Fig. 3-7f-j) noticeably differ from those of central Georgia, and display a significantly more pronounced negative Nb anomaly with respect to Th and Ce. North Carolina samples also exhibit considerably less enrichment in Zr and Ti relative to MORB, producing a positive Ce anomaly. Three samples display Ti and Y depletion relative to MORB, and all but one exhibit very low Ti/Y ratios. North Carolina data best compare with VAB variations in that they share a significant negative Nb anomaly, relative positive Ce anomaly, and low enrichments of Zr relative to MORB. Three samples differ from VAB by selective enrichment of Ti and Y relative to MORB, which might be better accommodated by the VAB/WPB transition pattern. The VAB/WPB comparison, however, does not represent the significant Nb anomaly, low Zr enrichment, and low Ti/Y ratios exhibited by those samples.

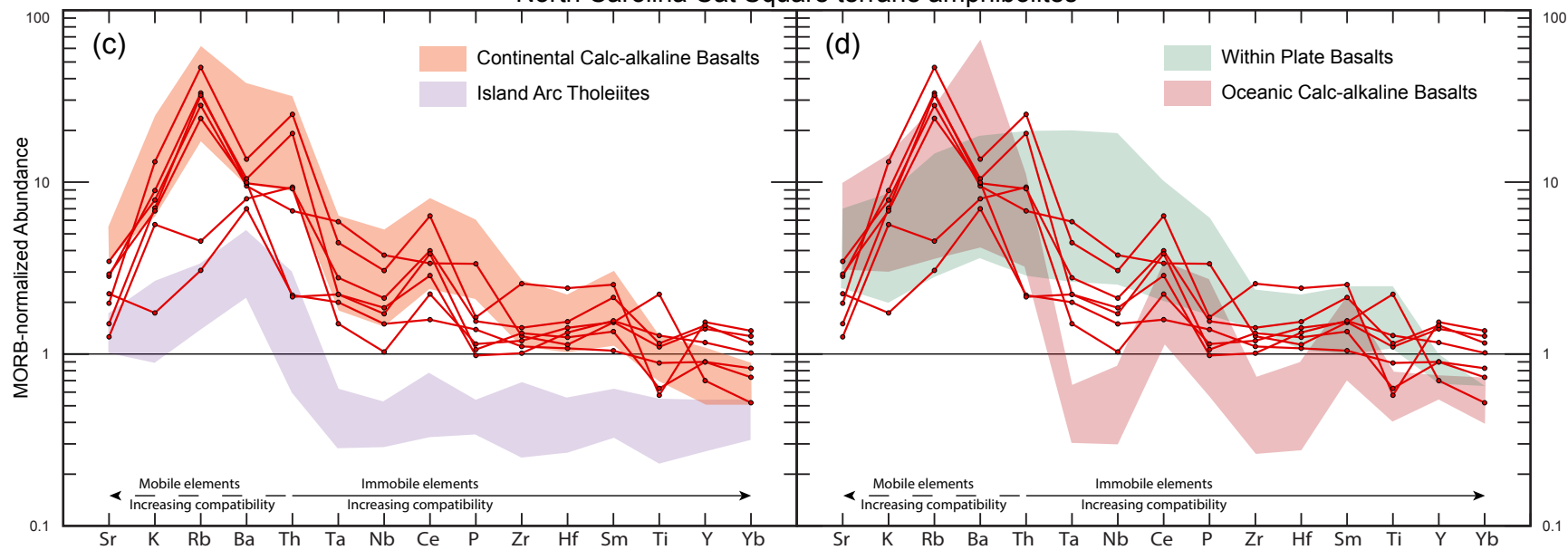
Based on the aforementioned observations, Cat Square terrane amphibolite geochemical data were plotted using an expanded set of elements, and compared to fields of representative basalt geochemical patterns after Pearce (1983). The expanded set includes LIL elements Sr, K, Rb, Ba, Th, along with HFS elements Ta, Nb, P, Zr, Hf, Ti, Y, and REE Ce, Sm and Yb (Fig. 3-8). Fields represent maximum and minimum element abundances, not averages, of geochemical patterns after Pearce (1983), which are composed of datasets from several sample locales. Georgia Cat Square terrane samples (Fig. 3-8a-b) exhibit considerable scatter in the enrichment of LIL elements, which are assumed to have potential for mobility, and all but sample S695 display enrichment of all HFS elements except Y and Yb, relative to MORB. The intensity of element enrichment increases with increasing incompatibility, such that Th and Ta exhibit the most enrichment, while Y and Yb display the least. This characteristic “humped” pattern along with the absence of a significant negative Ta and Nb anomaly is indicative of WPBs (Pearce, 1983). Georgia samples, with the exception of S695, plot exceptionally well within the field of WPBs (Fig. 3-8b). Sample S695 displays abundances similar to MORB, excluding the extensive enrichment of LIL elements K and Rb and slight enrichment of Ta, Ce, and Sm. North Carolina samples (Fig. 3-8c-d), with minor exceptions, display

Figure 3-8. MORB-normalized multi-element spider diagrams. (a-b) Central Georgia Cat Square terrane amphibolites. (c-d) North Carolina Cat Square terrane amphibolites. Background fields represent maximum and minimum element abundances from contrasting types of eruptive tectonic settings; fields are compiled from data after Pearce (1983). The within-plate basalts field represents basalts from both oceanic and continental settings. Normalizing values and element order are those of Pearce (1983).

Georgia Cat Square terrane amphibolites



North Carolina Cat Square terrane amphibolites



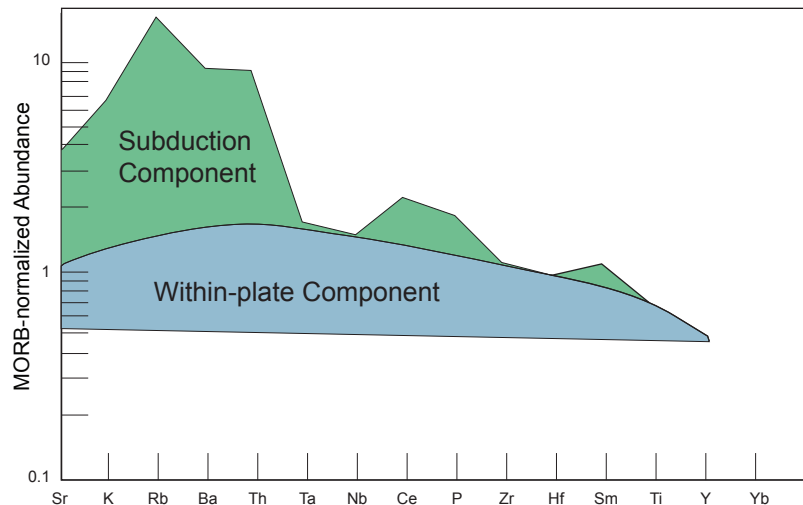


Figure 3-9. Interpretation of a bi-modal magma system that accounts for the continental calc-alkaline basalt geochemical pattern. Redrawn from Pearce (1983), his figure 8.

parallel patterns of similar elemental abundance. Some variation occurs in LIL elements as well as Zr, Hf, and Ti among these samples. Samples exhibit significant enrichment in LIL elements and Ce, along with a notable negative Ta and Nb anomaly, with respect to Th and Ce. The more compatible HFS elements trend toward MORB abundances. Selective enrichment of LIL elements and a significant Ta-Nb “trough” are indicative of arc basalt patterns (Pearce, 1983, 1996; Saunders and Tarney, 1991; Jenner, 1996); however, tholeiitic and calc-alkaline oceanic arc basalt patterns are distinguished by HFS element abundances depleted relative to MORB, with the exception of Ce, P, and Sm in calc-alkaline basalts, (Fig. 3-8c-d). The continental calc-alkaline basalt field of Pearce (1983) exhibits similar characteristics of the other arc varieties, but is distinguished from the island arc tholeiites and oceanic calc-alkaline basalts by the enrichment relative to MORB of the HFS elements, most notably Ta and Nb. Pearce (1983) attributed these characteristics to the addition of a magma component similar to that responsible for WPB enrichment (Fig. 3-9), and noted that effects of crustal contamination were not a contributing factor. North Carolina data best fit in the continental calc-alkaline basalt field (Fig. 3-8c), noting that the data plot at the low abundance portion and somewhat below the field.

In order to further consider the hypothesis for back-arc genesis of the Cat Square basin proposed by Wilson (2006) and refined by Huebner and Hatcher (in review), a series of MORB normalized (Pearce, 1983) spider diagrams depicting fields of basalt patterns from modern back-

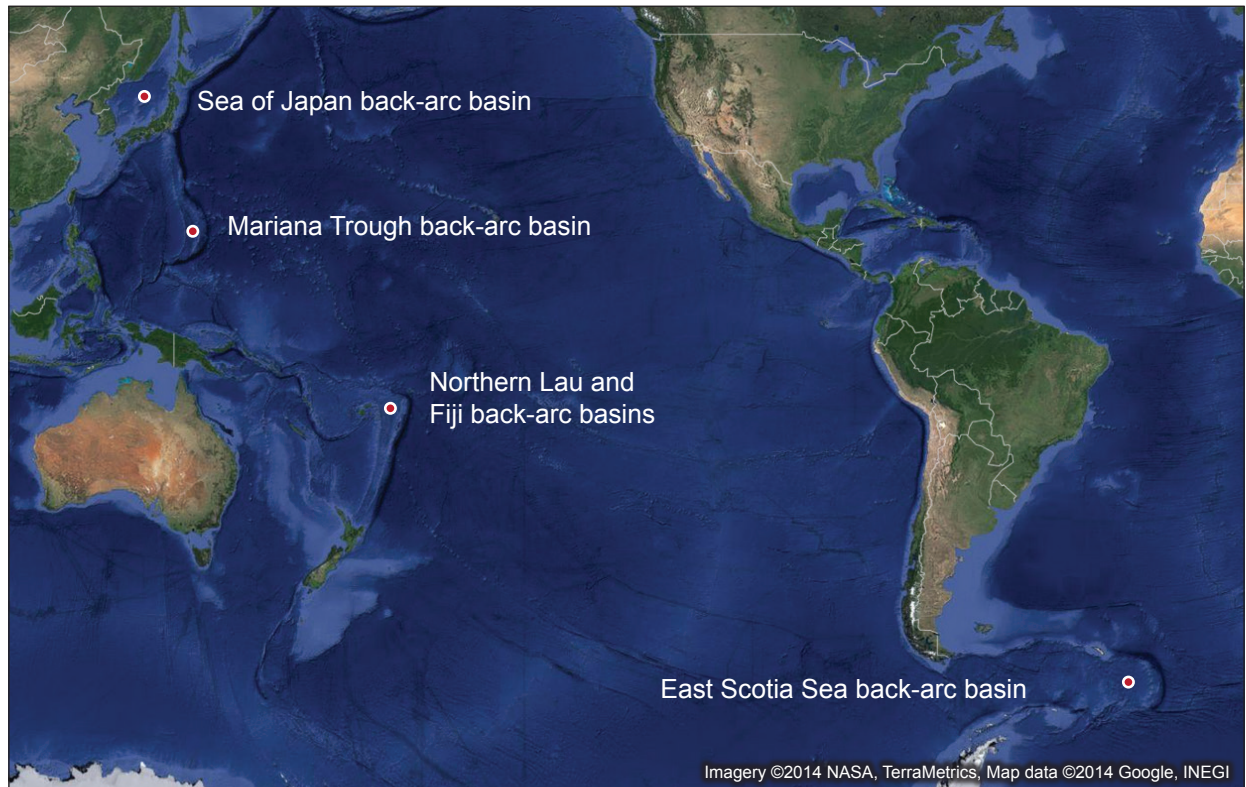
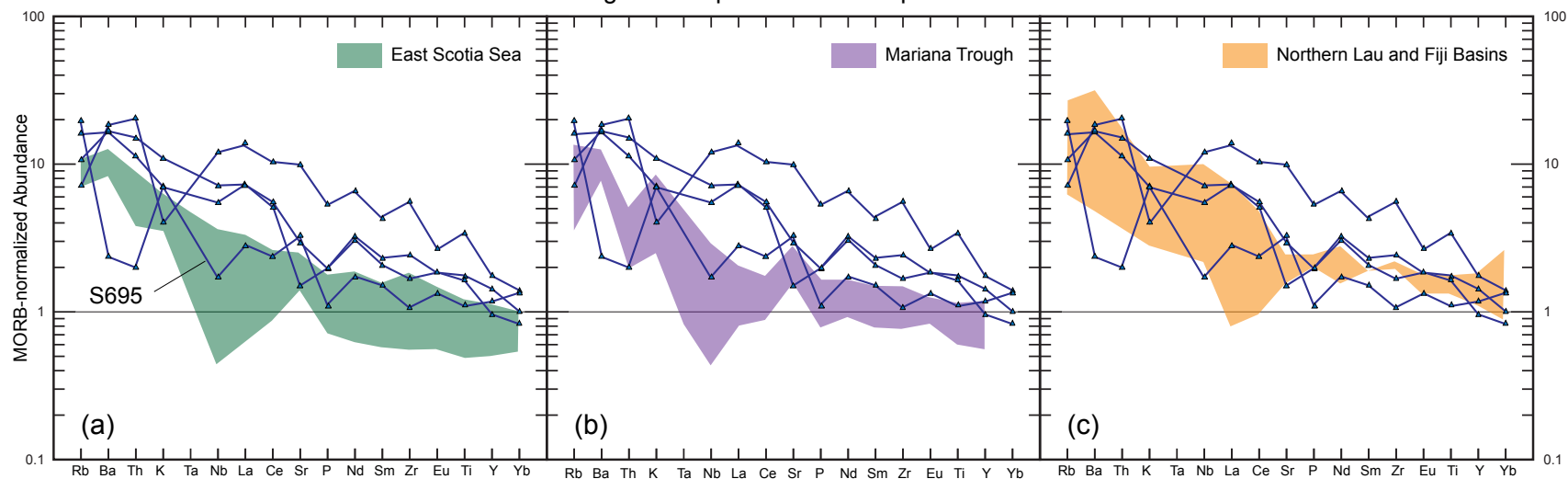


Figure 3-10. Google Earth image depicting the locations of several modern-day back-arc basin analogues. Locations correspond to spider diagrams depicted in Figures 3-11 and 3-12.

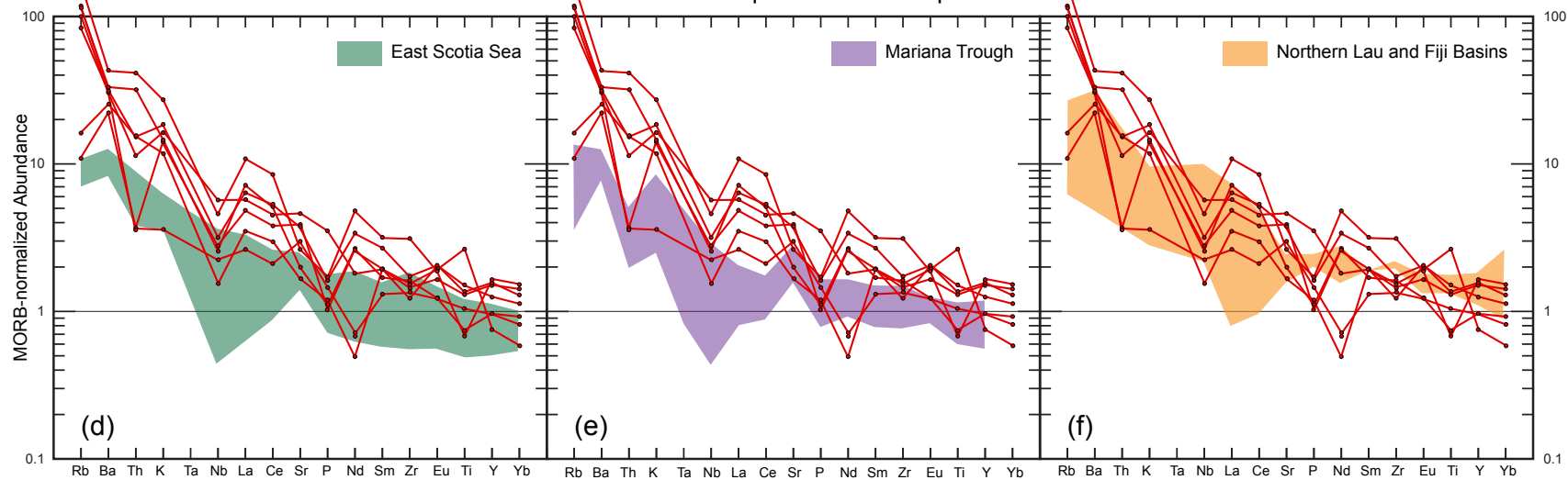
arc settings (Fig. 3-10) were constructed. These diagrams (Fig. 3-11, 3-12) facilitate a comparison between Cat Square terrane amphibolite geochemical patterns and patterns of modern day back-arc basalts. Of the four main types of recognized back-arc basins (Marsaglia, 1995), two extensional back-arc basin types are represented, and depict basalts from the more common intraoceanic back-arc setting (Fig. 3-11) and less typical continental margin back-arc setting (Fig. 3-12). The representative basalt fields all exhibit a selective enrichment of LIL elements and abundances of HFS elements that are more similar to MORB. The majority of fields also show a characteristic negative Nb anomaly, although it should be noted not all samples comprising the fields of intraoceanic back-arcs (Fig. 3-11) displayed this anomaly (Saunders and Tarney, 1991). The intermediate composition between MORB and arc basalts exhibited by these fields is characteristic of back-arc basalts (Saunders and Tarney, 1991; Jenner, 1996; Pearce, 1996) and is attributed to a mixing of different mantle sources, integrated by mechanisms of back-arc development (e.g., Ikeda and Yuasa, 1989; Nakamura et al., 1989; Allan and Gorton 1992). Of the central Georgia Cat Square

Figure 3-11. Comparison of Cat Square terrane amphibolite geochemistry with modern-day intraoceanic back arcs. (a-c) Central Georgia Cat Square terrane amphibolites. (d-f) North Carolina Cat Square terrane amphibolites. Background fields represent ranges of compiled data from Saunders and Tarney (1991). All data are normalized to N-MORB using values and element order from Sun and McDonough (1989).

Georgia Cat Square terrane amphibolites



North Carolina Cat Square terrane amphibolites



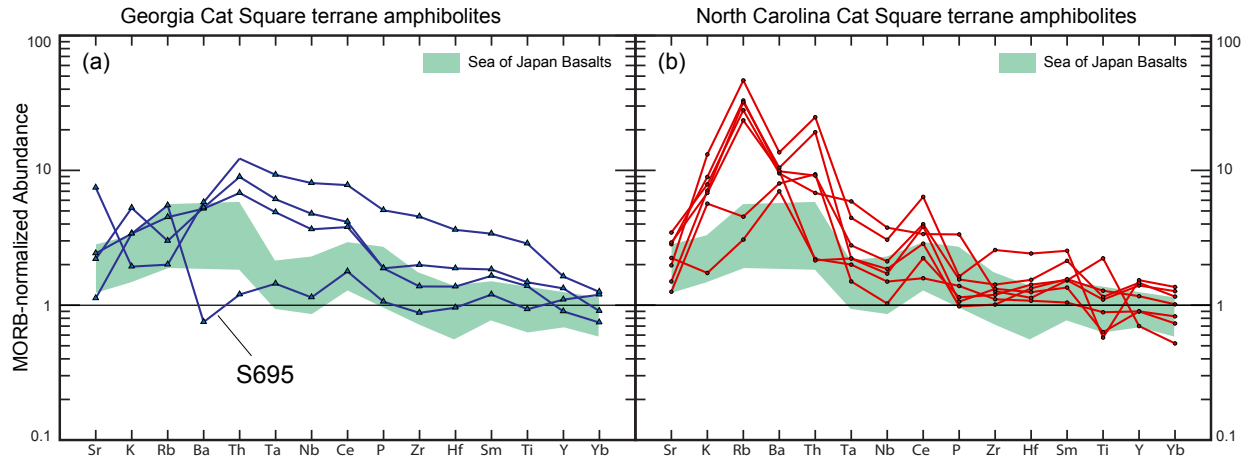


Figure 3-12. Comparison of Cat Square terrane amphibolite geochemistry with Sea of Japan basalts. (a) Central Georgia Cat Square terrane amphibolites. (b) North Carolina Cat Square terrane amphibolites. Background fields represent maximum and minimum element abundances for basalts dredged from the central Sea of Japan; data compiled from Allan and Gorton (1992) and Cousens and Allan (1992, using their site 795B).

terrane samples, only S695 exhibited a pattern similar to representative fields. A marginal fit between sample S695 and the East Scotia Sea and Mariana Trough basalts (Fig. 3-11a-b) is apparent, while an exceptionally good correlation, excluding few LIL element inconsistencies, exists between S695 and the Sea of Japan basalts (Fig. 3-12a). The same correlation pattern is evident between North Carolina samples and intraoceanic back-arc (Fig. 3-11d-f) and Sea of Japan basalts (Fig. 3-12b), again excluding some extensive LIL element enrichments of the North Carolina samples. The remaining central Georgia samples do not correlate well with these fields.

Tectonic Discriminant Diagrams

Bivariate and triangular trace element diagrams have been employed to investigate two main criteria of Cat Square terrane amphibolites—determination of rock type (Fig. 3-6) and discrimination of tectonic environment. Discrimination of tectonic setting was accomplished through the use of several tectonic discriminant diagrams, one of which was a Ti-Zr-Y diagram after Pearce and Cann (1973), employed to identify samples having a within-plate affinity (Fig. 3-13a). Ten percent probability ellipses (10% of data points from a group plot outside this contour) after Pearce (1996) demonstrate significant overlap between MORB and VAB fields, suggesting this diagram does not provide adequate discrimination between those environments, hence its use to identify only within-plate affinity. Another probability ellipse contours back-arc basin basalts and

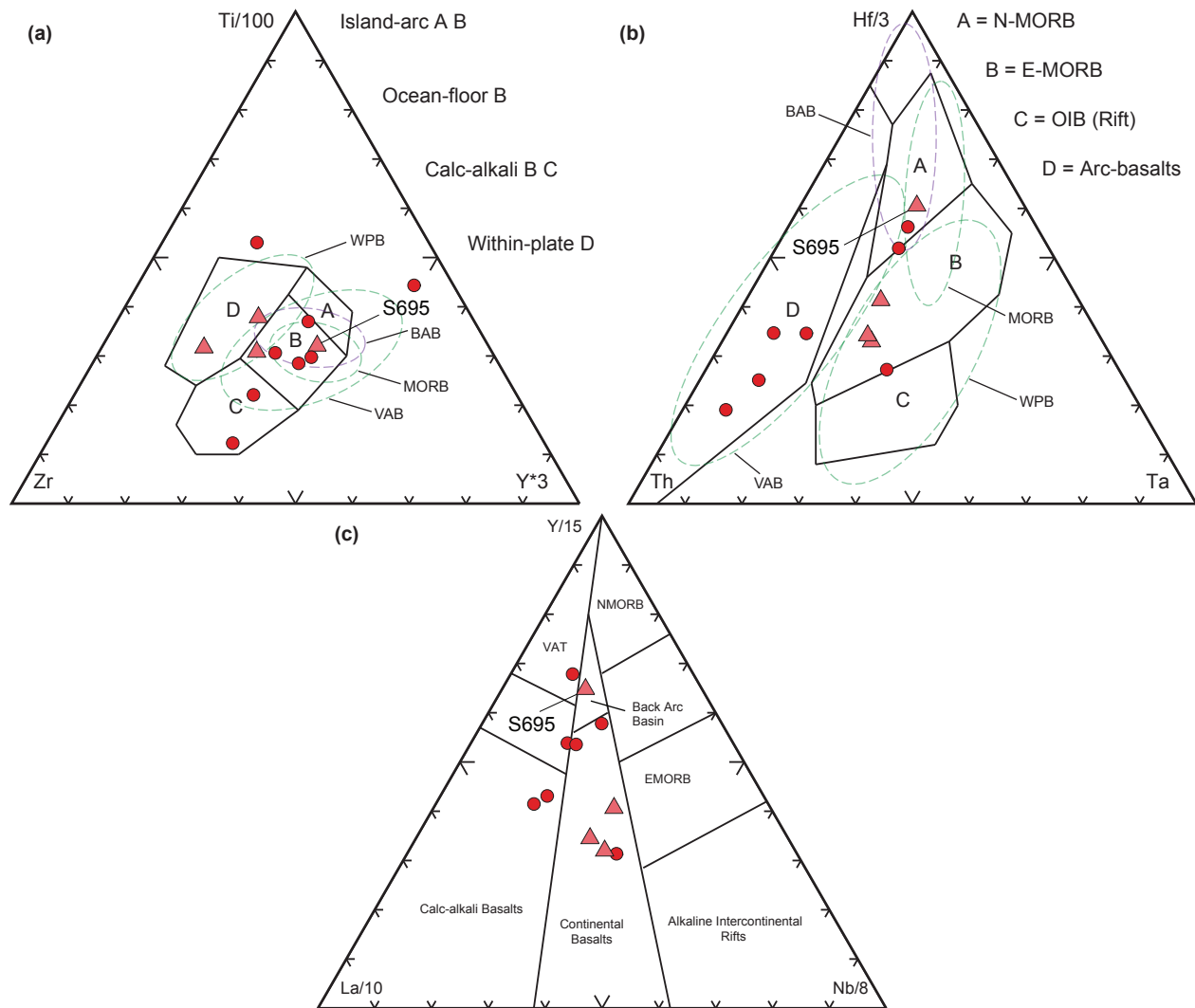


Figure 3-13. Tectonic discrimination diagrams. (a) Ti-Zr-Y diagram from Pearce and Cann (1973) used mainly to discriminate within-plate basalts. (b) Th-Ta-Hf diagram from Wood et al. (1979). (c) La-Y-Nb diagram after Cabanis and Lecomte (1989). Dashed lines represent 10 percent probability ellipses from Pearce (1996). The ellipses indicate that 90% of the author's representative data plot within those boundaries. BAB—back-arc basin basalts; WPB—within-plate basalt; MORB—mid-ocean ridge basalt; VAB—volcanic arc basalt; OIB—ocean island basalt; N-MORB—normal-mid-ocean ridge basalt; E-MORB—enriched-mid-ocean ridge basalt; VAT—volcanic arc tholeiite; Red triangles—central Georgia Cat Square terrane; Red circles—North Carolina Cat Square terrane.

expectedly overlap the fields for both MORB and VAB. Two central Georgia Cat Square terrane samples plot within the field of WPB suggested by Pearce and Cann (1973), with a third plotting within the 10 percent probability ellipse for that setting. Sample S695 plots within the ocean-floor field as well as both the MORB and back-arc basin probability ellipses. It does not plot within the WPB ellipse. One North Carolina sample plots outside the fields of this diagram, while others plot

within the fields of island arc, ocean floor, calc-alkali basalts and among all three probability ellipses. To identify basalts with a subduction zone affinity, Pearce (1996) recommended use of a Th-Ta-Hf diagram from Wood et al. (1979). Three Georgia samples plot within the E-MORB field and 10 percent probability ellipse of WPB using this diagram (Fig. 3-13b), while Sample S695 plots within the field of N-MORB and the 10 percent probability ellipse for MORB and back-arc basins. Several North Carolina samples plot in the field of arc basalts and the 10 percent probability ellipse of VAB, while others plot within the MORB fields and the 10 percent probability ellipse for back-arc basins and WPB. A third discriminant diagram after Cabanis and Lecolle (1989), employs La-Y-Nb and was used to further distinguish eruptive environments (Fig. 3-13c). Inferences made using this diagram are done so with some restraint because La is considered to be mobile under high-grade metamorphic conditions (Rollinson, 1993). La abundances from amphibolites used herein, however, do show a strong linear correlation with Zr (Fig. 3-3), suggesting they represent original magmatic concentrations. The La-Y-Nb diagram (Cabanis and Lecolle, 1989) is divided into fields that distinguish VAB, (left-hand portion) from continental basalts (center portion) and oceanic basalts (right-hand portion). Three of the Georgia samples plot within the continental basalt field, while S695 plots within the field of back-arc basin basalts. The majority of North Carolina samples plot within the VAB fields, with two plotting very near the back-arc basin basalt field but within the continental basalt field. One North Carolina sample plots well within the continental basalt field among samples from Georgia.

Discussion

Although no readily identifiable relict igneous textures were observed in amphibolite samples from Georgia, derivation from an igneous protolith, paralleling previously established igneous origins for North Carolina Inner Piedmont amphibolites, is supported by alternative means of discriminating between ortho- and para-amphibolites. Lithologic requirements of amphibolite protoliths, correlation with primary igneous trends on discrimination diagrams after Leake (1964), and coherence of data plotted on basaltic magma series diagrams support an igneous origin of central Georgia Inner Piedmont amphibolites. That conclusion is further confirmed by diagrams depicting rock type based on TAS content and abundance of trace elements, which suggest a basaltic protolith for those samples. Based on the aforementioned results, it can reasonably be inferred that

amphibolites occurring in the Cat Square terrane in central Georgia represent vestiges of ocean crust that once constituted the floor of the Cat Square basin; consequently, viable inferences regarding the development of that basin can be established through interpretation of amphibolite geochemistry.

Trace element geochemical patterns exhibited by Cat Square terrane amphibolites differ markedly between samples from North Carolina and central Georgia and require that interpretations from both locations, at least initially, be discussed separately.

Trace element patterns of North Carolina amphibolites correspond closely with patterns of volcanic arc basalts, while also displaying the enrichment of HFS elements relative to MORB that distinguish the continental calc-alkaline basalt field from the island arc tholeiite and oceanic calc-alkaline basalt fields (Fig. 3-8). This correlation of patterns might suggest a continental arc affinity for those amphibolites, but can also be accounted for by a unique interaction of magmas in a back-arc setting. The defining attributes of the continental calc-alkaline basalt pattern (significant enrichment of LIL elements, negative Ta-Nb anomaly, and slight enrichment of HFS elements) can be exhibited by basalts derived from the mixing(?) of an enriched mantle source (contributing characteristics of the WPB) with an N-MORB source metasomatized by interaction with subducting oceanic crust (e.g., Ikeda and Yuasa, 1989; Nakamura et al., 1989). This type of unique bi-modal volcanism can be accommodated in the eruptive setting of a back-arc basin and could result in basalts that display geochemical characteristics similar to continental calc-alkaline basalts. This scenario accounts for basalts that were generated in a back-arc basin setting but display geochemical patterns that appear indistinguishable from continental calc-alkaline basalts. These observations differ somewhat from those made by Wilson (2006) but still support that author's interpretation of derivation of North Carolina amphibolites from basalts generated in a back-arc setting. A similar explanation is plausible for the trace element pattern exhibited by sample S695, which is more representative of common back-arc basin basalts. Sample S695 is characterized by a trace element pattern intermediate between WPB and tholeiitic oceanic arc basalt (island arc tholeiite) that can be attributed to a process similar to what likely produced the geochemical patterns displayed by North Carolina samples, although the E-MORB influence for those samples must have been greater to account for the higher levels of enrichment.

Similarities were consistently observed between geochemical patterns from central Georgia amphibolites, excluding sample S695, and WPB fields. The enrichment patterns of incompatible elements displayed by WPB cannot be accommodated by processes involving only a homogenous depleted upper mantle, and requires the incorporation of an enriched mantle source. This type of enrichment is typically observed at locations of intraplate volcanism, such as ocean island “hot spots” and continental rifts, and is also recognized at divergent plate margins producing E-MORB type magmas. Several studies (e.g., Ikeda and Yuasa, 1989; Nakamura et al., 1989) have identified the existence and influence of E-MORB type magmas in modern back-arc basin settings, and addressed the complicated nature of generating E-MORB type magmas in a back-arc setting affected by the presence of a subduction zone and the influences that a subducting slab has on the overriding mantle. Basalts generated in back-arc settings should reflect specific geochemical attributes associated with subduction zone magmatism, such as the characteristic Ta-Nb trough, and should differ in that regard from basalts erupted at within-plate settings. This subset of Georgia amphibolite does not strongly resemble any of the basalt pattern analogues in Figures 3-11 and 3-12, and exhibits only a faint subduction zone signature indicated by a slight negative Nb anomaly and enrichment in Ce and Sm. The lack of a strong indication of subduction zone influence does not explicitly exclude these samples from back-arc genesis, as their trace element signature could be accounted for by having been generated during a later stage of basin development. Nakamura et al. (1989) proposed a model for development of the Sea of Japan back-arc basin where, after enough spreading had been established, the subducting slab was far enough removed from the spreading center that it no longer facilitated mixing enriched deep mantle material with metasomatized, N-MORB upper mantle. Taylor and Martinez (2003) noted a similar process for intraoceanic back-arc basins, and likewise in those scenarios the metasomatized upper mantle wedge did not extend far enough into the spreading portion of the basin to facilitate mixing with an enriched mantle source. These scenarios resulted in the generation of basalt magma at back-arc spreading centers that displayed geochemical characteristics of magma generated at within-plate settings. It is possible that central Georgia amphibolites, excluding sample S695, represent a similar later phase of development of the Cat Square basin, and were derived from basalts produced in a back-arc setting.

Trace element patterns displayed by amphibolite samples from central Georgia and North Carolina support the interpretation of their genesis in a back-arc setting, but the disparity among those samples demonstrates that development of the basin was not homogeneous and at least two phases are recorded. These observations are further substantiated by data patterns exhibited in tectonic discriminant diagrams (Fig. 3-13).

North Carolina samples consistently plot in or near fields discriminating volcanic arc basalts, while several of those samples also plot within probability ellipses that discriminate back-arc basin basalts, which often overlap the fields of volcanic arc basalts. Sample S695 plots in the overlapping MORB and back-arc basin basalt ellipses, and in the fields of ocean floor, mid-ocean ridge, and back-arc basin basalts. The remaining central Georgia samples, along with one sample from North Carolina, consistently plot in E-MORB, within-plate, and continental basalt fields, and the WPB ellipses. The consistent plotting of a sample from North Carolina among central Georgia samples in WPB fields could suggest the further existence of those types of amphibolites in North Carolina; a much larger sample suite from the Cat Square terrane in both locations could show the emergence of discrete populations that represent distinct stages of basin development.

Tectonic Synthesis

A tectonic model proposed by Huebner and Hatcher (in review) for development of the Cat Square basin is adopted here. This model involves an earlier (Ordovician-Silurian) soft collision between the Carolina superterrane and the eastern Laurentian margin followed by initiation of a west-dipping subduction zone east of the Carolina superterrane; this resulted in slab roll-back and a period of extension that formed a back-arc basin between the Carolina superterrane and Laurentian margin (Fig. 3-14). A subduction polarity reversal is subsequently required to close the Cat Square basin and subduct the Cat Square terrane and Laurentian margin beneath the approaching Carolina superterrane. The latter events are punctuated by intrusion of the Concord Plutonic Suite into the Carolina superterrane in the Late Silurian through Early Devonian (Huebner and Hatcher, in review) and anatectic magmatism in the Cat Square terrane by the Early Devonian (Huebner et al., 2014). Although this model necessitates an unidentified (possibly buried beneath the Coastal Plain) magmatic arc related to Ordovician-Silurian west-dipping subduction on the eastern margin of the Carolina superterrane, it is favored here over a previous model suggested by Wilson (2006).

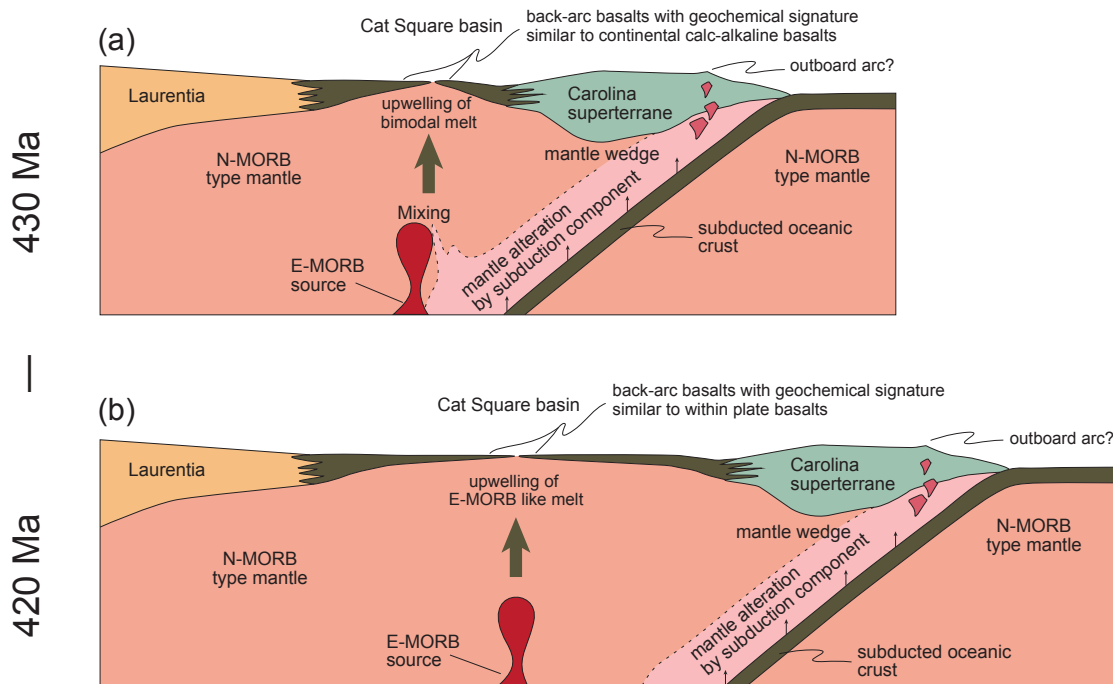


Figure 3-14. Tectonic diagrams illustrating two phases of Cat Square basin development. (a) Early development of Cat Square basin during which an E-MORB source mixed with weakly metasomatized N-MORB type mantle. (b) Later stage of basin development in which the subducting slab has been far enough removed from the basin spreading axis so as to have little effect on magma composition.

Wilson's (2006) model proposed east-dipping subduction outboard of the Laurentian margin and development of the Cat Square basin east of the Tugaloo terrane volcanic arc, which does not account for the variety of geochemical patterns exhibited by Cat Square terrane amphibolites. It also does not account for missing attributes that should be present if the Cat Square basin developed in an intraoceanic setting proximal to an active volcanic arc. Intraoceanic back-arc basins typically initiate rifting within a volcanic arc (Marsaglia, 1995) and contain one, if not several, abandoned arc fronts (e.g., Mariana trough, Lau and Fiji basins). They also should contain sediments composed of volcanoclastic debris sourced from the nearby arc (Marsaglia, 1995). Neither of these attributes has been identified to date in the Cat Square terrane. The terrane is instead composed of Laurentian and peri-Gondwanan-derived sediments (Bream, 2003; Merschat and Hatcher, 2007), deposition of which are adequately accommodated by the model of Huebner and Hatcher (in review), as both sources remained proximal to the basin throughout its development. The lack of volcanoclastic sediments recorded in the Cat Square terrane could be accounted for by the possible diversion of

those sediments by the large intervening landmass (Carolina superterrane) between the outboard arc on its eastern margin and the developing Cat Square basin on its western margin.

Correlation of Cat Square terrane amphibolite trace element patterns with basalt patterns from the Sea of Japan continental margin back-arc, noting differences with the intraoceanic East Scotia Sea, Mariana Trough, and northern Lau and Fiji Basin basalts, also supports the hypothesis suggesting west-dipping subduction beneath the Carolina superterrane. Possible heterogeneities in the mantle beneath continental landmasses (e.g., east Asian continental margin; Carolina superterrane) incorporated into magmas generated at continental margin back-arcs could account for geochemical similarities among Cat Square amphibolites and continental margin back-arc basalts; it could also account for geochemical differences between those amphibolites and intraoceanic back-arc basalts. These data suggest that the Cat Square basin likely developed as a continental margin back-arc basin, where the Carolina superterrane served to act as the continental margin, beneath which the subducting oceanic slab plunged (Fig. 3-14).

Summary

Geochemical analyses support the contention that amphibolite samples from the North Carolina Cat Square terrane, along with sample S695 from central Georgia, represent basalts from the initial stages of Cat Square basin development (Fig. 3-14a). Those basalts could have been produced by mixing an enriched mantle source with a slightly metasomatized N-MORB mantle wedge above a west-dipping subduction zone beneath the Carolina superterrane. Subsequent stages of basin development (Fig. 3-14b) are represented by the WPB characteristics of three central Georgia Cat Square terrane amphibolite samples, along with possibly one sample from North Carolina. These amphibolite samples are likely representative of basalts derived at a back-arc basin spreading axis far enough removed from the subduction zone that metasomatizing effects from the subducted slab were minimal. Mixing of an enriched mantle source with N-MORB upper mantle beneath recently formed oceanic crust is likely responsible for their trace element geochemical patterns.

Conclusions

- 1.) Although no relict igneous textures were observed in samples of this study, stratigraphic relationships and characteristics identified using major element data indicate an igneous origin of central Georgia Inner Piedmont amphibolites.
- 2.) Interpretation of trace element data demonstrate that North Carolina samples and sample S695 from central Georgia are characteristic of continental margin back-arc basalts generated by mixing two magma components. These amphibolite samples possibly represent early stages of Cat Square basin development, where the spreading axis of the basin and subducting oceanic slab were in closer proximity.
- 3.) Three central Georgia samples, along with possibly one from North Carolina, indicate a within-plate eruptive setting only slightly influenced by a subduction component, and possibly represent a stage of Cat Square basin development in which the subducting slab was far enough removed from the spreading axis that it had little effect on basalt composition.
- 4.) Amphibolites representing basalt generated during development of the Cat Square basin do not appear to be homogenous and at least two distinct compositions are represented. This necessitates the need for analysis of a larger suite of samples to better characterize Cat Square terrane amphibolite protoliths and indicates that a tectonic model that considers all Cat Square basin crust as derived from mixing an E-MORB source with metasomatized N-MORB type sub-oceanic mantle above a subduction zone is inadequate.

Chapter 4

Zircon geochronology of selected samples from the Cat Square terrane and Pine Mountain window, central Georgia

Introduction

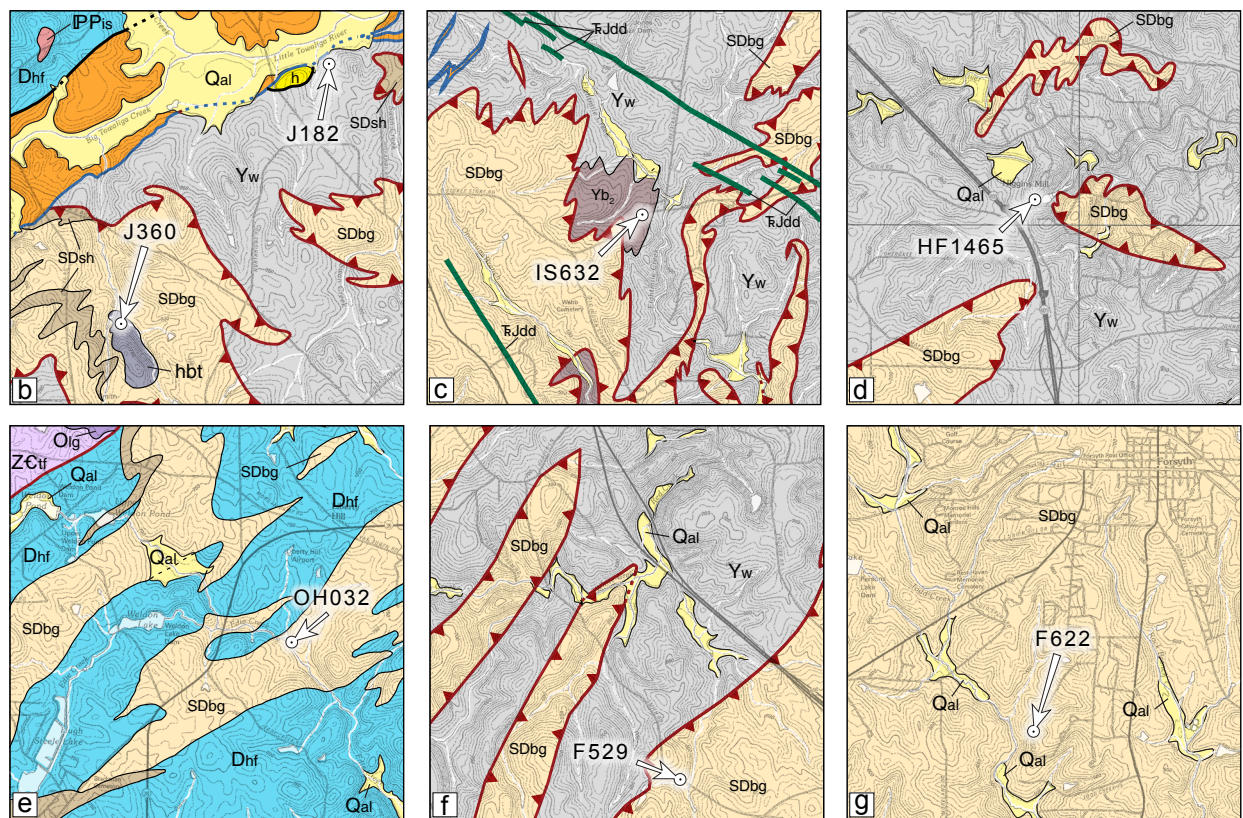
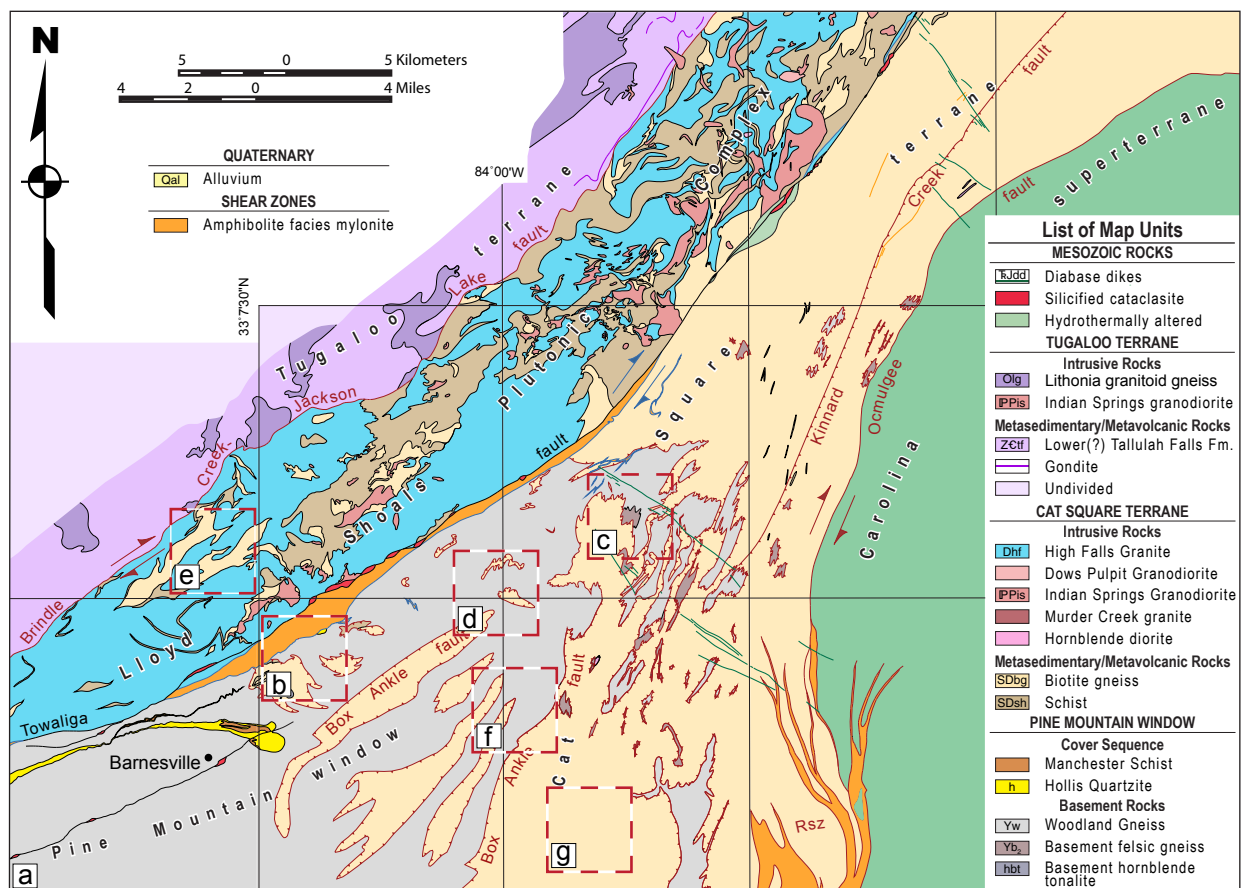
Several samples were collected for geochronologic study to further the characterization of the Cat Square terrane in central Georgia. The utilization of zircon as a geochronometer is indispensably useful in determining absolute ages of lithologic units, assessing provenance of metasedimentary rocks, and inferring timing of significant metamorphic events. Seven samples were collected for zircon analysis from different lithologic units in both the Cat Square terrane and Pine Mountain window (Fig. 4-1a) in order to delimit the timing of crystallization of two metaigneous bodies, timing of deformation of the Woodland Gneiss, and determine the provenance of biotite gneiss units and infer their maximum age of deposition.

Samples

Sample J360 was collected in order to resolve the timing of emplacement of a hornblende tonalite stock. The tonalite is located within a klippe of Cat Square terrane rocks in the northwestern corner of the Johnstonville quadrangle (Fig. 4-1b). Sample J360 was collected from an outcrop of large spheroidally weathered boulders in an unnamed creek east of Brook Road. Sample IS632 was collected to determine the crystallization age of several bodies of felsic gneiss that occur southeast of the Towaliga fault throughout the Indian Springs, Forsyth, and Berner 7.5-minute quadrangles. This sample was collected from an exposure in the central portion of the Indian Springs quadrangle along Stokes Store Road west of Eightmile Creek (Fig. 4-1c). Samples J182 and HF1465 were obtained in order to better delimit timing of deformation of sheared Woodland Gneiss, hypothesized to be the result of movement along the Box Ankle fault. Sample J182 was collected from outcrop near the southeastern margin of the Towaliga fault zone, east of Van Buren Road (Fig. 4-1b). Sample HF1465 was collected from a large exposure of Woodland Gneiss (Fig. 2-15c) exposed in shoals of the Little Towaliga River at Higgins Mill (Fig. 4-1d).

Samples OH032, F529, and F622 were collected to assess provenance of detrital zircons from Cat Square terrane(?) biotite gneiss. Sample OH032 was collected from a large exposure of

Figure 4-1. Sample locations for geochronologic analyses. (a) Simplified geologic map of the northeastern end of the Pine Mountain window, central Georgia. Modified from Huebner et al. (2014). Rsz—Rumble shear zone. (b) Locations of hornblende tonalite sample J360 and Woodland Gneiss sample J182. (c) Location of felsic gneiss sample IS632. (d) Location of Woodland Gneiss sample HF1465. (e) Location of detrital sample OH032. (f-g) Locations of detrital samples F529 and F622.



biotite gneiss along Edie Creek in the southeastern corner of the Orchard Hill quadrangle (Fig. 4-1e). It was sampled from Cat Square terrane biotite gneiss between the Brindle Creek-Jackson Lake and Towaliga faults in the Lloyd Shoals Plutonic Complex. Samples F529 and F622 (Fig. 4-1f-g) were collected southeast of the Towaliga fault in the west-central and south-central portions of the Forsyth quadrangle, respectively. Biotite gneiss there is confined to the hanging wall of the Box Ankle fault, which separates Cat Square terrane rocks from underlying basement units of the Pine Mountain window. Sample F529 was collected from a weathered outcrop along the east side of Smith Road, while sample F622 was collected from float boulders along the west side of Mitchell Road.

Methods

Sample Processing

Zircon separates for each sample were prepared from ~3 kg of bulk material using standard mechanical, gravity, and magnetic separation techniques. Material was reduced to ~5-cm diameter in the field to minimize the possibility of contamination from crushing large samples in rock preparation facilities. Bulk samples were systematically milled to a fine powder in rock preparation facilities at the Department of Earth and Planetary Sciences, University of Tennessee-Knoxville and the Department of Geological Sciences, University of North Carolina-Chapel Hill. Samples were first reduced to approximately 6 mm diameter using a Bico Inc. VD Chipmunk jaw-type crusher equipped with steel crushing plates. Crushed material was then milled to powder using a Bico Inc. UA disk-pulverizer equipped with 8 in standard iron alloy grinding plates. Each machine was thoroughly cleaned with compressed air and vacuum suction between processing of each sample. Crushing and grinding plates were removed, cleaned with wire brushes, and rinsed with isopropyl alcohol to remove any excess material between samples.

Concentration of zircon from powdered samples was accomplished at the University of North Carolina-Chapel Hill by employing standard density and magnetic separation techniques. Samples were first processed through a hydraulic percussion table, which uses water and a grooved shaker table to separate material based on density. Lighter material is washed over the grooves and diverted from heavier minerals (e.g., zircon), which settle into the grooves and are transported down the table and collected at the end of the table. This resulted in the separation of material into

three fractions. The lightest material (S_1) was discarded after the separation. The intermediate (S_2) and heaviest (S_3) separates were collected and dried under heat lamps. Percussion table parameters such as water volume and shaking frequency and intensity were set to optimize concentration of zircons in the S_3 material, which was further processed for greater zircon separation. S_2 material was retained as a contingency in the event there were not enough zircons recovered from the S_3 material. Occasionally S_3 material from well-foliated samples retained few millimeter-sized particles after milling and processing on the percussion table. This required dried material to be passed through a standard U.S. No. 35-mesh sieve to remove particles greater than 500 microns. Ferromagnetic minerals were removed from the S_3 fraction by use of a hand magnet, and the remaining sample was processed through heavy liquid separation. Zircon and other heavier minerals (e.g., apatite, pyrite) were separated from lighter constituents based on density contrasts exploited by mixing the sample with methylene iodide in a separatory funnel and allowing the mixture to settle. Minerals less dense than the methylene iodide (3.32 g/cm^3) floated above the liquid, while those of greater density settled into the bottom of the funnel where they were extracted. The extracted concentrate was rinsed with copious amounts of acetone to expedite evaporation of excess methylene iodide. A Frantz magnetic barrier laboratory separator was used to further separate weakly paramagnetic grains from diamagnetic ones. Samples were passed through an electromagnetic field along a vibrating chute, which was angled to provide a 25-degree forward slope and 15-degree side slope. The forward angle permitted grains to tumble down the chute through the magnetic field, while the side angle permitted grains not retained by the magnetic field to fall on the opposite side of a machined barrier at the end of the chute. Zircon typically has very low magnetic susceptibility and hence was concentrated on the diamagnetic side. Samples were initially processed through a 0.25-amp field, with the diamagnetic portion from each run progressively processed through incrementally increasing fields, up to 1.25 amps. Zircons from the 1.25-amp concentration were used to create mounts for geochronologic analyses. Paramagnetic fractions contained small amounts of magnetic zircon, which were collected and are maintained along with other residual material by R.D. Hatcher, Jr. at the University of Tennessee-Knoxville.

Three different mounting techniques were employed for samples from this study. Samples J182, HF1465, J360, and IS632 were collected to establish crystallization and metamorphic ages of zircons from igneous and meta-igneous rocks; mounts were prepared at the Stanford-USGS Micro

Analysis Center (SUMAC) at Stanford University, California. Two techniques were employed for mounting zircons from these samples (Fig. 4-2), which included the preparation of round 25.4-mm diameter standard epoxy resin pucks for all samples, and the use of premade pucks containing machined grooves filled with indium metal for samples J182 and HF1465. To create standard epoxy resin pucks, zircons from each sample were hand picked under a binocular microscope, transferred to a piece of adhesive tape, and arranged in horizontal rows inside a 15-mm analytical working diameter. After zircons from samples were arranged on the tape, SUMAC personnel added age and compositional standards and poured an epoxy resin into a 25.4-mm ring placed around the grains. Once cured, the epoxy resin puck was polished to expose inner sections of zircon grains (Fig. 4-2a). Thirty-one zircons from sample J360 along with 27 zircons from sample IS632 were mounted in a standard epoxy resin puck labeled MC-15. Twenty zircons from sample J182 and 21 zircons from sample HF1465 were mounted in a standard epoxy resin puck labeled MC-16.

An indium metal mounting technique (Fig. 4-2b) was employed to mount an additional 27 zircons from sample J182 and 28 zircons from sample HF1465, which was labeled MC-17. This facilitated analysis of the outermost surfaces of zircons to theoretically obtain ages from latest episodes of metamorphic recrystallization. Zircons were again hand picked, selecting only zircons with euhedral and flat crystal faces, and placed on a glass slide covered in a thin layer of vacuum grease. Once aligned on the slide, zircons were pressed into two 4 x 12-mm indium metal-filled troughs milled into a standard 25.4-mm epoxy resin puck. After removing the glass slide, flat euhedral faces of zircon specimen remained exposed above the indium metal surface of the mount. The indium metal mounts were not polished like standard epoxy resin mounts, thereby leaving the outermost surfaces of the zircons intact for analysis.

Mounts for detrital zircons from samples OH032, F529, and F622 were prepared by staff at the Arizona LaserChron Center, Department of Geosciences, University of Arizona. In order to maintain unbiased representative detrital samples, zircons were not handpicked but were collectively poured into a mounting tube on adhesive tape, after which 25.4-mm diameter epoxy resin pucks were cast and polished to expose inner sections of the zircons.

Zircon Imaging

Given the high variability of internal textures exhibited by zircon and the likelihood of recording multiple geologic events (e.g., episodes of magmatic and metamorphic crystallization), it is imperative that high-precision geochronology be guided by detailed imaging (e.g., Hanchar and Miller, 1993). Interpretation of these preserved textures can prove very useful in differentiating between igneous and metamorphic zircon, identifying sedimentary textures, and deciphering the geologic history of complex zircons that yield multiple ages (Hanchar and Miller, 1993; Corfu et al., 2003). Cathodoluminescent (CL), reflected light, backscattered electron, and secondary electron images of mounts were utilized in this study to identify spots for analysis of each zircon specimen. CL images of sectioned zircons in polished mounts provided the best foundation for spot selection, because complex zonation patterns, inherited cores, and inclusions in those zircons were readily identifiable. Spot locations were also observed in reflected light so that any irregularities, such as structural defects and inclusions, not already observed in cathodoluminescence could be avoided. Samples analyzed at the SUMAC lab had cathodoluminescence images of individual zircons acquired by the author at the SUMAC facility, using a Hamamatsu cathodoluminescence detector installed on a Jeol LV 5600 scanning electron microscope. Secondary electron images were used in conjunction with CL images to identify spots for samples J182 and HF1465, which were mounted using the indium metal technique. Since these mounts were not polished, internal sections of the zircons were not exposed, and consequently CL images did not reveal any complex zoning patterns. Those images instead were useful in determining whether or not a single continuous layer was exposed on the surface, as a discontinuous layer would luminesce differently. Secondary electron images presented surfaces far better than reflected light images and, given the requirement of the SHRIMP-RG to analyze a very smooth and flat surface, were employed to ensure that the spots selected for analysis were positioned on the most suitable surfaces, free of any structural defects. Cathodoluminescence images of detrital samples OH032 and F622 were obtained by staff at the Arizona LaserChron SEM facility, using a Hitachi 3400N scanning electron microscope equipped with a Gatan ChromaCL system. Because of the large number of zircons in these samples and the mounting technique, lower resolution images of groups of zircons were obtained as opposed to higher resolution images of individual zircons. Backscattered electron images, also composed by Arizona LaserChron staff, were used as the basis for spot selection of detrital sample F529 because the abundance and bright

luminescence of aluminosilicate minerals (likely kyanite), which were not removed during separation procedures, made it impractical to acquire CL images. Zircon growth zoning patterns were not as easily identifiable using backscattered electron images; however, the images were adequate to differentiate between cores and rims, while inclusions and structural defects were readily identified and avoided.

Analytical procedures

SHRIMP-RG at SUMAC

Standard operating procedures as outlined by Compston and Williams (1992), and Williams (1998) were followed for analyses via the SHRIMP-RG. The $^{16}\text{O}_2^-$ ion beam was run at ~15 nA, with a beam diameter of ~22 μm . A standard number of five scans through the mass stations for each analysis was maintained. Zircon standards R33 (Black et al., 2004) and TEM (Black et al., 2003) were utilized for calibration and were analyzed regularly. All data were reduced using SQUID v. 2.5 (Ludwig, 2009) with data plots constructed using Isoplot (Ludwig, 2012) routines.

LA-ICPMS at Arizona LaserChron Center

Operational parameters outlined by Gehrels et al. (2008) and Gehrels et al. (2009) were utilized for analysis conducted via LA-ICPMS. Laser ablation was achieved with a New Wave DUV193 Excimer laser operating at a wavelength of 193 nm. A beam diameter of ~30 μm was maintained for all analyses with the exception of sample F529, where a diameter of ~20 μm was utilized due to the need for better spatial resolution because of small diameter grains, resulting in ablation pits of ~12 μm depth. Zircon age standards SL (Gehrels et al., 2008) and R33 (Black et al., 2004) were utilized for calibration and were routinely analyzed. Data were reduced by Arizona LaserChron personnel using an excel spreadsheet (“agecalc”) with VBA macros (Gehrels, et al., 2009) and plotted by the author utilizing several Isoplot (Ludwig, 2012) routines and a routine called “Age Pick” (downloaded from <http://www.geo.arizona.edu/alc>).

Data representation

Zircon accepts modest amounts of radioactive isotopes of uranium and thorium into its structure during crystallization, but mostly excludes incorporation of common lead isotopes (Scherer et al., 2007). This enables the use of those isotopic systems, or “clocks”, to be used to

calculate dates for when the zircons crystallized. The U-Pb system is most commonly used for geochronology and consists of two decay series: ^{238}U decays to ^{206}Pb ; ^{235}U decays to ^{207}Pb . Isotopic ratios from these two series determined from just one analysis allow for calculation of three dates ($^{206}\text{Pb}/^{238}\text{U}$; $^{207}\text{Pb}/^{235}\text{U}$; $^{206}\text{Pb}/^{207}\text{Pb}$), which provides an internal check on the stability of the isotopic systems. If the zircon crystal has remained a closed system and the amounts of non-radiogenic “common” lead are accounted for, the values of all three dates would be the same, and the analysis is considered concordant. Values of concordant analyses plotted on a bivariate plot with $^{206}\text{Pb}/^{238}\text{U}$ plotted along the y-axis, $^{207}\text{Pb}/^{235}\text{U}$ plotted along the x-axis, and $^{206}\text{Pb}/^{207}\text{Pb}$ forming the slope of a line passing through the origin, comprise a concordia diagram and form a curve (concordia line). The amount by which an analysis does not plot along the concordia line is considered discordance. If an analysis plots above the concordia line it is considered negatively (or reversely) discordant, and if it plots below the concordia line it is considered positively discordant. Negative discordance is relatively rare and considered to be a result of instrumental inaccuracies (Gehrels, 2012). Therefore any analyses with considerable negative discordance have been excluded from further interpretation. Positive discordance can result from either perturbation of the U-Pb system causing some Pb-loss, therefore yielding anomalously young ages, or from simultaneous analysis of multiple temporally distinct zircon populations, or temporally distinct zones in one zircon crystal (Hanchar and Miller, 1993).

In nearly all instances only $^{206}\text{Pb}/^{238}\text{U}$ ages from analyses were reported, based on recommendations of precision for zircons less than 1500 Ma (Nemcin and Cawood, 2005; Gehrels, 2012). For some discordant analyses both the $^{206}\text{Pb}/^{238}\text{U}$ and $^{207}\text{Pb}/^{206}\text{Pb}$ ages were reported because of the greater accuracy of the $^{207}\text{Pb}/^{206}\text{Pb}$ age when a perturbation of the U-Pb system is suspected. Errors associated with both types of reported ages are expressed as 2σ . Meaningful ages are best interpreted from a cluster of overlapping analyses, and the more analyses used in interpreting an age the more robust that age becomes (Bowring et al., 2006; Gehrels, 2012). Reliable crystallization ages and ages of metamorphism were interpreted from weighted averages of clusters of analyses using Isoplot (Ludwig, 2012) routines employing the mean square of weighted deviates (MSWD) as measure of goodness of fit. The MSWD value highlights any lack of coherence among analyses so that the lower the MSWD value the better the fit, with a value of 1 or less being optimal (Schone et al., 2013). Detrital samples often contain a mixture of groups of ages that represent

differing source regions. To interpret the distribution of groups of ages from detrital samples, a relative age probability density plot routine from Isoplot (Ludwig, 2012) was utilized. This routine displayed an age distribution curve constructed by assigning a normal distribution to the age and uncertainty of each analysis, determined by summing the probability distribution of each analysis contributing to the curve and normalizing by dividing the area under the curve (Gehrels, 2012; Ludwig, 2012). A histogram was also plotted, which displayed the number of analyses whose dates fall within a certain range, or bin, which were stacked, thus indicating the number of analyses that fall within that range. A moderate discordance filter was applied to all detrital samples that excluded analyses with discordance between +10 percent and -3 percent. This resulted in two probability density plots for each analysis. Age groupings represented on the relative age probability density diagrams were analyzed using an “agepick” routine, which identified each age range consisting of three or more overlapping analyses and reported the number of analyses that composed the range. Peak ages within the range and the number of analyses that contributed to peak ages were also reported. One shortcoming of reported peak ages is that there is no uncertainty associated with those calculated values, and they do not represent the uncertainty of analyses used in calculations.

Results

SHRIMP-RG analyses

Sample J360

Eight zircons, out of the 31 mounted, were analyzed from sample J360 (hornblende tonalite) (Fig 4-3). Zircon grains exhibited complexly zoned interiors with thin outer rims of crystal growth and infrequent embayments. In all cases the outer rim material appeared homogenous, exhibited no patterns of zonation, and luminesced much brighter than interior portions of the grain. Interior portions of zircons do not exhibit typical concentric oscillatory-zoned patterns with doubly terminating ends, indicative of magmatic crystallization (Hanchar and Miller, 1993; Corfu et al., 2003), but instead exhibit commonly “banded” patterns parallel to the long axes of grains, with some grains exhibiting complex convoluted zoning (Fig. 4-3a-h). This type of disruption of concentric oscillatory zoning could be indicative of late- to post-magmatic modification of zircon grains, possibly in the presence of aqueous fluids (Corfu et al., 2003), or formation during high-

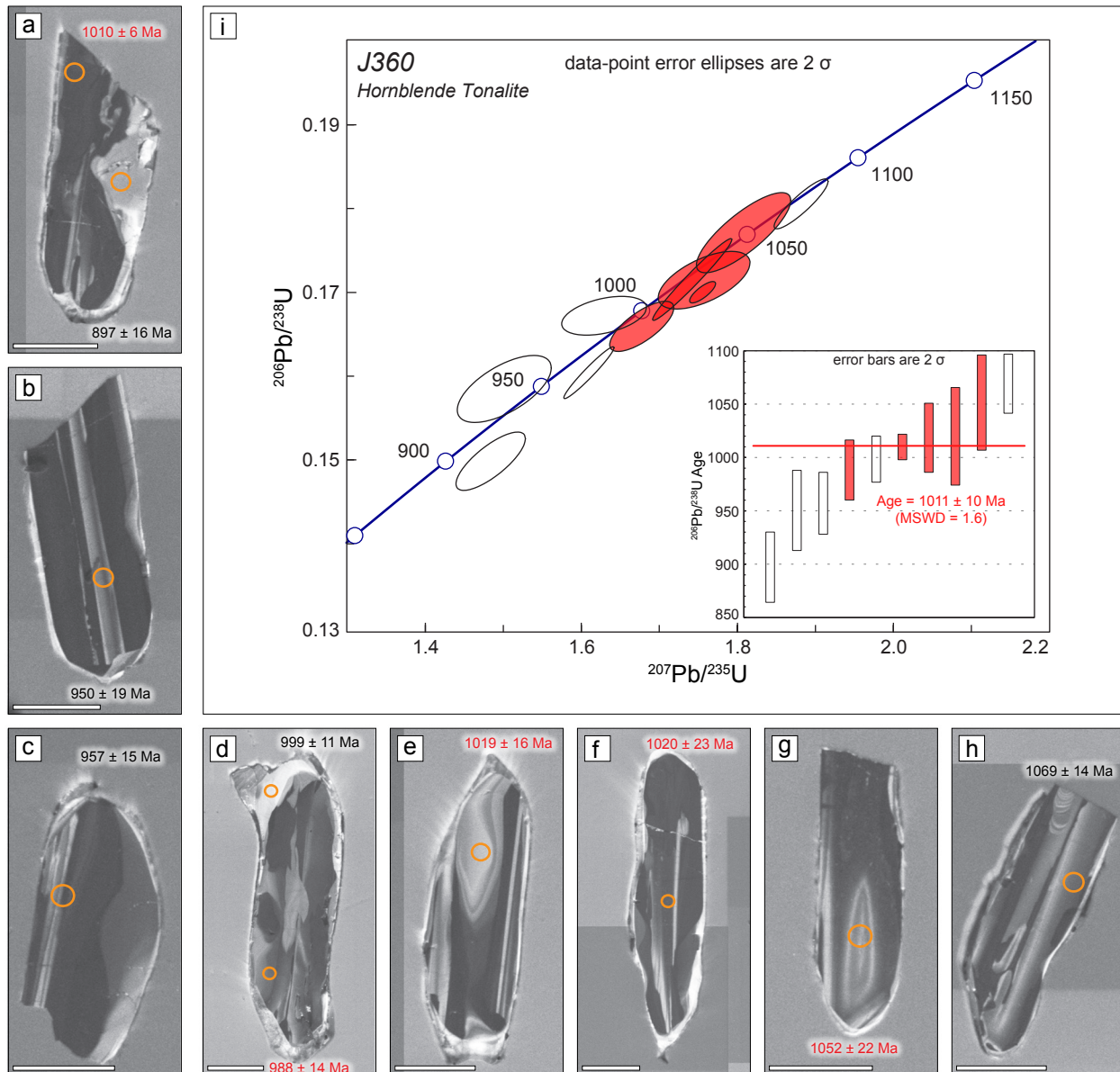


Figure 4-3. SHRIMP-RG analyses of sample J360 (hornblende tonalite). White bar represents 100 μm . Orange ellipses are drawn to scale and represent spot analyses. (a-h) Cathodoluminescent images of analyzed zircons with spot analyses and $^{206}\text{Pb}/^{238}\text{U}$ dates. Colors correspond to interpreted age populations. (i) Concordia diagram with 2σ error ellipses and weighted average of analyses shown in the inset box. Red filled ellipses and bars represent analyses which were used to calculate an age population.

temperature metamorphism (Harley et al., 2007). It is difficult to definitively determine the conditions under which these zircons formed because of both the lack of consensus on the interpretation of secondary zoning patterns and the absence of any observable truncation of primary concentric oscillatory zoning by secondary crystallization patterns in this sample. The entire interior portion of zircon grains appear to be composed of what could be interpreted as secondary textures and, as such, dates obtained for these areas were inferred to represent, at a minimum, a late-magmatic crystallization age or possibly a significant metamorphic recrystallization event. Zircons generally exhibit an elongate morphology and frequently contain blunt fractured ends. Fractures on the ends of grains always truncate zoning patterns, including the outermost rim, with no new crystal growth on the fractured ends. This indicates fracturing occurred post-crystallization, possibly during sample processing, and does not suggest a detrital origin, agreeing with the igneous classification of the sample. A crystallization age of 1011 ± 10 Ma was determined for sample J360 based on a weighted average of $^{206}\text{Pb}/^{238}\text{U}$ dates from a coherent group of five analyses with an MSWD of 1.6 (Fig. 4-3i). This age differs marginally from the 1007 ± 9 Ma reported by Huebner et al. (2014), which was based on preliminary data interpretation and was obtained from a weighted average of less than five analyses. The 1011 ± 10 Ma weighted average comprises dates that ranged from 1052 ± 22 Ma to 988 ± 14 Ma with a maximum positive discordance of 5 percent from an analysis that also exhibited the smallest error (1010 ± 6 Ma), and a maximum negative discordance of 1 percent from an analysis that yielded the oldest date in the group. Results from two analyses of homogenous outer rim material were excluded because of discordance. The older of those two analyses exhibited a -6 percent discordance while the younger of the two was +9 percent discordant. Sample J360 also yielded a concordant (+1% discordant) $^{206}\text{Pb}/^{238}\text{U}$ date of 1069 ± 14 Ma, which comprises the oldest date obtained from the sample. A moderately discordant (+5%) analysis with a $^{206}\text{Pb}/^{238}\text{U}$ date of 957 ± 15 Ma, and a highly discordant (-7%) analysis with a $^{206}\text{Pb}/^{238}\text{U}$ date of 950 ± 19 Ma were also obtained from sample J360. Although the oldest analysis is concordant and most likely yielded accurate dates, it does not lie near the younger overlapping cluster of analyses, suggesting they are not cogenetic, and as such it is difficult to ascertain its true age significance.

Sample IS632

From the 27 zircons mounted for sample IS632 (felsic gneiss), 11 were analyzed, yielding 14 spot analyses. Zircons from this sample commonly contain embayed bright xenocrystic cores with banded zoning patterns (Fig. 4-4d, f, I, k). Where present, cores are enclosed by a relatively thick, homogenous, and unzoned portion of dark material that truncate core-zoning patterns and fill embayed portions. Several grains do not contain xenocrystic cores, and instead contain interior portions composed entirely of dark homogenous unzoned material. Zircons also exhibit a relatively thin outermost rim of material that ranges in thickness from $< 1\ \mu\text{m}$ – $30\ \mu\text{m}$. One zircon (Fig. 4-4g) exhibits “patchy” or sector-zoning patterns, which, like convoluted zoning, can be indicative of crystallization during high-temperature metamorphism (Harley et al., 2007). Zircon morphology is generally elongate; displaying somewhat rounded ends with some grains exhibiting very anhedral form (e.g., Fig. 4-4h).

Analyses focused on different portions of grains that contained one of the aforementioned zoning patterns. Multiple analyses were conducted on three grains: two analyzed both xenocrystic core material and the dark homogenous enclosing material (Fig. 4-4d, f); while the third (Fig. 4-4a) analyzed dark homogenous material in a grain without a xenocrystic core and the thin outermost rim. A crystallization age of $1158 \pm 18\ \text{Ma}$ was interpreted from a coherent group of five analyses of xenocrystic cores that yielded a weighted average with an MSWD of 0.24 comprising $^{206}\text{Pb}/^{238}\text{U}$ dates ranging from $1195 \pm 20\ \text{Ma}$ to $1145 \pm 57\ \text{Ma}$ (Fig. 4-4l). Of these analyses, the two with the greatest amount of discordance also exhibited the greatest amount of error: the oldest analysis in the group exhibits a discordance of -9 percent, while the younger analysis ($1145 \pm 57\ \text{Ma}$) exhibits a +10 percent discordance. A second age population was determined from five analyses of dark homogenous material. The second population comprises a coherent group of $^{206}\text{Pb}/^{238}\text{U}$ dates ranging from $1071 \pm 48\ \text{Ma}$ to $986 \pm 61\ \text{Ma}$, which yielded a weighted average of $1014 \pm 12\ \text{Ma}$ with an MSWD of 0.13. Sample IS632 also yielded a moderately discordant (+8%) analysis with a $^{206}\text{Pb}/^{238}\text{U}$ date of $891 \pm 48\ \text{Ma}$ with error limits slightly below the weighted average for the younger age population. Analyses of the outermost rim material along with an analysis of dark homogenous material were excluded from further interpretation because of high positive discordance.

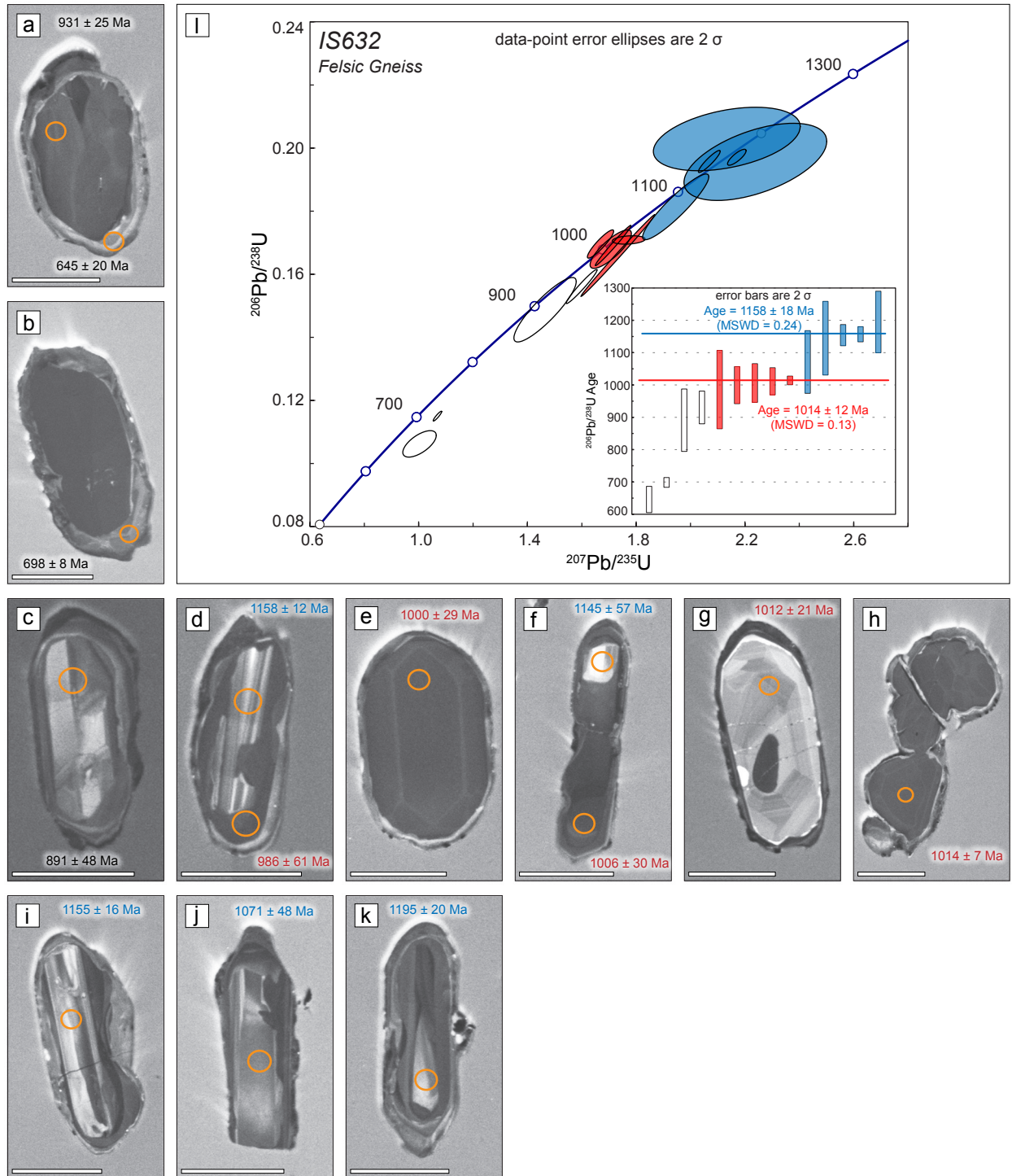


Figure 4-4. SHRIMP-RG analyses of sample IS632 (felsic gneiss). White bar represents 100 μm . Orange ellipses are drawn to scale and represent spot analyses. (a-k) Cathodoluminescent images of analyzed zircons with spot analyses and $^{206}\text{Pb}/^{238}\text{U}$ dates. Colors correspond to interpreted age populations. (l) Concordia diagram with 2σ error ellipses and weighted average of analyses shown in the inset box. Red filled ellipses and bars represent analyses which were used to calculate an age population.

Sample J182

Eight zircons from sample J182 (Woodland Gneiss) were analyzed from the 20 grains mounted using the standard epoxy resin technique (Fig. 4-5). These grains exhibit complex internal zoning patterns and often contain elongate and oscillatory-zoned cores (e.g., Fig. 4-5c). Some cores exhibit a euhedral blocky shape with squared ends (Fig. 4-5g). Embayments of cores are present along with truncation of core zoning patterns by homogenous unzoned outer material. Zircon grains also contain a relatively thin ($< 1\ \mu\text{m}$ in places) outer rim of material that is somewhat discontinuous and varied in thickness, being thinner along the long axes of the grain and thicker on the ends. Analyses again focused on portions of grains with one of the aforementioned zoning patterns, with multiple analyses performed on one grain (Fig. 4-5e). Interpretation of these analyses yielded two age populations (Fig. 4-5i). The older of the two populations comprises two concordant overlapping analyses composing a weighted average $^{206}\text{Pb}/^{238}\text{U}$ age of $1048 \pm 40\ \text{Ma}$ with an MSWD of 0.15. A concordia age of $1058 \pm 38\ \text{Ma}$ was also calculated using an Isoplot (Ludwig, 2012) routine. A weighted average of an additional two concordant overlapping analyses with an MSWD of 0.029 defines a younger population with an age of $985 \pm 30\ \text{Ma}$. A concordia age of $989 \pm 11\ \text{Ma}$ with an MSWD of 0.82 was also calculated for that population. One anomalously young but concordant (-1% discordant) analysis with a $^{206}\text{Pb}/^{238}\text{U}$ date of $918 \pm 14\ \text{Ma}$ was also identified.

Meaningful ages from two discordant analyses (Fig. 4-5a, c) have been inferred by application of differing assumptions. One collective assumption was that discordance observed in these analyses was due to one of three processes: (1) some lead loss event has perturbed the typically closed U-Pb system; (2) a mixing of different age populations from multiple zircons; or (3) an analysis has included two temporally distinct zones of zircon crystallization (Hanchar and Miller, 1993). The use of single crystal methods via ion microprobe, guided by high-resolution CL images, nearly eliminated the possibility of discordance caused by the latter two scenarios, and thus it can be reasonably assumed that the discordance here is caused by some perturbation of the U-Pb system. If the event occurred in relatively recent geologic time and the lead-loss trajectory passes through the origin, the $^{207}\text{Pb}/^{206}\text{Pb}$ date of the analyses would provide a more accurate age estimate; if the event occurred in ancient geologic time, any age constraints must be based on an upper concordia intercept age (Gehrels, 2012) defined by a lead-loss trajectory that does not pass through the origin. The older of the two analyses yielded a $^{207}\text{Pb}/^{206}\text{Pb}$ date of $1021 \pm 16\ \text{Ma}$, which falls

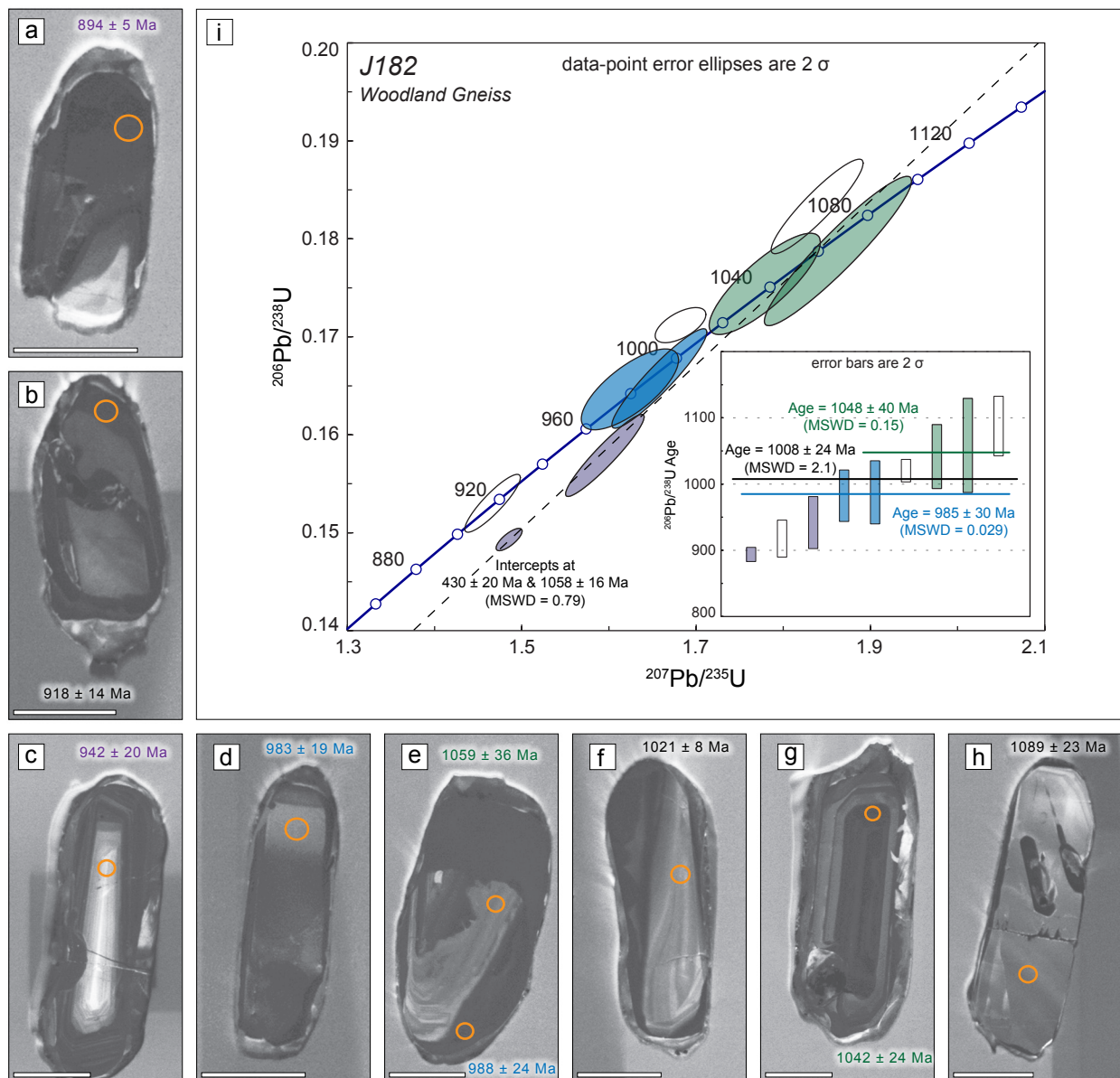


Figure 4-5. SHRIMP-RG analyses of sample J182 (Woodland Gneiss). White bar represents 100 μm . Orange ellipses are drawn to scale and represent spot analyses. (a-h) Cathodoluminescent images of analyzed zircons with spot analyses and $^{206}\text{Pb}/^{238}\text{U}$ dates. Colors correspond to interpreted age populations. (i) Concordia diagram with 2 σ error ellipses and weighted average of analyses shown in the inset box. Filled ellipses and bars represent analyses that were used to calculate an age population. Green corresponds to analyses comprising the older population, blue corresponds to analyses constituting the younger population, and lavender corresponds to discordant analyses used to infer a concordia intercept age. Lavender ellipses and dashed line indicate the lead-loss trajectory and chord used to define the upper intercept age.

within error of the interpreted age of the older population. The younger of the two discordant analyses yielded a $^{207}\text{Pb}/^{206}\text{Pb}$ date of 990 ± 11 Ma, which falls within error of the mean age interpreted for the younger of the two age populations. Assuming an ancient perturbation event, a two-point isochron was estimated using an Isoplot (Ludwig, 2012) routine that calculated a lead-loss trajectory passing through both discordant analyses with an MSWD of 0.79, forming a chord with a lower concordia intercept age of 430 ± 20 Ma and an upper concordia intercept age of 1058 ± 16 Ma. The younger age would represent timing of the perturbation event with the older representing the crystallization age of the zircon. The upper intercept age determined using this routine also falls within error of the interpreted age of the older population. When assessing validity of calculated isochron values, the more points used in defining the isochron, the more reliable the calculated age becomes. Based on this reasoning, a two-point isochron, which was calculated for sample J182, does not provide a very reliable age and some caution should be exercised in its application; however, given the close values for the upper intercept age and the $^{207}\text{Pb}/^{206}\text{Pb}$ date of the older analysis, it is reasonable to infer that at least the older of the two discordant grains is cogenetic with the older age population and both dates serve to improve the robustness of that population. Some speculation can still be made regarding the cogenesis of younger of the two discordant analyses, since it could be interpreted to represent either population.

Sample HF1465

Eight zircon grains from sample HF1465 (Woodland Gneiss) were analyzed from the 21 mounted using the standard epoxy resin technique (Fig. 4-6), nearly all of which contain concentric oscillatory-zoned xenocrystic cores. Cores vary in morphology from blocky to acicular, with some containing embayments and truncated zoning patterns. In most instances bright cores are enclosed in darker unzoned material surrounded by a thin outer rim of material. Some grains (e.g., Fig. 4-6b-c) exhibit multiple thin outer rims, some of which appear discontinuous in places. Zircon grain morphology is moderately elongate with rounded ends. Thirteen spot analyses yielded three identifiable age populations for this sample. The oldest population is defined by three analyses, of which two have moderate negative discordance (-3 and -6% discordant) and one is concordant (+1% discordant). Analysis spots from this population, with the exception of one (Fig. 4-6i) located in a core that exhibited a convoluted zoning pattern and less luminescence than the surrounding

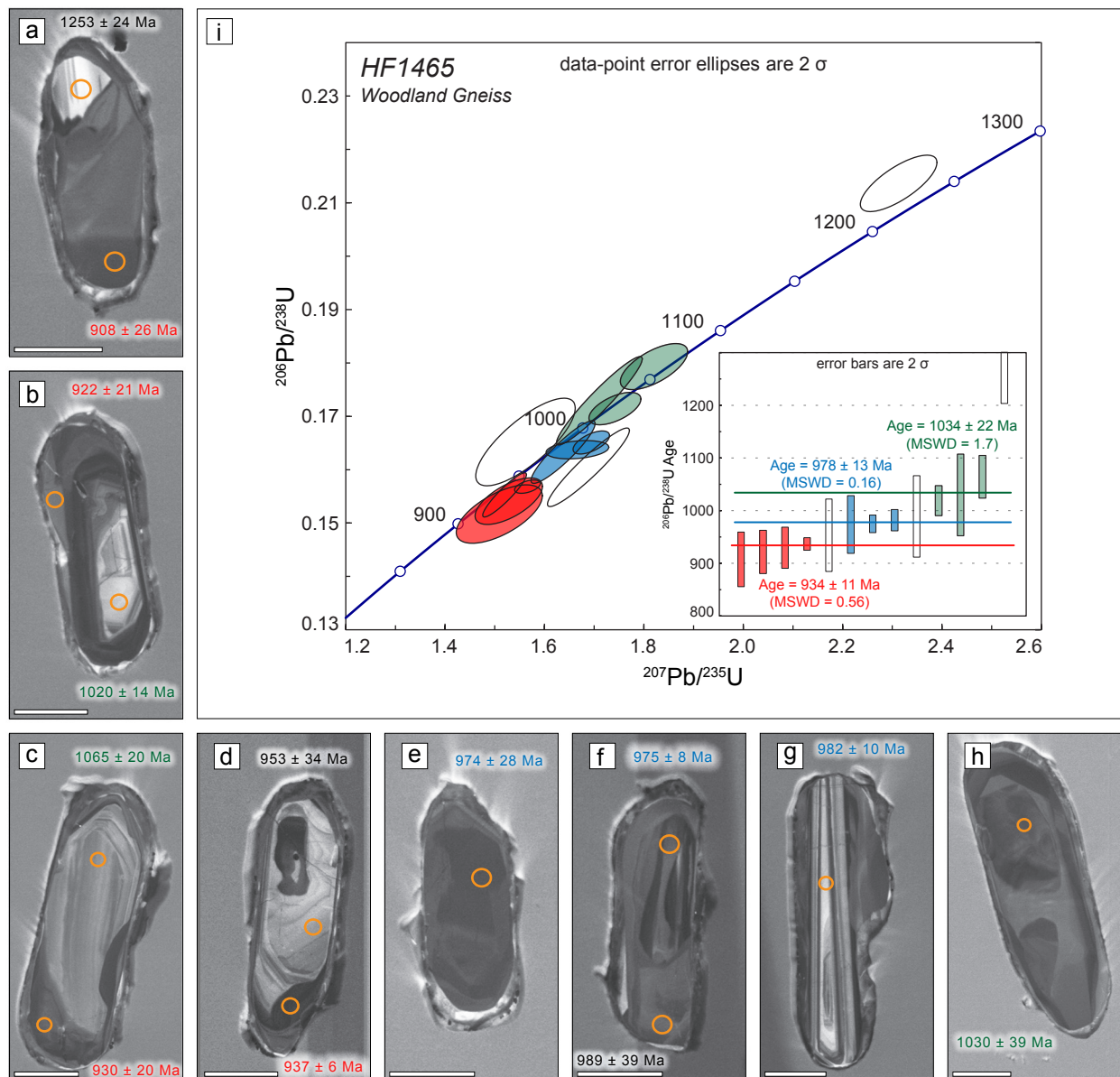


Figure 4-6. SHRIMP-RG analyses of sample HF1465 (Woodland Gneiss). White bar represents 100 μm . Orange ellipses are drawn to scale and represent spot analyses. (a-h) Cathodoluminescent images of analyzed zircons with spot analyses and $^{206}\text{Pb}/^{238}\text{U}$ dates. Colors correspond to interpreted age populations. (i) Concordia diagram with 2σ error ellipses and weighted average of analyses shown in the inset box. Filled ellipses and bars represent analyses that were used to calculate an age population. Green corresponds to analyses comprising the older population, while blue corresponds to analyses comprising middle population, and red corresponds to the youngest population.

material, were located within oscillatory zoned bright xenocrystic cores. A weighted average of $^{206}\text{Pb}/^{238}\text{U}$ dates with an MSWD of 1.7 yielded an age of 1034 ± 22 Ma. A younger population is defined by three analyses with slight to moderate positive discordance from 3–7 percent. A weighted average of $^{206}\text{Pb}/^{238}\text{U}$ dates with an MSWD of 0.16 yielded an age of 978 ± 13 Ma for this population. The youngest population identified in this sample is defined by four analyses with moderate positive discordance from 3–9 percent and focused on the dark unzoned portions of grains. A weighted average of $^{206}\text{Pb}/^{238}\text{U}$ dates with an MSWD of 0.56 yielded an age of 934 ± 11 Ma. The oldest date obtained from this sample was dismissed because of high negative discordance (-8% discordant) along with another analysis with a negative discordance of 12 percent, which accounts for the contradiction of having a younger core surrounded by older material (Fig. 4-6g). One analysis yielded a $^{206}\text{Pb}/^{238}\text{U}$ date of 953 ± 34 Ma with high positive discordance of 14 percent. This analysis was located well within a xenocrystic core and inferring any type of lead-loss history or mixing of temporally distinct zones would contribute no meaningful age.

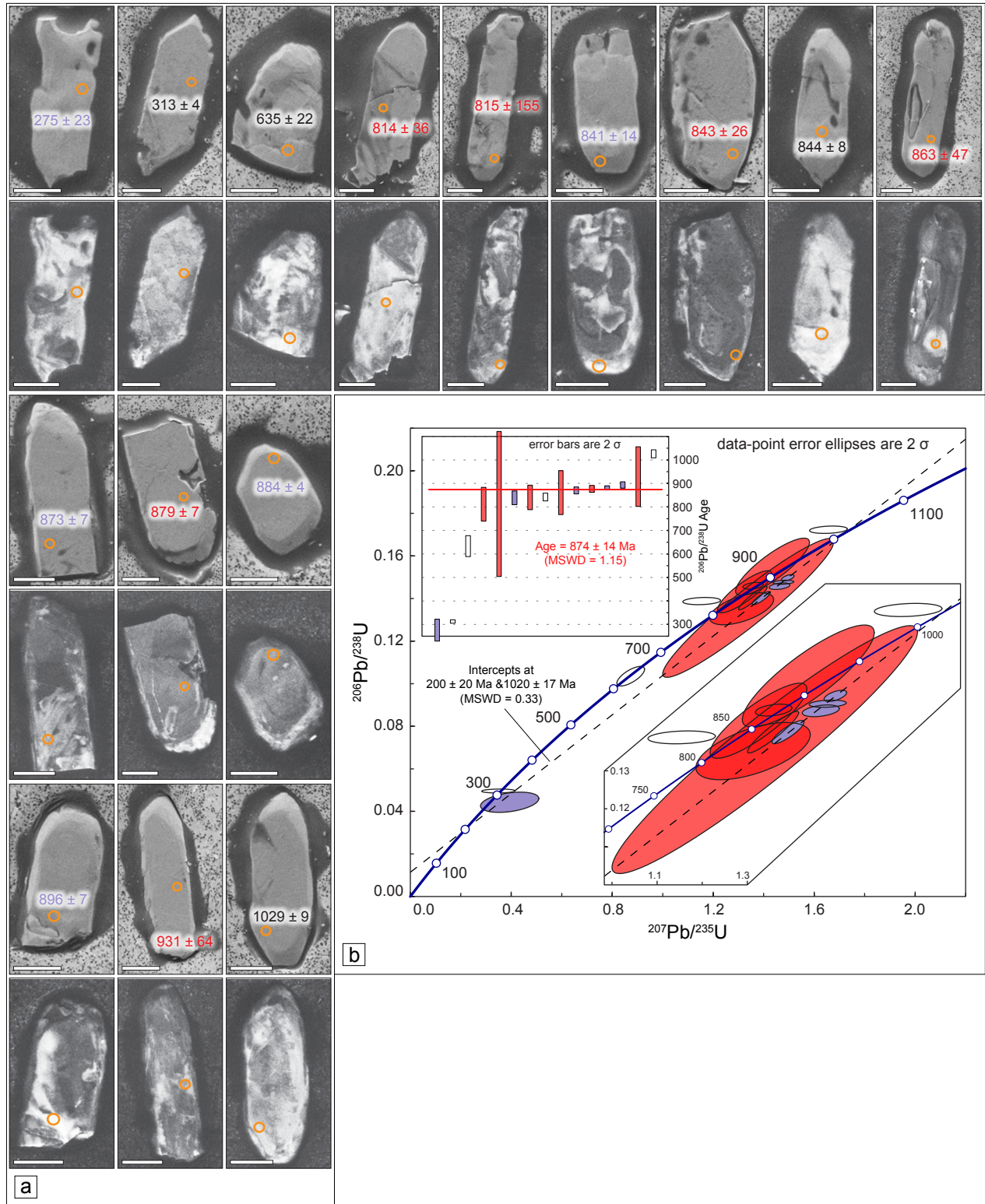
Samples of Woodland Gneiss (J182 and HF1465) were analyzed with the intent to infer the ages of significant metamorphic events by analyzing temporally distinct portions of grains that appeared to be crystallized by metamorphic, rather than magmatic, processes. Traditional mounting techniques, in which polishing exposes the interior portions of grains, revealed several distinct zones that could be targeted. One limitation of the traditional technique, however, is that while thin outer rims were observed in polished sections they could not be analyzed because of spatial restrictions imposed by the ~ 22 μm ion beam width (Fig. 4-2a). A beneficial attribute of the ion microprobe is that analyses can be conducted on very small volumes (~ 1 ng) of material (Gehrels, 2012), resulting in beam pits that are generally less than 1 μm deep that. That attribute, when coupled with the use of a unique indium metal mounting technique, afforded the ability to analyze the outermost rim surface and obtain dates that could be inferred to represent timing of the latest metamorphic event affecting these grains (Fig. 4-2b).

Sample J182 Indium

Fifteen spot analyses were obtained from 27 zircons mounted for sample J182 Indium (Fig. 4-7). Zircon morphology is generally consistent and exhibited an elongate form, with the exception of one that exhibits a more equidimensional shape. There is some variability among the shapes of

Figure 4-7. SHRIMP-RG analyses of sample J182 (Woodland Gneiss) mounted using the indium metal technique. White bar represents 100 μm . Orange ellipses are drawn to scale and represent spot analyses. (a) Cathodoluminescent and secondary electron images of analyzed zircons with spot analyses and $^{206}\text{Pb}/^{238}\text{U}$ dates. Colors correspond with interpreted age populations. (b) Concordia diagram with 2σ error ellipses and weighted average of analyses shown in the inset box. Filled ellipses and bars represent analyses that were used to calculate an age population. Red corresponds to analyses that were used to calculate an age population, and lavender corresponds to discordant analyses used to infer a concordia intercept age. Lavender ellipses and dashed line indicate the lead-loss trajectory and chord used to define the upper intercept age.

J182 Indium Woodland Gneiss



ends of grains; the majority of grains exhibit more rounded ends, some zircons exhibit doubly terminating ends, and a few zircons exhibit abrupt flat ends, which appear to have resulted from fracturing of the grain. CL images of zircons revealed both light and dark regions on the surfaces of the grains, which is probably representative of the somewhat discontinuous outer rims observed in sectioned grains (Fig. 4-7a). Analyses targeted the more brightly luminescent regions because of the likelihood of greater uranium concentrations, which should serve to increase instrumental precision. Sample J182 indium yielded a robust age population of 874 ± 14 Ma interpreted from a weighted average of a coherent group of six $^{206}\text{Pb}/^{238}\text{U}$ dates with an MSWD of 1.15 (Fig. 4-7b). Discordance among this group was generally moderate, with few exceptions of both high positive and negative discordance. High positive discordance of analyses yielding $^{206}\text{Pb}/^{238}\text{U}$ dates of 815 ± 155 Ma and 814 ± 36 Ma (+17% and +14% discordance, respectively) were included in the average because the large error associated with their respective $^{207}\text{Pb}/^{206}\text{Pb}$ dates precluded the usefulness of $^{207}\text{Pb}/^{206}\text{Pb}$ dates in providing more accurate ages. Including these analyses increased the robustness of the interpreted age of the population while having little effect on the numerical value of that age and only increasing the MSWD from a value of 0.88, therefore providing little purpose to exclude them. Five other analyses that displayed very high positive discordance, ranging from 10-64 percent, were used to calculate a lead-loss trajectory resulting in a five-point isochron with concordia intercept ages at 200 ± 20 Ma and 1020 ± 17 Ma, and an MSWD of 0.33. A five-point isochron with a “good fit” lead-loss trajectory, as exhibited by this sample, should provide a very reliable upper intercept age; however, it is still based on the assumption that the discordance exhibited by these analyses were due to a perturbation of the U-Pb system and not a mixing of temporally distinct zones. Given the potential risk for this type of analysis to drill through a thin outer rim and incorporate some material from an older zone beneath (e.g., Fig. 4-2b), the upper intercept age should be used with some caution. Close monitoring for abrupt changes in uranium and thorium concentrations during each scan of the analysis helped mitigate the risk of drilling through the outer rim, and analyses that showed such abrupt changes were discarded.

Sample HF1465 Indium

Twelve zircons were analyzed from the 28 grains mounted for sample HF1465 indium yielding 13 spot analyses (Fig. 4-8). Zircon morphology was similar to that of sample J182 indium,

and similar contrasts between light and dark CL zones were also observed. Both light and dark luminescent zones were targeted for spot analysis of this sample, which yielded two distinct age populations (Fig. 4-2a). A cluster of five analyses composed an older population comprising $^{206}\text{Pb}/^{238}\text{U}$ dates ranging from 945 ± 5 Ma to 927 ± 20 Ma with four moderately discordant (-4% to +7% discordance) analyses and one very concordant (+1% discordance) analysis. A weighted average of these dates yielded an age of 942 ± 8 Ma with an MSWD of 0.48 (Fig. 4-2b). These older analyses targeted darker areas of zircon grain surfaces. A cluster of four analyses defined a younger age population with $^{206}\text{Pb}/^{238}\text{U}$ dates ranging from 877 ± 24 Ma to 841 ± 19 Ma exhibiting moderate (+4–10 %) discordance. The younger analyses are from a combination of spots targeting both light and darker zones. Three analyses from this sample were excluded based on high positive discordance, none of which appeared to define any distinguishable lead-loss trajectory nor provided meaningful $^{207}\text{Pb}/^{206}\text{Pb}$ dates. One analysis yielded a $^{206}\text{Pb}/^{238}\text{U}$ date of 928 ± 20 Ma that fit, within error, among both age populations and, as it could not be confidently distinguished from one or the other, was excluded from both. Analyses were again monitored for abrupt changes in elemental concentrations and analyses that exhibited such changes were discarded.

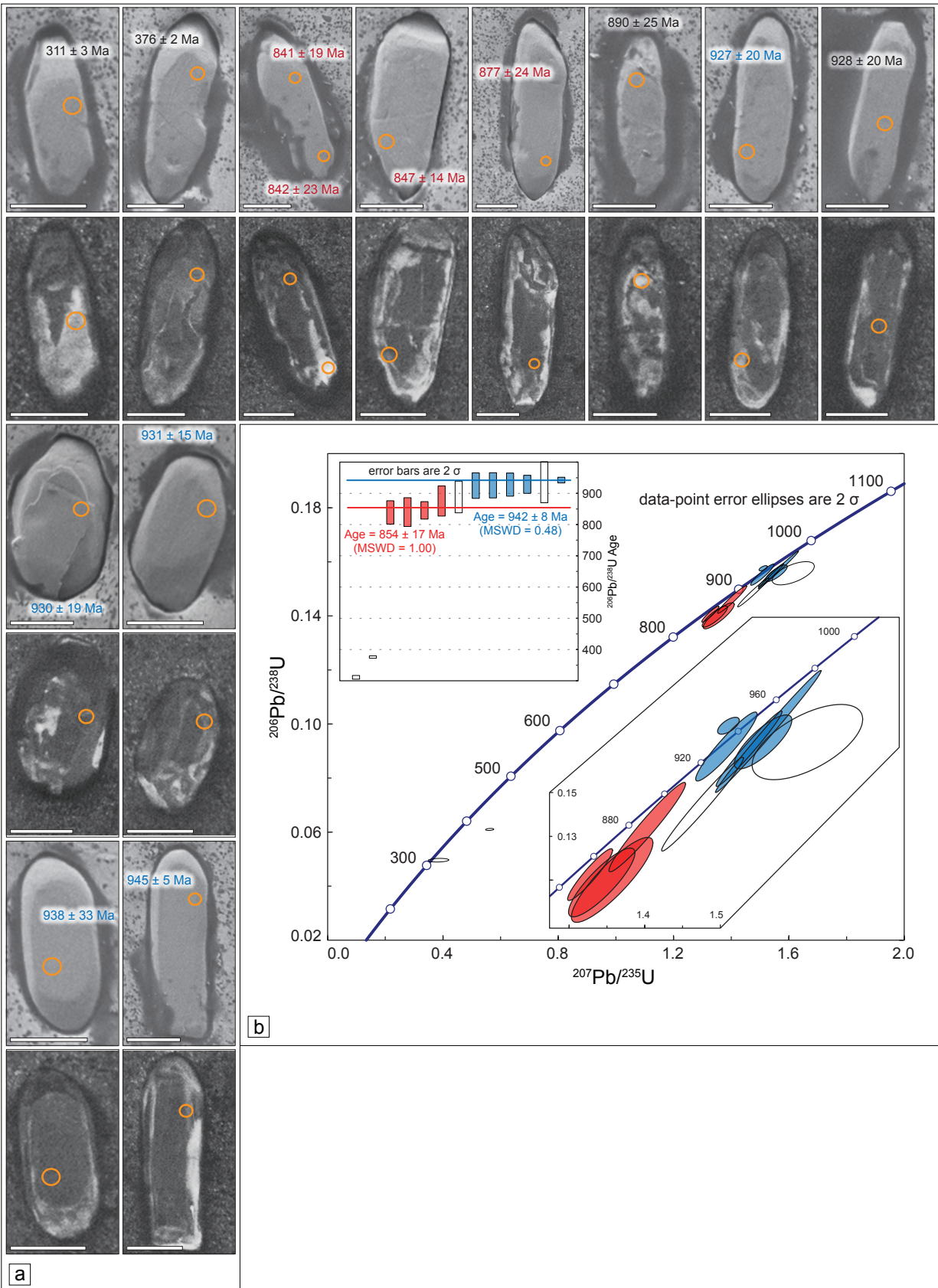
LA-ICPMS analyses

Sample OH032

Zircons from the detrital sample OH032 (biotite gneiss) exhibited highly variably morphology (Fig. 4-9a). Nearly all grains showed evidence of abrasion and transport by exhibiting high degrees of rounding, fracturing of grains, and truncation of zoning patterns. Interior portions of some grains contain obvious fractured pieces of once larger grains, which also exhibit post-fracturing rounding and abrasion. Few grains retain an elongate morphology but at a minimum still exhibit evidence of abrasion and truncation of zoning patterns at their ends. Zircons from this sample also exhibit highly variable zoning patterns. Nearly all exhibit some secondary crystallization of homogenous unzoned material around the rims of grains that was interpreted to represent metamorphic recrystallization. Interior portions of grains exhibit fractured portions of once larger grains, indicated by the truncation of zoning patterns, which vary from banded patterns, likely from the sides parallel to the long axis of a once larger zircon, to oscillatory-zoned doubly terminating ends. Some fractured interior portions of grains contain truncated oscillatory-zoned

Figure 4-8. SHRIMP-RG analyses of sample HF1465 (Woodland Gneiss) mounted using the indium metal technique. White bar represents 100 μm . Orange ellipses are drawn to scale and represent spot analyses. (a) Cathodoluminescent and secondary electron images of analyzed zircons with spot analyses and $^{206}\text{Pb}/^{238}\text{U}$ dates. Colors correspond with interpreted age populations. (b) Concordia diagram with 2σ error ellipses and weighted average of analyses shown in the inset box. Filled ellipses and bars represent analyses that were used to calculate an age population. Blue corresponds to analyses comprising the older population, while red corresponds to analyses constituting the younger population.

HF1465 Indium Woodland Gneiss



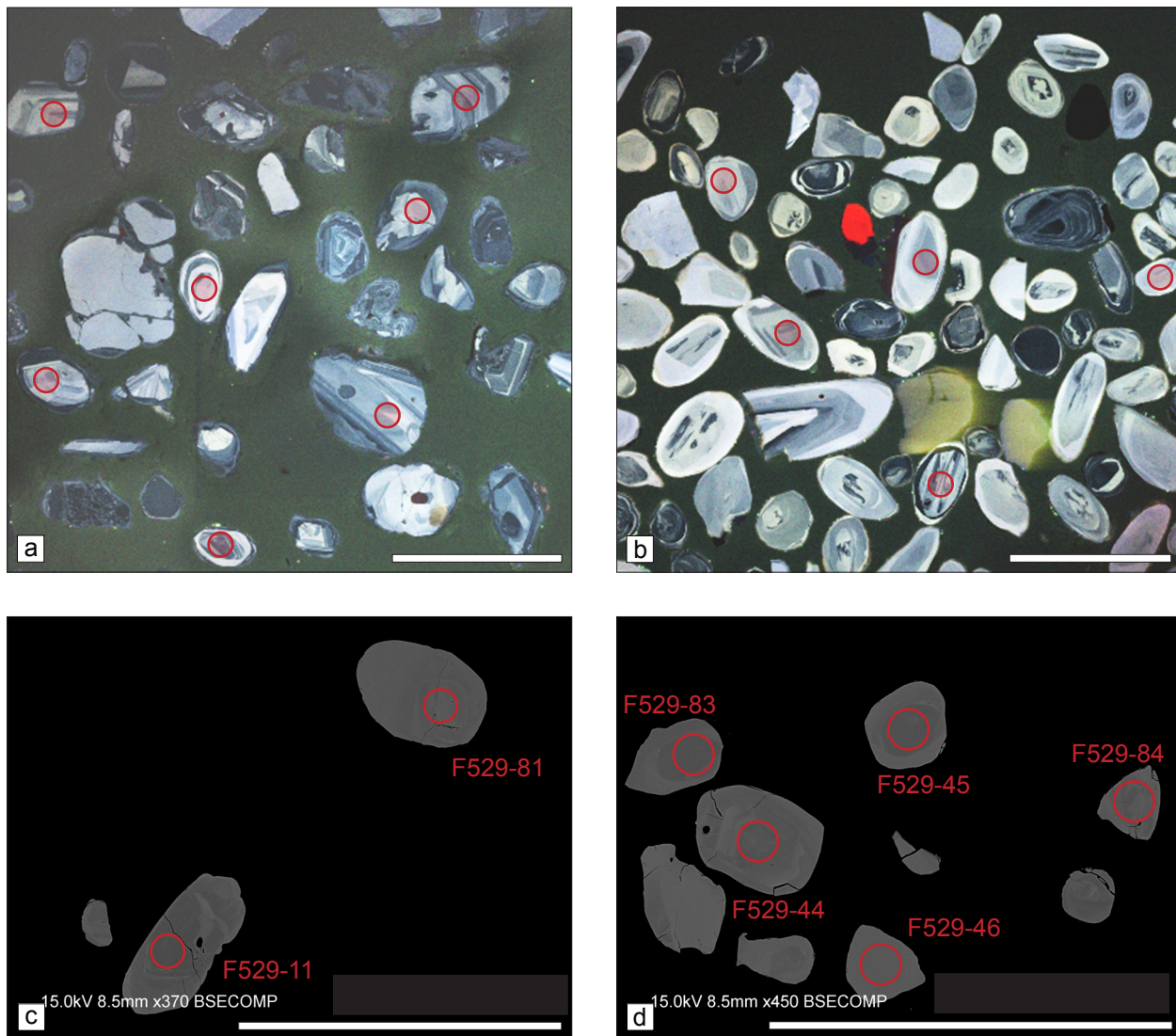


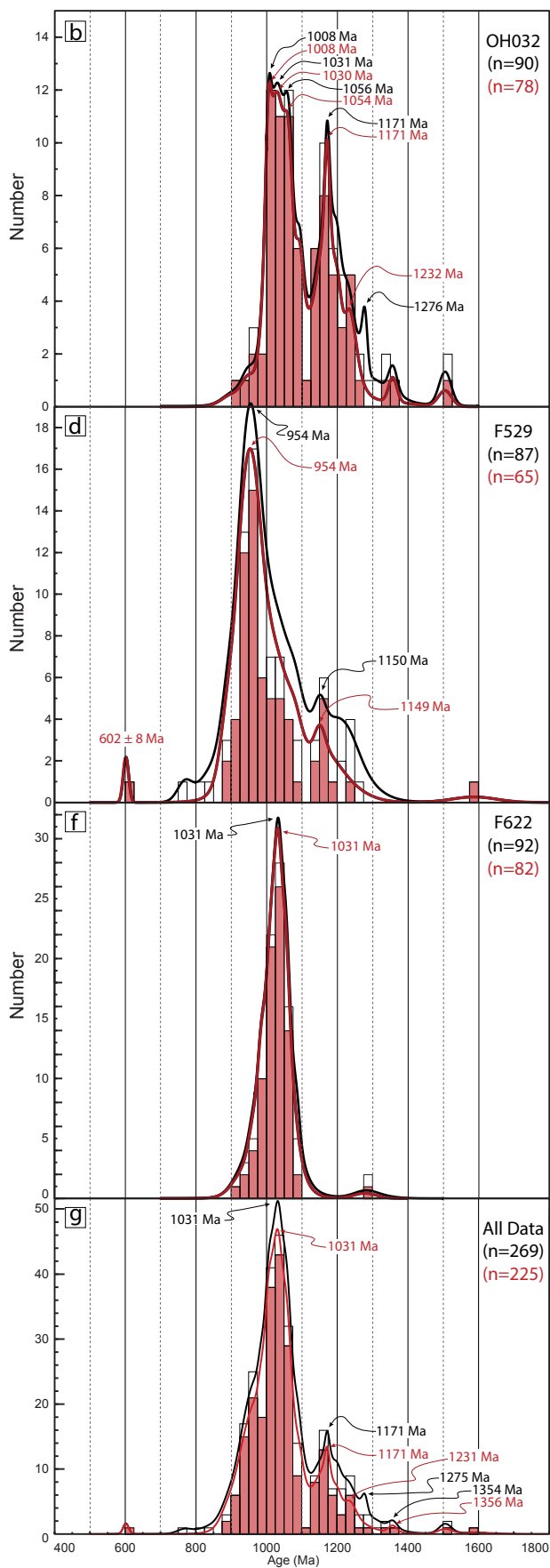
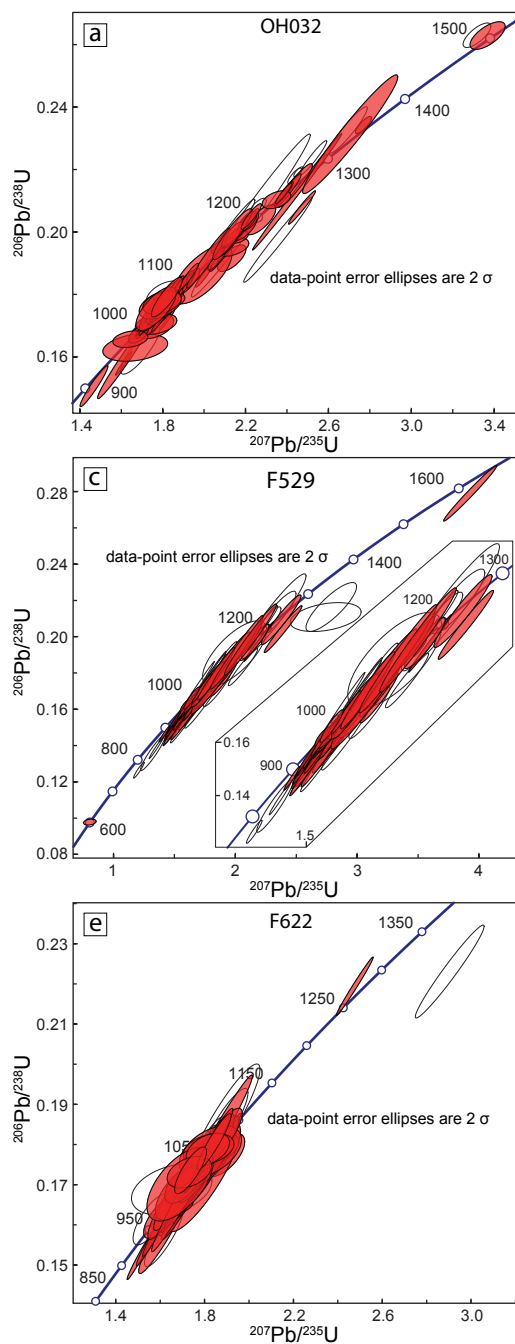
Figure 4-9. Representative zircons from detrital (biotite gneiss) samples analyzed via LA-ICPMS. White bar represents 200 μm . Red circles are drawn to scale and represent spot analyses. (a-b) Color cathodoluminescent images. (a) Representative zircons from detrital sample OH032. (b) Representative zircons from detrital sample F622. (c-d) Backscattered electron images of representative zircons from sample F529. Spot analysis F529-11 is the youngest detrital zircon analyzed from this study.

and embayed xenocrystic cores within themselves, indicating the source from which those zircons were derived likely contained some inheritance. Few grains exhibit convoluted zoning patterns in areas, which in some instances crosscuts oscillatory-zoned interior portions in thin bands. Minor amounts of larger (~200- μm diameter) anhedral grains exhibited no zoning patterns and are mostly homogenous and fractured, with darker homogenous material often filling spaces between fractures and surrounding the grain. Of the abundance of zircons mounted, 100 spot analyses were made, from which ten were discarded during data reduction processing performed by Arizona LaserChron Center personnel. Analyses plotted on a concordia diagram (Fig. 4-10a) indicate the relatively high concordance and small error of most analyses, with few exceptions. Twelve analyses were identified for exclusion through application of a discordance filter. Relative age probability density plots of $^{206}\text{Pb}/^{238}\text{U}$ ages (Fig. 4-10b) revealed a series of peaks between a range of 1412 Ma and 899 Ma for all analyses, and between 1381 Ma and 911 Ma for analyses remaining after application of the discordance filter. For post-filtered analyses, peak ages are reported as 1357, 1232, 1171, 1054, 1030, and 1008 Ma. One small peak does occur at ~1500 Ma, which is not considered a robust age because only two analyses contribute to its probability, one of which was filtered for discordance. The age significance of this peak should be interpreted with much caution. The range of peak ages representative of this sample denotes the potential for both Laurentian and non-Laurentian sources, namely Grenville massifs, the Granite-rhyolite province, and various Amazonian components. The largest peak is formed by an amalgamation of three smaller sub-peaks in the range of 1056–1008 Ma, likely representing material sourced from Grenville massifs. Material bearing geochronologic signatures of these sources could also merely have been recycled from western and central Blue Ridge terranes, as suggested by Mersch et al. (2010), and not sourced directly. The youngest statistically viable age peak is 1008 Ma, which provides a constraint on the maximum depositional age for this sample. Most notable, for the purposes of this study, is the obvious absence of any peri-Gondwanan signature, which is a major diagnostic feature, used to distinguish rocks of the Cat Square terrane.

Sample F529

Detrital sample F529 (biotite gneiss) contained large amounts of aluminosilicate minerals, which after mounting precluded the use of CL imaging and required the use of backscattered

Figure 4-10. Detrital (biotite gneiss) zircon analyses. (a-b) Detrital sample OH032. (a) Concordia diagram with 2σ error ellipses. (b) Relative $^{206}\text{Pb}/^{238}\text{U}$ age probability density plot. (c-d) Detrital sample F529. (c) Concordia diagram with 2σ error ellipses. (d) Relative $^{206}\text{Pb}/^{238}\text{U}$ age probability density plot. (e-f) Detrital sample F622. (e) Concordia diagram with 2σ error ellipses. (f) Relative $^{206}\text{Pb}/^{238}\text{U}$ age probability density plot. (g) Relative $^{206}\text{Pb}/^{238}\text{U}$ age probability density plot of the combined dataset. Red filled ellipses and bars represent analyses concordant within the applied filter. Hollow ellipses and bars represent all analyses including those identified as discordant. Red relative age probability curve represents only concordant analyses. Black relative age probability curve represents all analyses including those identified as discordant. Peak ages are identified by arrows and corresponding age.



electron imaging techniques (Fig. 4-9c-d). Zircons from this sample exhibit generally similar morphologies consisting of very rounded equidimensional grains, with few grains exhibiting an elongate shape but still retaining rounded edges. Internal growth-zoning patterns of zircons from this sample were not as readily distinguished due to the imaging technique used, although cores were mostly identifiable. Spot analyses were aimed at the interior portions of grains and at internal cores where they could be identified. Of the 100 analyses performed, 13 were removed during data reduction procedures, performed by Arizona LaserChron personnel. An additional 22 were identified for exclusion through the use of a discordance filter. Analyses plotted on a concordia diagram (Fig. 4-10c) demonstrate the minor abundance of discordant analyses and the difference in error associated with different isotopic dates of the same analysis. The prolate error ellipses representing sample F529 are indicative of the difference in error between $^{206}\text{Pb}/^{238}\text{U}$, $^{207}\text{Pb}/^{235}\text{U}$, and $^{206}\text{Pb}/^{207}\text{Pb}$ dates. Here the error associated with the $^{206}\text{Pb}/^{207}\text{Pb}$ dates is considerably less than the other two; however, the $^{206}\text{Pb}/^{238}\text{U}$ dates are still preferred because of the greater accuracy of these dates for zircons crystallized < 1500 Ma (Nemchin and Cawood, 2005; Gehrels, 2012). Relative age probability density plots of $^{206}\text{Pb}/^{238}\text{U}$ ages (Fig. 4-10d) indicate one major peak, one minor peak, and three very low-probability peaks. Peaks occur in a range of 1351–781 Ma for all analyses and between 1312–822 Ma after filtering for discordance. Differences between assigned ages of the peaks were almost nonexistent between peaks of filtered and non-filtered analyses. The minor peak has an assigned age of 1149 Ma with 14 contributing analyses. The major peak has an assigned age of 954 Ma from 47 contributing analyses and is the youngest statistically viable age, placing a constraint on the maximum depositional age of this sample. Both of these ages suggest sources from Grenville massifs or recycling of Blue Ridge terranes. The three low-probability peaks occur at 2124 ± 90 Ma (+20% discordant), 1587 ± 63 Ma (+4% discordant), and 602 ± 8 Ma (-1% discordant), and are composed of one analysis each. The oldest of these analyses would represent a central Amazonian affinity, but is highly discordant and exhibits a large associated error. The second oldest of these analyses is only moderately discordant but still carries a significantly high associated error. It would represent an affinity with the Laurentian Granite-rhyolite province or possibly an Amazonian component. The most intriguing analysis is the youngest analysis from sample F529, which is very concordant, has a very small associated error, and likely represents a peri-Gondwanan affinity. Although the age peak associated with this analysis is not statistically robust, it is

considered to be analytically precise and accurate, and could potentially be used to constrain the maximum depositional age of the Cat Square basin in central Georgia.

Sample F622

Zircons from detrital sample F622 (biotite gneiss) exhibit slight variations in morphology and size (Fig. 4-9b). A seemingly equal proportion of grains are mostly equidimensional to slightly elongate with moderately rounded surfaces. Few angular grains are present in the sample, which could have been fractured during sample processing. Grains vary in size from 50–100 μm in diameter for equidimensional grains, and from 75–200 μm long for elongate grains. Internal zoning patterns are also highly variable and exhibit oscillatory-zoned and banded patterns in most grains. Some grains exhibit convoluted zoning or sector zoning patterns, while nearly all grains exhibit a thick homogenous outer rim that luminesces brightly. Few grains exhibit homogenous unzoned interior portions as well. Of the 101 spot analyses for sample F622, eight were discarded during data reduction procedures and an additional ten were identified for exclusion through discordance filtering. Data plotted on a concordia diagram (Fig. 4-10e) demonstrate the high concordance and relatively small error of the majority of analyses. Relative age probability density diagrams of $^{206}\text{Pb}/^{238}\text{U}$ ages (Fig. 4-10f) display one prominent peak in a range from 1176–858 Ma, including all analyses, and from 1176–858 Ma for analyses filtered for discordance. An age of 1031 Ma was calculated from 67 contributing analyses for the only statistically viable peak observed from sample F622. One minor peak is present at ~ 1290 Ma, established by one concordant and one discordant analysis. The prominent 1031 Ma peak suggests a strong Laurentian (i.e., Grenville) affinity for this sample, while the older peak indicates the potential for either a Granite-rhyolite or Amazonian affinity.

A combined data set, composed of the aforementioned detrital samples (OH032, F529, F622), yielded four prominent age peaks, after discordance filtering, within a range of 1381–822 Ma. The most prominent peak occurs at 1031 Ma, and is comprised of 126 contributing analyses. It is the youngest statistically viable peak for the combined dataset, which would impose a Grenvillian constraint on the maximum depositional age of the Cat Square basin in this part of central Georgia.

Summary and discussion

Samples of the Woodland Gneiss yielded zircons with highly variable external morphology and internal zoning patterns. Analyses of these samples yielded several age populations ranging from 1048–854 Ma. The older populations of 1048 ± 48 Ma and 1034 ± 22 Ma from both samples were obtained from analyses of inherited xenocrystic cores that likely represent initial crystallization of the Woodland Gneiss protolith. These ages agree within error to the 1011 ± 12 Ma age assigned to the Woodland Gneiss by Heatherington et al. (2006). Several younger age populations occurring at 985 ± 30 Ma, 978 ± 13 Ma, 942 ± 8 Ma, and 934 ± 11 Ma were obtained from analyses of homogenous unzoned material surrounding xenocrystic cores. These populations postdate the accepted termination (~ 980 Ma) of the final, Rigolet phase of the Grenville orogeny (Rivers, 1997; Hynes and Rivers, 2010; Aleinikoff et al., 2013), but still could represent its waning stages. The youngest two age populations of 874 ± 14 Ma and 854 ± 17 Ma were obtained from the thin outermost rim of zircons and are interpreted by the author to represent the latest significant metamorphic event that affected these grains. They record an event that is much younger than the terminal phases of the Grenville orogeny and much older than the recorded breakup of the Rodinia supercontinent at ~ 750 Ma (Hatcher, 2010). This suggests that either the waning stages of the Grenville orogeny lasted until well into the Neoproterozoic, or that the breakup of Rodinia occurred ~ 100 Ma earlier than previously accepted. Graybill et al. (2012) proposed that Rodinia breakup started as early as ~ 960 Ma, and if that rifting event produced high temperature metamorphic conditions then it could account for some of the post ~ 980 Ma populations identified in the Woodland Gneiss. The younger 874–854 Ma populations could have implications for the hypothesis proposed by Huebner (2013) regarding the emplacement of the Pine Mountain terrane, which suggests the terrane originated as a micro-continent rifted from the Laurentian margin during Cambrian time. If that event again produced conditions suitable to recrystallizing zircon, then the younger populations could mark the departure of the Pine Mountain terrane from the Laurentian margin; although, that suggestion contradicts the Cambrian age constrain placed on the departure of the terrane based on correlation of sedimentary cover sequences (Huebner, 2013).

A crystallization age of 1011 ± 10 Ma was determined for the hornblende tonalite stock that is located with a klippe of Cat Square terrane biotite gneiss. This age is younger than, but within error of, the inferred crystallization age of the Woodland Gneiss that likely encloses the tonalite

body beneath over-thrust Cat Square terrane rocks. This indicates that the tonalite is intrusive into, or is in fault contact with the Woodland Gneiss. The inferred upper constraint of 1031 Ma on the depositional age for metasedimentary units interpreted to be thrust over the tonalite and surrounding Woodland Gneiss, does not preclude the possibility that the tonalite is intrusive into them as well, although there is an absence of more supporting evidence.

A crystallization age of 1158 ± 18 Ma was interpreted for felsic gneisses that occur as small enclaves within the Woodland Gneiss and Cat Square terrane biotite gneiss at the northeastern end of the Pine Mountain window. This age confirms the hypothesis that the felsic gneisses are xenoliths within the Woodland Gneiss (Huebner et al., 2013) and agrees, within error, with a reported age of 1136 ± 13 Ma determined from another Woodland Gneiss xenolith (Heatherington et al., 2006). A younger age population of 1014 ± 12 Ma was also identified from analyses of dark homogenous unzoned material surrounding xenocrystic cores, which is similar in age to the tonalite stock and crystallization of the Woodland Gneiss protolith. The younger age represents portions of grains that exhibit textures interpreted by this author to be indicative of growth that occurred subsequent to magmatic crystallization of the sample protolith. An alternate interpretation is that the xenocrystic cores were inherited from an older source and that the younger enclosing zircon material represents primary crystallization that happened to not form typical oscillatory zoning patterns. This interpretation would suggest that the 1014 ± 12 Ma age represents the crystallization age of sample IS632, which is the age reported by Huebner et al. (2014).

Three samples of biotite gneiss collected from different locations at southwestern end of the Cat Square terrane were analyzed to interpret their detrital provenance. Although the youngest single zircon analyzed yielded a very concordant age of 602 ± 8 Ma, the youngest statistically viable age peak, obtained from sample F622, occurs at 858 Ma. The older age puts a constraint on the maximum depositional age of one sample, however, after combining datasets from all three samples the youngest statistically viable peak occurred at 1031 Ma, which provides an upper limit on the depositional age of the southwestern end of the Cat Square basin in central Georgia. This limit only provides a maximum constraint and does not necessarily refute the younger interpreted age of the Cat Square basin proposed by other authors (e.g., Merschat and Hatcher, 2007, Huebner et al., in review).

Chapter 5

Structural analysis of the Inner Piedmont and Pine Mountain window at the southwestern end of the Cat Square terrane

Introduction

A vast pool of knowledge regarding the structure of the Inner Piedmont and Pine Mountain window has been assembled from geologic mapping and structural analysis by several geologists (e.g., Clarke, 1952; Griffin, 1971, 1972, 1978; Sears et al., 1981; Hopson and Hatcher, 1988; Higgins et al., 1988; Hooper and Hatcher, 1988a; Merschat et al., 2005; Huebner et al., 2014), which increases by the compilation of data from new and ongoing field and laboratory research. A new 1:50,000-scale map of the Inner Piedmont and Carolina superterrane at the northeast end of the Pine Mountain window by Huebner et al. (2014), compiled the work of 12 geologists spanning 3.5 decades. Geologic mapping was augmented by modern petrologic and geochronologic data, and contributes to the advancement of understanding of the complex structure of this area. Interpretations of these structural data have also been evolving, and inferences made about the structure of the Inner Piedmont in central Georgia are made here to weigh hypotheses previously formulated by geologists working in the northern portions of the Inner Piedmont (e.g., Merschat et al., 2008; Merschat, 2009). Interpretations of the Pine Mountain window have also advanced and are obvious when early cross sections (Fig. 5-1) are compared with more recent ones through the region (Fig. 5-2). Clarke (1952) was the first to suggest that rocks of the “Wacoochee belt” were exposed in a window and inferred a simple erosional hole in an overriding thrust sheet. Interpretations of the structure of the window have advanced to include a complex window framed by faults of different rheologies and timing (Hooper and Hatcher, 1988a; Steltenpohl et al., 2010) (Fig. 1-2; Fig. 5-2) and a new hypothesis suggesting the Pine Mountain terrane is a micro-continent rifted from the Laurentian margin following breakup of Rodinia and transported several hundred kilometers southwestward to its present position during the Acadian/Neocadian and Alleghanian orogenies (Huebner, 2013). Regardless of interpretations made, the first step in any structural analysis has been, and should remain, the accurate collection of field data .

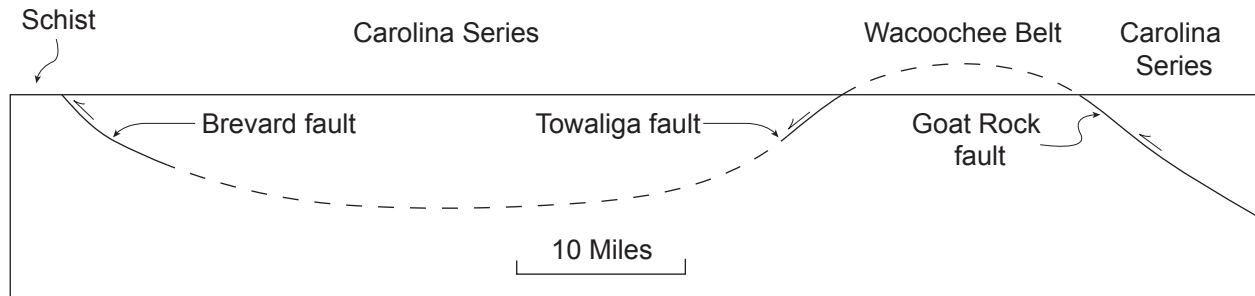


Figure 5-1. Early figure depicting the structure of the Pine Mountain window and surrounding terranes. The figure depicts the Goat Rock, Towaliga, and Brevard faults as being the same fault. The Carolina Series is equivalent to the Carolina superterrane, the Wacoochee Belt is equivalent to the Pine Mountain terrane, and the Carolina Series west of the Towaliga fault along with the Brevard Schist are equivalent to the composite Inner Piedmont. Figure is redrawn from Clarke (1952), his figure 24.

Structural observations

Observation and measurement of mesoscale structural features were made in the field and facilitated construction of a detailed geologic map of the Barnesville, Johnstonville, and part of the Orchard Hill quadrangles (Plate I). Data were recorded in a National Cooperative Geologic Mapping Program (NCGMP)-compliant database, constructed by A.L. Wunderlich, using a Trimble GeoXT 2005 series differential GPS unit operating ESRI ArcPad software. No post-processing differential corrections of location data were needed; the averaging feature of the GPS unit was utilized at the time of collection and produced sub-meter accuracy for these data. Measurements of mesoscale structures were made using standard methods and a Brunton compass. All measurements were recorded using geographic notation (0–360°) for orientation, and obeying the right-hand-rule, so that dip direction was always recorded 90 degrees clockwise from the strike direction. The direction of plunge of linear features was always recorded in the direction of the trend. These measurements are limited in accuracy and reproducibility by the amount of error inherent in the compass being used to measure them, and the ability of the geologist using it. Data were downloaded and plotted using ESRI ArcMap 10.1 software, which was also used to draft the initial geologic map.

A form-line map contouring data points of similar strike was constructed for the study area (Fig. 5-4; Plate III) and proved useful in both identifying homogeneous structural domains, and interpreting structural data represented in cross sections. Several distinct structural domains were identified and data from each was plotted separately using graphical methods.

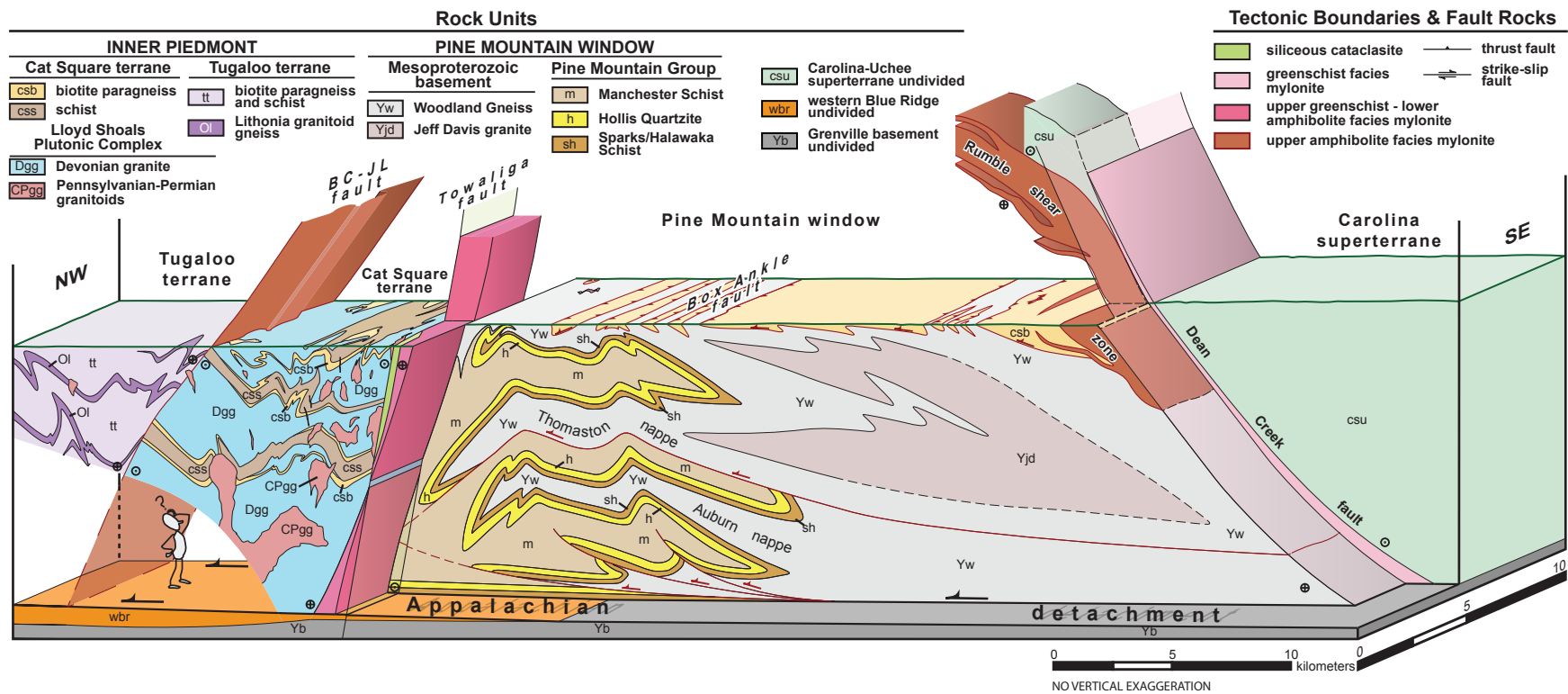


Figure 5-2. Cross section and 3-dimensional block model of the Inner Piedmont, Pine Mountain terrane, and Carolina superterrane at the northeast end of the Pine Mountain window. Imbricate stacking of thrust nappes and deep structure of the Pine Mountain terrane adapted from Sears and Cook (1984). BC-JL—Brindle Creek-Jackson Lake. Figure adopted from Huebner, 2013.

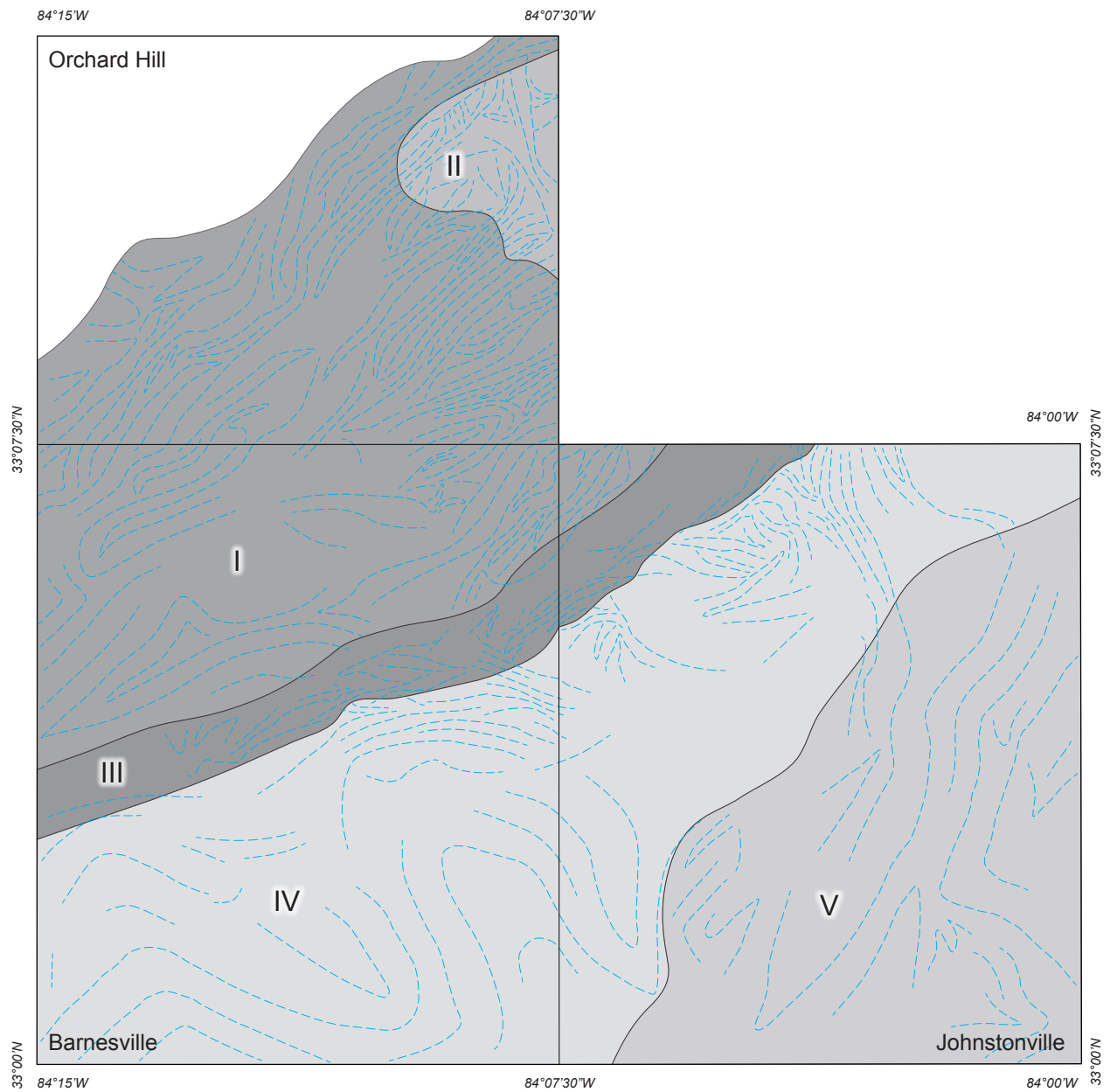


Figure 5-3. Form-line map of homogeneous structural domains of S_2 . Discrete structural domains are indicated by shading and roman numerals. Form lines indicated by dashed blue lines.

Equal-area stereonet projections were constructed to graphically display structural data (Fig. 5-5, 5-6). Diagrams were created using Stereonet 9 (copyright © Richard W. Allmendinger, 2014) and algorithms used therein (Allmendinger et al., 2013; Cardozo and Allmendinger, 2013). All data were plotted on a lower hemisphere equal-area projection. Poles to planes were calculated using Stereonet© and plotted as points. Where appropriate either a cylindrical best-fit line (great circle) and β point or conical best-fit line (small circle) and axis were calculated for poles to foliation planes. Statistically viable populations of point data from poles to planes of foliation and mineral lineations were contoured using the Kamb method (Kamb, 1959) at a 2-sigma contour interval. This method permits graphical analysis of the statistical significance of clusters of points and is therefore useful in eliminating the influence of data outliers. The Kamb method is most effective for large datasets and those with values below the 100-point “rule of thumb” (Hatcher, personal communication) were contoured as a percentage of the total number of points per 1 percent area of the stereonet. Plotted fold axes and axial surfaces are from direct measurements in the field and were not calculated.

Planar and Linear fabrics

Structural development of the Inner Piedmont and Pine Mountain window is very complex in that both were multiply deformed with a dominant regional foliation (S_2) and associated mineral stretching lineation (L_2) that formed close to peak metamorphic conditions (upper amphibolite-facies) (Huebner et al., 2014). No less than six deformational events are recorded by Inner Piedmont rocks in North and South Carolina (Mersch et al., 2005), several of which, along with the associated generation of fabrics, are readily identifiable within the study area. Original sedimentary features were likely obliterated during deformation and accompanying high temperature metamorphism, although features that could be interpreted to represent bedding (S_0) do exist. Lithologic contacts between metasedimentary rocks throughout Cat Square terrane rocks, along with gradational contacts in the Hollis Quartzite are often subparallel to S_2 foliation and are here inferred to represent transposed original sedimentary features. A fabric locally contained within amphibolite boudins (S_1) is commonly observed in the Inner Piedmont enveloped by regional S_2 foliation (Mersch et al., 2005; Davis, 2010; Huebner et al., 2014), but this relationship was not directly observed in amphibolites mapped during this study. A weak foliation (S_3) defined by

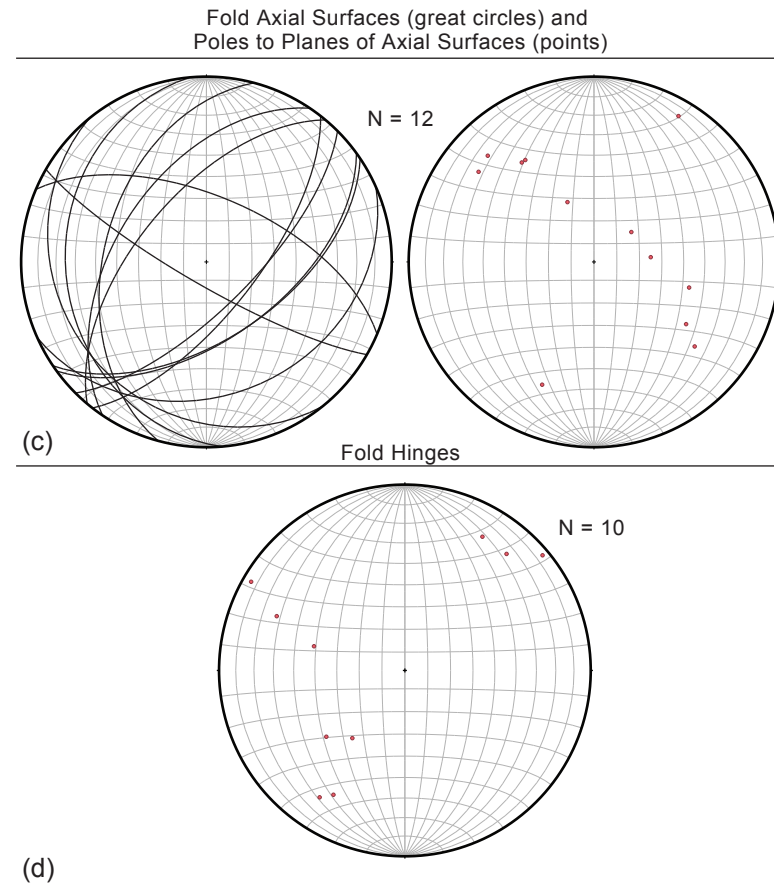
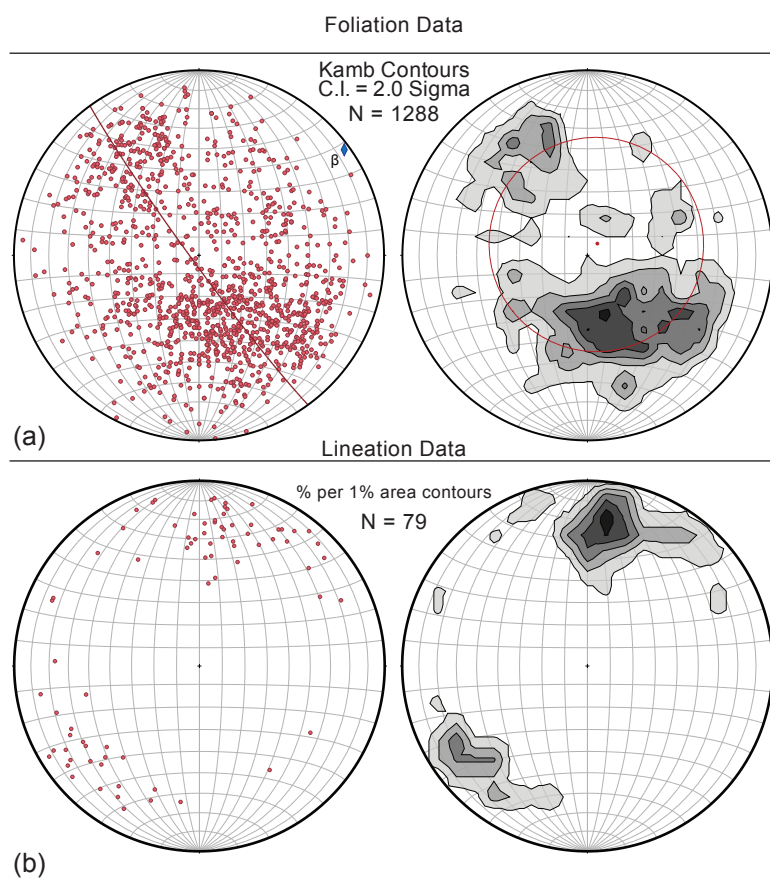
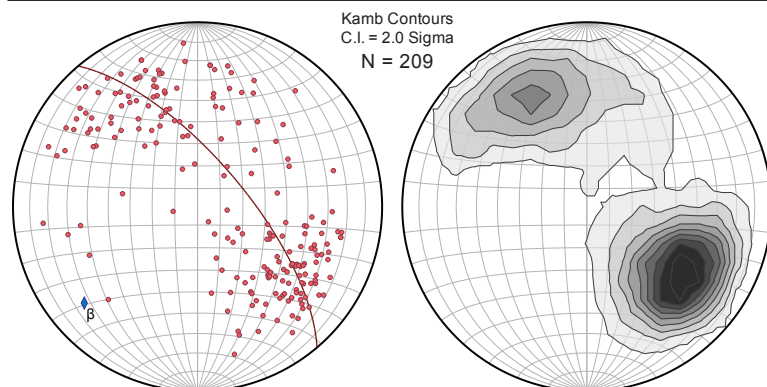


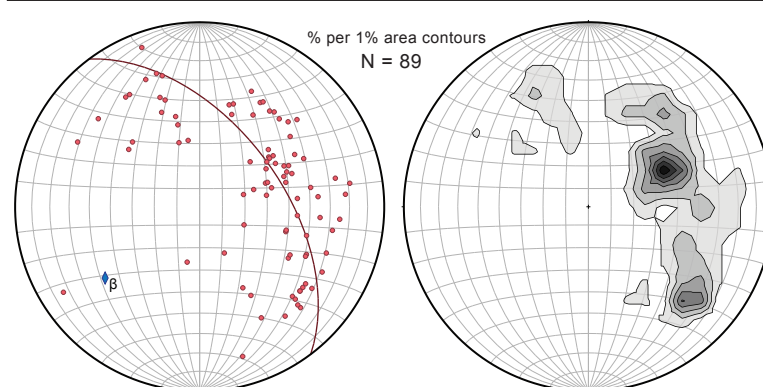
Figure 5-4. Stereonet plots of all fabric data. Compiled foliation data are plotted in one stereonet. (a) Poles to foliation planes are symbolized by red points. A best-fit great circle is plotted among the points, with a corresponding β point, symbolized by a blue diamond. Poles to foliation planes are contoured using the Kamb method and plotted on a separate stereogram with associated best-fit small circle. (b) Lineation data are symbolized by red points and contoured by measuring the percent per 1 percent area on an adjacent stereonet. (c) Fold axial surfaces are plotted as great circles adjacent to their calculated poles to planes, symbolized by red points on an adjacent stereonet. (d) Fold hinges are plotted on a separate stereonet and symbolized by red points.

Figure 5-5. Stereonet plots of planar fabrics. Stereonet plots of the dominant regional (S2) foliation are separated by homogenous structural domains identified in Fig. 5-4. Poles to planes of foliation are plotted and symbolized as red points. A best-fit great circle is also plotted among the points along with a corresponding β point, symbolized by a blue diamond. Point data for S2 were contoured using either the Kamb method and a contour interval of 2 sigma or by percent per 1 percent area.

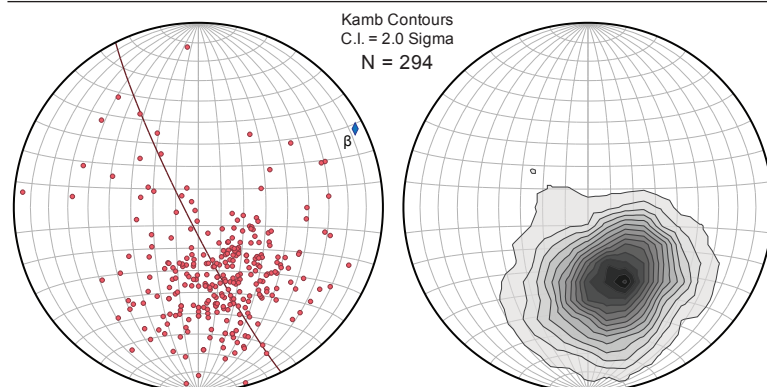
Domain I



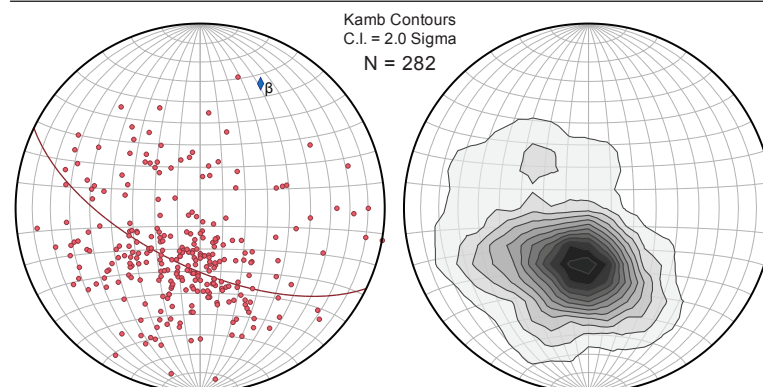
Domain II



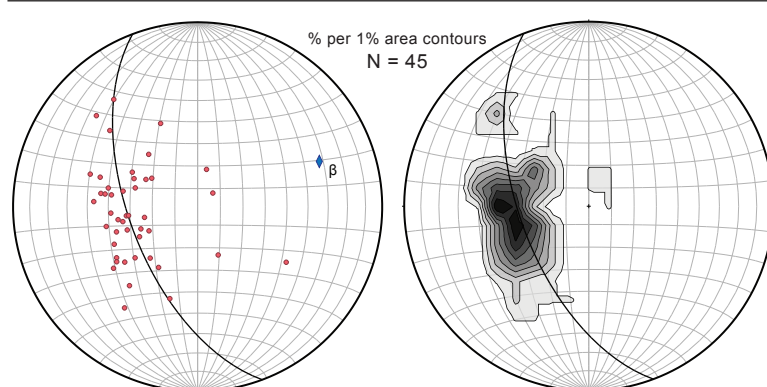
Domain III



Domain IV



Domain V



parallel alignment of micas in the Indian Springs Granodiorite often appears discordant with the surrounding regional S_2 foliation and has been identified by other geologists (e.g., Howard, 2012; Huebner 2013; Huebner et al., 2014). Given the fine-grained texture and limited occurrence of the Indian Springs Granodiorite in the study area, the subtle nature of S_3 was often difficult to distinguish. An upper greenschist/lower amphibolite facies (garnet-grade) shear zone associated with the Towaliga fault zone contains a mylonitic foliation and lineation termed S_4 and L_4 , respectively. This fabric commonly has a northeast strike and moderate to steep northwest dip, which, along with a shallowly plunging mineral lineation, supports the interpretation that the Towaliga fault is dominantly strike-slip with only a minor oblique component.

A form-line map of the study area (Fig. 5-4, Plate III), drawn from the strike of S_2 foliation, is divisible into five distinct homogeneous structural domains. Domains were separated on the basis of orientation of S_2 fabrics, which, although mostly homogeneous, do contain some minor heterogeneities that do not align with the majority of S_2 fabrics in the domain. It was not feasible, however, to construct a separate domain for every minor heterogeneous zone.

Domain I consists of the majority of Cat Square and Tugaloo terrane data northwest of the Towaliga fault. This domain displays a northeast-striking S_2 and a complex of tight folds. Folds here commonly verge northwest. A corresponding stereonet for this domain (Fig. 5-6) displays two clusters of data (poles to S_2 foliation) in both the northwest and southeast quadrants, indicating the strike of foliation is oriented northeast-southwest with a moderate to steep dip. This type of pattern is also indicative of a plunging asymmetric fold. A best-fit line through these clusters yields a southwest-oriented β axis with a shallow to moderate plunge. The orientation of β , along with dip-strike data and geologic map patterns, support the interpretation of a complex of northeast/southwest-oriented, gently southwest-plunging overturned folds.

Domain II represents a small area in the northeastern portion of the study area where dominant foliation typically has north-northwest orientation. This observation is also supported by the corresponding stereonet, which displays a dense cluster of points in the northeast quadrant along with a “girdle” that arcs from the northwest to the southeast quadrant, indicating a plunging asymmetric fold. The apparent scattering of data in Domain II could possibly result from including some data points from Domain I in the Domain II dataset (a sampling bias). The orientation of β

from Domain II is nearly the same as the Domain I β orientation, again possibly due to a sampling bias.

Domain III is comprised of data from a narrow strip paralleling the strike of the Towaliga fault. The majority of data points included in this domain are measurements from the Hollis Quartzite in the Barnesville quadrangle. Dominant foliation in this domain has a northeast/southwest orientation with a moderate northwest dip. This differs from the S_2 orientation of Domain I that exhibits both a northwest and southeast dip.

Domain IV consists predominantly of measurements of S_2 from Woodland Gneiss and small Cat Square terrane klippen southeast of the Towaliga fault. This domain is unique in that dominant foliation is commonly oriented northwest-southeast and dips moderately to the northeast, indicated by the cluster of points in the corresponding stereonet. Form-line patterns in this domain also appear to display a series of northwest-southeast oriented folds. This fold pattern contrasts with the outcrop fold pattern displayed by the Hollis Quartzite in the Barnesville quadrangle, and might suggest that at least two generations of map-scale folds are recognizable in this portion of the Pine Mountain window.

Domain V is comprised of S_2 foliation measurements from Woodland Gneiss and large Cat Square terrane klippen in the southeast corner of the Johnstonville quadrangle. Foliation in this domain typically has a north-northeast orientation with a shallow to moderate east-southeast dip, indicated by the cluster of points in the corresponding stereonet.

Mineral lineations (L_2) from the five structural domains have been compiled into one stereonet and consistently display a northeast-southwest orientation with a shallow plunge (Fig. 5-5).

Folds

Several generations of folds have been recognized through detailed geologic mapping and structural analysis of the Inner Piedmont and Pine Mountain terrane. Huebner et al. (2014) reported the occurrence of F_1 folds that developed with formation of S_1 , locally preserved within amphibolite boudins. While no S_1 folds were observed in amphibolite boudins in this study area, at least one potential isoclinal S_1 fold has been identified in a gondite nodule (Fig. 2-4b). The most commonly observed mesoscale folds occur as tight to isoclinal, overturned to recumbent folds that

are axial planar to S_2 and are termed F_2 (Huebner et al., 2014). These folds appear to be formed by flexural- and passive-flow mechanisms, although the former appears to be more common because there typically is some ductility contrast maintained between layers (Fig. 5-7). Several geologists proposed the classification of folds that either isoclinally fold S_2 or that coaxially refold intrafolial F_2 folds be termed F_3 (Davis, 2010; Huebner et al., 2014). Given the often limited extent of exposure, similar interlimb angle, and coaxial nature of F_2 and F_3 it is difficult to confidently distinguish one from the other in the field, where overprinting relationships are not evident. Ten mesoscale F_{2-3} fold measurements were made in the study area, which mostly exhibit northeast-southwest oriented axial surfaces dipping moderately northwest and southeast with axes oriented in similar directions plunging northeast and southwest (Fig. 5-5). The latest generation of identified folding, F_4 , consists of upright open folds that gently warp the S_2 fabric (Huebner et al., 2014). Possibly one macroscale F_4 antiformal fold with a gently plunging northeast-trending axis is present in the study area at the northeast end of the Pine Mountain window. This fold likely warps a series of northwest-vergent thrust nappes that comprise the deep structure of the Pine Mountain terrane (Fig. 5-2). The topographic expression of this fold is evident in the high topography along its axial trace and the curved outcrop pattern outlined by the Hollis Quartzite exposed along the northwest limb of the fold (Fig. 1-3b). In at least one location within the study area, several generations of folding and deformational events are observable in an exquisite saprolite exposure located along the northeast side of Crane Road at the western margin of the Barnesville quadrangle (Fig. 5-8). The outcrop consists mainly of thin layers of muscovite-biotite schist, metagraywacke, amphibolite, and at least one layer of gondite. Several generations of folding are evident at this outcrop (Fig. 5-8a-b); the most prominent is the thick folded boudin of amphibolite that has inclined, isoclinally folded (F_{2-3}) layers of amphibolite-metagraywacke directly below (Fig. 5-8c). Looking east toward the outcrop, close to ground level, and approximately two meters north of the large amphibolite boudin is a type 3 F_2 refold that folded a ~10 cm-long hooked-shaped layer of amphibolite and metagraywacke (Fig. 5-8d). Approximately five meters south of the large boudin is a set of shallowly plunging, upright, open, antiformal and synformal, possibly F_4 , folds. At numerous places between the type 3 fold and the open folds, the outcrop is crosscut by several small-scale brittle faults with various orientations having displacements of 2-3 cm; one fault cuts both the large amphibolite boudin and the isoclinal fold below.



Figure 5-6. Typical F_{2-3} fold mechanisms. (a) Flexural-flow fold in layer of gneiss. The ductility contrast between layers is evident in the ductile material from the light-colored layers that flowed to thicken the hinge of the fold, while the more rigid dark layers did not flow and instead buckled to accommodate the folding. (b) Passive flow fold in a migmatitic biotite gneiss. Passive flow is evident in the lack of any noticeable ductility contrast between layers. Both the light and dark layers flowed to accommodate the folding and neither layer had any impact on the shape of the fold.

Figure 5-7. Photomosaic of a saprolite outcrop along the northeast side of Crane Road. (a) Photo progresses left to right along the outcrop from northwest to southeast. The far left side of the photo is the location of the type 3 fold interference pattern. The center of the photo focuses on the large folded boudin of amphibolite with isoclinally folded layers beneath that verge southeast. (b) Continuation of the panoramic photo in (a) from left to right along the outcrop from northwest to southeast. Shown in the center of this image is an F4 antiform and synform. (c) Folded amphibolite boudin (resistant material) with isoclinally folded amphibolite-biotite gneiss directly beneath. Brittle faults cut the boudin and layers beneath as well as offset layers to the right of the boudin. Hoe pictured on right side center (~0.5 m length) for scale. (d) Type 3 refolded boudin of amphibolite. F3 is inclined to the right of the photo (southeast). Masonry trowel (~6 cm) for scale.





Figure 5-7 *continued.*

Faults

Brindle Creek-Jackson Lake fault

The Brindle Creek-Jackson Lake fault is the boundary between the Tugaloo terrane (western Inner Piedmont) and the Cat Square terrane (eastern Inner Piedmont), and is thought to be the southwest continuation of the Brindle Creek fault and terrane boundary identified in North and South Carolina (Huebner et al., 2009, 2010). While geochronologic evidence and correlation with a conspicuous lineament in aeromagnetic data support this hypothesis (Huebner et al., 2014), fault geometry varies significantly from the low-angle thrust geometry observed in the Carolinas. The Brindle Creek-Jackson Lake fault traverses the northern portion of the study area with a northeast-southwest strike and moderate northwest-dip, and continues southwest along the same orientation to where it likely is truncated by the Towaliga fault near Zebulon, Georgia. The fault locally exhibits a sinuous outcrop pattern, indicating it is variably folded along its trace. A relatively tight fold occurs in the fault in the northeastern corner of the study area. The fault is characterized by a relatively narrow (~10 m-wide) high-grade mylonite zone that contains a pervasive S-C fabric and several types of rotated porphyroclasts. Kinematic indicators exhibit a dominantly dextral shear sense, which, along with shallowly plunging mineral lineations, indicate dextral strike-slip motion (Huebner et al., 2014). Mylonitic protoliths vary from schist and biotite gneiss to megacrystic granite (High Falls Granite) along the trace of the fault, and as a result the mylonitic character varies as well. In the northeastern portion of the study area mylonite in the fault zone is phyllonitic and dominated by micas and small feldspar porphyroclasts. In contrast, a large exposure of the fault at the Woodfin Mill dam displays a coarse-grained high-temperature mylonite dominated by large (~0.5 cm) feldspar porphyroclasts. The Brindle Creek-Jackson Lake fault truncates metasedimentary and granitic rock units from terranes on either side. Based on those relationships, Huebner et al. (2014) reported an age bracketed by the ~ 371 Ma age of youngest granitoid truncated by the fault (High Falls Granite) and the ~305 Ma age of a possible stitching pluton of Indian Springs Granodiorite. Mylonitic foliation is also generally concordant with regional foliation suggesting that the fault was active pre- to syn-development of that fabric.

Towaliga fault

The Towaliga fault is a major feature in the Georgia Inner Piedmont and is one of the main bounding faults of the Pine Mountain window. The fault frames the northwest side of the window from Alabama to ~10 km northeast of the study area. Here the Towaliga fault continues northeast into the Inner Piedmont and changes from a ~070 to a ~030 strike, but does not, at the present erosion level, separate rocks of the Inner Piedmont from rocks of the Pine Mountain terrane; it merely juxtaposes rocks of the Cat Square terrane. The abrupt change in orientation and the fact that the fault is no longer a terrane boundary beyond that point might suggest a more complex polyphase reactivation history of the Towaliga fault. The fault is already characterized by two phases of movement: an earlier ductile Alleghanian phase and a later brittle phase, related to the breakup of Pangea at ~200 Ma. Both were strike-slip phases but produced opposite shear sense (Huebner and Hatcher, 2011; Huebner et al., 2014). The earlier movement phase is characterized by upper greenschist–lower amphibolite facies (garnet-grade) mylonite that ranges from a coarse protomylonite to fine-grained ultramylonite along different portions of the fault. The mylonite zone has the greatest width (~1 km) at its northeast extent in the study area, which contains the type locality where the fault was named (Crickmay, 1933) and where numerous exposures of various types of mylonite are present. Strain localization along the fault is evident by the sharp transition from protomylonite to mylonite to ultramylonite, which can be observed within small (meter-size) outcrops (Fig. 2-18d). The mylonite zone narrows significantly toward the southwest and any evidence of mylonite is almost completely absent from the fault zone west of Georgia Highway 41 to Highway 109. A small exposure of mylonite is present along the fault at the very western margin of the study area, which differs from mylonites at the northeast end of the study area and exhibits a more phyllonitic character dominated by a pervasive S-C fabric and abundant micas. Several asymmetric porphyroclasts, folds of quartz ribbons, and pressure shadows from Towaliga fault mylonites confirm a dominant dextral shear sense.

The brittle phase of the Towaliga fault is easily recognizable by the numerous pods of siliceous cataclasite that occur along its trace. These features likely developed as a result of formation of dilational stepovers and influx of hydrothermal fluids (Huebner and Hatcher, 2011). Their rhomb-shaped geometry is indicative of a sinistral motion sense. Where mylonite and siliceous cataclasite are not present along the fault, mostly at its southwestern end in the study area,

the brittle phase of the Towaliga fault is recognizable by the abrupt transition from lithologies of the Cat Square terrane to basement units (e.g., Woodland Gneiss) of the Pine Mountain window. In these areas extensive amounts of brecciated basement rocks are present and exhibit some evidence for hydrothermal alteration, such as large amounts of chlorite filling veins and fractures, and the presence of sulfide minerals (e.g., pyrite) (Fig. 5-9). At least one other large brittle fault occurs in the Barnesville quadrangle and is likely temporally related to the brittle movement phase along and near the Towaliga fault. The two faults exhibit a sinistral shear sense, although the unnamed fault problematically appears to dextrally offset a ridge of Hollis Quartzite. The presence of quartz mylonite is very frequent along the Towaliga fault zone, while the significance of its association with the Towaliga fault remains uncertain (Huebner and Hatcher, 2011).

Box Ankle fault

The Box Ankle fault is ~100 m-thick (Hooper and Hatcher, 1988a), gently southeast- and northwest-dipping, northwest-vergent thrust, high-temperature mylonite zone, and terrane boundary that juxtaposes Cat Square terrane rocks above the Pine Mountain window rocks. It closes the northeast end of the Pine Mountain window from the Goat Rock and Dean Creek faults in the southwest to the Towaliga fault in north-northwest. Mylonite along the fault contains an S-C fabric, and abundant rotated feldspar porphyroclasts (Hooper and Hatcher, 1988a; Rehrer et al., 2012). The fault was folded and exhibits upright open folds along with tight to isoclinal northwest-vergent overturned folds. The combination of the folded nature of the fault and the present erosion surface have resulted in the occurrence of several klippen of Cat Square terrane rocks in the Johnstonville quadrangle on the geologic map (Plate I). The klippen commonly only consist of biotite gneiss, with the exception of one that also contains exposures of a migmatitic sillimanite schist that contains a series of southwest-vergent tight to isoclinal overturned folds. The continuity of S_2 fabric across the fault zone, along with evidence that the fault is folded axial planar to S_2 , indicates that movement along the fault had to occur prior to development of the S_2 fabric (Hooper and Hatcher, 1989; Huebner et al., 2014). A relatively undeformed megacrystic orthogneiss, characterized by large euhedral feldspar megacrysts, occurs locally throughout the Pine Mountain window and always appears structurally beneath extensively sheared Woodland Gneiss. Hooper and Hatcher (1988a, 1989) proposed that the megacrystic orthogneiss is the protolith from which the sheared Woodland

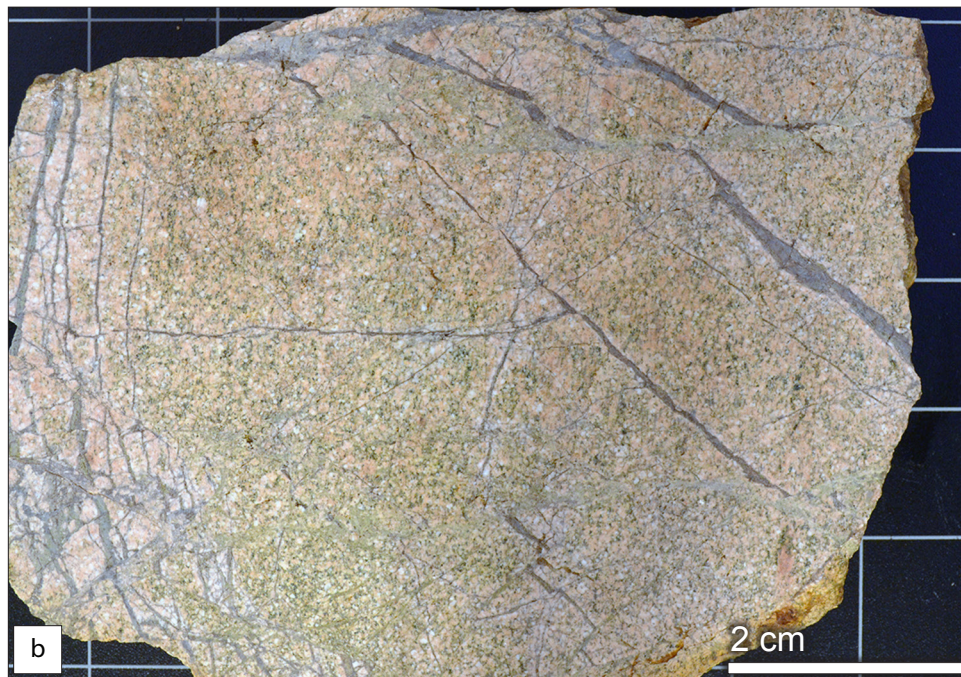
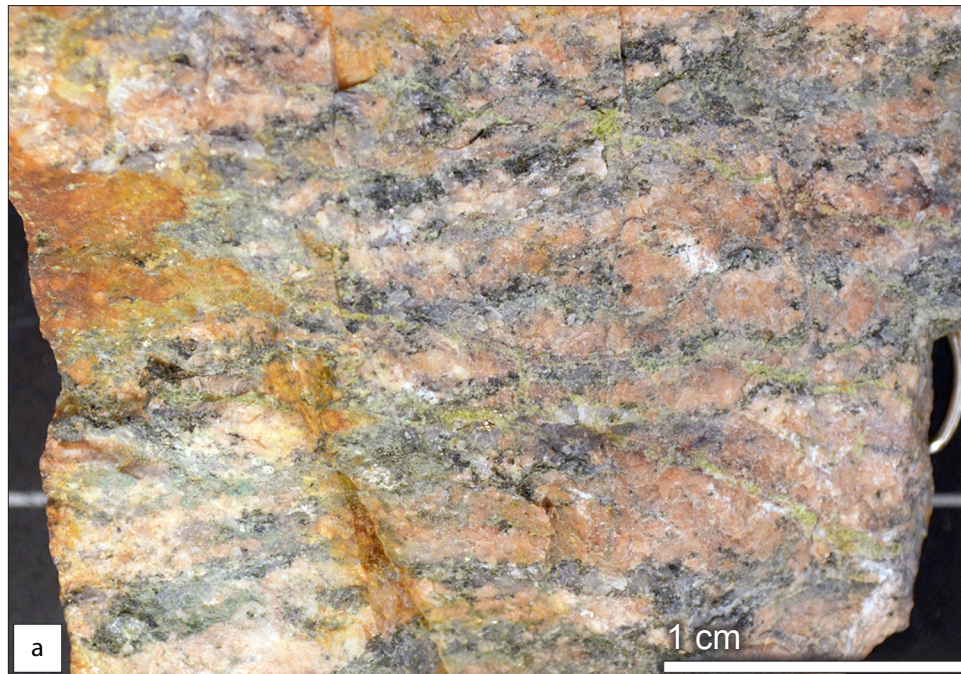


Figure 5-8. Towaliga fault brittle deformation of basement units of the Pine Mountain window. (a) Brecciated sample of Woodland Gneiss that contains large (~1 cm) sheared feldspar megacrysts crosscut by millimeter-sized fractures filled by chlorite. Small euhedral pyrite crystals are also present within the chlorite filled fractures. (b) Chaotic brittle fracturing of a basement unit. Cataclasis likely produced the more numerous and smaller fractures that are filled by chlorite. The sample then experienced a later phase of brittle deformation that produced the millimeter-sized fractures filled with quartz that chaotically overprint one another.

Gneiss was derived and they reference a location at which a strain gradient from one to the other is readily identifiable. Field relationships between the relatively undeformed megacrystic orthogneiss and sheared Woodland Gneiss observed during this study agree with those suggestions, although further geochronologic and isotopic analyses of both units would serve to reinforce the connection. I am inclined to disagree with Hooper and Hatcher (1989), however, in their suggestion that deformation observed in the Woodland Gneiss is due to the emplacement of the Cat Square terrane over the Pine Mountain terrane via the Box Ankle fault. While sheared Woodland Gneiss is often observed in close proximity to biotite gneiss units of the Cat Square terrane, generally within tens of meters, nowhere is the contact between the two observed directly, implying some uncertainty regarding the nature of that contact. A two-fold paradox also exists in the stratigraphic and structural relationships between the Woodland Gneiss, metasedimentary cover rocks of the Pine Mountain terrane, and the Box Ankle fault. At several locations in the Barnesville quadrangle relatively undeformed metasedimentary cover units (e.g., Sparks Schist, Hollis Quartzite, Manchester Schist) are observed lying unconformably above sheared Woodland Gneiss. Assuming that the Cat Square terrane once covered more of the central portion of the window and was subsequently removed by erosion, the Box Ankle fault would be required to have deformed greater than ~100 m of Woodland Gneiss without having imposed as much as a pervasive S-C fabric in the cover sequence. In fact, fabrics interpreted as representing transposed S_0 are recognizable in the Hollis Quartzite directly above sheared Woodland Gneiss in the vicinity of station DS156. The second part of the paradox regards the reported northeast plunge of the basement-cored, northwest-vergent, recumbent crystalline thrust nappes (Sears and Cooke, 1984; Hooper and Hatcher 1988a; Hatcher et al., 1988; Huebner, 2013). Hatcher et al. (1988) described the Box Ankle fault as a major thrust that has been eroded down-plunge toward the east from the Pine Mountain window antiform to the west. If this were the case, Woodland Gneiss exposed farther west in the vicinity of Barnesville should be well below the ~100 m reported thickness of the fault and should resemble its protolith material, the undeformed megacrystic orthogneiss. Deformed Woodland Gneiss is abundant in the central and southern portions of the Barnesville quadrangle and exposures of the undeformed megacrystic orthogneiss have yet to be identified, contradicting the notion that deformation of the Woodland Gneiss is confined to ~100 m below the structural position of the Box Ankle fault. I instead suggest that the Box Ankle fault is characterized by a much

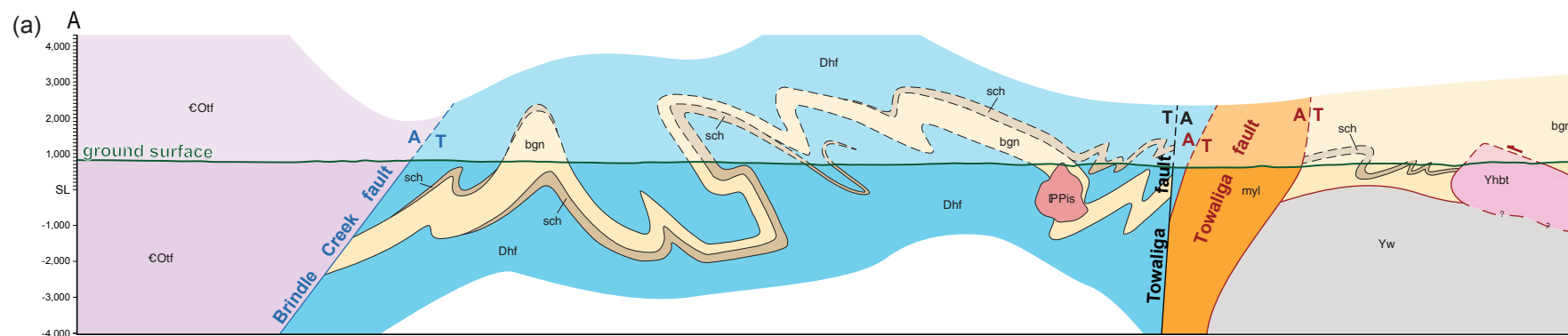
narrower zone of deformation concentrated in Cat Square terrane rocks in the hanging wall. This contention is supported by finer-grained mylonitic material identified close to the contact between Cat Square terrane biotite gneiss and the Woodland Gneiss. These mylonites have been identified in only a few localities and as such do not definitively define the nature of the Box Ankle fault.

Description of cross sections

Three cross sections (Fig. 5-10, 5-11; Plate I) were constructed through the study area and drawn at 1:24,000-scale with no vertical exaggeration. To create the cross sections, a profile line for each section was generated using ESRI ArcMap software and the National Elevation Dataset 1/3 arc second (~10 m) digital elevation model, was exported to Adobe Illustrator, and then fitted to a horizontal and vertical scale. Lithologic contacts and structural data were transferred from a digital version of the geologic map to the profile line using Adobe Illustrator. Drawing and final editing of the cross sections were also accomplished using the same program.

Cross section A–A'

Cross section A–A' was constructed from northwest to southeast through the central portion of the Orchard Hill quadrangle, the northeastern corner of the Barnesville quadrangle, and the central portion of the Johnstonville quadrangle (Fig. 5-10a). This cross section traverses all of the lithotectonic terranes in the study area and crosses several major structural boundaries, including the Brindle Creek-Jackson Lake, Towaliga, and Box Ankle faults. The northwest end of the section lies in the Tugaloo terrane and illustrates the moderate northwest dip of the Brindle Creek-Jackson Lake fault, separating Tugaloo terrane metasedimentary units from the High Falls Granite and Cat Square terrane biotite gneiss and sillimanite schist. The truncation of rock units from both terranes by the fault is obvious. A series of folds is exposed in the Cat Square terrane portion of the cross section east of the Brindle Creek-Jackson Lake fault. An open antiformal fold is followed by a series of tight to isoclinal northwest-vergent overturned folds. These folds produced the outcrop patterns observable in schist and biotite gneiss units on the geologic map (Plate I). Near the southeastern end of the Cat Square terrane, northwest of the Towaliga fault, is a small intrusive body of Indian Springs Granodiorite that intruded the High Falls Granite and truncated both Cat Square terrane metasedimentary units. The granitoid body is a dike-like intrusion extending from a larger plutonic body exposed in the southwestern corner of the adjacent High Falls quadrangle. The steeply dipping



NO VERTICAL EXAGGERATION

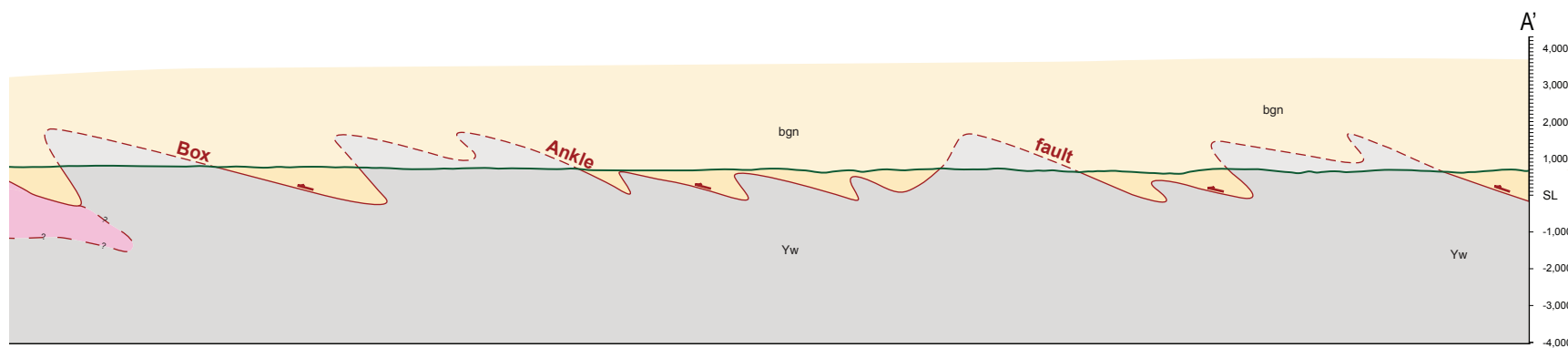
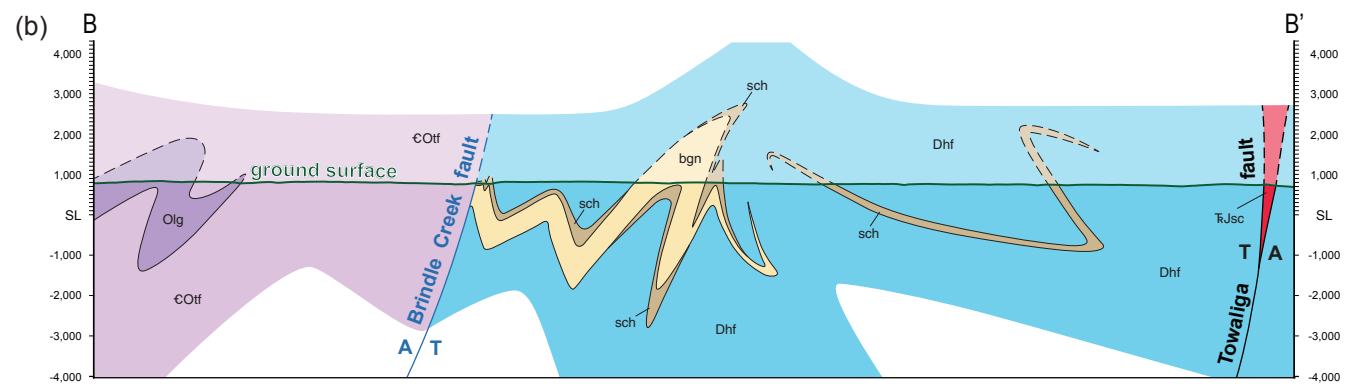


Figure 5-9. Reduced-scale cross sections through the study area. Cross sections correspond with those drawn in Plate I. (a) Cross section A-A'. (b) Cross section B-B'. (c) Cross section C-C'-C''.

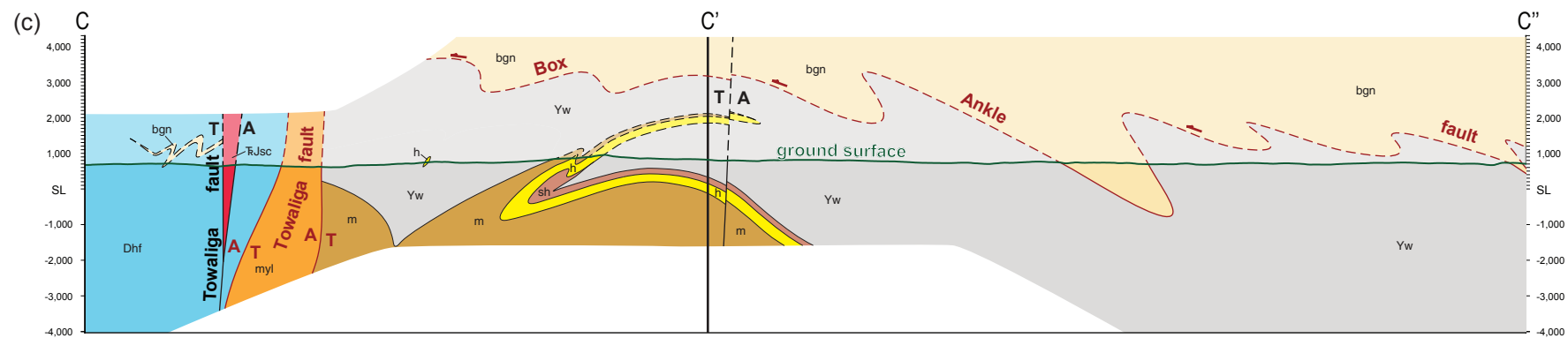
sinistral strike-slip brittle character of the Towaliga fault is apparent by the abrupt truncation of the metasedimentary units northwest of the fault, along with the juxtaposition of High Falls Granite on the southwest side. High Falls Granite is truncated along the northwestern side of the earlier, ductile, and dextral strike-slip phase of the Towaliga fault. That phase of the Towaliga fault is represented by a moderately dipping, ~1 km-wide, mylonite zone, which separates Cat Square terrane rocks from Pine Mountain terrane rocks; this is merely an artifact of the present-day erosional surface. The dextral phase of the Towaliga fault northeast of the abrupt change in strike appears to have juxtaposed only rocks of the Cat Square terrane and is not a terrane boundary beyond this point. Cat Square terrane rocks southeast of the Towaliga fault are separated from rocks of the Pine Mountain terrane by the northwest directed Box Ankle fault. The folded nature of the fault is evident and exhibits why the present-day erosion surface has created several klippen of Cat Square terrane rocks within the Pine Mountain window. The majority of klippen, with minor exceptions, are comprised of only Cat Square biotite gneiss. One klippe in the northwest corner of the Johnstonville quadrangle contains folded migmatitic sillimanite schist that, along with biotite gneiss, is truncated against a body of Pine Mountain window basement hornblende tonalite that is in fault contact with the overriding Cat Square terrane rocks and either fault or unconformable contact with the Woodland Gneiss below. The nature of the contact between the tonalite and the Woodland Gneiss was not resolvable in the field in this portion of the study area, nor was it resolvable based on geochronologic analyses of both units (see Chapter 4).

Cross Section B-B'

Cross section B-B' (Fig. 5-11a; Plate I) was constructed parallel to cross section A-A' but farther southwest in the Orchard Hill and Barnesville quadrangles. This section traverses portions of the Tugaloo and Cat Square terranes and crosses the Brindle Creek-Jackson Lake fault. At the northwest end of the cross section, a body of Lithonia Gneiss exhibits tight folds that are overturned to the southeast. The Brindle Creek-Jackson Lake fault in this portion of the study area displays a steeper northwest dip and noticeably truncates units on either side. The folds observed in cross section A-A' plunge gently to the southwest and, where metasedimentary units have not been assimilated into melt producing the High Falls Granite, are still observable in cross section B-B'. The character of folding changes from section A-A' to B-B' in that the interlimb angle decreases, the



NO VERTICAL EXAGGERATION



NO VERTICAL EXAGGERATION

Figure 5-9 continued.

folds become tighter, and they begin to overturn to the southeast. A relatively thin continuous unit of sillimanite schist is present southeast of the folded biotite gneiss unit and exhibits tight folds that are overturned to the northwest. On the geologic map this unit appears to consist of several distinct, independent “stringers” of schist; the interpretation I have made suggests that they are a single folded layer indicative of more extensive metasedimentary units that were removed by anatectic melting (Howard, 2012) that produced the High Falls Granite. The cross section terminates just southeast of the sinistral portion of the Towaliga fault, along which a dilational stepover is exposed. When the stepover formed, it likely created a negative pressure differential that drew hydrothermal fluids to the void and filled the space with multiply broken silicified cataclasite and boxwork quartz (Huebner and Hatcher, 2013). The stepover narrows significantly at depth and eventually terminates.

Cross section C–C’–C’’

Cross section C–C’–C’’ (Fig. 5-10c; Plate I) was constructed with a kink so that the northwest portion of the section C–C’ crosses the Towaliga fault and a large belt of Hollis Quartzite at right angles and the southeast portion of the section C’–C’’ crosses a large brittle Mesozoic fault and dominant regional foliation at right angles. The northwest portion of the cross section contains a thin unit of schist that is tightly folded and occurs above the present erosion level on the location of the cross section. This unit is observable on the geologic map just northeast of the section line, indicating that those folds likely plunge gently southwest also, but were removed by anatectic melting. The section crosses the Towaliga fault and displays the same brittle, cataclasite-filled, dilational stepover as section B–B’. The ductile portion of the fault represented by cross section C–C’ exhibits a steep to moderate dip to the northwest and contains a much narrower mylonite zone than the portion of the fault represented in A–A’. The Towaliga fault again separates Cat Square terrane rocks from the Woodland Gneiss, but only at the present erosion level because the fault juxtaposed portions of the Cat Square terrane. The Box Ankle fault separates Cat Square terrane rocks in the hanging wall from Woodland Gneiss in the footwall. Folding of the fault is mostly represented in this cross section as tight northwest-vergent folds, with the exception of one open upright antiform. This is the macroscale F_4 fold visible in the topography of the Barnesville quadrangle discussed earlier. Hollis Quartzite with a thin cover of Manchester Schist occurs directly beneath the hinge of the open

antiform. These units have been deformed into a northwest-vergent recumbent isoclinal fold that has been gently refolded by the F_4 antiform. The upper limb of the recumbent fold appears to be right-side-up, and the Hollis Quartzite terminates at the southeast end of this limb, above the current erosion level. The folding and termination of the quartzite unit, along with the gently northeast plunge of the F_4 fold, accounts for the curved outcrop pattern and the abrupt end of the Hollis Quartzite on the geologic map. A late brittle fault with a displacement of ~500 m occurs just southeast of the hinge of the F_4 antiform. The brittle fault has a steep northwest dip and a sinistral motion sense. This motion sense corresponds with that of similar faults of this type in the area and also agrees with the geometry of a rhomb-shaped dilational stepover located just southwest of the cross section line, and, although that motion sense is appropriate, the fault does appear to have dextrally offset a portion of the Hollis Quartzite and Manchester Schist. This offset is apparent in both topography and the lithologic contact between the Hollis Quartzite and Woodland Gneiss.

Structural and Tectonic Synthesis

The Pine Mountain window was initially interpreted to be the result of a simple erosional hole through an overriding thrust sheet, in which the “Carolina series” (Inner Piedmont) rocks were thrust over the “Wacoochee belt” (Pine Mountain terrane) (Clarke, 1952) (Fig. 5-1). Clarke (1952) suggested that the faults bounding the southeast and northwest flanks of the Pine Mountain window, the Goat Rock and Towaliga faults respectively, along with the Brevard fault, farther northwest, actually comprise a single thrust, which transported the “Carolina series” northwest over the “Wacoochee belt.” Subsequent investigations involving rheological and kinematic analyses of rocks from these fault zones have proven the relationships of the faults bounding the Pine Mountain window to not be as simple as was initially suggested. Like most faults in the eastern Inner Piedmont fault system, the ones mentioned by Clarke (1952) have been proven to be dextral stike-slip faults and not northwest directed thrusts. The nature of the fault that closes the northeast end of the Pine Mountain window was not investigated until Hooper and Hatcher (1988a) mapped in that area and suggested it is a northwest directed thrust, called the Box Ankle fault. Rheological contrasts (Hooper and Hatcher 1988b; Rehrer et al., 2012) and crosscutting relationships (Huebner, 2013) between the faults framing the window have also provided limits on timing of movement, which also complicates the nature of emplacement of Pine Mountain terrane. The Box Ankle fault

was active during upper amphibolite facies conditions, similar to those of peak metamorphism in the Inner Piedmont, and movement likely occurred during the Acadian/Neoacadian, and may be related to emplacement of the Cat Square terrane above the Pine Mountain terrane (Huebner, 2013). Earlier inferences that deformation observed in the Woodland Gneiss is due to movement along the Box Ankle fault are contradicted by recent detailed mapping efforts at the northeast end of the Pine Mountain window. My study instead suggests that the Box Ankle fault is characterized by a much narrower mylonite zone, mostly confined to rocks of the hanging wall Cat Square terrane. Zircon geochronologic investigations yielded absolute ages of several units in the Pine Mountain window and required new interpretations of their relationships to one another. Zircons from a felsic gneiss sample that represents several bodies occurring throughout the eastern end of the Pine Mountain window, were analyzed via the SHRIMP-RG and yielded an age of 1158 ± 18 Ma. These felsic gneiss xenoliths are among the oldest rocks in the Pine Mountain terrane and possibly represent earlier Grenville basement into which the Woodland Gneiss intruded. U-Pb ages of two samples of sheared Woodland Gneiss yielded a crystallization age of ~ 1040 Ma, which is in agreement with other reported ages of the Woodland Gneiss (Heatherington et al., 2006). Techniques were employed to make use of the high spatial resolution of the SHRIMP-RG, which yielded several younger age populations (985–854 Ma) that could be interpreted to represent different thermal events affecting the Woodland Gneiss after the accepted end of the Grenville orogeny. These dates could provide new insight into the tectonic history of the Pine Mountain terrane. A crystallization age of 1011 ± 10 Ma for a hornblende tonalite stock requires that it be intrusive into or in fault contact with the enclosing Woodland Gneiss. The age of the tonalite also requires that it be in fault contact with Cat Square terrane biotite gneiss that surrounds it.

The Towaliga fault experienced a polyphase reactivation history and frames the northwest end of the Pine Mountain window. Within the study area it separates rocks of the Cat Square terrane northwest of the fault from units of the Pine Mountain terrane to the southeast. The Cat Square terrane was initially identified from detrital zircon geochronologic analyses and detailed mapping in North Carolina (Bream, 2003). The investigation of a conspicuous lineament in aeromagnetic data, thought to be the southwest continuation of the Brindle Creek fault and terrane boundary (Huebner et al., 2009, 2010), lead to the realization of the southwestern end of the Cat Square terrane at the northeast end of the Pine Mountain window. While a high-grade fault separating

discrete lithologies and temporally distinct granitoid bodies was identified and likely represents the continuation of the Brindle Creek fault, contrast in geometry and structural style led to classification of the Brindle Creek-Jackson Lake fault. One of the main distinguishing characteristics of the Cat Square terrane is its mixed detrital provenance, being comprised of sediment derived from both Laurentian and peri-Gondwanan sources. In order to better define sedimentary provenance for rocks from the southwestern end of the terrane, several samples of Cat Square terrane biotite gneiss were obtained for detrital zircon analyses. Detrital suites from these samples were analyzed via LA-ICPMS, and yielded ages ranging from 2124 ± 90 Ma to 602 ± 8 Ma. The younger of these ages is represented by only one zircon, but is a very concordant analysis with small error. This age could be interpreted to represent the maximum depositional age of the southwestern end of the Cat Square basin. Geochemical analyses were also conducted on Cat Square terrane amphibolites as a part of this study so as to better define the developmental history of the Cat Square basin. Results of these analyses agreed with inferences made by other geologists (e.g., Wilson, 2006; Byars, 2010) and suggest that Cat Square amphibolites were derived from basalt and do represent vestiges of ocean crust that once comprised the floor of the basin. Trace element geochemical patterns and tectonic discriminant diagrams also support the hypothesis that the basin developed in a continental margin back-arc setting, but also suggest that basin development was not homogeneous or as simple as was previously thought.

Ongoing geologic investigations aimed at examining the occurrence of rocks within the Pine Mountain window, and the relationships of that structural feature with surrounding terranes have tremendously advanced our understanding of southern Appalachian tectonics and deep crustal processes associated with orogenesis. Although recent investigations have shed new light on seemingly unanswerable problems associated with the emplacement of the Pine Mountain terrane, it would appear that the more we learn about this region the more complicated it becomes, and perhaps there is no unique solution to the problem.

References Cited

- Allan, J.F., and Gorton, M.P., 1992, Geochemistry of igneous rocks from legs 127 and 128, Sea of Japan: Proceedings of the Ocean Drilling Program, Scientific Results, v. 127/128, pt. 2, p. 905-929.
- Allmendinger, R. W., Cardozo, N. C., and Fisher, D., 2013, Structural Geology Algorithms: Vectors & Tensors: Cambridge, England, Cambridge University Press, 289 p.
- Atkins, R.L., and Lineback, J.A., 1992, Structural relations, origin and emplacement of granitic rocks in the Cedar Rock Complex, Georgia Piedmont: Department of Natural Resources Environmental Protection Division, Georgia Geologic Survey, Bulletin 115, 40 p.
- Bentley, R.D., and Neathery, T.N., 1970, Geology of the Brevard zone and related rocks of the Inner Piedmont of Alabama: Alabama Geological Society, Eighth Annual Field Trip Guidebook, 119 P.
- Bier, S.E., 2001, Geology of the southeastern South Mountains, North Carolina [M.S. thesis]: Knoxville, University of Tennessee, 162 p.
- Black, L.P., Kamo, S.L., Allen, C.M., Aleinikoff, J.N., Davis, D.W., Korsch, R.J., Foudoulis, C., 2003, TEMORA 1: a new zircon standard for Phanerozoic U-Pb geochronology: Chemical Geology, v. 200, p. 155-170.
- Black, L.P., Kamo, S.L., Allen, C.M., Davis, D., Aleinikoff, J.N., Valley, J., Mundil, R., Campbell, I., Korsch, R.J., Williams, I., and Foudoulis, C., 2004, Improved $^{206}\text{Pb}/^{238}\text{U}$ microprobe geochronology by the monitoring of a trace-element-related matrix effect; SHRIMP, ID-TIMS, ELA-ICP-MS and oxygen isotope documentation for a series of zircon standards: Chemical Geology, v. 205, p. 115-140.
- Bowring, S.A., Schoene, B., Crowley, J.L., Ramezani, J., and Condon, D.J., 2006, High precision U-Pb zircon geochronology and the stratigraphic record: Progress and promise: The Paleontological Society Papers, v. 12, p. 25-45.
- Bream, B.R., 1999, Geology of the Glenwood and Sugar Hill quadrangles, North Carolina, and the structure of the northeast end of the Henderson Gneiss [M.S. thesis]: Knoxville, University of Tennessee, 155 p.
- Bream, B.R., 2002, The southern Appalachian Inner Piedmont: new perspectives based on recent detailed geologic mapping, Nd isotopic evidence, and zircon geochronology, *in* Hatcher, R.D., Jr. and Bream, B.R., eds., Inner Piedmont geology in the South Mountains-Blue Ridge Foothills and the southwestern Brushy Mountains, central-western North Carolina: North Carolina Geological Survey, Carolina Geological Society annual field trip guidebook, p. 45-63.
- Bream, B.R., 2003, Tectonic implications of para- and orthogneiss geochronology and geochemistry from the southern Appalachian crystalline core [Ph.D. dissertation]: Knoxville, University of Tennessee, 296 p.
- Bream, B.R., Hatcher, R.D., Jr., Miller, C.F., and Fullagar, P.D., 2004, Detrital zircon ages and Nd isotopic data from the southern Appalachian crystalline core, GA-SC-NC-TN: New provenance constraints for part of the Laurentian margin, *in* Tollo, R.P., Corriveau, L., McLelland, J., and

- Bartholomew, M.J., eds., Proterozoic Evolution of the Grenville orogen in North America: Boulder, Colorado, Geological Society of America Memoir 197, p. 459-475.
- Byars, H.E., 2010, Tectonic evolution of the west-central portion of the newton window, North Carolina Inner Piedmont: Timing and implications for the emplacement of the Paleozoic Vale charnockite, Walker Top Granite, and mafic complexes [M.S. thesis]: Knoxville, University of Tennessee, 248 p.
- Cabanis, B., and Lecolle, M., 1989, Le diagramme La/10-Y/15-Nb/8: un outil pour la discrimination des series volcaniques et la mise en evidence des processus de mélange et/ou de contamination crustale: Comptes Rendus de l'Académie des Sciences, Series II, v. 309, p. 2023-2029.
- Cannon, R.T., 1963, Classification of amphibolites: Geological Society of America Bulletin, v. 74, p. 1087-1088.
- Cardozo, N., and Allmendinger, R. W., 2013, Spherical projections with OSXStereonet: Computers & Geosciences, v. 51, no. 0, p. 193-205.
- Clarke, J.W., 1952, Geology and mineral resources of the Thomaston Quadrangle, Georgia: Georgia Geological Survey Bulletin 59, 99 p.
- Compston, W., and Williams, I., 1992, Ion probe ages for the British Ordovician and Silurian stratotypes, *in* Webby, B., and Laurie, J., eds., Global Perspectives on Ordovician Geology: Rotterdam, Netherlands, Balkema, p. 59-67.
- Coney, P.J., Jones, D.L., and Monger, J.W.H., 1980, Cordilleran suspect terranes: Nature, v. 288, p 329-333.
- Corfu, F., Hanchar, J.M., Hoskin, P.W.O., and Kinny, P., 2003, Atlas of zircon textures: Reviews in Mineralogy and Geochemistry, v. 53, p. 469-500.
- Cousens, B.L., and Allan, J.F., 1992, A Pb, Sr, and Nd Isotopic study of basaltic rocks from the Sea of Japan, legs 127/128, *in* Tamaki, K., Suyehiro, K., Allan, J.F., and McWilliams, M., eds., Proceedings of the Ocean Drilling Program, Scientific Results, v. 127/128, pt. 2, p. 805-817.
- Coutinho, J., Kräutner, H., Sassi, F., Schmid, R., and Sen, S., 2007, Amphibolite and granulite, *in* Fettes, D., and Desmons, J., eds., Metamorphic Rocks: A Classification and Glossary of Terms, Recommendations of the International Union of Geological Sciences Subcommittee on the Systematics of Metamorphic Rocks: New York, Cambridge University Press, p. 51-57.
- Crickmay, G.W., 1933, The occurrence of mylonites in the crystalline rocks of Georgia: American Journal of Science, v. 26, p. 161-177.
- Crickmay, G.W., 1952, Geology of the crystalline rocks of Georgia: Georgia Geological Survey Bulletin 58, 56 p.
- Davis, B.A., 2010, Tectonic evolution of the southern Appalachian Inner Piedmont: Identification and interpretation of crustal features from aeromagnetic data and detailed geologic mapping in central Georgia [M.S. thesis]: Knoxville, University of Tennessee, 262 p.

- Davis, T.L., 1993, Lithostratigraphy, structure, and metamorphism of a crystalline thrust terrane, western Inner Piedmont, North Carolina [Ph.D. dissertation]: Knoxville, University of Tennessee, 245 p.
- Donato, M.M., 1991, Geochemical recognition of a captured back-arc basin metabasaltic complex, southwestern Oregon: *Journal of Geology*, v. 99, p. 711-728.
- Fermor, L.L., 1909, The manganese-ore deposits of India: *Memoirs of the Geological Survey of India*, v. 37, pt. I, p. 161-186.
- Galpin, S.L., 1915, A preliminary report on the feldspar and mica deposits of Georgia: *Georgia Geological Survey Bulletin* 30, 190 p.
- Gatewood, M.P., 2007, Tectonics of the northeastern Inner Piedmont from detailed geologic mapping, geochronologic, geochemical, and petrologic studies with macro- and mesostructural analyses of ductile fault zones [M.S. thesis]: Knoxville, University of Tennessee, 279 p.
- Gehrels, G.E., 2012, Detrital zircon U-Pb geochronology: Current methods and new opportunities, *in* Busby, C., and Azor, A., eds., *Tectonics of Sedimentary Basins*: Chichester, United Kingdom, Blackwell Publishing Ltd., p. 47-62.
- Gehrels, G.E., Valencia, V.A., and Ruiz, J., 2008, Enhanced precision, accuracy, efficiency, and spatial resolution of U-Pb ages by laser ablation-multicollector-inductively coupled plasma-mass spectrometry: *Geochemistry, Geophysics, Geosystems*, v. 9, Q03017, doi:10.1029/2007GC001805.
- Gilliam, W.G., 2010, Structural and metamorphic evolution of the west-central Newton window, eastern Inner Piedmont, North Carolina [M.S. thesis]: Knoxville, University of Tennessee, 142 p.
- Giorgis, S.D., 1999, Inner Piedmont geology of the northwestern South Mountains near Morganton, North Carolina [M.S. thesis]: Knoxville, University of Tennessee, 191 p.
- Goldsmith, R., Milton, D.J., and Wright, J.W., Jr., 1988, Geologic map of the Charlotte 1° X 2° quadrangle, North Carolina and South Carolina: U. S. Geological Survey Map I-1251-E, scale 1:250,000.
- Grant, W.H., 1967, Geology of the Barnesville area and Towaliga fault, Lamar County, Georgia: *Georgia Geological Society 2nd Annual Field Trip*, 16 p.
- Graybill, E., Ganis, G.R., Mathur, R., Bosbyshell, H., 2012, Evidence for post-Grenville rifting at ~960 Ma in the Sams Creek Volcanics/Wakefield Carbonates Complex, western Piedmont, MD: *Geological Society of America Abstracts with Programs*, v. 44, no. 4, p. 64.
- Griffin, V.S., Jr., 1971, the Inner Piedmont belt of the southern crystalline Appalachians: *Geological Society of America Bulletin*, v. 82, p. 1885-1898.
- Griffin, V. S., Jr., 1972, Inner Piedmont belt of the southern crystalline Appalachians: Reply: *Geological Society of America Bulletin*, v. 83, p. 1897-1900.
- Griffin, V.S., Jr., 1978, Detailed analysis of tectonic levels in the Appalachian Piedmont: *Geologische Rundschau*, v. 67, p. 179-201.

- Hadizadeh, J., Babaie, H.A., and Babaei, A., 1991, Development of interlaced mylonites, cataclasites and breccias: example from the Towaliga fault, south central Appalachians: *Journal of Structural Geology*, v. 13, no. 1, p. 63-70.
- Hadley, J.B., and Goldsmith, R., 1963, *Geology of the Great Smoky Mountains, Tennessee and North Carolina*: United States Geological Survey Professional Paper 349-B, 118 p.
- Hanchar, J.M., and Miller, C.F., 1993, Zircon zonation patterns as revealed by cathodoluminescence and backscattered electron images: Implication for interpretation of complex crustal histories: *Chemical Geology*, v. 110, p. 1-13.
- Harley, S.L., Kelly, N.M., and Möller, A., 2007, Zircon behaviour and the thermal histories of mountain chains: *Elements*, v. 3, p. 25-30.
- Hatcher, R.D., Jr., 1971, *Geology of Rabun and Habersham Counties, Georgia: A reconnaissance study*: Georgia Department of Mines, Mining, and Geology Bulletin 83, 48 p.
- Hatcher, R.D., Jr., 2001, Rheological partitioning during multiple reactivation of the Paleozoic Brevard fault zone, southern Appalachians, USA, *in* Holdsworth, R.E., Strachan, R.A., Magloughlin, J.F., and Knipe, R.J., eds., *The nature and significance of fault zone weakening*: Geological Society of London Special Publication 186, p. 255-269.
- Hatcher, R.D., Jr., 2002, An Inner Piedmont primer, *in* Hatcher, R.D., Jr. and Bream, B.R., eds., *Inner Piedmont geology in the South Mountains-Blue Ridge Foothills and the southwestern Brushy Mountains, central-western North Carolina*: North Carolina Geological Survey, Carolina Geological Society annual field trip guidebook, p. 1-18.
- Hatcher, R.D., Jr., 2010, The Appalachian orogen: A brief summary, *in* Tollo, R.P., Bartholomew, M.J., Hibbard, J.P., and Karabinos, P.M., eds., *From Rodinia to Pangea: the Lithotectonic Record of the Appalachian Region*: Boulder, Colorado, Geological Society of America Memoir 206, p. 1-19.
- Hatcher, R.D., Jr., Bream, B.R., and Mersch, A.J., 2007, Tectonic map of the southern and central Appalachians: A tale of three orogens and a complete Wilson cycle, *in* Hatcher, R.D., Jr., Carlson, M.P., McBride, J.H., and Martinez Catalan, J.R., eds., *4-D Framework of Continental Crust*: Boulder, Colorado, Geological Society of America Memoir 200, p. 1-19.
- Hatcher, R.D., Jr., Hooper, R.J., McConnell, K.I., Heyn, T., and Costello, J.O., 1988, Geometric and time relationships between thrusts in the crystalline southern Appalachians, *in* Wojtal, S., and Mitra, G., eds., *Geometries and Mechanisms of Thrusting, with Special Reference to the Appalachians*: Boulder, Colorado, Geological Society of America Special Paper 222, p. 185-196.
- Heatherington, A.L., Mueller, P.A., Kamenov, G., Steltenpohl, M.G., Hanley, T.B., and Wooden, J.L., 2006, Pine Mountain terrane: Geochemistry and geochronology of basement gneisses and xenoliths: *Geological Society of America Abstracts with Programs*, v. 38, no. 3, p. 63.
- Hewitt, D.F., and Crickmay, G.W., 1937, *The Warm Springs of Georgia, their geologic relations and origin: a summary report*: U.S. Geological Survey Water Supply Paper 819, 40 p.

- Hibbard, J.P., 2000, Docking Carolina: Mid-Paleozoic accretion in the southern Appalachians: *Geology*, v. 28, p. 127-130.
- Higgins, M.W., Atkins, R.L., Crawford, T.J., Crawford, R.F., Brooks, R., and Cook, R.B., 1988, The structure, stratigraphy, tectonostratigraphy, and evolution of the southernmost part of the Appalachian orogen: U.S. Geological Survey Professional Paper 1475, 173 p.
- Hoffman, E.L., 1992, Instrumental neutron activation in geoanalysis: *Journal of Geochemical Exploration*, v. 44, p. 297-319.
- Hooper, R.J., 1986, Geologic studies at the east end of the Pine Mountain window and adjacent Piedmont, central Georgia [Ph.D. dissertation]: Columbia, University of South Carolina, 322 p.
- Hooper, R.J., and Hatcher, R.D., Jr., 1988a, The Pine Mountain terrane, a complex window in the Georgia and Alabama Piedmont; evidence for the eastern termination: *Geology*, v. 16, p. 307-310.
- Hooper, R.J., and Hatcher, R.D., Jr., 1988b, Mylonites from the Towaliga fault zone, central Georgia: products of heterogeneous non-coaxial deformation: *Tectonophysics*, v. 152, p. 1-17.
- Hooper, R.J., and Hatcher, R.D., Jr., 1989, The geology of the east end of the Pine Mountain window and adjacent Piedmont, central Georgia: Atlanta, Georgia Geological Society, Premeeting Field Trip Guide for Southeastern Section Geological Society of America, 37 p.
- Hopson, J. L., and Hatcher, R. D., Jr., 1988, Structural and stratigraphic setting of the Alto allochthon, northeast Georgia: *Geological Society of America Bulletin*, v. 100, p. 339-350.
- Howard, C.W., 2012, Investigating the evolution of two southern Appalachian terrane boundaries and a plutonic complex: Tectonic implications of structural, geochemical, and geochronologic studies in the central Georgia Inner Piedmont [M.S. thesis]: Knoxville, University of Tennessee, 208 p.
- Huebner, M.T., 2013, Geologic investigations in the central Georgia Inner Piedmont and the western flank of the Carolina superterrane: Implications regarding Acadian and Alleghanian collisional orogenesis, fault reactivation, and the Mesozoic breakup of Pangea [Ph.D. dissertation]: Knoxville, University of Tennessee, 345 p.
- Huebner, M.T., and Hatcher, R.D., Jr., 2011, Evidence for sinistral Mesozoic inversion of the dextral Alleghanian Towaliga fault, *in* Huebner, M.T., and Hatcher, R.D., Jr., eds., The geology of the Inner Piedmont at the northeast end of the Pine Mountain window: Georgia Geological Society 16th Annual Field Trip, v. 31, no. 1, p. 55-72.
- Huebner, M.T., and Hatcher, R.D., Jr., 2013, Polyphase reactivation history of the Towaliga fault, central Georgia: Implications regarding the amalgamation and breakup of Pangea: *The Journal of Geology*, v. 121, p. 75-90.
- Huebner, M.T., and Hatcher, R.D., Jr., in review, The transition from B- to A-subduction during closure of the Rheic remnant ocean: Marking the Acadian/Neocadian accretion of the Carolina superterrane, southern Appalachians: *Geosphere*.

- Huebner, M.T., Davis, B.A., and Hatcher, R.D., Jr., 2009, Triassic-Jurassic reactivation of the Alleghanian (Pennsylvanian-Permian) Towaliga fault, central Georgia, Appalachians: Geological Society of America Abstracts with Programs, v. 41, p. 693.
- Huebner, M.T., Hatcher, R.D., Jr., and Howard, C.W., 2011a, Geologic overview of the Inner Piedmont at the northeast end of the Pine Mountain window, *in* Huebner, M.T., and Hatcher, R.D., Jr., eds., The geology of the Inner Piedmont at the northeast end of the Pine Mountain window: Georgia Geological Society 16th Annual Field Trip, v. 31, no. 1, p. 1-25.
- Huebner, M.T., Hatcher, R.D., Jr., and Howard, C.W., 2011b, Insights into Paleozoic orogenesis and Mesozoic rifting from detailed mapping in the Georgia Inner Piedmont: Geological Society of America Abstracts with Programs, v. 43, no. 2, p. 68.
- Huebner, M.T., Hatcher, R.D., Jr., and Mersch, A.J., in review, Confirmation of the southwest continuation of the Cat Square terrane, southern Appalachian Inner Piedmont, with implications for collisional orogenesis: American Journal of Science.
- Huebner, M.T., Rehner, J.R., Hatcher, R.D., Jr., and Wunderlich, A.L., 2014, Detailed geologic map of the Inner Piedmont and Carolina superterrane at the northeast end of the Pine Mountain window, Georgia: Geological Society of America Map and Chart Series MCH-105, scale 1:50,000.
- Huebner, M.T., Wooden, J.L., and Hatcher, R.D., Jr., 2010, A terrane boundary in the central Georgia (USA) Inner Piedmont confirmed using new U-PB SHRIMP ages of granitic rocks: Geological Society of America Abstracts with Programs, v. 42, no. 5, p. 196.
- Hynes, A., and Rivers, T., 2010, Protracted continental collision—evidence from the Grenville Orogen: Canadian Journal of Earth Science, v. 47, p. 591-620.
- Ikeda, Y., and Yuasa, M., 1989, Volcanism in nascent back-arc basins behind the Shichito Ridge and adjacent areas in the Izu-Ogasawara arc, northwest Pacific: evidence for mixing between E-type MORB and island arc magmas at the initiation of back-arc rifting: Contributions to Mineralogy and Petrology, v. 101, p. 377-393.
- Irvine, T.N., and Baragar, W.R.A., 1971, A guide to the chemical classification of common rocks: Canadian Journal of Earth Science, v. 8, p. 523-548.
- Jenner, G.A., 1996, Trace element geochemistry of igneous rocks: Geochemical nomenclature and analytical geochemistry, *in* Wyman, D.A., ed., Trace Element Geochemistry of Volcanic Rocks: Applications for Massive Sulphide Exploration: Geological Association of Canada, Short Course Notes, v. 12, p. 79-113.
- Kalbas, J.L., 2003, Geology of part of the southwestern Brushy Mountains, Inner Piedmont [M.S. thesis]: Knoxville, University of Tennessee, 206 p.
- Kamb, W.B., 1959, Petrofabric observations from Blue Glacier, Washington, in relation to theory and experiment: Journal of Geophysical Research, v. 64, p. 1908-1909.
- Leake, B.E., 1964, The chemical distinction between ortho- and para-amphibolites: Journal of Petrology, v. 5, p. 238-254.

- Le Maitre, R.W., Bateman, P., Dudek, A., Keller, J., Lameyre Le Bas, M.J., Sabine, P.A., Schmid, R., Sorensen, H., Streckeisen, A., Woolley, A.R., and Zanettin, B., 1989, A classification of igneous rocks and glossary of terms: Oxford, United Kingdom, Blackwell Scientific Publications, 193 p.
- Lett, R.E., and Paterson, K., 2011, A comparison of several commercially available methods for the geochemical analysis of rare earth, rare metal and high field strength elements in geological samples: BC Ministry of Energy and Mines, Geological Fieldwork (2010): 2011-1, p. 181-188.
- Ludwig, K.R., 2009, Squid 2: a user's manual, rev. 2.50: Berkeley, CA, Berkeley Geochronology Center Special Publication No. 5, 110 p.
- Ludwig, K.R., 2012, User's manual for Isoplot 3.75, a geochronologic toolkit for Microsoft Excel: Berkeley, CA, Berkeley Geochronology Center Special Publication No. 5, 75 p.
- Marsaglia, K.M., 1995, Interarc and back-arc basins, *in* Busby, C.J., and Ingersoll, R.V., eds., *Tectonics of Sedimentary Basins*: Oxford, United Kingdom, Blackwell Science Inc., 592 p.
- Merschat, A.J., 2003, Inner Piedmont tectonics in the southwestern Brushy Mountains, North Carolina: Field and laboratory data revealing a 3-D crustal flow and sillimanite I and II metamorphism [M.S. thesis]: Knoxville, University of Tennessee, 199 p.
- Merschat, A. J., 2009, Assembling the Blue Ridge and Inner Piedmont: Insights into the nature and timing of terrane accretion in the southern Appalachian orogen from geologic mapping, stratigraphy, kinematic analysis, petrology, geochemistry, and modern geochronology [Ph.D. dissertation]: Knoxville, University of Tennessee, 455 p.
- Merschat, A.J., and Hatcher, R.D., Jr., 2007, The Cat Square terrane: Possible Siluro-Devonian remnant ocean basin in the Inner Piedmont, southern Appalachians, *in* Hatcher, R.D., Jr., Carlson, M.P., McBride, J.H., and Martinez Catalan, J.R., eds., *4-D Framework of Continental Crust*: Boulder, Colorado, Geological Society of America Memoir 200, p. 553-565.
- Merschat, A. J., Hatcher, R. D., Jr., and Davis, T. L., 2005, 3-D deformation, kinematics, and crustal flow in the northern Inner Piedmont, southern Appalachians, USA: *Journal of Structural Geology*, v. 27, p. 1252-1281, doi: 10.1016/j.jsg.2004.08.005.
- Merschat, A.J., Hatcher, R.D., Jr., Byars, H.E., and Gilliam, W.G., 2008, Inner Piedmont Geotraverse from the Brushy Mountains to Lincolnton, North Carolina: Architecture of the Cat Square and Tugaloo terranes: Geological Society of America Southeastern Section, Field Trip Guidebook, 64 p.
- Merschat, A.J., Hatcher, R.D., Jr., Bream, B.R., Miller, C.F., Byars, H.E., Gatewood, M.P., and Wooden, J.L., 2010, Detrital zircon geochronology and provenance of southern Appalachian Blue Ridge and Inner Piedmont crystalline terranes, *in* Tollo, R.P., Bartholomew, M.J., Hibbard, J.P., and Karabinos, P.M., eds., *From Rodinia to Pangea: the Lithotectonic Record of the Appalachian Region*: Boulder, Colorado, Geological Society of America Memoir 206, p. 661-699.
- Middlemost, E.A.K., 1989, Iron oxidation ratios, norms and the classification of volcanic rocks: *Chemical Geology*, v. 77, p. 19-26.

- Misra, K.C., and Conte, J.A., 1991, Amphibolites of the Ashe and Alligator Back Formations, North Carolina: Samples of late Proterozoic-early Paleozoic oceanic crust: Geological Society of America Bulletin, v. 103, p. 737-750.
- Nakamura, E., Campbell, I.H., and McCulloch, M.T., 1989, Chemical geodynamics in a back arc region around the Sea of Japan: Implications for the genesis of alkaline basalts in Japan, Korea, and China: Journal of Geophysical Research, v. 94, p. 4634-4654.
- Nemchin, A.A., and Cawood, P.A., 2005, Discordance of the U-Pb system in detrital zircons: Implication for provenance studies of sedimentary rocks: Sedimentary Geology, v. 182, p. 143-162.
- Nesse, W.D., 2004, Introduction to Optical Mineralogy, Third Edition: New York, Oxford University Press, 348 p.
- Pearce, J.A., 1983, Role of the sub-continental lithosphere in magma genesis at active continental margins, *in* Hawkesworth, C.J., and Norry, M.J., eds., Continental Basalts and Mantle Xenoliths: Cheshire, United Kingdom, Shiva Publishing Ltd., p. 230-249.
- Pearce, J.A., 1996, A user's guide to basalt discrimination diagrams, *in* Wyman, D.A., ed., Trace Element Geochemistry of Volcanic Rocks: Applications for Massive Sulphide Exploration: Geological Association of Canada, Short Course Notes, v. 12, p. 79-113.
- Pearce, J.A., and Cann, J.R., 1973, Tectonic setting of basic volcanic rocks determined using trace element analyses: Earth and Planetary Science Letters, v. 19, p. 290-300.
- Pettijohn, F.J., 1949, Sedimentary rocks: New York, Harper and Brothers, 526 p.
- Pickering, S., ed., 1976, Geologic map of Georgia: Georgia Department of Natural Resources and Georgia Geologic Survey, scale 1:500,000.
- Rankin, D.W., 1975, The continental margin of eastern North America in the southern Appalachians: The opening and closing of the Proto-Atlantic Ocean: American Journal of Science, v. 295-A, p. 298-336.
- Rehrer, J.R., Huebner, M.T., and Hatcher, R.D., Jr., 2012, Rheological and timing contrasts of major faults framing the northeastern end of the Pine Mountain window, central Georgia: Geological Society of America Abstracts with Programs, v. 44, no. 7, p. 595.
- Rivers, T., 1997, Lithotectonic elements of the Grenville Province: review and tectonic implications: Precambrian Research, v. 86, p. 117-154.
- Rollinson, H.R., 1983, The geochemistry of mafic and ultramafic rocks from the Archaean greenstone belts of Sierra Leone: Mineral Magazine, v. 47, p. 267-280.
- Rollinson, H.R., 1993, Using geochemical data: Evaluation, presentation, and interpretation: New York, John Wiley and Sons, Inc., 352 p.
- Roy, S., and Purkait, P.K., 1968, Mineralogy and genesis of the metamorphosed manganese silicate rocks (gondite) of Gowari Wadhona, Madhya Pradesh, India: Contributions to Mineralogy and Petrology, v. 20, p. 86-114.
- Saunders, A., and Tarney, J., 1991, Back-arc basins, *in* Floyd, P.A., ed., Oceanic Basalts: New York, Van Nostrand Reinhold, 456 p.

- Schamel, S., and Bauer, D., 1980, Remobilized Grenville basement in the Pine Mountain window, *in* Wones, D.R., ed., *Proceedings: The Caledonides in the U.S.A.: Department of Geological Sciences, Virginia Polytechnic Institute and State University, Memoir 2*, p. 313-316.
- Scherer, E.E., Whitehouse, M.J., and Münker, C., 2007, Zircon as a monitor of crustal growth: *Elements*, v. 3, p. 19-24.
- Schoene, B., Condon, D.J., Morgan, L., and McLean, N., 2013, Precision and accuracy in geochronology: *Elements*, v. 9, p. 19-24.
- Sears, J.W., and Cook, R.B., Jr., 1984, An overview of the Grenville basement complex of the Pine Mountain window, Alabama and Georgia *in* Bartholomew, M.J., ed., *The Grenville event in the Appalachians and related topics: Geological Society of America Special Paper 194*, p. 281-287.
- Sears, J.W., Cook, R.B., Gilbert, O.E., Jr., Carrington, T.J., and Schamel, S., 1981, Stratigraphy and structure of the Pine Mountain window in Georgia and Alabama, *in* Wigley, P.B., ed., *Latest Thinking on the Stratigraphy of Selected Areas in Georgia: Georgia Geological Survey Information Circular 54A*, p. 41-54.
- Sneyd, D., 1995, Geology of the Barnesville hydrologic research site, Lamar County, Georgia: Georgia Geologic Survey Information Circular 98, 27 p.
- Steltenpohl, M.G., Hatcher, R.D., Jr., Mueller, P.A., Heatherington, A.L., and Wooden, J.L., 2010, Geologic history of the Pine Mountain window, Alabama and Georgia: Insights from a new geologic map and U-Pb isotopic dates, *in* Tollo, R.P., Bartholomew, M.J., Hibbard, J.P., and Karabinos, P.M., eds., *From Rodinia to Pangea: The lithotectonic record of the Appalachian region: Boulder, Colorado, Geological Society of America Memoir 206*, p. 1-21.
- Stose, G.W., and Smith, R.W., 1939, Geologic map of Georgia: Georgia Division of Mines, Mining, and Geology, and U. S. Geological Survey, scale 1:500,000.
- Streckeisen, A., 1976, To each plutonic rock its proper name: *Earth Science Reviews*, v. 12, p. 1-33.
- Sun, S.S., and McDonough, W.F., 1989, Chemical and isotopic systems of oceanic basalts: implications for mantle composition and processes, *in* Saunders, A.D., and Norry, M.J., eds., *Magmatism in Ocean Basins: Geological Society of London Special Publications 42*, p. 313-345.
- Taylor, B., and Martinez, F., 2003, Back-arc basin basalt systematic: *Earth and Planetary Sciences Letters*, v. 210, p. 481-497.
- Thomas, W.A., 2006, Tectonic inheritance at a continental margin: *GSA Today*, v. 16, no. 2, p. 4-11.
- Watson, T.L., 1902, A preliminary report on a part of the granites and gneisses of Georgia: Georgia Geological Survey Bulletin 9-A, 367 p.
- West, T.E., Jr., 1994, Field evidence that the Appalachian décollement is exposed in central Georgia at the east end of the Pine Mountain terrane [M.S. thesis]: Columbia, University of South Carolina, 26 p.
- Williams, H., and Hatcher, R.D., Jr., 1983, Appalachian suspect terranes, *in* Hatcher, R.D., Jr., Williams, H., and Zietz, I., eds., *Contributions to the Tectonics and Geophysics of Mountain Chains: Boulder, Colorado, Geological Society of America Memoir 158*, p. 33-53.

- Williams, I.S., 1998, U-TH-Pb geochronology by ion microprobe *in* McKibben, M.A., Shanks III, W.C., Ridley, W.I., eds., Applications of Microanalytical Techniques to Understanding Mineralizing Processes: Reviews in Economic Geology, Society of Economic Geologists, Socorro, New Mexico, p. 1-35.
- Williams, S.T., 2000, Structure, stratigraphy, and migmatization in the southwestern South Mountains, North Carolina [M.S. thesis]: Knoxville, University of Tennessee, 111 p.
- Wilson, C.G., 2006, Origin and tectonic evolution of the southern Appalachian Neocadian crystalline core: Evidence from the geology of the Gilreath 7.5-minute quadrangle, North Carolina [M.S. thesis]: Knoxville, University of Tennessee, 200 p.
- Wilson, J.T., 1966, Did the Atlantic close and then re-open?: *Nature*, v. 211, p. 676-681.
- Wilson, J.T., 1968, Static or mobile earth: The current scientific revolution: *Proceedings of the American Philosophical Society*, v. 112, no. 5, p. 309-320.
- Winchester, J.A., and Floyd, P.A., 1977, Geochemical discrimination of different magma series and their differentiation products using immobile elements: *Chemical Geology*, v. 20, p. 325-343.
- Wood, D.A., Joron, J.L., and Treuil, M., 1979, A re-appraisal of the use of trace elements to classify and discriminate between magma series erupted in different tectonic settings: *Earth and Planetary Science Letters*, v. 45, p. 326-336.
- Yanagihara, G.M., 1994, Structure, stratigraphy, and metamorphism of a part of the Columbus Promontory, North Carolina [M.S. thesis]: Knoxville, University of Tennessee, 214 p.

Appendices

Appendix I
Geologic Map Station Data

Station ID	Location Data		Planar Features		Linear Features		Station Type	Rock Type
	Northing ⁽¹⁾	Easting ⁽¹⁾	Strike ⁽²⁾	Dip ⁽³⁾	Trend ⁽²⁾	Plunge ⁽⁴⁾		
Barnesville Quadrangle								
B1	3662673	765510					float	Si Cataclasite
B2	3660747	758675					float	Quartzite
B3	3660906	758788					float	Quartzite
B4	3660962	758753					float	Quartzite
B5	3660590	758398	263	30			outcrop	Gneiss
B6	3660635	758569					float	Gneiss
B7	3660683	758562					float	Quartzite
B8	3660690	758567					outcrop	Gneiss
B9	3660729	758561					float	Quartzite
B10	3660759	758553					float	MS Schist
B11	3660788	758545					outcrop	Quartzite
B12	3674094	766327					float	Granite
B13	3664875	767899					float	Metagraywacke
B14	3664880	767836					float	MS Schist
B15	3664878	767836					float	Gneiss
B16	3664878	767850	278	21			foliation inclined	Metagraywacke
B17	3664898	767768					float	Gneiss
B18	3664890	767754	190	26			foliation inclined	MS Schist
B19	3664867	767756					float	BT Schist
B20	3664812	767791					float	Quartzite
B21	3664813	767806					float	Woodland Gneiss
B22	3665070	767979					float	Woodland Gneiss
B23	3665034	768137					float	Metagraywacke
B24	3665067	767844					float	Quartzite
B25	3662622	766914					float	Quartzite
B26	3664492	767321	160	62			foliation inclined	Quartzite
B27	3664763	767495	358	32			lineation inclined	Woodland Gneiss
B28	3665601	768526					float	Metagraywacke
B29	3665771	768765					float	Metagraywacke
B30	3666951	767212					float	Granite
B31	3666922	767271					float	BT Schist
B32	3666596	767805					outcrop	Granite
B33	3665565	768331					float	Gneiss
B34	3665683	768711					float	Metagraywacke
B35	3665771	768768	022	24			foliation inclined	Schist
B35	3665771	768768	268	44			joint inclined	Schist
B35	3665771	768768	095	31			joint inclined	Schist
B36	3665643	768626					float	Metagraywacke
B37	3664817	767500	276	06			foliation inclined	Gneiss
B38	3664867	767510	198	18			foliation inclined	Gneiss
B38	3664867	767510			018	09	lineation inclined	Gneiss
B39	3664914	767556					float	Schist
B40	3667016	766993	105	19			foliation inclined	Granite
B41	3668140	768927					float	Granite
B42	3668126	768879					float	Granite
B43	3668114	768754					outcrop	Granite
B44	3667771	768040					float	Granite
B45	3667782	767821					float	Granite
B46	3667726	767761					float	Metagraywacke
B47	3667793	767688	238	44			foliation inclined	Granite
B48	3667285	768082					float	Gneiss
B49	3667336	768561	216	54			foliation inclined	Granite
B50	3667245	768105					float	High Falls Granite
B51	3667394	767950					float	High Falls Granite

Station ID	Location Data		Planar Features		Linear Features		Station Type	Rock Type
	Northing ⁽¹⁾	Easting ⁽¹⁾	Strike ⁽²⁾	Dip ⁽³⁾	Trend ⁽²⁾	Plunge ⁽⁴⁾		
B52	3667675	767802					float	High Falls Granite
B53	3667785	767740					float	Granite
B54	3667783	767653					float	Indian Springs Gr.
B55	3667685	767618					float	Indian Springs Gr.
B56	3667104	767583					float	High Falls Granite
B57	3666879	767690	130	24			foliation inclined	Schist
B58	3666948	767886					float	High Falls Granite
B59	3667827	767672					float	Indian Springs Gr.
B60	3667977	767869					float	Indian Springs Gr.
B61	3667973	767880					float	Indian Springs Gr.
B62	3668025	767926					float	Indian Springs Gr.
B63	3668077	767690					outcrop	High Falls Granite
B64	3668244	767720					float	High Falls Granite
B65	3668360	767695					float	High Falls Granite
B66	3667026	766963					float	Indian Springs Gr.
B67	3667067	767266					float	Granite
B68	3667104	767313					float	Granite
B69	3667431	767429					float	Indian Springs Gr.
B70	3667584	767500					float	Indian Springs Gr.
B71	3667742	767523					float	Indian Springs Gr.
B72	3666308	760517					float	High Falls Granite
B73	3663113	759468					float	High Falls Granite
B74	3662042	760308					float	Woodland Gneiss
B75	3663618	761888					float	Schist
B76	3662417	762964					float	MS Schist
B77	3661802	759719					float	Woodland Gneiss
B78	3661716	756901					float	Indian Springs Gr.
B79	3668562	767492					float	High Falls Granite
B80	3668716	767526					float	High Falls Granite
B81	3668778	768174					float	Metagraywacke
B82	3666837	767280	280	54			foliation inclined	High Falls Granite
B83	3666720	767227	045	55			foliation inclined	High Falls Granite
B84	3666694	767182	058	56			foliation inclined	High Falls Granite
B85	3666626	767136					float	Indian Springs Gr.
B86	3666582	767049					float	Indian Springs Gr.
B87	3666504	767080					float	Indian Springs Gr.
B88	3666419	767053					float	High Falls Granite
B89	3666321	767055					float	High Falls Granite
B90	3666171	766651					float	Si Cataclasite
B91	3666230	766619					float	Si Cataclasite
B92	3666432	766587					float	Si Cataclasite
B93	3666319	766713					float	Si Cataclasite
B94	3666522	766778	220	58			foliation inclined	Indian Springs Gr.
B95	3666458	767020	197	66			foliation inclined	High Falls Granite
B96	3666367	767034	226	58			foliation inclined	High Falls Granite
B97	3665082	767913					float	Mylonite
B98	3665045	767827					float	Woodland Gneiss
B99	3665012	767786					float	Gneiss
B100	3666135	768103					float	Mylonite
B101	3666110	768003					float	Mylonite
B102	3666085	767820					float	Mylonite
B103	3665190	768201					float	MS Schist
B104	3665413	768177	230	68			foliation inclined	Gneiss
B105	3665453	768176	280	68			foliation inclined	Gneiss
B106	3665531	768264	125	40			foliation inclined	MS Schist

Station ID	Location Data		Planar Features		Linear Features		Station Type	Rock Type
	Northing ⁽¹⁾	Eastng ⁽¹⁾	Strike ⁽²⁾	Dip ⁽³⁾	Trend ⁽²⁾	Plunge ⁽⁴⁾		
B107	3663893	766771	299	28			foliation inclined	Gneiss
B108	3663927	766783	265	34			foliation inclined	Gneiss
B108	3663927	766783			006	23	lineation inclined	Gneiss
B109	3663988	766786	250	39			foliation inclined	Gneiss
B109	3663988	766786			013	23	lineation inclined	Gneiss
B110	3664053	766770	282	26			foliation inclined	Gneiss
B110	3664053	766770	358	19	358	19	lineation inclined	Gneiss
B111	3664085	766763	323	55			foliation inclined	Migmatite
B112	3664139	766768	299	31			foliation inclined	Gneiss
B113	3664151	766779	265	43			foliation inclined	Quartzite
B113	3664151	766779			295	14	lineation inclined	Quartzite
B114	3664169	766791	285	27			foliation inclined	Quartzite
B115	3664205	766784	290	34			foliation inclined	MS-BT Schist
B116	3664269	766754	330	24			foliation inclined	MS Schist
B117	3664550	766850					float	Gneiss
B118	3664638	766895	320	46			foliation inclined	Gneiss
B119	3664761	766857	020	21			foliation inclined	Gneiss
B120	3664782	766852	200	24			foliation inclined	Gneiss
B120	3664782	766852			294	14	lineation inclined	Gneiss
B121	3664894	766848	200	25			foliation inclined	Gneiss
B122	3664926	766847					float	Mylonite
B123	3665066	766855	042	60			foliation inclined	Gneiss
B124	3665119	766790					float	Mylonite
B125	3662039	760303	020	56			foliation inclined	Mylonite
B126	3664589	767331	250	34			foliation inclined	Schist
B127	3664463	767330	175	60			foliation inclined	Quartzite
B128	3664420	767328	035	09			foliation inclined	MS Schist
B129	3664231	767330	061	38			foliation inclined	MS Schist
B130	3664099	767342	212	42			foliation inclined	MS Schist
B131	3664756	767483	240	24			foliation inclined	Gneiss
B131	3664756	767483			005	34	lineation inclined	Gneiss
B132	3664767	767619	059	10			foliation inclined	MS Schist
B133	3662690	764418	252	37			foliation inclined	Quartzite
B134	3662644	764431	259	35			foliation inclined	Quartzite
B135	3662830	764355	265	40			foliation inclined	Quartzite
B136	3662932	764305	237	43			foliation inclined	Quartzite
B137	3662486	762952	255	32			foliation inclined	Quartzite
B138	3662434	762972	239	27			foliation inclined	MS Schist
B139	3667822	769068					float	Indian Springs Gr.
B140	3667877	768998	222	42			foliation inclined	High Falls Granite
B141	3667837	768961	122	56			foliation inclined	High Falls Granite
B142	3668117	768755	024	32			foliation inclined	High Falls Granite
B143	3667891	768552	042	63			foliation inclined	High Falls Granite
B144	3667846	768537	041	44			foliation inclined	High Falls Granite
B145	3667900	768692	024	66			foliation inclined	High Falls Granite
B146	3667619	768650	239	53			foliation inclined	High Falls Granite
B147	3667830	768155	160	41			foliation inclined	High Falls Granite
B148	3667654	768192	036	38			foliation inclined	High Falls Granite
B149	3667468	768106	064	34			foliation inclined	High Falls Granite
B150	3667627	767986	068	70			foliation inclined	High Falls Granite
B151	3667787	767820	070	67			foliation inclined	High Falls Granite
B152	3667778	767771	210	37			foliation inclined	Metagraywacke
B153	3668027	767515	196	48			foliation inclined	High Falls Granite
B154	3667268	767245	050	78			foliation inclined	Metagraywacke
B155	3667360	767054	045	31			foliation inclined	High Falls Granite

Station ID	Location Data		Planar Features		Linear Features		Station Type	Rock Type
	Northing ⁽¹⁾	Eastings ⁽¹⁾	Strike ⁽²⁾	Dip ⁽³⁾	Trend ⁽²⁾	Plunge ⁽⁴⁾		
B156	3668370	766629	297	44			foliation inclined	High Falls Granite
B157	3668025	766499	160	44			foliation inclined	High Falls Granite
B158	3667961	766500	126	38			foliation inclined	High Falls Granite
B159	3667594	766058	116	53			foliation inclined	Metagraywacke
B160	3667551	766016	102	31			foliation inclined	High Falls Granite
B161	3667439	765519	200	55			foliation inclined	High Falls Granite
B162	3667477	765519					float	Metagraywacke
B163	3667597	765538	082	68			foliation inclined	High Falls Granite
B164	3663686	765580	271	30			foliation inclined	Mylonite
B164	3663686	765580			350	24	lineation inclined	Mylonite
B165	3665582	765957					float	Si Cataclasite
B166	3665538	766088					float	Si Cataclasite
B167	3665573	766349					float	Quartzite
B168	3665660	766262					float	Si Cataclasite
B169	3665911	766232					float	Si Cataclasite
B170	3665992	766222					float	Si Cataclasite
B171	3666240	766105	236	70			foliation inclined	Metagraywacke
B171	3666240	766105			044	09	lineation inclined	Metagraywacke
B172	3668734	766166	055	49			foliation inclined	High Falls Granite
B173	3668645	765920	063	60			foliation inclined	High Falls Granite
B174	3668649	765772	084	22			foliation inclined	High Falls Granite
B175	3668278	766508	064	49			foliation inclined	High Falls Granite
B176	3668317	766421	075	53			foliation inclined	High Falls Granite
B177	3668587	765953	060	60			foliation inclined	High Falls Granite
B178	3668561	765856	056	50			foliation inclined	Metagraywacke
B179	3668558	765537	068	62			foliation inclined	High Falls Granite
B180	3668466	765613	254	73			foliation inclined	High Falls Granite
B181	3668539	765753	094	53			foliation inclined	High Falls Granite
B182	3668630	765540	076	48			foliation inclined	Biotite Gneiss
B183	3668628	763747	157	54			foliation inclined	High Falls Granite
B184	3666231	769419	215	45			foliation inclined	Mylonite
B185	3666442	769488					float	Mylonite
B186	3666050	767112					float	High Falls Granite
B187	3666064	767140	214	64			foliation inclined	High Falls Granite
B188	3666069	767141			240	10	lineation inclined	High Falls Granite
B189	3665949	767551					float	Biotite Gneiss
B190	3665985	767663					float	Biotite Gneiss
B191	3665944	767576	244	38			foliation inclined	Biotite Gneiss
B192	3665726	766762	299	58			foliation inclined	High Falls Granite
B193	3665817	766780	316	69			foliation inclined	High Falls Granite
B194	3666409	768244	214	58			foliation inclined	Schist
B195	3668242	758148	216	40			foliation inclined	Biotite Gneiss
B196	3668231	758112	195	68			foliation inclined	Schist
B197	3668308	758214	208	34			foliation inclined	Metagraywacke
B198	3668317	758248	206	55			foliation inclined	Biotite Gneiss
B199	3668376	758257	212	56			foliation inclined	Biotite Gneiss
B200	3664338	765561	250	12			foliation inclined	MS Schist
B200	3664338	765561			345	08	lineation inclined	MS Schist
B201	3667245	759036	242	68			foliation inclined	High Falls Granite
B202	3666855	759154	068	70			foliation inclined	MS Schist
B203	3668488	757535	222	67			foliation inclined	Metagraywacke
B204	3668523	757517	235	42			foliation inclined	MS Schist
B205	3669453	757527	226	68			foliation inclined	Metagraywacke
B206	3667038	767251	185	58			foliation inclined	Metagraywacke
B207	3667033	767270	142	42			foliation inclined	High Falls Granite

Station ID	Location Data		Planar Features		Linear Features		Station Type	Rock Type
	Northing ⁽¹⁾	Easting ⁽¹⁾	Strike ⁽²⁾	Dip ⁽³⁾	Trend ⁽²⁾	Plunge ⁽⁴⁾		
B208	3667091	767278	198	72			foliation inclined	Metagraywacke
B209	3667209	766575	212	58			foliation inclined	Metagraywacke
B210	3667858	765249	082	48			foliation inclined	Biotite Gneiss
B211	3664863	765933	256	56			foliation inclined	Mylonite
Johnstonville Quadrangle								
J1	3665785	769555					float	Metagraywacke
J2	3665658	768458					float	Mylonite
J3	3665715	768537					float	Mylonite
J4	3665870	768489					float	Mylonite
J5	3665970	768476					float	Mylonite
J6	3665990	768480					float	Mylonite
J7	3665975	768441					float	Mylonite
J8	3665957	768236					float	Mylonite
J9	3666043	768130					float	Mylonite
J10	3665907	768407					float	Mylonite
J11	3665515	768417					float	Migmatite
J12	3665490	768412	180	49			foliation inclined	Metagraywacke
J13	3665491	768433	220	45			foliation inclined	Metagraywacke
J14	3665373	768447	224	37			foliation inclined	Metagraywacke
J15	3665343	768488					float	Mylonite
J16	3665292	768478					float	Metagraywacke
J17	3665222	768469	224	43			foliation inclined	Metagraywacke
J18	3665191	768459	250	56			foliation inclined	Migmatite
J19	3665155	768459					float	Metagraywacke
J20	3665601	768526	289	26			foliation inclined	Mylonite
J20	3665601	768526			002	24	lineation inclined	Mylonite
J21	3665499	768405	220	34			foliation inclined	Gneiss
J22	3665444	768444	225	30			foliation inclined	Gneiss
J23	3665372	768452	235	23			foliation inclined	Gneiss
J24	3665226	768611					float	Granite
J25	3665203	768522	250	46			foliation inclined	Metagraywacke
J25	3665203	768522			030	22	lineation inclined	Metagraywacke
J26	3665199	768461			002	29	lineation inclined	Migmatite
J27	3665029	768471	054	63			foliation inclined	MS Schist
J27	3665029	768471			020	40	lineation inclined	MS Schist
J28	3665038	768469	306	63			foliation inclined	Schist
J29	3664945	768529	229	44			foliation inclined	Metagraywacke
J29	3664945	768529			009	25	lineation inclined	Metagraywacke
J30	3664883	768562	237	28			foliation inclined	MS Schist
J31	3664811	768604					float	Gneiss
J32	3664781	768633					float	Gneiss
J33	3664918	768635					float	MS Schist
J34	3664929	768594	229	24			foliation inclined	Metagraywacke
J34	3664929	768594			016	33	lineation inclined	Metagraywacke
J35	3664966	768706					float	MS Schist
J36	3664984	768702					float	Metagraywacke
J37	3665056	768707					float	Metagraywacke
J38	3665177	768627					float	Metagraywacke
J39	3665362	768630					float	Biotite Gneiss
J40	3665461	768544					float	Metagraywacke
J41	3665544	768548					float	Metagraywacke
J42	3675865	767522	240	46			foliation inclined	Mylonite
J43	3665502	768359					float	Metagraywacke
J44	3665437	768389	225	43			foliation inclined	Migmatite
J45	3665276	768446					float	Mylonite

Station ID	Location Data		Planar Features		Linear Features		Station Type	Rock Type
	Northing ⁽¹⁾	Eastings ⁽¹⁾	Strike ⁽²⁾	Dip ⁽³⁾	Trend ⁽²⁾	Plunge ⁽⁴⁾		
J46	3665187	768401					float	Mylonite
J47	3665034	768338	230	35			foliation inclined	MS-BT Schist
J47	3665034	768338			009	12	lineation inclined	MS-BT Schist
J48	3664744	768461					float	Schist
J49	3664713	768544	245	39			foliation inclined	Gneiss
J50	3664637	768465	320	41			foliation inclined	Gneiss
J51	3664519	768401	295	25			foliation inclined	Gneiss
J52	3665164	769157	330	21			foliation inclined	Metagraywacke
J53	3665000	768740					float	BT Schist
J54	3664830	768836					float	Gneiss
J55	3664877	768928					float	Gneiss
J56	3672419	761702	180	40			foliation inclined	Metagraywacke
J56	3672419	761702			035	19	lineation inclined	Metagraywacke
J57	3673376	763281	195	61			foliation inclined	Metagraywacke
J58	3665905	769455	288	59			foliation inclined	Gneiss
J58	3665905	769455			318	19	lineation inclined	Gneiss
J59	3666013	769403	232	38			foliation inclined	Gneiss
J60	3666093	769392					float	Si Cataclasite
J61	3666117	769403					float	Mylonite
J62	3666245	769379					float	Mylonite
J63	3666262	769413	294	61			foliation inclined	Mylonite
J63	3666262	769413			010	50	lineation inclined	Mylonite
J64	3666344	769458	242	48			foliation inclined	Mylonite
J65	3666489	769508	145	51			foliation inclined	Mylonite
J66	3666494	769547	260	45			foliation inclined	Mylonite
J67	3666431	769576	220	68			foliation inclined	Mylonite
J68	3666260	769540	152	36			foliation inclined	Gneiss
J69	3666155	769508					float	Mylonite
J70	3666048	769524					float	Gneiss
J71	3665888	769583					float	Gneiss
J72	3665864	769543	301	44			foliation inclined	Gneiss
J72	3665864	769543			006	22	lineation inclined	Gneiss
J73	3667769	768406	032	41			foliation inclined	High Falls Granite
J74	3667823	768359	025	21			foliation inclined	High Falls Granite
J75	3668386	774499					float	Quartzite
J76	3668551	774423					float	Quartzite
J77	3668614	774230					float	Quartzite
J78	3668651	774176	012	49			foliation inclined	Gneiss
J79	3668637	774129					float	Gneiss
J80	3668626	774104	014	53			foliation inclined	Gneiss
J81	3668809	774080	016	65			foliation inclined	Mylonite
J81	3668809	774080			035	12	lineation inclined	Mylonite
J82	3668780	774060	293	61			fold axes surface	Gneiss
J82	3668780	774060			293	26	fold hinge	Gneiss
J82	3668780	774060	280	53			foliation inclined	Gneiss
J83	3668559	774109	325	38			foliation inclined	Gneiss
J84	3668444	774195					float	Woodland Gneiss
J85	3668159	774781	350	46			foliation inclined	Gneiss
J86	3668912	774801					float	Quartzite
J87	3669001	774942					float	Gneiss
J88	3665738	769617	284	39			foliation inclined	Metagraywacke
J89	3665787	769683					float	Metagraywacke
J90	3665820	769758					float	Mylonite
J91	3665897	769793					float	Biotite Gneiss
J92	3666097	769927					float	Biotite Gneiss

Station ID	Location Data		Planar Features		Linear Features		Station Type	Rock Type
	Northing ⁽¹⁾	Eastings ⁽¹⁾	Strike ⁽²⁾	Dip ⁽³⁾	Trend ⁽²⁾	Plunge ⁽⁴⁾		
J93	3666120	769866	280	49			foliation inclined	Biotite Gneiss
J94	3666165	769594					float	Mylonite
J95	3666197	769585	256	70			foliation inclined	Mylonite
J96	3666249	769550	304	56			foliation inclined	Gneiss
J97	3666198	769538					float	Mylonite
J98	3665886	769580	249	64			foliation inclined	Gneiss
J99	3666513	769507	259	44			foliation inclined	Mylonite
J100	3666589	769577					float	Mylonite
J101	3666640	769620					float	Mylonite
J102	3666604	769636	198	34			foliation inclined	Mylonite
J102	3666604	769636			330	34	lineation inclined	Mylonite
J103	3666622	769701	219	54			foliation inclined	Mylonite
J103	3666622	769701			356	34	lineation inclined	Mylonite
J104	3666610	769722	191	59			foliation inclined	Mylonite
J105	3666621	769758	216	46			foliation inclined	Mylonite
J105	3666621	769758			026	28	lineation inclined	Mylonite
J106	3666665	769830	210	53			foliation inclined	Metagraywacke
J107	3666519	769815					float	Mylonite
J108	3666446	769491	214	49			foliation inclined	Mylonite
J109	3667676	772589	229	54			foliation inclined	Gneiss
J109	3667676	772589			272	23	lineation inclined	Gneiss
J110	3667865	772564	226	68			foliation inclined	Mylonite
J111	3668106	772450					float	Gneiss
J112	3668111	772440	201	76			foliation inclined	Mylonite
J112	3668111	772440			010	26	lineation inclined	Mylonite
J113	3668039	772492					float	Mylonite
J114	3667716	772592	246	60			foliation inclined	Gneiss
J115	3667609	772663	244	46			foliation inclined	MS-BT Schist
J116	3667632	772914	274	61			foliation inclined	MS Schist
J117	3667720	772928					float	Mylonite
J118	3668098	773293					float	Gneiss
J119	3668294	773365	320	31			foliation inclined	Gneiss
J120	3668746	773625	192	62			foliation inclined	Gneiss
J121	3668909	773560	211	72			foliation inclined	Gneiss
J121	3668909	773560			015	31	lineation inclined	Gneiss
J122	3668950	773523	218	36			foliation inclined	Gneiss
J123	3669143	773365	262	62			foliation inclined	MS Schist
J124	3669027	773462	318	39			foliation inclined	Gneiss
J125	3669026	773462	318	39			foliation inclined	Gneiss
J126	3669022	773511	226	56			foliation inclined	Gneiss
J127	3669017	773602					float	Mylonite
J128	3668919	773627	244	35			foliation inclined	Gneiss
J128	3668919	773627			004	11	lineation inclined	Gneiss
J129	3668825	773690	186	49			foliation inclined	Gneiss
J130	3668476	769712					float	High Falls Granite
J131	3668540	769636	170	35			foliation inclined	High Falls Granite
J132	3668626	769520	204	64			foliation inclined	High Falls Granite
J133	3668727	769405	210	40			foliation inclined	High Falls Granite
J134	3668763	769386					float	MS Schist
J135	3668769	769374	141	41			foliation inclined	MS-BT Schist
J135	3668769	769374			225	26	lineation inclined	MS-BT Schist
J136	3668786	769026	044	38			foliation inclined	MS-BT Schist
J137	3668723	768901					float	Indian Springs Gr.
J138	3668743	768750	227	69			foliation inclined	Indian Springs Gr.
J139	3668695	768642	038	42			foliation inclined	Indian Springs Gr.

Station ID	Location Data		Planar Features		Linear Features		Station Type	Rock Type
	Northing ⁽¹⁾	Easting ⁽¹⁾	Strike ⁽²⁾	Dip ⁽³⁾	Trend ⁽²⁾	Plunge ⁽⁴⁾		
J140	3668639	768628	068	46			foliation inclined	Indian Springs Gr.
J141	3668520	768795					float	MS-BT Schist
J142	3668506	768807	188	36			foliation inclined	MS Schist
J142	3668506	768807			229	23	lineation inclined	MS Schist
J143	3668512	768869					float	Indian Springs Gr.
J144	3668533	768931	240	66			foliation inclined	High Falls Granite
J145	3668537	769026	244	68			foliation inclined	High Falls Granite
J146	3668550	769040	038	68			fold axes surface	High Falls Granite
J146	3668550	769040			210	24	fold hinge	High Falls Granite
J147	3668581	769050	200	64			foliation inclined	High Falls Granite
J148	3668565	769110	234	60			foliation inclined	High Falls Granite
J149	3668712	769189	229	54			foliation inclined	High Falls Granite
J150	3668528	769290	208	54			foliation inclined	High Falls Granite
J151	3668677	769510	156	61			foliation inclined	High Falls Granite
J152	3668650	770058					float	High Falls Granite
J153	3667410	771275					float	Quartzite
J154	3667383	771370	214	68			foliation inclined	Quartzite
J154	3667383	771370	002	78			joint inclined	Quartzite
J154	3667383	771370	104	58			joint inclined	Quartzite
J155	3667438	771650					float	Mylonite
J156	3667433	771660	252	46			foliation inclined	Gneiss
J156	3667433	771660			003	41	lineation inclined	Gneiss
J157	3667428	771687	244	46			foliation inclined	Gneiss
J157	3667428	771687			006	40	lineation inclined	Gneiss
J158	3667492	772208					float	Gneiss
J159	3667516	772342	295	65			foliation inclined	MS Schist
J159	3667516	772342			354	36	lineation inclined	MS Schist
J160	3667651	771878	220	35			foliation inclined	Gneiss
J160	3667651	771878			010	15	lineation inclined	Gneiss
J161	3667635	771787	204	50			foliation inclined	Gneiss
J162	3667580	771719	252	69			foliation inclined	Gneiss
J163	3667553	771681	230	52			foliation inclined	Gneiss
J164	3666307	768375					float	Si Cataclasite
J165	3666253	768570					float	Schist
J166	3666217	768539					float	Schist
J167	3666322	768491					float	Mylonite
J168	3668748	770320	200	28			foliation inclined	High Falls Granite
J169	3666094	771446					float	Quartz Vein
J170	3666052	771393	319	22			foliation inclined	Metagraywacke
J171	3666088	771384	326	50			foliation inclined	Metagraywacke
J172	3666149	771372	318	50			foliation inclined	Biotite Gneiss
J173	3666168	771350	240	64			foliation inclined	Biotite Gneiss
J174	3666152	771398	300	50			foliation inclined	Granite
J175	3666213	771438					float	Gneiss
J176	3666470	771487	326	51			foliation inclined	Granite
J177	3666607	771453	260	44			foliation inclined	Gneiss
J177	3666607	771453			005	10	lineation inclined	Gneiss
J178	3666657	771467	290	41			foliation inclined	Gneiss
J179	3666679	771489	300	35			foliation inclined	Gneiss
J180	3666690	771521	280	28			foliation inclined	Gneiss
J181	3667869	771002					float	High Falls Granite
J182	3667811	771147					float	Quartzite
J183	3667891	771185					float	Quartzite
J184	3668254	771334					float	Mylonite
J185	3668326	771230					float	Mylonite

Station ID	Location Data		Planar Features		Linear Features		Station Type	Rock Type
	Northing ⁽¹⁾	Eastng ⁽¹⁾	Strike ⁽²⁾	Dip ⁽³⁾	Trend ⁽²⁾	Plunge ⁽⁴⁾		
J186	3668767	771072					float	Metagraywacke
J187	3668904	771095	290	10			foliation inclined	Metagraywacke
J188	3668830	770977	205	50			foliation inclined	Metagraywacke
J189	3668843	770939					float	Metagraywacke
J190	3668897	770846					float	Si Cataclasite
J191	3668838	770838					float	Diabase Dike
J192	3668857	770523					float	High Falls Granite
J193	3668594	771741					float	Mylonite
J194	3668874	772307					float	Mylonite
J195	3665853	772510	226	33			foliation inclined	Metagraywacke
J196	3665922	772491	284	33			foliation inclined	Metagraywacke
J197	3666039	772498	291	64			foliation inclined	Metagraywacke
J198	3666235	772510	286	46			foliation inclined	Metagraywacke
J199	3666336	772489					float	Gneiss
J200	3666541	772498	327	36			foliation inclined	Gneiss
J200	3666541	772498			009	18	lineation inclined	Gneiss
J201	3666578	772488	300	32			foliation inclined	Gneiss
J202	3666588	772476	292	35			foliation inclined	Gneiss
J203	3666656	772439	262	28			foliation inclined	Gneiss
J204	3666658	772442	282	28			foliation inclined	Gneiss
J205	3666850	772412	280	55			foliation inclined	Biotite Gneiss
J206	3666904	772401					float	Gneiss
J207	3666952	772419	342	32			foliation inclined	Gneiss
J208	3667279	772402					float	MS Schist
J209	3667369	772481	254	34			foliation inclined	MS Schist
J210	3667361	772460	260	22			foliation inclined	MS Schist
J210	3667361	772460			344	09	lineation inclined	MS Schist
J211	3667406	772536	275	44			foliation inclined	MS Schist
J212	3667318	772562	218	23			foliation inclined	MS Schist
J213	3667377	772678					float	Metagraywacke
J214	3667325	772623	345	60			foliation inclined	Gneiss
J215	3667286	772589	020	60			foliation inclined	Gneiss
J216	3667247	772617	010	63			foliation inclined	Gneiss
J217	3667451	772802	165	38			foliation inclined	Gneiss
J218	3667456	772869					float	Gneiss
J219	3667457	772871	135	23			foliation inclined	Gneiss
J220	3667490	773290					float	Gneiss
J221	3668318	773369	290	58			foliation inclined	Gneiss
J222	3666291	769608	220	58			foliation inclined	Gneiss
J223	3666651	769795	224	38			foliation inclined	Mylonite
J224	3666762	769845	206	35			foliation inclined	Mylonite
J225	3666761	769904	210	18			foliation inclined	Mylonite
J226	3666844	769976					float	Mylonite
J227	3666823	770001	264	56			foliation inclined	Mylonite
J227	3666823	770001			006	53	lineation inclined	Mylonite
J228	3666816	770032	253	59			foliation inclined	Mylonite
J229	3666932	770034	230	55			foliation inclined	Granite
J230	3666973	770131					float	Mylonite
J231	3666980	770182	230	43			foliation inclined	Mylonite
J231	3666980	770182			020	25	lineation inclined	Mylonite
J232	3666906	770140					float	Mylonite
J233	3666825	770073	242	38			foliation inclined	Gneiss
J234	3666755	769982	248	48			foliation inclined	Mylonite
J234	3666755	769982			020	20	lineation inclined	Mylonite
J235	3666208	769847	208	36			foliation inclined	Metagraywacke

Station ID	Location Data		Planar Features		Linear Features		Station Type	Rock Type
	Northing ⁽¹⁾	Easting ⁽¹⁾	Strike ⁽²⁾	Dip ⁽³⁾	Trend ⁽²⁾	Plunge ⁽⁴⁾		
J236	3666164	769809	005	58			foliation inclined	Metagraywacke
J237	3665891	769582	275	57			foliation inclined	Gneiss
J238	3666524	768943					float	Mylonite
J239	3666582	768931					float	Mylonite
J240	3666632	768795					float	Mylonite
J241	3666881	769473					float	Mylonite
J242	3667054	769747					float	Amphibolite
J243	3667044	769765					float	MS Schist
J244	3667043	769853					float	Amphibolite
J245	3667059	769879					float	Mylonite
J246	3667203	770067					float	MS Schist
J247	3667284	770066					float	Amphibolite
J248	3667110	769588					float	MS Schist
J249	3667600	768869	200	56			foliation inclined	High Falls Granite
J250	3667596	768891	201	62			foliation inclined	Indian Springs Gr.
J251	3667436	768889	190	54			foliation inclined	High Falls Granite
J252	3667246	768872					float	High Falls Granite
J253	3666835	768734					float	Mylonite
J254	3666973	768483					float	High Falls Granite
J255	3667226	768420	230	58			foliation inclined	High Falls Granite
J256	3667245	768460	190	54			foliation inclined	MS Schist
J257	3667402	768630	216	46			foliation inclined	High Falls Granite
J258	3667442	768699	209	62			foliation inclined	Indian Springs Gr.
J259	3667880	769347			285	48	fold hinge	High Falls Granite
J259	3667880	769347	245	64			foliation inclined	High Falls Granite
J259	3667880	769347	160	41			foliation inclined	High Falls Granite
J260	3666855	773721					float	Gneiss
J261	3666930	773542	339	30			foliation inclined	Metagraywacke
J262	3666932	773534	315	34			foliation inclined	Gneiss
J263	3666953	773482	328	47			foliation inclined	Gneiss
J264	3666971	773435	317	18			foliation inclined	Gneiss
J265	3666995	773431	329	69			foliation inclined	Gneiss
J266	3667043	773365	106	15			foliation inclined	Mylonite
J267	3667097	773352	094	14			foliation inclined	Gneiss
J268	3667107	773313	111	22			foliation inclined	Gneiss
J269	3667146	773295	095	43			foliation inclined	Gneiss
J270	3667236	773241	109	36			foliation inclined	Gneiss
J270	3667236	773241			252	20	lineation inclined	Gneiss
J271	3667280	773238	324	64			foliation inclined	Gneiss
J272	3667336	773241	340	64			foliation inclined	Gneiss
J273	3667388	773317	339	34			foliation inclined	Gneiss
J274	3667478	773512	244	15			foliation inclined	Biotite Gneiss
J275	3667530	773540	010	50			foliation inclined	Metagraywacke
J276	3667807	773392	320	56			foliation inclined	Gneiss
J277	3667770	773881	245	50			foliation inclined	Gneiss
J278	3667792	773872	254	54			foliation inclined	Gneiss
J279	3667819	773872	290	36			foliation inclined	Gneiss
J280	3667722	774042	286	66			foliation inclined	Mylonite
J281	3667700	774069	292	68			foliation inclined	Metagraywacke
J282	3667712	774118	335	40			foliation inclined	Gneiss
J283	3665701	769437	231	49			foliation inclined	Biotite Gneiss
J284	3665689	769490	238	24			foliation inclined	Metagraywacke
J285	3665655	769481	252	26			foliation inclined	Metagraywacke
J286	3665278	769572	354	62			foliation inclined	Biotite Gneiss
J287	3665282	769561	334	62			foliation inclined	Biotite Gneiss

Station ID	Location Data		Planar Features		Linear Features		Station Type	Rock Type
	Northing ⁽¹⁾	Easting ⁽¹⁾	Strike ⁽²⁾	Dip ⁽³⁾	Trend ⁽²⁾	Plunge ⁽⁴⁾		
J288	3665263	769570	085	80			joint inclined	Biotite Gneiss
J289	3665226	769571	345	70			foliation inclined	Biotite Gneiss
J290	3665202	769589	120	80			fold axes surface	Biotite Gneiss
J290	3665202	769589			300	05	fold hinge	Biotite Gneiss
J290	3665202	769589	101	19			foliation inclined	Biotite Gneiss
J290	3665202	769589	299	26			foliation inclined	Biotite Gneiss
J291	3665173	769627	318	37			foliation inclined	BT Schist
J292	3665120	769652	322	40			foliation inclined	Biotite Gneiss
J293	3664958	769649	265	37			foliation inclined	Metagraywacke
J293	3664958	769649			010	30	lineation inclined	Metagraywacke
J294	3664913	769650					float	Granite
J295	3664913	769652	344	62			foliation inclined	Granite
J296	3664828	769660	025	64			foliation inclined	Granite
J297	3664754	769565	222	46			foliation inclined	Biotite Gneiss
J298	3664700	769568	164	72			foliation inclined	Biotite Gneiss
J299	3664634	769542	200	60			foliation inclined	MS Schist
J300	3664569	769409					float	Mylonite
J301	3664727	769302					float	MS Schist
J302	3664777	769285	182	72			foliation inclined	MS Schist
J303	3664852	769159	250	25			foliation inclined	MS Schist
J304	3665034	769158	260	34			foliation inclined	MS Schist
J305	3665926	769189	255	24			foliation inclined	MS Schist
J306	3665896	769243	260	72			foliation inclined	MS Schist
J307	3665175	769512	010	34			foliation inclined	Biotite Gneiss
J308	3664621	769583	201	36			foliation inclined	Gneiss
J309	3664550	769567	180	63			foliation inclined	Biotite Gneiss
J310	3664469	769581	252	53			foliation inclined	Metagraywacke
J310	3664469	769581			355	31	lineation inclined	Metagraywacke
J311	3664404	769593	234	62			foliation inclined	BT Schist
J312	3664329	769615	214	42			foliation inclined	MS Schist
J313	3664228	769733	185	50			foliation inclined	Gneiss
J314	3664527	769790	340	55			foliation inclined	Gneiss
J315	3664562	770012	324	59			foliation inclined	Biotite Gneiss
J316	3664684	769932	339	54			foliation inclined	Biotite Gneiss
J317	3664778	769889	324	54			foliation inclined	Biotite Gneiss
J318	3668813	775593	150	58			foliation inclined	Mylonite
J319	3668759	775736					float	Mylonite
J320	3668817	775889	345	58			foliation inclined	Gneiss
J321	3668861	775874	010	44			foliation inclined	Gneiss
J322	3668868	775868	250	44			foliation inclined	Gneiss
J323	3668873	775819	348	32			foliation inclined	Gneiss
J324	3668877	775783					float	Mylonite
J325	3668851	775579					float	Mylonite
J326	3666915	771480	031	66			foliation inclined	Granite
J327	3666901	771497	259	32			foliation inclined	Granite
J328	3665458	772691	275	47			foliation inclined	Gneiss
J329	3665429	772715	256	60			foliation inclined	Gneiss
J330	3667017	774106	310	54			foliation inclined	Gneiss
J331	3667047	774143	332	36			foliation inclined	Metagraywacke
J332	3667066	774164	328	40			foliation inclined	Metagraywacke
J332	3667066	774164			338	10	lineation inclined	Metagraywacke
J333	3667116	774215	312	25			foliation inclined	Indian Springs Gr.
J334	3667191	774338	022	12			foliation inclined	Granite
J335	3667228	774382	332	32			foliation inclined	Granite
J336	3667306	774455	321	28			foliation inclined	Granite

Station ID	Location Data		Planar Features		Linear Features		Station Type	Rock Type
	Northing ⁽¹⁾	Easting ⁽¹⁾	Strike ⁽²⁾	Dip ⁽³⁾	Trend ⁽²⁾	Plunge ⁽⁴⁾		
J337	3667367	774528	324	34			foliation inclined	Granite
J338	3662315	781120					float	Biotite Gneiss
J339	3656522	784738					float	Biotite Gneiss
J340	3671883	782323	087	41			foliation inclined	Gneiss
J340	3671883	782323			003	06	lineation inclined	Gneiss
J341	3659498	750008	231	78			foliation inclined	Other
J342	3659192	750105	231	51			foliation inclined	Metagraywacke
J343	3659182	750110	263	63			foliation inclined	MS Schist
J344	3658716	750334	258	49			foliation inclined	Quartzite
J345	3658663	751034	207	23			foliation inclined	Granite
J346	3658899	752005					float	Granite
J347	3658942	752009	281	44			foliation inclined	Quartzite
J347	3658942	752009			341	41	lineation inclined	Quartzite
J348	3659605	753837	229	53			foliation inclined	Quartzite
J349	3660861	753766	292	77			foliation inclined	Mylonite
J349	3660861	753766	341	24			foliation inclined	Mylonite
J350	3665792	769542	170	25			foliation inclined	Biotite Gneiss
J351	3665659	769759	345	48			foliation inclined	Biotite Gneiss
J352	3665687	769716	340	47			foliation inclined	Biotite Gneiss
J353	3665591	769943	338	65			foliation inclined	Gneiss
J354	3665399	770404	322	40			foliation inclined	Metagraywacke
J355	3665573	771021	310	72			foliation inclined	Gneiss
J356	3665947	771023	275	36			foliation inclined	Woodland Gneiss
J357	3664433	772527	136	57			foliation inclined	Gneiss
J358	3662623	773971	018	82			foliation inclined	Gneiss
J359	3664824	769650	165	43			foliation inclined	Diorite
J359	3664824	769650			004	10	lineation inclined	Diorite
J360	3664883	769688	170	65			foliation inclined	Diorite
J361	3669418	779554	306	29			foliation inclined	Gneiss
J361	3669418	779554			326	08	lineation inclined	Gneiss
J362	3669401	779573	031	73			brittle fault surface	Gneiss
J363	3669397	779574	170	82			foliation inclined	Gneiss
J364	3666014	770338					float	Diorite
J365	3666101	770342	315	52			foliation inclined	Diorite
J366	3666296	770236	311	25			foliation inclined	Diorite
J367	3666398	770266					float	Mylonite
Orchard Hill Quadrangle								
OH1	3668930	767232					float	High Falls Granite
OH2	3668727	767355					float	High Falls Granite
OH3	3669001	767623					float	High Falls Granite
OH4	3669158	767859					float	High Falls Granite
OH5	3669170	767854	282	78			foliation inclined	High Falls Granite
OH6	3669186	767956					float	High Falls Granite
OH7	3668868	768162	084	61			foliation inclined	Gneiss
OH8	3669112	768015					float	High Falls Granite
OH9	3669280	767879	062	54			foliation inclined	High Falls Granite
OH10	3669217	767712	060	72			foliation inclined	High Falls Granite
OH11	3669218	767711	060	72			foliation inclined	High Falls Granite
OH12	3669261	767640					float	High Falls Granite
OH13	3669287	767648	146	34			foliation inclined	High Falls Granite
OH14	3669283	767411					float	High Falls Granite
OH15	3669262	767390	136	40			foliation inclined	High Falls Granite
OH16	3675926	765189	195	50			foliation inclined	BT Schist
OH17	3675725	765609	224	59			foliation inclined	Schist
OH18	3676668	767578					float	Gondite

Station ID	Location Data		Planar Features		Linear Features		Station Type	Rock Type
	Northing ⁽¹⁾	Eastings ⁽¹⁾	Strike ⁽²⁾	Dip ⁽³⁾	Trend ⁽²⁾	Plunge ⁽⁴⁾		
OH19	3675879	767521					float	Mylonite
OH20	3670904	766590	046	55			foliation inclined	High Falls Granite
OH21	3670911	766688	070	46			foliation inclined	High Falls Granite
OH22	3670876	766746	063	52			foliation inclined	High Falls Granite
OH23	3670958	766269					float	Metagraywacke
OH24	3670866	766241					float	High Falls Granite
OH25	3670902	766266					float	High Falls Granite
OH26	3670921	766393					float	High Falls Granite
OH27	3670921	766530	069	54			foliation inclined	Metagraywacke
OH28	3670960	766535					float	High Falls Granite
OH29	3670867	766750	056	56			fold axes surface	Metagraywacke
OH29	3670867	766750			230	44	fold hinge	Metagraywacke
OH30	3670834	766792	074	52			foliation inclined	Biotite Gneiss
OH31	3670852	766873	045	47			foliation inclined	Metagraywacke
OH32	3670825	766927	073	58			foliation inclined	Metagraywacke
OH33	3670730	766930	050	59			foliation inclined	Metagraywacke
OH34	3670661	766991	069	68			foliation inclined	Metagraywacke
OH35	3670569	767095					float	High Falls Granite
OH36	3670531	767127	072	56			foliation inclined	Biotite Gneiss
OH37	3670408	767211					float	High Falls Granite
OH38	3670264	767313					float	Indian Springs Gr.
OH39	3670158	767320	057	66			foliation inclined	High Falls Granite
OH40	3670223	767267	041	57			foliation inclined	High Falls Granite
OH41	3670220	767040					float	Indian Springs Gr.
OH42	3670078	766539					float	Calc-silicate
OH43	3670312	766728					float	Metagraywacke
OH44	3670401	766789	081	50			foliation inclined	Biotite Gneiss
OH45	3670757	766536					float	Metagraywacke
OH46	3670878	766420					float	High Falls Granite
OH47	3670902	766379					float	Metagraywacke
OH48	3670859	766321					float	High Falls Granite
OH49	3671696	767812					float	Biotite Gneiss
OH50	3671620	767679					float	Metagraywacke
OH51	3671549	767605					float	Biotite Gneiss
OH52	3671423	767483	044	48			foliation inclined	Metagraywacke
OH53	3671350	767413	068	52			foliation inclined	Metagraywacke
OH54	3670936	767189	031	11			foliation inclined	Metagraywacke
OH55	3670807	767308					float	Metagraywacke
OH56	3670784	767419	044	57			foliation inclined	Metagraywacke
OH57	3670805	767474					float	Amphibolite
OH58	3670816	767592	049	50			foliation inclined	Metagraywacke
OH59	3670758	767697	065	62			foliation inclined	High Falls Granite
OH60	3670672	767681	056	65			foliation inclined	Biotite Gneiss
OH61	3670388	767597					float	High Falls Granite
OH62	3670330	767567	070	71			foliation inclined	High Falls Granite
OH63	3670294	767527	052	68			foliation inclined	Metagraywacke
OH64	3670379	767429					float	High Falls Granite
OH65	3670427	767410	059	72			foliation inclined	Metagraywacke
OH66	3670423	767324	048	77			foliation inclined	Metagraywacke
OH67	3670222	767457					float	Metagraywacke
OH68	3670177	767639	060	49			foliation inclined	High Falls Granite
OH69	3670215	767661	030	60			foliation inclined	High Falls Granite
OH70	3670463	767795	054	54			foliation inclined	Metagraywacke
OH71	3673531	766336	220	71			foliation inclined	Schist
OH72	3673660	762983	219	62			foliation inclined	Schist

Station ID	Location Data		Planar Features		Linear Features		Station Type	Rock Type
	Northing ⁽¹⁾	Eastng ⁽¹⁾	Strike ⁽²⁾	Dip ⁽³⁾	Trend ⁽²⁾	Plunge ⁽⁴⁾		
OH73	3673498	763137	215	56			foliation inclined	Schist
OH74	3673341	763337	175	25			fold axes surface	Schist
OH74	3673341	763337			050	04	fold hinge	Schist
OH75	3673351	763309	215	56			foliation inclined	Schist
OH76	3673879	764966					float	BT Schist
OH77	3674211	764511					float	Schist
OH78	3674642	764873	028	64			foliation inclined	Schist
OH79	3674453	765041					float	Gondite
OH80	3674428	765074	044	42			foliation inclined	Metagraywacke
OH81	3674393	765101	160	44			foliation inclined	Schist
OH82	3673453	766299	165	49			foliation inclined	High Falls Granite
OH83	3673443	766263	226	26			foliation inclined	High Falls Granite
OH84	3673449	766190	222	54			foliation inclined	High Falls Granite
OH85	3673206	766188	206	46			foliation inclined	High Falls Granite
OH86	3672545	766951					float	Diabase Dike
OH87	3672518	766941					float	Diabase Dike
OH88	3672493	766915					float	Diabase Dike
OH89	3673462	766358	211	63			foliation inclined	High Falls Granite
OH90	3673465	766365			229	34	lineation inclined	High Falls Granite
OH91	3673470	766380	021	40			foliation inclined	High Falls Granite
OH92	3673334	766336	044	68			foliation inclined	Schist
OH93	3673400	766334	046	49			foliation inclined	High Falls Granite
OH94	3673634	766321	207	56			foliation inclined	High Falls Granite
OH95	3672466	766820	036	35			foliation inclined	High Falls Granite
OH96	3672507	766819	075	66			foliation inclined	High Falls Granite
OH96	3672507	766819			060	26	lineation inclined	High Falls Granite
OH97	3671988	767166	162	60			foliation inclined	High Falls Granite
OH98	3672224	766480	052	59			foliation inclined	High Falls Granite
OH99	3671225	767970	076	66			foliation inclined	High Falls Granite
OH100	3671194	767977	053	52			foliation inclined	Metagraywacke
OH101	3671182	768042	060	42			foliation inclined	Metagraywacke
OH102	3670842	768115	070	59			foliation inclined	Metagraywacke
OH103	3670786	768130	074	56			foliation inclined	High Falls Granite
OH104	3670718	768135	070	46			foliation inclined	High Falls Granite
OH105	3670287	767883	044	44			foliation inclined	Metagraywacke
OH106	3670033	767761	280	66			foliation inclined	High Falls Granite
OH107	3669964	767760	035	42			foliation inclined	High Falls Granite
OH108	3669778	767695	210	74			foliation inclined	High Falls Granite
OH109	3669916	767794	213	74			foliation inclined	High Falls Granite
OH110	3669932	767850	056	74			foliation inclined	High Falls Granite
OH111	3669933	767849	056	74			foliation inclined	High Falls Granite
OH112	3669928	767995	062	79			foliation inclined	High Falls Granite
OH113	3670525	765480	041	64			foliation inclined	Metagraywacke
OH113	3670525	765480			009	14	lineation inclined	Metagraywacke
OH114	3670703	765402	115	69			foliation inclined	High Falls Granite
OH115	3670903	765628	130	36			foliation inclined	High Falls Granite
OH116	3670919	765653	236	34			foliation inclined	High Falls Granite
OH117	3670942	765751	034	54			foliation inclined	High Falls Granite
OH118	3670974	765725	051	60			foliation inclined	High Falls Granite
OH119	3671107	765763	039	42			foliation inclined	High Falls Granite
OH120	3671010	765862	145	41			foliation inclined	High Falls Granite
OH121	3670934	766114					float	High Falls Granite
OH122	3671155	765671					float	Indian Springs Gr.
OH123	3670861	765224	049	38			foliation inclined	High Falls Granite
OH124	3670216	766390	095	24			foliation inclined	Schist

Station ID	Location Data		Planar Features		Linear Features		Station Type	Rock Type
	Northing ⁽¹⁾	Eastng ⁽¹⁾	Strike ⁽²⁾	Dip ⁽³⁾	Trend ⁽²⁾	Plunge ⁽⁴⁾		
OH125	3669981	766588	145	52			foliation inclined	Schist
OH126	3669817	766860	117	54			foliation inclined	Schist
OH127	3669637	767131	114	32			foliation inclined	High Falls Granite
OH128	3669568	767193	116	48			foliation inclined	High Falls Granite
OH129	3669438	767307	321	21			foliation inclined	High Falls Granite
OH130	3669324	767322	336	19			foliation inclined	High Falls Granite
OH131	3669251	767309	022	13			foliation inclined	High Falls Granite
OH132	3669051	767283	184	36			foliation inclined	High Falls Granite
OH133	3668989	767244					float	Pegmatite
OH134	3668977	767227	080	12			foliation inclined	High Falls Granite
OH135	3668646	766918	018	39			foliation inclined	High Falls Granite
OH136	3669948	765153					float	High Falls Granite
OH137	3670197	765074					float	High Falls Granite
OH138	3670199	765156					float	High Falls Granite
OH139	3670247	765180	044	71			foliation inclined	High Falls Granite
OH140	3670278	765278	054	56			fold axes surface	High Falls Granite
OH140	3670278	765278			030	18	fold hinge	High Falls Granite
OH140	3670278	765278	044	55			foliation inclined	High Falls Granite
OH141	3670173	765148	048	76			foliation inclined	High Falls Granite
OH142	3669869	765187	029	58			foliation inclined	High Falls Granite
OH143	3669922	765292	019	72			foliation inclined	High Falls Granite
OH144	3670192	766954	051	65			foliation inclined	High Falls Granite
OH145	3670187	767057	246	38			foliation inclined	High Falls Granite
OH146	3669953	767348					float	High Falls Granite
OH147	3670025	767467	060	80			foliation inclined	High Falls Granite
OH148	3669953	767593	055	62			foliation inclined	High Falls Granite
OH149	3669856	767221	234	54			foliation inclined	High Falls Granite
OH150	3669947	767191	262	74			foliation inclined	High Falls Granite
OH151	3670066	766968	222	38			foliation inclined	High Falls Granite
OH152	3669336	767433	058	61			foliation inclined	High Falls Granite
OH153	3669457	767535	045	55			foliation inclined	High Falls Granite
OH154	3669449	767596	149	42			foliation inclined	High Falls Granite
OH155	3671986	764738	132	60			foliation inclined	High Falls Granite
OH156	3672023	764796	160	44			foliation inclined	High Falls Granite
OH157	3671923	765056					float	Metagraywacke
OH158	3672027	765118	234	53			foliation inclined	MS-BT Schist
OH159	3672009	765142	192	28			foliation inclined	Metagraywacke
OH160	3672001	765150	230	30			foliation inclined	High Falls Granite
OH161	3671925	765334					float	Metagraywacke
OH162	3671897	765382	212	58			foliation inclined	Metagraywacke
OH163	3671809	765931					float	Metagraywacke
OH164	3671784	765905	044	64			foliation inclined	Metagraywacke
OH165	3671685	764732					float	Metagraywacke
OH166	3671786	764927					float	Metagraywacke
OH167	3671694	764932	046	44			foliation inclined	Metagraywacke
OH168	3671481	766119	066	67			foliation inclined	Metagraywacke
OH169	3671429	765969	030	58			foliation inclined	High Falls Granite
OH170	3671263	766058	054	26			foliation inclined	High Falls Granite
OH171	3671227	766092	102	71			foliation inclined	High Falls Granite
OH172	3670949	766187	106	42			foliation inclined	Biotite Gneiss
OH173	3671045	766769	060	54			foliation inclined	High Falls Granite
OH174	3669532	765607	241	31			foliation inclined	Metagraywacke
OH175	3669484	766026					float	Metagraywacke
OH176	3669488	766132	072	51			foliation inclined	High Falls Granite
OH177	3669585	766431					float	High Falls Granite

Station ID	Location Data		Planar Features		Linear Features		Station Type	Rock Type
	Northing ⁽¹⁾	Eastng ⁽¹⁾	Strike ⁽²⁾	Dip ⁽³⁾	Trend ⁽²⁾	Plunge ⁽⁴⁾		
OH178	3669160	765883					float	High Falls Granite
OH179	3669022	765841	080	44			foliation inclined	High Falls Granite
OH179	3669022	765841			039	07	lineation inclined	High Falls Granite
OH180	3668671	765876					float	High Falls Granite
OH181	3668650	765875	085	75			foliation inclined	High Falls Granite
OH182	3668660	766187					float	Gondite
OH183	3668845	766281					float	Gondite
OH184	3669358	765530	069	49			foliation inclined	High Falls Granite
OH185	3669410	765528	085	36			foliation inclined	Schist
OH186	3669506	765510	239	58			foliation inclined	Metagraywacke
OH187	3669647	765524	078	39			foliation inclined	Metagraywacke
OH188	3669833	765525	071	62			foliation inclined	Metagraywacke
OH189	3670174	765716	111	56			foliation inclined	Metagraywacke
OH190	3669520	765648	069	68			foliation inclined	High Falls Granite
OH191	3672026	764577	069	74			foliation inclined	High Falls Granite
OH192	3671985	764539	058	60			foliation inclined	High Falls Granite
OH193	3669018	763628	130	71			foliation inclined	Schist
OH194	3668980	763596	100	46			foliation inclined	Schist
OH194	3668980	763596			220	36	lineation inclined	Schist
OH195	3669318	763594	214	56			foliation inclined	Schist
OH196	3669348	763593	241	36			foliation inclined	Metagraywacke
OH197	3669854	758978	208	20			foliation inclined	Schist
OH197	3669854	758978			048	22	lineation inclined	Schist
OH198	3669838	758988	224	44			foliation inclined	Schist
OH199	3671472	758801					float	Gondite
OH200	3671421	758799					float	Gondite
OH201	3671367	758828					float	Gondite
OH202	3671352	758858					float	Granite
OH203	3671286	758924					float	BT Schist
OH204	3671218	758886					float	Gondite
OH205	3671176	758934					float	Amphibolite
OH206	3671110	758922					float	BT Schist
OH207	3671177	758866					float	Amphibolite
OH208	3671215	758807	194	32			foliation inclined	BT Schist
OH209	3671206	758805	032	68			foliation inclined	Amphibolite
OH210	3669059	761016	105	56			foliation inclined	High Falls Granite
OH211	3669220	760862	031	54			foliation inclined	Schist
OH212	3669208	760875	350	11			foliation inclined	Schist
OH212	3669208	760875			065	17	lineation inclined	Schist
OH213	3670889	760082	256	71			foliation inclined	Indian Springs Gr.
OH214	3670889	759854	238	50			foliation inclined	Metagraywacke
OH215	3670873	760032	314	59			foliation inclined	Metagraywacke
OH216	3670869	759998	261	39			foliation inclined	Metagraywacke
OH217	3670775	759950	214	63			foliation inclined	Schist
OH218	3670699	759933	228	53			foliation inclined	Schist
OH218	3670699	759933			031	15	lineation inclined	Schist
OH219	3670601	759965	250	24			foliation inclined	Schist
OH220	3670589	759930	212	58			foliation inclined	Schist
OH221	3670591	759904	195	44			fold axes surface	Metagraywacke
OH221	3670591	759904			218	52	fold hinge	Metagraywacke
OH222	3670558	759888	244	64			foliation inclined	Metagraywacke
OH223	3670517	759846	080	55			foliation inclined	Metagraywacke
OH224	3670486	759788	205	60			foliation inclined	Schist
OH225	3670460	759732	221	51			foliation inclined	Metagraywacke
OH226	3670448	759664	190	40			foliation inclined	Schist

Station ID	Location Data		Planar Features		Linear Features		Station Type	Rock Type
	Northing ⁽¹⁾	Eastng ⁽¹⁾	Strike ⁽²⁾	Dip ⁽³⁾	Trend ⁽²⁾	Plunge ⁽⁴⁾		
OH227	3672288	768002					float	High Falls Granite
OH228	3672346	768072	053	58			foliation inclined	High Falls Granite
OH229	3672528	767973					float	High Falls Granite
OH230	3672701	767734	102	67			foliation inclined	High Falls Granite
OH231	3672695	767714	075	64			foliation inclined	High Falls Granite
OH232	3673197	767660	056	61			foliation inclined	Biotite Gneiss
OH233	3673205	767723	058	61			foliation inclined	Metagraywacke
OH234	3673197	767948	041	62			foliation inclined	Metagraywacke
OH235	3673196	767994	328	76			foliation inclined	High Falls Granite
OH236	3673189	768063	072	51			foliation inclined	High Falls Granite
OH237	3673031	768031	114	58			foliation inclined	High Falls Granite
OH238	3672864	767953	225	66			foliation inclined	High Falls Granite
OH239	3672849	767874	216	60			foliation inclined	High Falls Granite
OH240	3672756	767224					float	Amphibolite
OH241	3672655	767168					float	Metagraywacke
OH242	3672706	767175	222	44			foliation inclined	Metagraywacke
OH243	3671998	767772	068	18			foliation inclined	Metagraywacke
OH244	3672010	767867	222	47			foliation inclined	Metagraywacke
OH244	3672010	767867			030	16	lineation inclined	Metagraywacke
OH245	3670568	766140	070	54			foliation inclined	Metagraywacke
OH246	3670689	766185	074	54			foliation inclined	High Falls Granite
OH247	3670755	766209	057	57			foliation inclined	High Falls Granite
OH248	3671134	766308	074	55			foliation inclined	High Falls Granite
OH249	3671174	766318	064	66			foliation inclined	High Falls Granite
OH250	3671009	764423					float	Metagraywacke
OH251	3670914	764362					float	Calc-silicate
OH252	3670904	764368	036	61			foliation inclined	Metagraywacke
OH253	3670494	764284	241	51			foliation inclined	Metagraywacke
OH254	3670458	764077	156	45			foliation inclined	Metagraywacke
OH255	3670916	763666	056	48			foliation inclined	High Falls Granite
OH256	3671137	764221	210	54			foliation inclined	Schist
OH257	3671821	758397					float	Schist
OH258	3671907	758597					float	Pegmatite
OH259	3671929	758691					float	Gondite
OH260	3671998	758737					float	Gondite
OH261	3672051	758817					float	Gondite
OH262	3672226	758643					outcrop	Gondite
OH263	3672282	758620	130	18			foliation inclined	Granite
OH264	3672497	759056	074	66			foliation inclined	Granite
OH265	3672026	759362	040	72			foliation inclined	Granite
OH266	3672618	765997	210	63			foliation inclined	Metagraywacke
OH267	3672797	765811	226	56			foliation inclined	Metagraywacke
OH268	3673004	765357	232	40			foliation inclined	Metagraywacke
OH269	3672981	765449	069	74			foliation inclined	Metagraywacke
OH270	3673031	765354	023	67			foliation inclined	Schist
OH271	3673449	764854					float	Gondite
OH272	3673539	764811	206	46			foliation inclined	Schist
OH273	3673530	764815	214	50			fold axes surface	Schist
OH273	3673530	764815			214	19	fold hinge	Schist
OH274	3673927	764649	226	19			foliation inclined	Schist
OH275	3675176	763997	049	71			foliation inclined	Schist
OH276	3676399	766257	224	61			foliation inclined	Schist
OH277	3676252	766428	120	48			foliation inclined	Schist
OH278	3676170	766365	242	41			foliation inclined	Metagraywacke
OH279	3676098	766420					float	Gondite

Station ID	Location Data		Planar Features		Linear Features		Station Type	Rock Type
	Northing ⁽¹⁾	Eastng ⁽¹⁾	Strike ⁽²⁾	Dip ⁽³⁾	Trend ⁽²⁾	Plunge ⁽⁴⁾		
OH280	3676108	766480					float	Metagraywacke
OH281	3676104	766482	283	25			foliation inclined	Metagraywacke
OH282	3676076	766562					float	Granite
OH283	3675979	766904					float	Gondite
OH284	3675945	767125					float	Gondite
OH285	3675892	767209	160	31			foliation inclined	Granite
OH286	3675945	767218	109	44			foliation inclined	Granite
OH287	3675960	767247	242	23			foliation inclined	Mylonite
OH288	3676125	767212					float	Granite
OH289	3676136	767230	168	64			foliation inclined	Metagraywacke
OH290	3676404	767043					float	Granite
OH291	3676486	766904	158	42			foliation inclined	Metagraywacke
OH292	3676449	766772	070	81			foliation inclined	Metagraywacke
OH293	3676453	766733	074	63			foliation inclined	Metagraywacke
OH294	3676451	766647	202	21			foliation inclined	Metagraywacke
OH295	3676361	766694					float	Calc-silicate
OH296	3676350	766752					float	Gondite
OH297	3676258	766805					float	Gondite
OH298	3676271	766714					float	Gondite
OH299	3676195	766677					float	Gondite
OH300	3670664	758455	049	36			foliation inclined	Schist
OH301	3670325	766669					float	Amphibolite
OH302	3670301	766684	116	58			foliation inclined	High Falls Granite
OH303	3670391	766776	086	19			foliation inclined	Metagraywacke
OH304	3670411	766810	098	50			foliation inclined	High Falls Granite
OH305	3671434	763396					float	Metagraywacke
OH306	3671425	763426					float	MS Schist
OH307	3671540	763646					float	Biotite Gneiss
OH308	3671538	763675					float	Mylonite
OH309	3671539	763747					float	Mylonite
OH310	3671531	763775					float	MS Schist
OH311	3671676	763861					float	Granite
OH312	3671723	763916					float	Biotite Gneiss
OH313	3671861	764127	200	34			foliation inclined	High Falls Granite
OH314	3672115	764086					float	Amphibolite
OH315	3672254	764078					float	MS Schist
OH316	3672231	763648					float	High Falls Granite
OH317	3672746	764650					float	Gondite
OH318	3672736	764791					float	Metagraywacke
OH319	3673006	764892					float	Metagraywacke
OH320	3673040	764893	104	46			foliation inclined	Metagraywacke
OH321	3673082	764977					float	Calc-silicate
OH322	3673120	765056					float	Metagraywacke
OH323	3673121	765061	216	48			foliation inclined	BT Schist
OH324	3673229	765002	053	44			foliation inclined	Metagraywacke
OH325	3673200	764945	059	40			foliation inclined	Metagraywacke
OH326	3673182	764886					float	Gondite
OH327	3673114	764856	056	64			foliation inclined	Metagraywacke
OH328	3673116	764826	031	72			foliation inclined	Metagraywacke
OH329	3673086	764779	068	54			foliation inclined	Metagraywacke
OH330	3672994	764645					float	Amphibolite
OH331	3673027	764626					float	Metagraywacke
OH332	3673068	764526					float	Gondite
OH333	3673330	764287	116	42			foliation inclined	MS Schist
OH334	3673218	764270	126	22			foliation inclined	MS Schist

Station ID	Location Data		Planar Features		Linear Features		Station Type	Rock Type
	Northing ⁽¹⁾	Eastings ⁽¹⁾	Strike ⁽²⁾	Dip ⁽³⁾	Trend ⁽²⁾	Plunge ⁽⁴⁾		
OH335	3673452	765705					float	Mylonite
OH336	3673498	765827					float	Mylonite
OH337	3673507	765900	104	64			foliation inclined	Mylonite
OH338	3673533	765740					float	Schist
OH339	3673709	765684					float	Gondite
OH340	3673791	765653					float	Gondite
OH341	3673833	765652	071	45			foliation inclined	Schist
OH342	3673859	765614					float	Schist
OH343	3673733	765294					float	Granite
OH344	3673484	765173	074	64			foliation inclined	Schist
OH345	3674640	767212	185	65			foliation inclined	Metagraywacke
OH346	3674594	766958	120	55			foliation inclined	High Falls Granite
OH347	3674557	767003	200	62			foliation inclined	Schist
OH348	3674009	763112					float	Schist
OH349	3674404	763525					float	Schist
OH350	3674540	763445	208	70			foliation inclined	Schist
OH351	3675069	763342	065	66			foliation inclined	MS Schist
OH352	3675098	762844	216	70			foliation inclined	Schist
OH353	3674746	763130					float	Gondite
OH354	3674236	763039	170	36			foliation inclined	Schist
OH355	3673676	762564	152	46			foliation inclined	Schist
OH355	3673676	762564			200	30	lineation inclined	Schist
OH356	3673670	762537	194	50			foliation inclined	Schist
OH357	3672245	762033					float	Granite
OH358	3671411	761840	234	08			foliation inclined	Metagraywacke
OH359	3671103	762696	148	28			foliation inclined	Metagraywacke
OH360	3669421	763516	225	22			foliation inclined	Metagraywacke
OH361	3670216	761136					float	Gondite
OH362	3669728	761108	233	74			foliation inclined	MS Schist
OH363	3669406	761056	074	46			foliation inclined	MS Schist
OH363	3669406	761056			200	24	lineation inclined	MS Schist
OH364	3669294	760884					float	Gondite
OH365	3669295	760952	224	44			foliation inclined	MS Schist
OH365	3669295	760952			244	24	lineation inclined	MS Schist
OH366	3669159	761134	254	49			foliation inclined	High Falls Granite
OH367	3668576	761112	190	49			foliation inclined	High Falls Granite
OH368	3669436	760428					float	MS Schist
OH369	3669589	760614	054	65			foliation inclined	MS Schist
OH370	3670203	760444	211	50			foliation inclined	Schist
OH371	3675514	764718	155	52			foliation inclined	Metagraywacke
OH372	3675481	764797	075	38			foliation inclined	Granite
OH373	3675434	765012	216	64			foliation inclined	Schist
OH374	3675461	765101	039	41			foliation inclined	Schist
OH375	3675656	765285	175	54			foliation inclined	Granite
OH376	3675776	765457					float	Granite
OH377	3675911	765443	175	68			foliation inclined	Schist
OH378	3675852	763918	066	66			foliation inclined	Schist
OH379	3676465	766229	170	51			foliation inclined	Granite
OH380	3676463	766101	164	40			foliation inclined	Granite
OH381	3676455	766066	136	56			foliation inclined	Granite
OH382	3676346	765950	155	44			foliation inclined	Granite
OH383	3676332	765929	175	44			foliation inclined	Granite
OH384	3676324	765873	144	38			foliation inclined	Granite
OH385	3676322	765841	140	40			foliation inclined	Granite
OH386	3676236	765778	210	46			foliation inclined	Granite

Station ID	Location Data		Planar Features		Linear Features		Station Type	Rock Type
	Northing ⁽¹⁾	Eastings ⁽¹⁾	Strike ⁽²⁾	Dip ⁽³⁾	Trend ⁽²⁾	Plunge ⁽⁴⁾		
OH387	3676185	765760	075	42			foliation inclined	Granite
OH388	3676142	765738	150	39			foliation inclined	Granite
OH389	3676085	765688	070	53			foliation inclined	Granite
OH390	3676064	765658	145	40			foliation inclined	Granite
OH391	3676029	765621	154	42			foliation inclined	Granite
OH392	3676109	765479	121	56			foliation inclined	Schist
OH393	3676131	765475	225	64			foliation inclined	Schist
OH394	3676652	765378	226	60			foliation inclined	Schist
OH395	3676963	766280	045	80			foliation inclined	Metagraywacke
OH396	3676619	766289	190	62			foliation inclined	Schist
OH397	3673114	763160	208	55			foliation inclined	Metagraywacke
OH397	3673114	763160			234	15	lineation inclined	Metagraywacke
OH398	3673103	763234					float	Gondite
OH399	3673174	763289	030	55			foliation inclined	Schist
OH400	3673233	763267	047	78			foliation inclined	Biotite Gneiss
OH401	3673028	763383					float	Gondite
OH402	3672904	763136					float	Gondite
OH403	3672938	762946					float	Granite
OH404	3672934	762936	336	54			foliation inclined	Granite
OH405	3673094	762977	065	40			foliation inclined	Schist
OH406	3675739	767654					float	High Falls Granite
OH407	3675693	767865					float	High Falls Granite
OH408	3676156	768053	234	30			foliation inclined	Metagraywacke
OH409	3676317	767828					float	High Falls Granite
OH410	3676473	767631	072	30			foliation inclined	Granite
OH411	3676442	767534	196	40			foliation inclined	Metagraywacke
OH412	3676530	767535	165	33			foliation inclined	Metagraywacke
OH413	3676088	767510	160	32			foliation inclined	Schist
OH414	3673862	766603					float	High Falls Granite
OH415	3673857	766918	204	53			foliation inclined	Schist
OH416	3673848	767103	241	58			foliation inclined	High Falls Granite
OH417	3673648	767523					float	High Falls Granite
OH418	3673219	767087	220	60			foliation inclined	Metagraywacke
OH419	3673339	767008	185	55			foliation inclined	Schist
OH420	3673583	766463	190	66			foliation inclined	Schist
OH421	3673735	766334	215	72			foliation inclined	Schist
OH422	3674213	766900	128	55			foliation inclined	High Falls Granite
OH423	3674303	766929	232	64			foliation inclined	High Falls Granite
OH424	3674286	767011	185	44			foliation inclined	High Falls Granite
OH425	3674273	767041	208	46			foliation inclined	High Falls Granite
OH426	3674281	767376					float	Schist
OH427	3674322	767512					float	High Falls Granite
OH428	3674318	767592	150	34			foliation inclined	High Falls Granite
OH429	3673908	767703					float	Metagraywacke
OH430	3673812	767725	080	30			foliation inclined	Metagraywacke
OH431	3673702	767754	160	40			foliation inclined	High Falls Granite
OH432	3673635	767771	151	49			foliation inclined	High Falls Granite
OH433	3673386	767887	162	25			foliation inclined	High Falls Granite
OH434	3673306	767960	072	65			foliation inclined	High Falls Granite
OH435	3673339	768240	071	56			foliation inclined	High Falls Granite
OH436	3673364	768378	095	46			foliation inclined	High Falls Granite
OH437	3674295	766042	205	53			foliation inclined	Granite
OH438	3674354	766826	138	60			foliation inclined	High Falls Granite
OH439	3674725	766295					float	Diabase Dike
OH440	3674726	766297	145	38			foliation inclined	MS Schist

Station ID	Location Data		Planar Features		Linear Features		Station Type	Rock Type
	Northing ⁽¹⁾	Eastng ⁽¹⁾	Strike ⁽²⁾	Dip ⁽³⁾	Trend ⁽²⁾	Plunge ⁽⁴⁾		
OH441	3674745	766297	068	46			foliation inclined	Metagraywacke
OH441	3674745	766297			237	26	lineation inclined	Metagraywacke
OH442	3674902	766680	170	30			foliation inclined	Schist
OH443	3674511	765665	067	64			foliation inclined	Metagraywacke
OH444	3674497	765669					float	Gondite
OH445	3674412	765699	208	64			foliation inclined	MS Schist
OH446	3674180	765748					float	Metagraywacke
OH447	3673942	765592					float	Gondite
OH448	3674298	765411					float	MS Schist
OH449	3674394	765410					float	Gondite
OH450	3674851	765173	195	40			foliation inclined	Metagraywacke
OH451	3676764	764693	192	58			foliation inclined	Schist
OH452	3676960	766403	136	54			foliation inclined	Schist
OH453	3676997	766622	171	71			foliation inclined	Schist
OH454	3677597	767462	078	32			foliation inclined	Metagraywacke
OH455	3677914	767689	082	32			foliation inclined	Metagraywacke
OH456	3677385	767319	182	62			foliation inclined	Schist
OH456	3677385	767319			238	16	lineation inclined	Schist
OH457	3677746	766820	212	42			foliation inclined	MS Schist
OH458	3677657	766900	252	60			foliation inclined	MS Schist
OH459	3676918	767418	132	54			foliation inclined	Granite
OH460	3676771	767558	164	20			foliation inclined	Schist
OH460	3676771	767558			260	14	lineation inclined	Schist
OH461	3676630	767561	106	48			foliation inclined	Schist
OH462	3675340	767753	218	60			foliation inclined	High Falls Granite
OH463	3674821	767885	126	54			foliation inclined	Metagraywacke
OH464	3674775	767825	146	36			foliation inclined	Metagraywacke
OH465	3674762	767361	220	60			foliation inclined	High Falls Granite
OH466	3674927	767241	142	52			foliation inclined	High Falls Granite
OH467	3675318	767230	138	30			foliation inclined	Metagraywacke
OH468	3672562	765432	075	40			foliation inclined	Metagraywacke
OH469	3673582	764634					float	Gondite
OH470	3673497	764405	190	68			foliation inclined	Schist
OH470	3673497	764405			214	23	lineation inclined	Schist
OH471	3673844	763945					float	Schist
OH472	3674110	764103	060	56			foliation inclined	Schist
OH473	3674140	764301	036	70			foliation inclined	Schist
OH474	3674261	764247	214	44			foliation inclined	Schist
OH475	3674443	764121	046	57			foliation inclined	Schist
OH476	3669379	762362	220	59			foliation inclined	Metagraywacke
OH476	3669379	762362			256	37	lineation inclined	Metagraywacke
OH477	3669369	762328	220	62			foliation inclined	Schist
OH478	3669564	763357	201	61			foliation inclined	Metagraywacke
OH479	3669517	763412	238	45			foliation inclined	Metagraywacke
OH480	3670354	759410	020	70			foliation inclined	MS Schist
OH481	3670456	759568	211	23			foliation inclined	Metagraywacke
OH482	3670259	759109	038	58			foliation inclined	Schist
OH483	3670106	759365	213	65			foliation inclined	Schist
OH484	3669685	759049	225	56			foliation inclined	Schist
OH484	3669685	759049			235	26	lineation inclined	Schist
OH485	3669775	759030	196	62			foliation inclined	Schist
OH486	3669793	759009	225	45			foliation inclined	Schist
OH486	3669793	759009			233	12	lineation inclined	Schist
OH487	3669956	758920	192	68			foliation inclined	Schist
OH488	3669976	758902	199	64			foliation inclined	Metagraywacke

Station ID	Location Data		Planar Features		Linear Features		Station Type	Rock Type
	Northing ⁽¹⁾	Eastings ⁽¹⁾	Strike ⁽²⁾	Dip ⁽³⁾	Trend ⁽²⁾	Plunge ⁽⁴⁾		
OH489	3669912	758661	199	40			foliation inclined	Metagraywacke
OH490	3669906	758648	220	65			foliation inclined	Granite
OH491	3669895	758592	201	35			foliation inclined	Metagraywacke
OH491	3669895	758592	297	88			joint inclined	Metagraywacke
OH492	3669897	758575	210	52			foliation inclined	Metagraywacke
OH493	3669883	758556	222	42			foliation inclined	Biotite Gneiss
OH493	3669883	758556			229	10	lineation inclined	Biotite Gneiss
OH494	3669883	758544	212	50			foliation inclined	Metagraywacke
OH495	3669894	758487	187	58			foliation inclined	Biotite Gneiss
OH496	3669933	758454	222	40			foliation inclined	Metagraywacke
OH497	3669905	758387	201	36			foliation inclined	Metagraywacke
OH498	3669880	758365	216	60			foliation inclined	Schist
OH499	3669750	758388	216	59			foliation inclined	Schist
OH500	3669635	759000	238	40			foliation inclined	Schist
OH501	3669226	758333					float	Granite
OH502	3669410	758203					float	Schist
OH503	3669322	758036					float	Granite
OH504	3669052	758185					float	Schist
OH505	3668682	757686	224	60			foliation inclined	Schist
OH506	3668731	757729	223	66			foliation inclined	Schist
OH507	3668772	757793	045	49			foliation inclined	Schist
OH508	3668785	757794	235	54			foliation inclined	Schist
OH509	3668860	757727	216	50			foliation inclined	Metagraywacke
OH510	3668911	757629	221	60			foliation inclined	Metagraywacke
OH511	3668938	757798	010	34			foliation inclined	Schist
OH512	3668624	757841	224	45			foliation inclined	Metagraywacke
OH513	3668599	757758	238	46			foliation inclined	Metagraywacke
OH514	3668660	758992	202	59			foliation inclined	Metagraywacke
OH515	3668663	758533	209	55			foliation inclined	Schist
OH516	3668665	758490	222	64			foliation inclined	Metagraywacke
OH517	3668675	758317	200	55			foliation inclined	Metagraywacke
OH517	3668675	758317			226	30	lineation inclined	Metagraywacke
OH518	3668691	758306	211	52			foliation inclined	Metagraywacke
OH519	3668699	758266	223	29			foliation inclined	Schist
OH520	3668704	758219	220	54			foliation inclined	Metagraywacke
OH520	3668704	758219			208	14	lineation inclined	Metagraywacke
OH521	3668697	758016	228	70			foliation inclined	Metagraywacke
OH522	3668253	758200	204	35			foliation inclined	Metagraywacke
OH523	3668261	758165	222	44			foliation inclined	Schist
OH524	3675299	766315	108	49			foliation inclined	Schist
OH525	3675264	766295	254	73			foliation inclined	Metagraywacke
OH526	3671713	768003	249	30			foliation inclined	High Falls Granite
OH527	3671731	767952	055	74			foliation inclined	High Falls Granite
OH527	3671731	767952			239	06	lineation inclined	High Falls Granite
OH528	3668996	757133	238	14			foliation inclined	MS Schist
OH529	3669830	757528	211	50			foliation inclined	Metagraywacke
OH530	3670236	757513	085	68			foliation inclined	Metagraywacke
OH531	3670112	758842	222	70			foliation inclined	Schist
OH531	3670112	758842			219	16	lineation inclined	Schist
OH532	3670227	758811	249	41			foliation inclined	MS Schist
OH532	3670227	758811			049	12	lineation inclined	MS Schist
OH533	3670305	758783	186	13			foliation inclined	Granite
OH534	3670375	758759	212	64			foliation inclined	Schist
OH535	3670502	758692	114	64			foliation inclined	Metagraywacke
OH536	3670452	757950	228	56			foliation inclined	MS Schist

Station ID	Location Data		Planar Features		Linear Features		Station Type	Rock Type
	Northing ⁽¹⁾	Easting ⁽¹⁾	Strike ⁽²⁾	Dip ⁽³⁾	Trend ⁽²⁾	Plunge ⁽⁴⁾		
OH536	3670452	757950			242	22	lineation inclined	MS Schist
OH537	3670828	758453	045	70			fold axes surface	Metagraywacke
OH537	3670828	758453			041	18	fold hinge	Metagraywacke
OH538	3670811	758456	085	78			foliation inclined	Metagraywacke
OH539	3672416	761726	165	65			foliation inclined	MS Schist
OH540	3672413	761783	140	46			foliation inclined	Metagraywacke
OH541	3672616	761235	198	56			foliation inclined	Metagraywacke
OH542	3672744	761069	192	68			foliation inclined	Biotite Gneiss
OH543	3671883	759386	252	62			foliation inclined	Granite
OH544	3671752	759359	071	58			foliation inclined	Biotite Gneiss
OH545	3671539	759244	201	50			foliation inclined	Granite
OH546	3671438	759222	190	50			foliation inclined	Biotite Gneiss
OH547	3671437	759222			212	18	lineation inclined	Biotite Gneiss
OH548	3671155	759255	224	68			foliation inclined	Metagraywacke

⁽¹⁾ Coordinates are expressed in meters using universal transverse mercator projection and North American datum 1983 zone 16N.

⁽²⁾ Orientation measurements are expressed using geographic notation.

⁽³⁾ Inclinations measurements are expressed using the right-hand rule, so that the down-dip direction is 90° clockwise rotation from the strike direction.

⁽⁴⁾ The down-plunge direction is in the same orientation as the direction of the trend.

Appendix II
SHRIMP-RG Data

Spot Analysis	% comm 206	U (ppm)	Th (ppm)	²³² Th/ ²³⁸ U	Totals				Isotopic Ratios ⁽¹⁾								Ages (Ma)					
					²³⁸ U/ ²⁰⁶ Pb % err	²⁰⁷ Pb/ ²⁰⁶ Pb % err	% err	²³⁸ U/ ²⁰⁶ Pb % err	²⁰⁷ Pb/ ²⁰⁶ Pb % err	²⁰⁷ Pb/ ²³⁵ U % err	²⁰⁶ Pb/ ²³⁸ U % err	err corr	²³⁸ U/ ²⁰⁶ Pb ⁽²⁾	± 1σ	²⁰⁷ Pb/ ²⁰⁶ Pb ⁽¹⁾	± 1σ	% Discord					
Hornblende Tonalite (J360)																						
J360-1.1	0.32	383	89	0.24	6.0	1.5	.0748	1.2	6.0	1.5	.0733	1.4	1.68	2.0	.1659	1.5	0.7	988	14	1022	27	+ 3
J360-1.2R	0.42	101	16	0.16	5.9	1.1	.0760	1.4	6.0	1.1	.0707	2.5	1.63	2.7	.1672	1.1	0.4	999	11	947	51	- 6
J360-2.1	0.26	903	26	0.03	5.9	0.6	.0751	0.5	5.9	0.6	.0749	0.5	1.76	0.8	.1700	0.6	0.8	1010	6	1064	9	+ 5
J360-2.2R	0.57	162	14	0.09	6.7	1.9	.0737	1.2	6.7	1.9	.0718	1.5	1.48	2.4	.1498	1.9	0.8	897	16	980	32	+ 9
J360-3.1	0.11	164	60	0.38	5.8	1.6	.0741	2.2	5.8	1.6	.0743	2.2	1.76	2.7	.1715	1.6	0.6	1019	16	1050	44	+ 3
J360-4.1	0.08	478	277	0.60	5.5	1.3	.0757	0.6	5.5	1.3	.0756	0.7	1.88	1.5	.1806	1.3	0.9	1069	14	1083	13	+ 1
J360-5.1	0.10	830	633	0.79	5.8	2.3	.0741	0.5	5.8	2.3	.0737	0.5	1.74	2.4	.1715	2.3	1.0	1020	23	1031	10	+ 1
J360-6.1	0.51	232	111	0.50	5.6	2.2	.0787	0.9	5.6	2.2	.0740	1.6	1.81	2.7	.1771	2.2	0.8	1052	22	1041	33	- 1
J360-7.1	0.21	1252	30	0.02	6.2	1.6	.0727	0.4	6.2	1.6	.0728	0.4	1.61	1.6	.1604	1.6	1.0	957	15	1007	9	+ 5
J360-8.1	3.47	350	125	0.37	6.1	2.1	.0997	0.6	6.3	2.1	.0687	2.5	1.50	3.3	.1585	2.1	0.6	950	19	889	53	- 7
Felsic Gneiss (IS632)																						
IS632-1.1	-0.36	194	31	0.16	4.9	4.0	.0769	9.4	4.9	4.0	.0763	9.5	2.13	10.3	.2029	4.0	0.4	1195	48	1101	190	- 9
IS632-2.1	0.13	605	67	0.11	6.0	3.0	.0736	2.1	6.0	3.0	.0737	2.1	1.71	3.6	.1680	3.0	0.8	1000	29	1032	43	+ 3
IS632-3.1	-0.17	232	98	0.44	5.9	2.2	.0715	1.0	5.9	2.2	.0714	1.0	1.67	2.4	.1696	2.2	0.9	1012	21	967	20	- 5
IS632-4.1	0.25	649	73	0.12	5.9	0.6	.0751	2.7	5.9	0.6	.0752	2.7	1.77	2.8	.1709	0.6	0.2	1014	7	1074	55	+ 6
IS632-5.1	0.55	539	54	0.10	6.4	2.8	.0747	0.6	6.4	2.8	.0743	0.7	1.60	2.9	.1561	2.8	1.0	931	25	1049	14	+12
IS632-5.2R	1.23	570	43	0.08	9.4	3.2	.0713	3.6	9.4	3.2	.0685	3.8	1.00	5	.1062	3.2	0.6	645	20	882	79	+28
IS632-6.1	-0.16	522	483	0.96	5.1	1.5	.0770	0.6	5.1	1.5	.0767	0.6	2.07	2	.1957	1.5	0.9	1155	16	1111	12	- 4
IS632-7.1	0.40	410	156	0.39	5.5	4.7	.0785	2.0	5.5	4.7	.0778	2.0	1.95	5	.1814	4.7	0.9	1071	48	1141	41	+ 6
IS632-8.1	0.62	188	20	0.11	5.1	5.1	.0832	8.1	5.1	5.1	.0830	8.1	2.24	9.6	.1956	5.1	0.5	1145	57	1268	158	+10
IS632-8.2R	0.11	981	3	0.00	5.9	3.1	.0736	0.5	5.9	3.1	.0736	0.5	1.72	3.1	.1691	3.1	1.0	1006	30	1029	10	+ 2
IS632-9.1	0.57	1251	31	0.03	8.7	1.1	.0674	0.5	8.7	1.1	.0674	0.5	1.07	1.2	.1150	1.1	0.9	698	8	849	9	+18
IS632-10.1	0.22	301	108	0.37	5.1	1.1	.0803	0.7	5.1	1.1	.0799	0.7	2.17	1.3	.1971	1.1	0.8	1158	12	1193	15	+ 3
IS632-10.2	0.47	743	40	0.06	6.0	6.4	.0759	0.5	6.0	6.4	.0757	0.5	1.73	6.4	.1660	6.4	1.0	986	61	1087	10	+10
IS632-11.1	0.48	518	43	0.09	6.7	5.6	.0727	3.0	6.7	5.6	.0714	3.1	1.46	6.4	.1487	5.6	0.9	891	48	969	63	+ 8
Woodland Gneiss (J182; HF1465)																						
J182-1.1	0.40	806	165	0.21	6.7	0.6	.0722	0.5	6.7	0.6	.0722	0.5	1.49	0.8	.1493	0.6	0.8	894	5	990	11	+10
J182-2.1	-0.06	1509	68	0.05	5.7	2.4	.0736	1.7	5.7	2.4	.0736	1.7	1.78	2.9	.1754	2.4	0.8	1042	24	1028	34	- 1
J182-3.1	-0.31	208	129	0.64	5.5	2.1	.0732	0.9	5.5	2.1	.0728	0.9	1.84	2.3	.1833	2.1	0.9	1089	23	1006	19	- 9
J182-4.1	-0.18	186	94	0.52	5.8	0.9	.0717	1.0	5.8	0.9	.0713	1.1	1.68	1.4	.1712	0.9	0.6	1021	8	964	23	- 6
J182-5.1	0.37	427	180	0.44	6.3	2.2	.0735	0.8	6.3	2.2	.0733	0.8	1.60	2.3	.1579	2.2	0.9	942	20	1021	16	+ 8
J182-6.1	0.05	450	98	0.22	6.5	1.6	.0701	0.8	6.5	1.6	.0695	0.8	1.47	1.8	.1530	1.6	0.9	918	14	913	17	- 1
J182-7.1	0.09	215	138	0.66	6.0	2.5	.0728	0.9	6.0	2.5	.0725	1.0	1.66	2.7	.1657	2.5	0.9	988	24	1000	20	+ 1
J182-7.2	0.11	1118	206	0.19	5.6	3.5	.0756	1.3	5.6	3.5	.0756	1.3	1.86	3.7	.1788	3.5	0.9	1059	36	1083	25	+ 2
J182-8.1	0.02	196	75	0.40	6.1	2.0	.0721	1.9	6.1	2.0	.0715	1.9	1.62	2.8	.1646	2.0	0.7	983	19	972	39	- 1
HF1465-1.1	0.61	98	37	0.38	6.2	3.7	.0760	1.3	6.2	3.7	.0763	1.4	1.69	4.0	.1605	3.7	0.9	953	34	1103	28	+14
HF1465-1.2	0.27	640	78	0.13	6.4	0.6	.0726	1.2	6.4	0.6	.0724	1.2	1.57	1.4	.1568	0.6	0.5	937	6	997	24	+ 6
HF1465-2.1	-0.25	378	136	0.37	5.8	3.9	.0715	1.3	5.8	3.9	.0718	1.3	1.71	4.1	.1729	3.9	0.9	1030	39	978	27	- 6
HF1465-3.1	-0.21	83	37	0.45	4.7	2.0	.0806	1.4	4.7	2.0	.0785	1.8	2.31	2.7	.2136	2.0	0.7	1253	24	1159	36	- 8
HF1465-3.2	0.40	254	139	0.56	6.6	2.9	.0727	3.6	6.6	2.9	.0722	3.7	1.51	4.7	.1517	2.9	0.6	908	26	990	74	+ 9
HF1465-4.1	-0.08	130	62	0.49	5.6	2.0	.0742	2.3	5.6	2.0	.0736	2.3	1.82	3.0	.1793	2.0	0.6	1065	20	1030	47	- 3

Spot Analysis	% comm 206	U (ppm)	Th (ppm)	²³² Th/ ²³⁸ U	Totals				Isotopic Ratios ⁽¹⁾								Ages (Ma)					
					²³⁸ U/ ²⁰⁶ Pb % err	²⁰⁷ Pb/ ²⁰⁶ Pb % err	% err	²³⁸ U/ ²⁰⁶ Pb % err	²⁰⁷ Pb/ ²⁰⁶ Pb % err	²⁰⁷ Pb/ ²³⁵ U % err	²⁰⁶ Pb/ ²³⁸ U % err	err corr	²³⁸ U/ ²⁰⁶ Pb ⁽²⁾	± 1σ	²⁰⁷ Pb/ ²⁰⁶ Pb ⁽¹⁾	± 1σ	% Discord					
HF1465-4.2	0.23	283	104	0.38	6.4	2.2	.0720	0.8	6.4	2.2	.0710	0.9	1.52	2.4	.1553	2.2	0.9	930	20	956	19	+ 3
HF1465-5.1	0.13	136	63	0.48	6.1	1.1	.0730	1.2	6.1	1.1	.0744	1.4	1.69	1.8	.1651	1.1	0.6	982	10	1052	28	+ 7
HF1465-6.1	0.16	601	167	0.29	6.1	2.9	.0729	1.3	6.1	2.9	.0727	1.3	1.64	3.2	.1633	2.9	0.9	974	28	1005	27	+ 3
HF1465-7.1	-0.02	48	23	0.50	5.8	1.4	.0731	1.8	5.8	1.4	.0737	2.0	1.74	2.5	.1714	1.4	0.6	1020	14	1032	40	+ 1
HF1465-7.2	0.33	143	116	0.84	6.5	2.3	.0726	2.7	6.5	2.3	.0719	2.8	1.53	3.6	.1541	2.3	0.6	922	21	983	57	+ 6
HF1465-8.1	0.24	250	83	0.34	6.1	0.9	.0737	3.0	6.1	0.9	.0738	3.0	1.67	3.1	.1637	0.9	0.3	975	8	1035	60	+ 6
HF1465-8.2	-0.37	166	95	0.59	6.0	4.1	.0691	3.3	6.1	4.1	.0686	3.3	1.56	5.2	.1652	4.1	0.8	989	39	885	69	-12
Woodland Gneiss Indium Mounts (J182In; HF1465In)																						
J182In-1.1	0.57	436	101	0.24	6.9	0.9	.0729	2.1	6.9	0.9	.0728	2.1	1.46	2.3	.1458	0.9	0.4	873	7	1007	43	+14
J182In-2.1	0.18	170	127	0.77	6.8	0.9	.0698	1.6	6.9	0.9	.0675	2.3	1.36	2.4	.1460	0.9	0.4	879	7	852	47	- 3
J182In-3.1	0.66	318	107	0.35	7.1	1.8	.0726	0.7	7.1	1.8	.0719	1.1	1.39	2.1	.1402	1.8	0.9	841	14	983	22	+15
J182In-4.1	1.13	144	94	0.68	9.6	3.6	.0701	1.3	9.7	3.6	.0612	3.6	0.87	5.1	.1035	3.6	0.7	635	22	645	78	+ 2
J182In-5.1	0.24	139	76	0.56	7.1	1.0	.0693	3.4	7.2	1.0	.0603	5.2	1.15	5.3	.1388	1.0	0.2	844	8	614	112	-39
J182In-6.1	3.12	38	10	0.26	22.2	8.6	.0768	4.6	22.6	8.8	.0645	22.3	0.39	24.0	.0443	8.8	0.4	275	23	756	471	+64
J182In-7.1	0.66	180	144	0.82	7.4	19.6	.0717	6.3	7.4	19.6	.0716	6.4	1.34	20.7	.1356	19.6	1.0	815	155	974	131	+17
J182In-9.1	-0.42	221	111	0.52	5.8	0.8	.0701	3.4	5.8	0.8	.0697	3.6	1.66	3.7	.1723	0.8	0.2	1029	9	919	74	-12
J182In-11.1	0.68	166	82	0.51	7.4	4.5	.0719	6.1	7.4	4.5	.0704	6.5	1.31	7.9	.1352	4.5	0.6	814	36	940	132	+14
J182In-12.1	-0.05	312	109	0.36	6.4	7.1	.0697	4.0	6.5	7.1	.0672	4.4	1.44	8.3	.1549	7.1	0.9	931	64	843	91	-11
J182In-13.1	0.34	358	145	0.42	7.1	3.2	.0700	1.0	7.1	3.2	.0702	1.2	1.36	3.4	.1402	3.2	0.9	843	26	934	25	+10
J182In-14.1	0.48	313	85	0.28	6.7	0.8	.0730	0.8	6.7	0.8	.0724	1.1	1.50	1.4	.1497	0.8	0.6	896	7	997	23	+10
J182In-15.1	0.60	229	136	0.62	6.8	0.5	.0735	1.4	6.8	0.5	.0726	2.2	1.48	2.3	.1477	0.5	0.2	884	4	1002	45	+12
J182In-16.1	3.60	115	48	0.43	19.4	1.2	.0816	2.6	20.2	1.5	.0510	15.4	0.35	15.5	.0496	1.5	0.1	313	4	242	355	-30
J182In-17.1	-0.10	163	76	0.48	7.0	5.6	.0671	3.2	7.0	5.6	.0671	3.5	1.32	6.6	.1432	5.6	0.9	863	47	840	72	- 3
HF1465In-2.1	1.35	428	30	0.07	16.4	0.5	.0650	1.7	16.4	0.5	.0669	2.0	0.56	2.0	.0610	0.5	0.2	376	2	833	41	+56
HF1465In-3.1	0.23	938	86	0.09	6.5	2.3	.0719	0.4	6.5	2.3	.0720	0.5	1.54	2.3	.1550	2.3	1.0	927	20	984	9	+ 6
HF1465In-4.1	-0.13	1362	143	0.11	6.3	0.5	.0695	0.6	6.3	0.5	.0695	0.6	1.51	0.8	.1576	0.5	0.6	945	5	913	12	- 4
HF1465In-6.1	0.22	1235	172	0.14	6.4	3.6	.0722	0.4	6.4	3.6	.0722	0.4	1.56	3.7	.1570	3.6	1.0	938	33	992	9	+ 6
HF1465In-7.1	0.25	220	72	0.34	6.4	1.6	.0722	0.9	6.4	1.6	.0725	1.2	1.56	2.0	.1558	1.6	0.8	931	15	998	24	+ 7
HF1465In-8.1	0.62	827	100	0.13	6.4	2.3	.0752	2.9	6.4	2.3	.0752	2.9	1.62	3.7	.1558	2.3	0.6	928	20	1073	59	+14
HF1465In-11.1	1.90	209	46	0.23	19.9	1.0	.0679	2.2	20.2	1.1	.0562	7.5	0.38	7.6	.0496	1.1	0.1	311	3	460	167	+33
HF1465In-12.1	0.44	925	142	0.16	6.7	2.9	.0724	0.5	6.7	2.9	.0720	0.6	1.48	3.0	.1487	2.9	1.0	890	25	986	12	+10
HF1465In-13.1	0.38	1231	130	0.11	7.2	2.3	.0703	1.3	7.2	2.3	.0697	1.4	1.34	2.7	.1397	2.3	0.9	841	19	919	28	+ 9
HF1465In-13.2	0.57	1188	147	0.13	7.1	2.8	.0719	1.5	7.1	2.8	.0703	1.6	1.36	3.2	.1400	2.8	0.9	842	23	935	33	+10
HF1465In-14.1	0.04	1100	104	0.10	6.4	2.1	.0704	0.7	6.4	2.1	.0704	0.7	1.51	2.2	.1553	2.1	0.9	930	19	941	15	+ 1
HF1465In-15.1	0.14	1099	154	0.14	7.1	1.7	.0685	0.6	7.1	1.7	.0685	0.6	1.33	1.8	.1406	1.7	0.9	847	14	882	13	+ 4
HF1465In-16.1	0.17	1076	141	0.13	6.8	2.9	.0698	0.7	6.8	2.9	.0697	0.8	1.40	3.0	.1461	2.9	1.0	877	24	918	16	+ 5

Abbreviations: comm—common; err—error; err corr—error correction; discord—discordant (difference between Pb-Pb age and ²³⁸U/²⁰⁶Pb age in percent); R—rim.

⁽¹⁾ 204-corrected

⁽²⁾ 207-corrected

Spot	Trace Element										
	Y (ppm)	La (ppm)	Ce (ppm)	Nd (ppm)	Sm (ppm)	Eu (ppm)	Gd (ppm)	Dy (ppm)	Er (ppm)	Yb (ppm)	Hf (ppm)
Hornblende Tonalite (J360)											
J360-1.1	256	0.734	5.5	0.67	0.8	0.40	5	22	46	107	9743
J360-1.2R	343	0.058	5.3	0.23	0.6	0.14	6	32	65	131	10697
J360-2.1	232	0.017	1.5	0.04	0.1	0.04	1	13	54	183	10458
J360-2.2R	397	0.732	5.6	0.72	1.2	0.52	9	37	71	142	8257
J360-3.1	276	0.007	7.3	0.13	0.5	0.07	4	23	51	111	10841
J360-4.1	2642	0.247	27.4	5.77	13.0	1.40	97	300	408	575	10737
J360-5.1	4643	1.147	27.2	6.39	15.2	2.12	143	483	684	961	8724
J360-6.1	1258	0.188	17.6	1.81	5.0	0.73	41	142	205	306	9870
J360-7.1	256	0.026	1.7	0.07	0.1	0.08	2	16	53	165	10838
J360-8.1	762	0.628	14.2	1.23	2.9	0.95	23	77	124	214	8465
Felsic Gneiss (IS632)											
IS632-1.1	1799	0.024	1.2	0.82	3.7	0.26	45	199	271	375	12176
IS632-2.1	397	0.045	2.4	1.40	5.7	0.08	42	72	43	38	14147
IS632-3.1	736	0.036	9.3	1.45	3.8	0.10	30	88	115	195	11025
IS632-4.1	399	0.028	2.2	1.38	5.7	0.08	44	72	42	39	14127
IS632-5.1	331	0.027	2.2	1.28	4.9	0.05	36	60	34	31	14502
IS632-5.2R	494	1.697	7.6	4.55	5.2	2.02	28	68	62	71	12849
IS632-6.1	6473	0.17	19.7	7.14	16.8	1.09	142	619	1010	1491	10175
IS632-7.1	2176	0.165	8.8	2.03	7.1	0.65	67	233	361	567	10399
IS632-8.1	1449	0.022	0.8	0.66	3.3	0.23	44	186	173	188	12858
IS632-8.2R	577	0.031	0.2	0.04	0.5	0.06	7	53	81	96	14439
IS632-9.1	377	0.172	1.4	0.66	2.4	0.12	20	54	45	47	15230
IS632-10.1	4327	0.077	3.6	4.65	13.8	0.83	118	451	673	1008	12345
IS632-10.2	376	0.05	1.1	0.71	2.9	0.11	28	70	33	25	13980
IS632-11.1	712	1.263	3.3	1.79	2.7	0.42	28	102	74	87	16187
Woodland Gneiss (J182; HF1465)											
J182-1.1	982	0.04	12.6	0.39	1.4	0.03	15	94	191	382	14622
J182-2.1	2500	0.039	1.1	0.38	2.4	0.04	39	255	337	470	13838
J182-3.1	2115	0.04	13.5	3.09	8.6	0.43	68	240	351	545	11143
J182-4.1	1025	0.012	9.5	0.94	3.0	0.09	25	108	183	322	12187
J182-5.1	1632	3.264	21.3	3.24	5.2	0.29	41	172	286	483	11590
J182-6.1	915	1.07	6.7	1.30	2.9	0.07	28	120	106	100	12966
J182-7.1	1669	0.026	11.8	1.82	5.0	0.19	45	181	290	480	11860
J182-7.2	2277	2.532	17.3	2.99	5.3	0.26	46	229	401	719	11979
J182-8.1	942	0.018	10.7	0.83	2.8	0.13	24	99	166	283	11303
HF1465-1.1	481	25.44	266.9	27.97	17.2	2.43	42	68	77	126	9457
HF1465-1.2	618	0.027	5.7	0.27	1.0	0.02	11	59	117	242	13454
HF1465-2.1	968	0.086	12.2	0.76	2.5	0.11	24	103	170	290	11326
HF1465-3.1	754	0.046	3.6	1.79	4.1	0.58	30	90	118	181	9892
HF1465-3.2	183	0.123	6.1	1.24	3.0	0.10	21	37	16	13	11544
HF1465-4.1	786	0.018	6.9	0.91	2.4	0.20	21	84	136	236	10626
HF1465-4.2	576	69.218	69.5	15.52	5.2	0.53	18	62	102	183	11051
HF1465-5.1	596	0.036	5.2	0.93	2.6	0.16	18	67	103	178	10701
HF1465-6.1	485	0.227	8.0	1.04	3.7	0.70	34	88	42	23	12136
HF1465-7.1	486	0.019	4.3	0.63	1.6	0.18	13	52	85	151	10306
HF1465-7.2	174	0.034	4.5	0.74	2.2	0.07	18	35	14	9	11465
HF1465-8.1	302	0.005	4.1	0.56	2.0	0.06	18	52	30	23	11833
HF1465-8.2	161	0.025	4.3	0.63	2.3	0.06	18	34	12	9	11175
Woodland Gneiss Indium Mounts (J182In; HF1465In)											
J182In-1.1	190	0.052	4.3	0.75	2.6	0.09	22	41	14	9	12450
J182In-2.1	149	92.224	56.8	18.89	6.6	0.55	23	34	11	7	9795
J182In-3.1	166	2.163	12.0	1.72	3.1	0.17	20	36	13	9	12007
J182In-4.1	116	12.473	27.6	3.41	2.5	0.19	13	22	10	9	7242
J182In-5.1	149	13.329	39.5	5.49	3.7	0.43	14	26	15	17	11905
J182In-6.1	175	25.542	287.9	23.10	15.2	2.19	34	53	20	19	9285
J182In-7.1	137	0.204	4.9	0.87	2.5	0.08	16	28	11	8	10474
J182In-9.1	180	7.799	23.6	4.49	4.2	0.28	20	37	16	12	11707
J182In-11.1	176	10.113	64.8	8.90	6.5	0.64	22	35	18	19	10840
J182In-12.1	239	13.047	105.5	13.55	9.8	1.05	34	55	21	17	12315
J182In-13.1	196	0.234	11.6	1.13	3.4	0.13	24	38	16	11	12108
J182In-14.1	152	0.435	21.6	0.94	2.3	0.11	15	27	14	13	10435

Spot	Trace Element										
	Y (ppm)	La (ppm)	Ce (ppm)	Nd (ppm)	Sm (ppm)	Eu (ppm)	Gd (ppm)	Dy (ppm)	Er (ppm)	Yb (ppm)	Hf (ppm)
J182In-15.1	228	21.161	42.2	6.53	4.4	0.88	25	43	20	13	11324
J182In-16.1	307	28.382	15.3	6.13	1.5	0.31	6	32	40	52	13236
J182In-17.1	168	0.314	4.5	0.60	1.6	0.10	12	27	18	20	11308
HF1465In-2.1	482	105.522	52.9	19.84	5.6	0.39	9	37	93	201	14835
HF1465In-3.1	722	0.2	5.4	0.57	2.2	0.03	21	90	91	106	12375
HF1465In-4.1	903	0.266	7.9	0.91	2.8	0.04	28	106	119	157	13621
HF1465In-6.1	766	0.045	7.4	0.81	2.8	0.04	24	87	108	139	13189
HF1465In-7.1	824	165.733	108.4	31.39	10.2	0.65	33	93	143	237	10114
HF1465In-8.1	1090	4.188	21.7	2.58	3.6	0.10	28	116	162	220	10088
HF1465In-11.1	276	6.411	4.9	1.57	0.6	0.07	3	20	51	98	16023
HF1465In-12.1	622	12.817	11.1	3.18	2.9	0.08	20	70	91	139	12556
HF1465In-13.1	609	1.863	14.4	1.14	2.4	0.09	21	79	76	73	11229
HF1465In-13.2	651	1.434	8.1	1.38	2.7	0.21	23	85	79	79	11997
HF1465In-14.1	726	0.097	5.8	0.65	2.5	0.04	24	91	89	95	13812
HF1465In-15.1	540	0.947	8.1	0.80	2.4	0.07	21	61	71	101	10425
HF1465In-16.1	675	0.079	7.8	0.71	2.5	0.03	21	76	99	146	12384

Appendix III
LA-ICPMS Data

Spot Analysis	U (ppm)	U/Th	Totals			Isotopic Ratios ⁽¹⁾					Ages (Ma)						
			²⁰⁶ Pb/ ²⁰⁴ Pb	²⁰⁶ Pb/ ²⁰⁷ Pb	% err	²⁰⁷ Pb/ ²³⁵ U	% err	²⁰⁶ Pb/ ²³⁸ U	% err	err corr	²⁰⁶ Pb/ ²³⁸ U	± 1σ	²⁰⁷ Pb/ ²³⁵ U	± 1σ	²⁰⁶ Pb/ ²⁰⁷ Pb	± 1σ	% Discord
Orchard Hill Quadrangle (OH032)																	
OH032-1	54	2.1	39722	12.3408	2.1	2.3496	2.4	.2103	1.1	0.46	1230.4	12.4	1227.4	17.1	1222.2	41.9	100.7
OH032-6	334	1.7	307925	13.0009	0.3	1.8227	1.6	.1719	1.6	0.98	1022.4	14.8	1053.7	10.4	1119.1	5.7	91.4
OH032-7	238	1.9	266668	13.6363	0.7	1.7497	3.0	.1730	2.9	0.97	1028.9	27.7	1027.1	19.3	1023.2	13.6	100.6
OH032-8	165	0.8	139066	12.7190	0.7	2.1588	0.9	.1991	.5	0.61	1170.7	5.7	1167.9	6.1	1162.6	13.8	100.7
OH032-9	191	2.0	258152	12.2285	0.7	2.4047	2.2	.2133	2.1	0.95	1246.2	23.3	1244.0	15.5	1240.2	13.2	100.5
OH032-10	152	2.8	69767	12.7153	1.7	2.2258	10.5	.2053	10.4	0.99	1203.5	114.1	1189.2	74.0	1163.2	34.7	103.5
OH032-11	117	1.2	47086	13.2658	1.3	1.8293	2.8	.1760	2.5	0.89	1045.1	23.9	1056.0	18.2	1078.7	25.2	96.9
OH032-12	71	2.3	50987	12.1577	1.1	2.4363	2.9	.2148	2.7	0.93	1254.5	30.5	1253.4	20.8	1251.5	21.3	100.2
OH032-13	77	3.0	47640	12.3693	1.8	2.2725	2.6	.2039	1.9	0.73	1196.1	20.8	1203.8	18.5	1217.7	35.6	98.2
OH032-14	322	2.2	172624	12.2819	0.4	2.3840	1.3	.2124	1.3	0.95	1241.4	14.4	1237.8	9.7	1231.6	8.5	100.8
OH032-15	160	2.1	120918	12.2746	0.5	2.3843	1.6	.2123	1.5	0.94	1240.9	16.8	1237.9	11.3	1232.8	10.7	100.7
OH032-16	46	4.6	35518	12.6684	3.3	2.1248	3.5	.1952	1.3	0.37	1149.6	13.5	1156.9	24.2	1170.5	64.5	98.2
OH032-17	146	1.1	110841	13.2957	0.7	1.9266	2.0	.1858	1.8	0.93	1098.5	18.4	1090.4	13.1	1074.2	14.5	102.3
OH032-18	283	1.1	69426	11.5572	1.0	2.3567	5.7	.1975	5.7	0.99	1162.1	60.2	1229.6	41.0	1349.9	18.6	86.1
OH032-19	262	2.1	229674	13.5826	1.3	1.6226	6.9	.1598	6.8	0.98	955.9	60.1	979.0	43.4	1031.1	26.9	92.7
OH032-20	166	2.1	84736	12.3141	0.5	2.4550	0.7	.2193	.6	0.79	1278.0	6.8	1258.9	5.4	1226.5	9.0	104.2
OH032-21	33	1.1	21949	12.3841	1.9	2.1332	2.6	.1916	1.8	0.69	1130.0	18.8	1159.6	18.2	1215.3	37.5	93.0
OH032-23	117	1.9	109191	13.3666	0.8	1.8856	1.5	.1828	1.3	0.84	1082.2	12.8	1076.0	10.2	1063.5	16.8	101.8
OH032-24	233	2.2	144999	13.2758	1.1	1.9018	2.3	.1831	2.0	0.87	1084.0	20.1	1081.7	15.3	1077.2	22.6	100.6
OH032-27	140	3.0	71352	13.1750	1.2	1.9279	2.2	.1842	1.8	0.83	1090.0	18.3	1090.8	14.6	1092.4	24.2	99.8
OH032-28	365	12.0	121419	13.2464	0.7	1.8451	4.5	.1773	4.4	0.99	1052.0	42.7	1061.7	29.3	1081.6	14.0	97.3
OH032-29	155	1.7	81195	13.6959	1.9	1.6835	2.3	.1672	1.4	0.59	996.8	12.7	1002.3	14.8	1014.3	37.8	98.3
OH032-30	28	0.8	32668	13.2818	3.8	1.7619	4.2	.1697	1.9	0.44	1010.6	17.5	1031.6	27.4	1076.3	76.0	93.9
OH032-31	198	2.5	216063	12.6376	0.4	2.1738	1.1	.1992	1.0	0.93	1171.2	10.7	1172.7	7.5	1175.4	7.7	99.6
OH032-32	156	2.6	155821	12.6679	0.5	2.1785	0.9	.2002	.7	0.82	1176.1	7.6	1174.2	6.0	1170.6	9.7	100.5
OH032-33	85	1.3	35168	12.6073	1.3	2.1998	2.0	.2011	1.5	0.76	1181.5	16.6	1181.0	14.2	1180.1	26.4	100.1
OH032-34	381	2.1	505015	13.6654	0.7	1.7131	2.0	.1698	1.9	0.93	1010.9	17.5	1013.4	12.9	1018.8	15.2	99.2
OH032-35	76	1.2	42495	13.3152	1.6	1.8587	1.8	.1795	.8	0.46	1064.2	8.3	1066.5	12.2	1071.3	33.0	99.3
OH032-36	56	1.9	26305	13.6050	3.9	1.7970	4.2	.1773	1.7	0.40	1052.3	16.2	1044.4	27.5	1027.8	78.3	102.4
OH032-37	206	5.4	45244	12.9125	4.2	1.9907	5.9	.1864	4.1	0.70	1102.0	41.9	1112.4	40.0	1132.6	84.1	97.3
OH032-38	116	1.4	81392	12.6962	1.0	2.2602	1.5	.2081	1.0	0.72	1218.8	11.6	1200.0	10.3	1166.2	20.2	104.5
OH032-40	129	2.7	207125	12.6427	1.2	2.2168	1.7	.2033	1.2	0.70	1192.8	12.8	1186.4	11.8	1174.6	24.0	101.6
OH032-41	53	2.0	28751	13.7069	3.6	1.8107	4.1	.1800	1.9	0.48	1067.0	19.2	1049.3	26.5	1012.7	72.0	105.4
OH032-42	118	2.9	104488	13.6169	1.0	1.7626	1.4	.1741	1.0	0.68	1034.5	9.1	1031.8	9.1	1026.1	21.0	100.8
OH032-43	109	1.6	83425	12.8598	1.4	2.1366	3.6	.1993	3.3	0.92	1171.5	35.8	1160.7	25.1	1140.8	28.4	102.7
OH032-44	37	1.5	24532	13.6186	4.2	1.7888	4.7	.1767	2.1	0.45	1048.8	20.6	1041.4	30.4	1025.8	84.1	102.2
OH032-45	124	2.2	154571	12.6999	0.6	2.1369	1.7	.1968	1.6	0.94	1158.3	17.1	1160.8	11.9	1165.6	11.8	99.4
OH032-46	58	2.2	36212	13.6791	3.1	1.7681	4.5	.1754	3.2	0.72	1041.9	31.2	1033.8	29.0	1016.8	62.6	102.5
OH032-47	46	1.6	28506	13.4961	2.2	1.7770	2.5	.1739	1.3	0.51	1033.8	12.5	1037.1	16.6	1044.1	44.1	99.0
OH032-48	101	0.9	60798	13.5033	2.5	1.8100	4.1	.1773	3.3	0.80	1052.0	31.6	1049.1	26.8	1043.0	50.1	100.9
OH032-49	166	1.5	124060	12.6870	0.8	2.2274	1.8	.2050	1.6	0.91	1201.9	17.8	1189.7	12.5	1167.6	14.9	102.9
OH032-50	228	1.0	88688	11.9836	0.5	2.4490	7.2	.2128	7.2	1.00	1244.0	81.1	1257.1	51.9	1279.7	10.3	97.2
OH032-51	39	2.4	15525	13.8923	4.0	1.6441	4.2	.1657	1.3	0.31	988.1	12.0	987.3	26.6	985.4	81.4	100.3

Spot Analysis	U (ppm)	U/Th	Totals			Isotopic Ratios ⁽¹⁾					Ages (Ma)						
			²⁰⁶ Pb/ ²⁰⁴ Pb	²⁰⁶ Pb/ ²⁰⁷ Pb	% err	²⁰⁷ Pb/ ²³⁵ U	% err	²⁰⁶ Pb/ ²³⁸ U	% err	err corr	²⁰⁶ Pb/ ²³⁸ U	± 1σ	²⁰⁷ Pb/ ²³⁵ U	± 1σ	²⁰⁶ Pb/ ²⁰⁷ Pb	± 1σ	% Discord
OH032-52	123	1.4	76696	12.8565	1.1	2.1370	2.0	.1993	1.6	0.81	1171.4	17.0	1160.9	13.5	1141.3	22.8	102.6
OH032-53	693	17.9	396949	13.7441	0.3	1.6909	1.0	.1686	.9	0.96	1004.2	8.7	1005.1	6.3	1007.2	5.9	99.7
OH032-55	156	1.7	77850	11.9005	1.0	2.6957	2.8	.2327	2.6	0.94	1348.5	31.7	1327.3	20.6	1293.2	18.8	104.3
OH032-56	859	2.4	132441	13.5054	0.4	1.6121	2.0	.1579	2.0	0.98	945.1	17.3	974.9	12.6	1042.7	8.2	90.6
OH032-57	40	1.0	67426	11.7881	1.8	2.7053	6.9	.2313	6.7	0.97	1341.3	81.2	1329.9	51.5	1311.7	34.2	102.3
OH032-58	248	1.9	205480	11.5902	0.4	2.4724	2.2	.2078	2.1	0.98	1217.3	23.3	1264.0	15.6	1344.4	8.7	90.5
OH032-59	187	3.1	119156	12.7291	0.7	2.0784	2.1	.1919	1.9	0.95	1131.5	20.2	1141.7	14.1	1161.1	13.0	97.5
OH032-60	182	0.9	19474	13.2174	2.4	1.6913	4.5	.1621	3.9	0.85	968.6	34.8	1005.2	28.9	1086.0	47.4	89.2
OH032-61	667	3.1	180085	13.5427	0.3	1.7162	0.8	.1686	.7	0.90	1004.2	6.5	1014.6	5.0	1037.1	6.9	96.8
OH032-62	66	1.6	49155	13.5675	1.7	1.8203	3.3	.1791	2.9	0.87	1062.2	28.4	1052.8	21.9	1033.4	33.6	102.8
OH032-63	150	1.8	166916	11.6636	0.6	2.7689	1.1	.2342	1.0	0.84	1356.6	11.8	1347.2	8.5	1332.2	11.8	101.8
OH032-64	208	2.1	72547	12.2091	0.6	2.5267	2.1	.2237	2.0	0.96	1301.6	23.8	1279.8	15.3	1243.3	12.1	104.7
OH032-65	214	3.3	372678	12.6615	0.5	2.2320	1.1	.2050	1.0	0.90	1201.9	11.0	1191.1	7.9	1171.6	9.9	102.6
OH032-66	215	2.4	196954	13.2390	1.1	1.8521	1.8	.1778	1.4	0.80	1055.1	13.9	1064.2	11.8	1082.8	21.8	97.4
OH032-67	18	2.2	9794	13.4767	7.3	1.6677	7.7	.1630	2.2	0.29	973.5	20.0	996.3	48.7	1047.0	148.1	93.0
OH032-68	798	2.8	390713	13.6097	0.3	1.7398	2.1	.1717	2.1	0.99	1021.7	20.0	1023.4	13.8	1027.1	5.5	99.5
OH032-69	193	1.3	213675	13.2190	0.6	1.9302	1.1	.1851	.9	0.81	1094.5	8.8	1091.6	7.2	1085.8	12.7	100.8
OH032-70	179	1.6	126409	12.8226	0.5	1.9976	1.6	.1858	1.5	0.94	1098.4	15.1	1114.7	10.7	1146.6	10.5	95.8
OH032-71	456	5.0	186442	14.1458	1.1	1.4685	3.7	.1507	3.6	0.96	904.6	30.2	917.5	22.6	948.6	21.7	95.4
OH032-72	116	3.9	118028	12.6870	1.1	2.2093	1.7	.2033	1.3	0.77	1193.0	14.2	1184.0	11.8	1167.6	21.5	102.2
OH032-74	164	2.3	102791	13.4251	1.0	1.8412	1.4	.1793	1.0	0.71	1063.0	10.0	1060.3	9.5	1054.7	20.6	100.8
OH032-75	171	2.2	81582	13.3598	0.8	1.7603	1.9	.1706	1.7	0.91	1015.2	16.4	1031.0	12.4	1064.5	16.2	95.4
OH032-76	167	5.9	98459	13.0794	1.1	2.0203	4.2	.1916	4.1	0.97	1130.3	42.4	1122.4	28.7	1107.0	21.2	102.1
OH032-77	53	1.5	22938	13.5490	2.4	1.8175	2.8	.1786	1.4	0.49	1059.3	13.6	1051.8	18.5	1036.2	49.4	102.2
OH032-78	246	3.6	203883	13.5749	0.7	1.7442	1.3	.1717	1.1	0.85	1021.6	10.8	1025.0	8.6	1032.3	14.2	99.0
OH032-79	304	1.2	181363	13.4068	0.5	1.7775	1.6	.1728	1.5	0.95	1027.7	14.2	1037.3	10.2	1057.5	9.6	97.2
OH032-80	266	3.2	189337	12.6727	0.5	2.1161	2.1	.1945	2.0	0.97	1145.7	21.1	1154.1	14.2	1169.9	9.2	97.9
OH032-81	163	3.2	65821	13.4323	1.0	1.7884	2.3	.1742	2.0	0.89	1035.4	19.2	1041.2	14.7	1053.6	20.6	98.3
OH032-82	266	9.6	153227	13.7289	0.5	1.7065	1.3	.1699	1.1	0.90	1011.7	10.6	1011.0	8.1	1009.5	11.1	100.2
OH032-83	217	2.1	236858	12.3339	0.6	2.4366	1.1	.2180	.9	0.85	1271.1	10.8	1253.5	7.9	1223.3	11.5	103.9
OH032-84	146	2.5	171804	12.7943	0.9	2.0664	1.9	.1917	1.7	0.88	1130.8	17.6	1137.7	13.1	1150.9	18.0	98.3
OH032-85	176	2.6	166987	12.7664	0.8	2.2002	1.3	.2037	1.0	0.79	1195.2	11.3	1181.1	9.1	1155.3	15.8	103.5
OH032-86	52	1.3	59047	13.4341	3.4	1.8267	3.6	.1780	1.2	0.33	1055.9	11.8	1055.1	23.7	1053.4	68.7	100.2
OH032-87	324	10.2	215948	13.2519	0.5	1.8297	2.4	.1759	2.4	0.98	1044.3	22.7	1056.2	15.8	1080.8	10.1	96.6
OH032-88	136	2.1	66581	12.9469	1.2	2.1217	4.8	.1992	4.6	0.97	1171.2	49.4	1155.9	32.9	1127.3	23.2	103.9
OH032-89	208	2.7	199278	12.7761	0.8	2.1401	1.6	.1983	1.4	0.85	1166.2	14.4	1161.9	11.0	1153.7	16.5	101.1
OH032-90	324	2.3	56715	13.5664	0.5	1.8101	3.6	.1781	3.6	0.99	1056.6	34.6	1049.1	23.5	1033.6	10.8	102.2
OH032-91	78	2.0	77539	12.6043	1.4	2.1700	1.6	.1984	.8	0.49	1166.6	8.6	1171.5	11.4	1180.6	28.1	98.8
OH032-92	296	2.2	386426	12.7338	0.6	2.1170	1.4	.1955	1.3	0.90	1151.2	13.3	1154.4	9.6	1160.3	12.0	99.2
OH032-93	88	1.0	37346	13.6343	1.4	1.7328	2.0	.1714	1.5	0.73	1019.6	13.9	1020.8	13.0	1023.5	27.8	99.6
OH032-94	67	0.9	45405	10.7610	1.5	3.3683	2.1	.2629	1.4	0.67	1504.6	18.4	1497.0	16.1	1486.4	29.0	101.2
OH032-95	417	3.8	285261	13.6376	0.3	1.6997	1.0	.1681	1.0	0.95	1001.7	8.9	1008.4	6.4	1023.0	6.3	97.9
OH032-96	68	1.3	41358	13.6141	2.1	1.7637	3.5	.1741	2.8	0.80	1034.9	27.0	1032.2	22.9	1026.5	42.7	100.8
OH032-97	140	6.9	93227	13.4931	1.1	1.8241	3.6	.1785	3.4	0.96	1058.8	33.2	1054.2	23.4	1044.5	21.3	101.4

Spot Analysis	U (ppm)	U/Th	Totals			Isotopic Ratios ⁽¹⁾					Ages (Ma)						
			²⁰⁶ Pb/ ²⁰⁴ Pb	²⁰⁶ Pb/ ²⁰⁷ Pb	% err	²⁰⁷ Pb/ ²³⁵ U	% err	²⁰⁶ Pb/ ²³⁸ U	% err	err corr	²⁰⁶ Pb/ ²³⁸ U	± 1σ	²⁰⁷ Pb/ ²³⁵ U	± 1σ	²⁰⁶ Pb/ ²⁰⁷ Pb	± 1σ	% Discord
OH032-98	57	1.5	41872	13.6225	2.0	1.7876	2.3	.1766	1.0	0.44	1048.4	9.6	1040.9	14.7	1025.2	41.1	102.3
OH032-99	55	1.4	68043	10.9319	1.1	3.3170	1.7	.2630	1.2	0.74	1505.1	16.3	1485.1	12.9	1456.5	21.3	103.3
OH032-100	39	1.6	18309	13.3009	4.4	1.7679	4.6	.1705	1.6	0.34	1015.1	15.0	1033.8	30.1	1073.4	87.6	94.6
Forsyth Quadrangle (F529; F622)																	
F529-1	322	9.7	81220	13.9224	0.7	1.5319	2.6	.1547	2.5	0.96	927.2	21.3	943.3	15.8	981.1	14.9	94.5
F529-2	225	3.0	104569	13.6655	1.6	1.6164	3.4	.1602	3.0	0.88	957.9	26.7	976.6	21.4	1018.8	33.2	94.0
F529-3	519	3.1	53772	13.7269	0.7	1.5661	2.2	.1559	2.0	0.94	934.0	17.7	956.9	13.3	1009.8	14.3	92.5
F529-4	392	10.8	201560	13.1879	7.6	1.9945	10.8	.1908	7.7	0.71	1125.6	79.5	1113.7	73.1	1090.5	151.5	103.2
F529-5	181	2.2	127223	13.3225	1.3	1.6701	6.7	.1614	6.5	0.98	964.4	58.5	997.2	42.3	1070.2	26.5	90.1
F529-6	507	6.4	54225	12.7593	1.7	1.8517	5.0	.1714	4.7	0.94	1019.5	44.7	1064.0	33.3	1156.4	34.4	88.2
F529-7	185	1.3	133376	10.7016	3.3	2.7878	6.1	.2164	5.1	0.84	1262.7	58.3	1352.3	45.5	1496.9	63.3	84.4
F529-8	321	20.4	178884	13.4284	1.4	1.8438	6.8	.1796	6.6	0.98	1064.6	65.0	1061.2	44.7	1054.2	28.9	101.0
F529-9	481	24.1	118266	14.1576	0.6	1.3521	3.6	.1388	3.6	0.99	838.1	28.3	868.5	21.3	946.8	11.9	88.5
F529-11	138	0.4	25991	16.7407	5.0	.8054	5.2	.0978	1.3	0.26	601.5	7.7	599.9	23.5	594.0	108.7	101.3
F529-12	467	17.1	157590	13.4077	1.4	1.6805	10.2	.1634	10.1	0.99	975.7	91.6	1001.2	65.1	1057.3	28.5	92.3
F529-13	487	2.2	249904	12.6236	0.4	2.1340	1.4	.1954	1.4	0.97	1150.4	14.5	1159.9	9.9	1177.6	7.4	97.7
F529-14	251	3.6	204370	12.5124	2.5	2.3470	5.3	.2130	4.6	0.88	1244.7	52.5	1226.7	37.5	1195.0	49.2	104.2
F529-15	848	2.0	61413	12.8372	0.3	1.9622	1.8	.1827	1.8	0.99	1081.7	17.8	1102.6	12.2	1144.3	5.4	94.5
F529-16	362	13.6	108389	13.9532	1.1	1.6411	3.2	.1661	3.0	0.94	990.5	27.7	986.1	20.3	976.5	22.9	101.4
F529-17	709	8.3	348428	13.9134	0.3	1.5444	2.6	.1558	2.5	0.99	933.6	22.1	948.3	15.8	982.4	5.8	95.0
F529-18	389	5.6	6778	14.1729	2.1	1.3237	6.3	.1361	5.9	0.94	822.4	45.8	856.1	36.4	944.6	43.1	87.1
F529-19	620	10.2	310325	13.6167	0.7	1.6087	2.9	.1589	2.9	0.97	950.5	25.4	973.6	18.5	1026.1	13.3	92.6
F529-20	350	6.1	208248	13.7963	1.0	1.6182	3.7	.1619	3.5	0.96	967.4	31.5	977.3	22.9	999.5	21.1	96.8
F529-21	542	13.7	192871	13.7047	0.8	1.7233	4.0	.1713	3.9	0.98	1019.2	36.7	1017.2	25.6	1013.0	16.9	100.6
F529-21	372	1.4	298644	12.7921	1.3	1.9057	4.6	.1768	4.4	0.96	1049.5	42.3	1083.1	30.4	1151.3	26.2	91.2
F529-22	158	3.9	97972	12.7698	1.0	2.2428	3.8	.2077	3.7	0.96	1216.7	41.1	1194.5	27.0	1154.7	20.4	105.4
F529-23	603	12.2	231062	12.9841	1.5	1.7332	7.0	.1632	6.8	0.98	974.6	61.9	1021.0	45.1	1121.7	30.1	86.9
F529-24	631	7.4	240685	13.6497	0.4	1.6908	4.4	.1674	4.4	1.00	997.7	40.3	1005.1	27.9	1021.2	7.7	97.7
F529-25	247	1.9	213389	12.5772	1.7	2.1625	4.3	.1973	4.0	0.92	1160.6	42.1	1169.1	29.9	1184.9	33.4	98.0
F529-26	155	6.0	59096	12.6016	3.0	2.3058	9.7	.2107	9.3	0.95	1232.8	104.0	1214.1	69.1	1181.0	59.5	104.4
F529-27	583	14.3	174754	14.0117	0.6	1.5311	4.3	.1556	4.3	0.99	932.2	37.3	942.9	26.6	968.0	11.3	96.3
F529-28	358	8.8	129884	13.9662	0.7	1.4917	3.7	.1511	3.6	0.98	907.1	30.6	927.0	22.4	974.6	14.6	93.1
F529-29	192	1.4	122929	9.7942	0.7	3.9282	4.5	.2790	4.5	0.99	1586.5	63.1	1619.5	36.8	1662.7	12.9	95.4
F529-30	404	3.4	146280	13.2713	1.3	1.6491	9.0	.1587	8.9	0.99	949.7	78.9	989.2	57.1	1077.9	25.5	88.1
F529-32	531	8.0	22985	13.4722	1.0	1.7102	6.5	.1671	6.4	0.99	996.2	59.5	1012.4	41.8	1047.7	19.5	95.1
F529-33	569	8.8	157302	13.7313	0.8	1.6053	6.0	.1599	6.0	0.99	956.1	53.0	972.3	37.7	1009.1	16.6	94.7
F529-34	834	15.8	273768	13.6178	1.8	1.7046	4.0	.1684	3.5	0.89	1003.1	32.9	1010.3	25.5	1025.9	36.8	97.8
F529-35	412	10.5	171701	13.4806	1.0	1.6587	4.3	.1622	4.1	0.97	968.9	37.3	992.9	27.1	1046.4	20.3	92.6
F529-36	291	6.1	174270	13.0283	1.0	1.8925	3.3	.1788	3.1	0.96	1060.6	30.7	1078.5	21.8	1114.8	19.2	95.1
F529-39	121	3.5	76259	13.2062	2.5	1.8800	10.5	.1801	10.2	0.97	1067.3	100.7	1074.1	70.0	1087.8	50.7	98.1
F529-40	989	10.6	983775	13.8174	0.5	1.5619	3.1	.1565	3.1	0.99	937.4	27.0	955.2	19.4	996.5	9.2	94.1
F529-41	304	5.0	128326	13.7389	0.8	1.6319	3.0	.1626	2.9	0.96	971.3	26.3	982.6	19.1	1008.0	17.2	96.4
F529-42	491	4.7	259811	13.5260	1.0	1.6476	2.3	.1616	2.1	0.91	965.8	18.5	988.6	14.4	1039.6	19.2	92.9
F529-44	215	0.7	313662	12.2485	1.3	2.0628	4.8	.1833	4.6	0.96	1084.7	45.8	1136.6	32.6	1237.0	25.2	87.7

Spot Analysis	U (ppm)	U/Th	Totals			Isotopic Ratios ⁽¹⁾					Ages (Ma)						
			²⁰⁶ Pb/ ²⁰⁴ Pb	²⁰⁶ Pb/ ²⁰⁷ Pb	% err	²⁰⁷ Pb/ ²³⁵ U	% err	²⁰⁶ Pb/ ²³⁸ U	% err	err corr	²⁰⁶ Pb/ ²³⁸ U	± 1σ	²⁰⁷ Pb/ ²³⁵ U	± 1σ	²⁰⁶ Pb/ ²⁰⁷ Pb	± 1σ	% Discord
F529-45	235	5.7	114994	12.8801	1.6	2.1245	8.2	.1985	8.1	0.98	1167.0	86.3	1156.8	57.0	1137.7	32.3	102.6
F529-47	409	2.7	197155	11.7653	1.0	2.3925	5.3	.2042	5.2	0.98	1197.6	56.7	1240.4	37.9	1315.4	19.7	91.0
F529-48	366	9.5	148354	10.6014	8.1	2.7419	8.7	.2108	3.1	0.36	1233.2	34.6	1339.9	64.6	1514.7	153.2	81.4
F529-49	388	3.6	300874	12.9653	0.9	2.1134	4.4	.1987	4.3	0.98	1168.5	45.8	1153.2	30.2	1124.6	18.4	103.9
F529-50	307	7.2	131068	13.9156	2.0	1.6048	2.9	.1620	2.2	0.74	967.7	19.4	972.1	18.3	982.0	40.0	98.5
F529-51	342	5.0	109875	13.1644	0.7	1.8045	3.9	.1723	3.8	0.98	1024.7	36.2	1047.1	25.3	1094.1	13.7	93.7
F529-52	351	6.3	147220	13.8739	0.6	1.5935	2.6	.1603	2.5	0.98	958.7	22.4	967.7	16.1	988.1	11.5	97.0
F529-54	172	2.8	48223	12.6328	1.7	2.2813	3.3	.2090	2.9	0.86	1223.6	32.1	1206.5	23.7	1176.1	33.7	104.0
F529-55	496	15.8	394345	13.8949	0.6	1.5413	2.6	.1553	2.5	0.97	930.8	21.8	947.0	16.0	985.1	13.1	94.5
F529-56	637	13.4	159317	13.6965	0.5	1.5879	2.9	.1577	2.8	0.99	944.2	24.8	965.5	17.9	1014.3	9.6	93.1
F529-58	362	5.0	147233	12.9695	0.9	2.0515	5.3	.1930	5.2	0.99	1137.5	54.1	1132.8	35.9	1123.9	17.8	101.2
F529-59	639	12.0	232365	13.9130	0.3	1.5973	4.7	.1612	4.7	1.00	963.3	42.1	969.2	29.5	982.4	6.3	98.1
F529-60	324	6.4	48842	13.6954	1.1	1.5893	9.4	.1579	9.3	0.99	944.9	81.9	966.0	58.5	1014.4	21.5	93.1
F529-61	632	13.7	117865	13.7631	1.4	1.5164	4.6	.1514	4.4	0.95	908.6	37.1	937.0	28.2	1004.4	29.3	90.5
F529-62	455	17.3	230272	13.7798	1.5	1.6394	3.9	.1638	3.7	0.93	978.1	33.3	985.5	24.9	1002.0	29.9	97.6
F529-64	415	5.7	134141	13.7503	0.8	1.7635	7.5	.1759	7.5	0.99	1044.4	71.9	1032.1	48.6	1006.3	17.2	103.8
F529-65	633	11.3	95252	13.8564	0.9	1.5230	5.7	.1531	5.6	0.99	918.0	47.8	939.7	34.7	990.7	18.6	92.7
F529-66	760	14.6	106168	13.6461	1.8	1.6008	3.5	.1584	3.0	0.85	948.0	26.6	970.5	22.1	1021.7	37.1	92.8
F529-67	485	9.0	129051	13.7994	0.4	1.6191	4.1	.1620	4.1	1.00	968.2	37.0	977.7	25.9	999.1	7.9	96.9
F529-68	336	5.1	106826	13.6105	1.1	1.6089	3.5	.1588	3.4	0.95	950.2	29.8	973.7	22.2	1027.0	22.0	92.5
F529-69	295	4.5	45703	13.6870	1.1	1.5058	4.8	.1495	4.7	0.97	898.0	39.4	932.7	29.5	1015.7	23.2	88.4
F529-72	544	9.7	128221	13.9783	0.6	1.5822	3.0	.1604	2.9	0.98	959.0	25.7	963.2	18.4	972.9	12.9	98.6
F529-73	426	9.8	173880	13.5454	0.7	1.6095	2.9	.1581	2.8	0.97	946.3	24.8	973.9	18.1	1036.7	13.2	91.3
F529-74	246	11.9	37156	13.5059	1.9	1.7715	6.1	.1735	5.8	0.95	1031.5	55.0	1035.1	39.5	1042.6	38.8	98.9
F529-75	604	11.4	408253	13.1439	0.6	1.6742	2.4	.1596	2.3	0.97	954.5	20.7	998.8	15.3	1097.2	12.6	87.0
F529-76	343	7.7	179438	13.3717	1.0	1.7645	3.1	.1711	2.9	0.95	1018.3	27.7	1032.5	20.1	1062.7	19.6	95.8
F529-77	241	3.9	82101	12.1453	1.6	2.3765	5.6	.2093	5.3	0.96	1225.3	59.6	1235.6	40.0	1253.5	31.9	97.7
F529-78	535	5.5	42723	13.4132	0.9	1.7616	3.7	.1714	3.6	0.97	1019.6	34.0	1031.4	24.0	1056.5	17.5	96.5
F529-80	747	4.5	129028	12.4011	0.5	2.1928	4.5	.1972	4.5	0.99	1160.4	47.9	1178.8	31.6	1212.6	9.0	95.7
F529-81	340	5.3	127262	13.1892	2.3	1.8124	6.0	.1734	5.5	0.92	1030.6	52.4	1049.9	39.0	1090.3	46.0	94.5
F529-82	389	6.4	249653	13.9846	0.6	1.5424	3.3	.1564	3.3	0.98	936.9	28.6	947.4	20.6	971.9	12.7	96.4
F529-83	172	2.6	82911	13.4265	1.3	1.7897	6.1	.1743	5.9	0.98	1035.6	56.9	1041.7	39.7	1054.5	26.2	98.2
F529-84	325	3.8	13265	13.1135	1.7	2.0125	8.8	.1914	8.7	0.98	1129.0	90.0	1119.7	60.1	1101.8	33.0	102.5
F529-86	250	1.3	18140	5.5587	0.5	9.6818	5.0	.3903	4.9	0.99	2124.3	89.5	2405.0	45.8	2651.9	8.3	80.1
F529-87	294	8.3	88200	12.9713	1.6	1.9140	5.0	.1801	4.7	0.95	1067.3	46.4	1086.0	33.2	1123.6	31.3	95.0
F529-88	883	25.4	142158	13.9195	0.4	1.4643	2.1	.1478	2.0	0.98	888.8	16.8	915.8	12.5	981.5	8.7	90.6
F529-89	709	17.7	214507	14.0903	0.3	1.4840	2.9	.1517	2.9	1.00	910.2	24.4	923.9	17.5	956.5	5.5	95.2
F529-90	405	5.9	74165	14.4269	0.9	1.2079	3.0	.1264	2.8	0.95	767.2	20.4	804.2	16.4	908.1	18.3	84.5
F529-90	408	0.7	31893	12.9034	1.1	2.1049	4.4	.1970	4.2	0.96	1159.1	44.7	1150.4	30.0	1134.0	22.8	102.2
F529-91	310	5.9	199659	13.5380	1.5	1.8518	7.1	.1818	7.0	0.98	1076.9	69.1	1064.1	47.1	1037.8	31.2	103.8
F529-92	397	4.9	68365	13.7199	1.0	1.7646	7.2	.1756	7.1	0.99	1042.8	68.8	1032.5	46.8	1010.8	20.7	103.2
F529-95	340	1.4	45423	13.7454	0.8	1.6261	3.1	.1621	3.0	0.97	968.5	27.0	980.4	19.5	1007.0	15.9	96.2
F529-96	524	15.5	154543	14.0577	0.7	1.6534	8.6	.1686	8.6	1.00	1004.3	79.7	990.9	54.5	961.3	14.4	104.5
F529-97	564	1.4	246916	12.9588	0.9	1.8767	2.8	.1764	2.7	0.94	1047.2	26.0	1072.9	18.8	1125.5	18.6	93.0

Spot Analysis	U (ppm)	U/Th	Totals			Isotopic Ratios ⁽¹⁾					Ages (Ma)						
			²⁰⁶ Pb/ ²⁰⁴ Pb	²⁰⁶ Pb/ ²⁰⁷ Pb	% err	²⁰⁷ Pb/ ²³⁵ U	% err	²⁰⁶ Pb/ ²³⁸ U	% err	err corr	²⁰⁶ Pb/ ²³⁸ U	± 1σ	²⁰⁷ Pb/ ²³⁵ U	± 1σ	²⁰⁶ Pb/ ²⁰⁷ Pb	± 1σ	% Discord
F529-98	763	6.9	227642	14.2320	0.6	1.4186	2.5	.1464	2.5	0.98	880.9	20.3	896.8	15.0	936.1	11.4	94.1
F529-99	607	53.4	540343	14.1224	0.5	1.5092	3.6	.1546	3.6	0.99	926.6	31.0	934.1	22.1	951.9	10.4	97.3
F529-100	583	21.1	265105	13.8345	0.5	1.6275	3.8	.1633	3.7	0.99	975.1	33.7	980.9	23.6	993.9	10.9	98.1
F622-2	72	1.0	23147	13.6740	1.6	1.6836	2.2	.1670	1.4	0.66	995.4	13.3	1002.4	13.9	1017.6	33.1	97.8
F622-3	65	1.9	30456	13.8423	1.8	1.6556	4.2	.1662	3.7	0.90	991.2	34.4	991.7	26.4	992.8	37.5	99.8
F622-4	78	2.5	88044	13.7510	2.6	1.6880	3.2	.1683	1.8	0.57	1003.0	16.9	1004.0	20.2	1006.2	52.6	99.7
F622-5	75	1.8	74102	13.7786	2.0	1.7368	3.4	.1736	2.7	0.81	1031.7	26.1	1022.3	21.8	1002.1	40.1	103.0
F622-6	55	1.1	61890	13.7902	3.1	1.6998	3.8	.1700	2.2	0.59	1012.2	20.9	1008.5	24.2	1000.4	62.0	101.2
F622-7	62	1.1	45763	13.2731	3.1	1.8385	4.5	.1770	3.3	0.73	1050.5	31.5	1059.3	29.4	1077.6	61.4	97.5
F622-8	64	1.1	44085	14.2648	2.8	1.5589	4.2	.1613	3.2	0.75	963.9	28.5	954.1	26.3	931.3	57.7	103.5
F622-9	50	2.0	38891	13.9673	2.5	1.5945	3.5	.1615	2.5	0.70	965.2	22.1	968.1	22.0	974.5	51.4	99.1
F622-10	102	1.0	15308	13.4816	1.6	1.7435	2.3	.1705	1.7	0.72	1014.8	15.5	1024.8	14.8	1046.3	32.3	97.0
F622-11	392	4.5	91216	13.5562	0.9	1.6918	4.2	.1663	4.1	0.98	991.9	37.5	1005.4	26.7	1035.1	18.5	95.8
F622-12	105	1.2	93502	13.5155	1.6	1.7883	10.4	.1753	10.3	0.99	1041.2	98.7	1041.2	67.7	1041.1	32.7	100.0
F622-13	59	1.4	38372	13.4562	2.4	1.8020	3.0	.1759	1.9	0.62	1044.3	17.9	1046.2	19.6	1050.1	47.8	99.5
F622-14	100	0.8	72237	13.4789	2.5	1.7808	3.3	.1741	2.1	0.63	1034.6	20.0	1038.5	21.4	1046.7	51.4	98.8
F622-16	82	0.9	99607	13.7131	1.5	1.7804	2.6	.1771	2.1	0.81	1051.0	20.5	1038.3	17.0	1011.8	31.3	103.9
F622-17	35	3.0	47579	13.4583	5.5	1.8262	6.3	.1783	2.9	0.47	1057.4	28.5	1054.9	41.2	1049.7	111.9	100.7
F622-18	108	0.7	64990	13.5692	1.8	1.7715	2.2	.1743	1.3	0.59	1035.9	12.6	1035.1	14.5	1033.2	36.3	100.3
F622-19	167	3.8	58464	13.3886	1.5	1.7481	6.7	.1697	6.5	0.97	1010.7	60.9	1026.5	43.2	1060.2	30.3	95.3
F622-20	670	10.3	156317	13.8162	0.8	1.5487	2.9	.1552	2.8	0.96	930.0	24.6	950.0	18.2	996.6	15.8	93.3
F622-21	76	0.9	49172	13.8171	1.5	1.7158	1.9	.1719	1.1	0.60	1022.8	10.7	1014.5	12.0	996.5	30.4	102.6
F622-22	86	1.2	128302	13.5710	1.7	1.7584	2.6	.1731	1.9	0.74	1029.0	18.1	1030.3	16.5	1032.9	34.6	99.6
F622-23	200	0.6	83117	13.5801	0.9	1.6694	2.2	.1644	2.0	0.91	981.3	18.5	996.9	14.1	1031.5	18.6	95.1
F622-24	50	1.0	35044	13.4794	2.5	1.8194	3.3	.1779	2.2	0.66	1055.3	21.4	1052.5	21.8	1046.6	50.5	100.8
F622-25	99	1.8	90264	13.3312	1.6	1.7527	3.2	.1695	2.7	0.86	1009.2	25.6	1028.2	20.7	1068.8	33.1	94.4
F622-26	48	2.0	41786	13.7051	1.9	1.7374	2.8	.1727	2.0	0.73	1026.9	19.2	1022.5	17.8	1013.0	38.0	101.4
F622-27	66	1.4	53536	13.3646	2.6	1.7597	3.5	.1706	2.2	0.65	1015.3	21.0	1030.8	22.4	1063.8	53.1	95.4
F622-28	411	2.3	123008	13.1569	0.6	1.9025	2.2	.1815	2.1	0.96	1075.4	20.7	1082.0	14.5	1095.2	12.0	98.2
F622-29	211	2.3	94286	13.8961	0.6	1.5143	3.4	.1526	3.3	0.98	915.6	28.6	936.2	20.8	984.9	13.1	93.0
F622-30	68	1.0	16097	13.7889	3.7	1.6784	4.9	.1679	3.2	0.66	1000.3	29.8	1000.4	31.0	1000.6	74.3	100.0
F622-31	59	1.1	28148	13.5930	2.8	1.6692	3.4	.1646	2.0	0.57	982.1	17.9	996.9	21.8	1029.6	56.8	95.4
F622-32	69	1.9	69931	13.3648	1.3	1.8026	2.0	.1747	1.5	0.74	1038.1	14.4	1046.4	13.2	1063.8	27.1	97.6
F622-32b	59	1.9	7233	13.5077	1.9	1.6188	5.8	.1586	5.5	0.95	948.9	48.7	977.5	36.6	1042.3	37.8	91.0
F622-33	52	1.5	37183	13.7294	2.3	1.7450	3.6	.1738	2.7	0.77	1032.8	26.2	1025.3	23.0	1009.4	45.9	102.3
F622-34	38	2.2	38915	13.5611	4.8	1.8182	5.1	.1788	1.8	0.35	1060.5	17.4	1052.0	33.7	1034.4	97.5	102.5
F622-35	62	4.1	46021	13.5533	2.9	1.8865	7.1	.1854	6.4	0.91	1096.6	64.9	1076.4	46.9	1035.5	58.8	105.9
F622-36	53	1.2	20668	13.8656	2.1	1.6353	4.5	.1645	4.0	0.88	981.5	36.6	983.9	28.6	989.3	43.0	99.2
F622-37	68	3.0	1343	12.9503	3.1	1.8884	4.0	.1774	2.5	0.62	1052.6	24.1	1077.0	26.5	1126.8	62.4	93.4
F622-38	216	0.6	47951	13.6039	0.8	1.7625	1.2	.1739	.9	0.72	1033.5	8.2	1031.8	7.7	1028.0	16.7	100.5
F622-39	79	1.1	50224	13.7363	1.8	1.6984	2.2	.1692	1.3	0.60	1007.7	12.5	1007.9	14.3	1008.4	36.3	99.9
F622-40	117	0.8	159718	13.7367	1.9	1.7422	2.4	.1736	1.6	0.64	1031.8	14.8	1024.3	15.7	1008.3	38.0	102.3
F622-41	464	2.0	122931	12.2159	0.4	2.4763	2.7	.2194	2.7	0.99	1278.7	31.5	1265.1	19.9	1242.2	7.4	102.9
F622-44	136	0.8	81083	13.6538	0.6	1.7004	1.3	.1684	1.1	0.88	1003.2	10.6	1008.7	8.3	1020.6	12.3	98.3

Spot Analysis	U (ppm)	U/Th	Totals			Isotopic Ratios ⁽¹⁾					Ages (Ma)						
			²⁰⁶ Pb/ ²⁰⁴ Pb	²⁰⁶ Pb/ ²⁰⁷ Pb	% err	²⁰⁷ Pb/ ²³⁵ U	% err	²⁰⁶ Pb/ ²³⁸ U	% err	err corr	²⁰⁶ Pb/ ²³⁸ U	± 1σ	²⁰⁷ Pb/ ²³⁵ U	± 1σ	²⁰⁶ Pb/ ²⁰⁷ Pb	± 1σ	% Discord
F622-47	78	1.7	185581	13.1795	2.1	1.8418	3.0	.1761	2.1	0.71	1045.4	20.6	1060.5	19.7	1091.8	42.1	95.8
F622-48	71	2.6	61484	13.3757	1.7	1.7796	5.2	.1726	4.9	0.94	1026.6	46.4	1038.0	33.7	1062.1	34.9	96.7
F622-49	75	1.0	38968	13.7041	2.0	1.7349	2.6	.1724	1.7	0.66	1025.5	16.4	1021.6	16.8	1013.1	39.5	101.2
F622-50	147	0.7	141262	13.6480	1.1	1.7261	1.7	.1709	1.3	0.76	1016.8	12.3	1018.3	11.0	1021.4	22.4	99.6
F622-51	52	2.8	51974	13.3118	2.2	1.8146	3.2	.1752	2.3	0.73	1040.6	22.3	1050.7	20.9	1071.8	44.3	97.1
F622-52	53	1.8	27190	13.5825	2.3	1.6813	3.9	.1656	3.1	0.80	987.9	28.3	1001.5	24.6	1031.2	46.8	95.8
F622-53	75	1.3	47301	13.4867	2.2	1.8873	4.7	.1846	4.1	0.88	1092.1	41.6	1076.6	31.1	1045.5	44.0	104.5
F622-54	507	3.0	299896	13.7797	0.9	1.6159	4.8	.1615	4.7	0.98	965.1	42.5	976.4	30.3	1002.0	18.4	96.3
F622-56	52	1.5	25449	13.7950	2.8	1.7636	3.4	.1765	1.9	0.57	1047.6	18.6	1032.2	21.8	999.7	55.9	104.8
F622-57	52	1.6	47026	13.4332	2.2	1.7507	3.2	.1706	2.2	0.71	1015.2	20.9	1027.4	20.4	1053.5	45.1	96.4
F622-58	87	1.4	56081	13.5244	1.5	1.7965	2.4	.1762	2.0	0.80	1046.3	18.9	1044.2	15.9	1039.8	29.5	100.6
F622-59	193	0.6	150909	13.6392	0.5	1.7213	1.2	.1703	1.1	0.90	1013.6	10.0	1016.5	7.6	1022.7	10.6	99.1
F622-60	52	1.6	38695	13.3948	3.5	1.8315	3.9	.1779	1.7	0.43	1055.6	16.5	1056.8	25.8	1059.3	71.4	99.7
F622-61	113	0.7	51637	13.5896	1.2	1.7506	1.8	.1725	1.4	0.78	1026.1	13.4	1027.4	11.8	1030.1	23.3	99.6
F622-62	53	2.2	50321	13.4813	3.7	1.7980	4.8	.1758	3.1	0.64	1044.0	29.9	1044.7	31.6	1046.3	74.9	99.8
F622-64	82	1.9	76940	13.5487	2.1	1.8677	2.3	.1835	.8	0.34	1086.2	7.6	1069.7	15.0	1036.2	43.1	104.8
F622-65	50	1.6	39178	13.3852	2.9	1.7689	4.7	.1717	3.7	0.79	1021.6	35.0	1034.1	30.4	1060.7	57.9	96.3
F622-66	32	2.6	17540	13.7852	4.3	1.7315	4.7	.1731	1.9	0.39	1029.2	17.7	1020.3	30.4	1001.2	88.1	102.8
F622-67	73	1.8	61075	13.3914	2.1	1.6158	4.4	.1569	3.8	0.87	939.7	33.3	976.3	27.4	1059.8	42.9	88.7
F622-68	53	1.1	49202	13.5799	4.0	1.8145	4.4	.1787	1.9	0.43	1059.9	18.4	1050.7	28.8	1031.5	80.4	102.8
F622-69	108	5.4	91811	13.7180	1.6	1.7194	2.7	.1711	2.2	0.81	1018.0	20.7	1015.8	17.5	1011.1	32.6	100.7
F622-70	121	3.0	82740	13.5172	1.3	1.8428	3.4	.1807	3.2	0.93	1070.6	31.3	1060.9	22.5	1040.9	25.4	102.9
F622-71	46	1.3	24284	13.3777	3.2	1.8163	3.5	.1762	1.4	0.40	1046.3	13.5	1051.3	22.9	1061.8	64.4	98.5
F622-72	84	0.9	37046	13.5485	2.1	1.6731	4.1	.1644	3.5	0.86	981.2	32.3	998.4	26.2	1036.2	42.2	94.7
F622-73	71	1.1	85666	13.3465	2.1	1.8888	3.5	.1828	2.8	0.79	1082.4	27.5	1077.1	23.1	1066.5	42.6	101.5
F622-74	109	1.2	86691	13.5803	1.7	1.7716	1.9	.1745	1.0	0.52	1036.8	9.6	1035.1	12.5	1031.5	33.4	100.5
F622-75	15	2.6	8514	14.0858	8.4	1.6521	9.0	.1688	3.1	0.34	1005.4	28.5	990.4	56.8	957.2	172.5	105.0
F622-76	233	3.9	185330	13.5936	0.7	1.6308	1.6	.1608	1.4	0.91	961.1	12.8	982.2	10.0	1029.5	13.6	93.4
F622-77	94	1.5	45880	13.7221	1.7	1.7422	1.9	.1734	.8	0.43	1030.7	7.7	1024.3	12.1	1010.5	34.2	102.0
F622-79	189	2.5	113008	13.5142	1.2	1.6583	2.6	.1625	2.2	0.87	970.9	20.3	992.7	16.3	1041.4	25.1	93.2
F622-80	114	0.8	70657	13.4662	1.1	1.7260	2.6	.1686	2.3	0.90	1004.3	21.3	1018.3	16.4	1048.6	22.6	95.8
F622-81	109	1.1	96280	13.5275	1.5	1.7472	2.2	.1714	1.7	0.76	1019.9	15.9	1026.1	14.3	1039.4	29.3	98.1
F622-82	74	1.5	106080	13.7226	1.5	1.6557	1.7	.1648	.8	0.48	983.3	7.6	991.7	11.0	1010.4	30.9	97.3
F622-83	183	1.7	84855	13.3680	0.6	1.8137	1.6	.1758	1.5	0.92	1044.3	14.0	1050.4	10.3	1063.3	12.3	98.2
F622-84	46	2.1	19067	13.5915	3.5	1.6731	3.7	.1649	1.1	0.31	984.1	10.2	998.4	23.3	1029.8	70.6	95.6
F622-85	55	1.2	45120	13.5039	2.1	1.7421	2.9	.1706	2.1	0.71	1015.5	19.6	1024.2	18.9	1042.9	41.7	97.4
F622-87	41	2.9	33944	13.3043	4.0	1.8570	4.3	.1792	1.7	0.40	1062.5	16.7	1065.9	28.4	1072.9	79.4	99.0
F622-88	70	1.9	52751	13.5414	1.2	1.8175	4.9	.1785	4.8	0.97	1058.8	46.9	1051.8	32.4	1037.3	24.2	102.1
F622-89	77	1.0	52785	13.5275	1.3	1.7744	3.3	.1741	3.0	0.91	1034.6	28.7	1036.1	21.4	1039.4	27.2	99.5
F622-90	292	0.7	504928	10.5912	1.0	2.9040	4.4	.2231	4.2	0.97	1298.1	49.8	1383.0	32.9	1516.5	19.3	85.6
F622-91	148	0.7	82759	13.3686	1.1	1.8363	1.4	.1780	.8	0.60	1056.3	8.0	1058.5	8.9	1063.2	21.7	99.3
F622-92	75	1.8	62483	13.3002	2.1	1.8683	3.8	.1802	3.1	0.83	1068.2	30.7	1069.9	24.9	1073.5	42.2	99.5
F622-93	108	0.9	81080	13.4013	1.0	1.8292	1.4	.1778	.9	0.69	1054.9	9.1	1056.0	8.9	1058.3	19.8	99.7
F622-94	92	0.9	68631	13.6733	1.7	1.8262	3.1	.1811	2.6	0.84	1073.0	26.0	1054.9	20.5	1017.7	33.9	105.4

Spot Analysis	U (ppm)	U/Th	Totals			Isotopic Ratios ⁽¹⁾					Ages (Ma)						
			²⁰⁶ Pb/ ²⁰⁴ Pb	²⁰⁶ Pb/ ²⁰⁷ Pb	% err	²⁰⁷ Pb/ ²³⁵ U	% err	²⁰⁶ Pb/ ²³⁸ U	% err	err corr	²⁰⁶ Pb/ ²³⁸ U	± 1σ	²⁰⁷ Pb/ ²³⁵ U	± 1σ	²⁰⁶ Pb/ ²⁰⁷ Pb	± 1σ	% Discord
F622-95	113	3.3	110453	13.2011	0.9	1.8476	5.1	.1769	5.0	0.98	1050.0	48.9	1062.6	33.8	1088.5	18.5	96.5
F622-96	21	2.1	13917	13.2000	4.0	1.7952	7.6	.1719	6.4	0.85	1022.4	61.0	1043.7	49.4	1088.7	79.2	93.9
F622-97	167	3.1	189283	13.4901	1.2	1.8071	2.2	.1768	1.9	0.85	1049.5	18.2	1048.0	14.4	1045.0	23.5	100.4
F622-98	22	1.7	11894	13.8810	5.7	1.6897	7.2	.1701	4.4	0.61	1012.7	41.2	1004.6	46.0	987.1	116.3	102.6
F622-99	58	2.3	30434	13.4767	2.5	1.8072	5.7	.1766	5.1	0.90	1048.6	49.6	1048.1	37.4	1047.0	51.1	100.2
F622-100	144	1.6	79748	13.4534	1.8	1.8278	2.6	.1783	1.9	0.74	1057.9	19.0	1055.5	17.2	1050.5	35.3	100.7
F622-101	92	1.4	81024	13.5971	0.9	1.7387	1.8	.1715	1.6	0.86	1020.2	14.9	1023.0	11.8	1029.0	18.6	99.1

Abbreviations: err—error; err corr—error correction; discord—discordant (difference between Pb-Pb age and ²³⁸U/²⁰⁶Pb age in percent).

⁽¹⁾ 204-corrected

VITA

Justin Randolph Rehrer was born in Pottsville, Pennsylvania, on August 5, 1982 to Randolph R. and Cindy L. Rehrer and was raised in Pine Grove, Pennsylvania. He graduated from Pine Grove Area High School in 2000 and enlisted in the United States Army later that year. Justin served four years on active duty as a Sapper assigned to the 307th Engineer Battalion, 82nd Airborne Division, and completed combat deployments to both Afghanistan, in support of Operation Enduring Freedom in 2002, and Iraq, in support of Operation Iraqi Freedom in 2003. Following his discharge from active service Justin enlisted in the Pennsylvania Army National Guard and pursued several civilian jobs ranging from construction to heavy equipment maintenance. In the fall of 2005 he decided to pursue his goal of achieving an engineering degree and attended classes for two years at the Pennsylvania State University fulfilling that interest until the desire to study natural sciences became too great to resist. In 2007 Justin transferred to Bloomsburg University of Pennsylvania, realized his true passion for geology, and recieved a Bachelor of Science degree in 2009. Justin also completed the Reserve Officer Training Corps program at Bloomsburg University and received his commission as an engineer officer in United States Army; he elected to continue serving in the Army National Guard. Justin gained employment with an environmental consulting firm in Pittsburgh, Pennsylvania, before deciding to further his educational interests in geology. In 2011 he accepted a graduate teaching assistantship from the University of Tennessee and moved to Knoxville to study under the advisement of Dr. Robert D. Hatcher, Jr. in the field of tectonics and structural geology. Like his colleague, Matt Huebner, and undergraduate mentor, Joe Hill, Justin hates to refer to himself in the third person.